BROADBAND INTERFEROMETRY OF LIGHTNING

by

Michael Stock

Submitted in Partial Fulfillment
of the Requirements for the Degree of
Doctor of Science in Physics

New Mexico Institute of Mining and Technology
Socorro, New Mexico
December, 2014

UMI Number: 3684400

UMI

Dissertation Publishing

UMI 3684400

ProQuest®

BROADBAND INTERFEROMETRY OF LIGHTNING

by

Michael Stock

ABSTRACT

A lightning interferometer is an instrument which determines the direction to a lightning-produced radio point source by correlating the signal received at two or more antennas. Such instruments have been used with great success for several decades in the study of the physical processes present in a lightning flash. However, previous instruments have either been sensitive to only a narrow radio bandwidth so that the correlation can be done using analog hardware, or have been sensitive to a wide bandwidth but only recorded a short duration of the radiation produced by a lightning flash.

In this dissertation, a broad bandwidth interferometer is developed which is capable of recording the VHF radio emission over the entire duration of a lightning flash. In order to best utilize the additional data, the standard processing techniques have been redeveloped from scratch using a digital cross correlation algorithm. This algorithm can and does locate sources as faint as the noise level of the antennas, typically producing 100,000 or more point source locations over the course of a lightning flash.

At very low received power levels, the likelihood that a signal received at the antenna will be affected by the environmental noise is substantially higher. For this reason, the processing allows for the integration windows of the cross correlation to be heavily overlapped. In this way, the location of each event can be based on a distribution of windows. Further, noise identification techniques which leverage the heavily overlapped windows have been developed based on: the closure delay, the standard deviation, the correlation amplitude, and the number of contributing windows. The filtration techniques have proven to be very successful at identifying and removing mis-located sources, while removing the minimum number of low amplitude sources which are well located.

In the past, lightning interferometers have been limited to using only two perpendicular baselines to determine the direction to each point source. Additional techniques are developed in this dissertation for efficiently computing the image of a point source in the sky using an arbitrary number of antennas in an arbitrary configuration. The multiple baseline techniques further improves the sensitivity and accuracy of the locations provided by broadband interferometers.

To demonstrate the usefulness of broadband interferometers, the activity of 6 flashes spanning a diverse selection of lightning flash types are examined in

this dissertation. This includes detailed analysis of negative stepped leaders, positive un-stepped leaders, K-changes, and fast positive breakdown. Initial breakdown pulses which are seen at the beginning of the flash are found to be no different than horizontal negative leader steps seen later in the flash. Evidence is found that positive leaders produce VHF radiation, as opposed to all of the radiation in the positive breakdown region being produced by retrograde negative breakdown. The time resolved three-dimensional velocity of 47 K-changes occurring in two flashes is measured. And finally, fast positive breakdown is characterized and found to be produced by a positive streamer process instead of a leader process.

Observations made with the instrument showcase the capabilities of a continuous sampling broadband interferometer. The instrument makes possible measurements which were difficult or impossible to obtain in the past, and the preliminary observations allude to many exciting scientific findings to come.

ACKNOWLEDGMENTS

CONTENTS

LIST OF TABLES

LIST OF FIGURES

xi

This dissertation is accepted on behalf of the faculty of the Institute by the following committee:

_____

Paul Krehbiel, Advisor

_____

William Rison, Committee Memeber

_____

Ron Thomas, Committee Memeber

_____

Ken Minschwaner, Committee Memeber

_____

Dave Meier, Committee Memeber

I release this document to the New Mexico Institute of Mining and Technology.

_____

Michael Stock   Date

CHAPTER 1

INTRODUCTION

1.1   Introduction

Lightning discharges produce electromagnetic radiation over a broad spectrum of radio frequencies, extending from the ULF through UHF and higher. VLF/LF sferics are a manifestation of impulsive current events such as those produced by cloud-to-ground strikes and some in-cloud processes, and are commonly used to locate where lightning strikes ground (*Cummins et al.*, 1998) and, increasingly, the locations of in-cloud events (*Schultz et al.*, 2011). VHF radiation (30–300 MHz) is produced by smaller-scale breakdown activity itself and can be used to map the detailed development of individual flashes within storms.

VHF lightning mapping has traditionally been done in one of two ways: a) by using interferometric techniques to determine the direction of arrival of the radiation (*Warwick et al.*, 1979; *Hayenga*, 1984; *Richard et al.*, 1986; *Rhodes et al.*, 1994; *Shao et al.*, 1996; *Ushio et al.*, 1997; *Kawasaki et al.*, 2000; *Cao et al.*, 2010), or b) using time of arrival (TOA) measurements to map the lightning in 3-dimensions (*Proctor*, 1981; *Maier et al.*, 1995; *Rison et al.*, 1999; *Thomas et al.*, 2004). The primary difference between TOA and interferometric lightning location systems is the use of coherence during processing. A TOA system makes use of a peak detector, which instantaneously determines the time of an event at each station independent of what another station may have recorded. An interferometric system determines the time or phase difference by correlating the signal arriving at two antennas, requiring the measurement to be integrated over a time window.

TOA systems accurately measure the arrival times of impulsive VHF events at a number of ground locations, usually widely spaced over distances of kilometers to tens of kilometers. For the New Mexico Tech Lightning Mapping Array (LMA), the timing uncertainty is empirically found to be about 30 ns rms, corresponding to source location accuracies as good as 10 m rms over the network (*Thomas et al.*, 2004). Although the VHF radiation is incoherently detected at each station, the TOA values are coherently combined to produce detailed 3-dimensional observations of the spatial and temporal development of individual

flashes. Up to a thousand or more impulsive sources are frequently located in a single large flash, in time resolution windows of 80 μs or 10 μs duration. With current technology, real-time processing is possible for data decimated to successive 400 μs windows.

Interferometer systems receive the VHF signals coherently at an array of closely spaced antennas, typically a few wavelengths apart (10–20 m or so), and obtain one- or two-dimensional directions of arrival of the lightning radiation sources. The signals from pairs of sensing antennas are coherently correlated to accurately determine the phase or time difference of arrival of the two signals and hence the angle cosines of the source direction. Measurements along two orthogonal baselines can be used to determine the spherical angles of sources and thereby their azimuth and elevation angles.

By correlating the signals arriving at each antenna, interferometers are capable of determining the time difference of arrival with extremely high precision. The timing uncertainty of interferometer systems depends on several attributes of the signal being recorded, including its signal-to-noise ration and duration, but timing uncertainties around 0.1 ns are typical. For the 2013 antenna arrangement, this timing uncertainty produces an angular uncertainty of approximately 0.1°, which corresponds to a spatial uncertainty of less than 20 m for sources within 10 km of the interferometer site (which includes most sources of interest). The time resolution of interferometer systems is also very high, with up to 100,000 and sometimes more VHF sources being located during a single lightning flash by using 1.4 μs integration windows.

1.2   A Brief History of Lightning Interferometry

The very first interferometric study of lightning was reported in 1979 (*Warwick et al.*, 1979). This study employed a single baseline interferometer operating over a narrow band centered at 34 MHz as a proof of concept that such an instrument was useful for tracking the motions of lightning. In narrowband interferometric systems, the coherent interference is determined using analog multipliers ('mixers') and quadrature phase detection techniques to determine the phase difference of arrival ϕ at the two antennas. The mixed signal is then time averaged, and recorded at a rate much lower than that required to unambiguously sample the operating frequency ($F_{Nyquist} = 2f_c$, in this case 68 MS/s). At the same time, TOA lightning mapping techniques were being developed in Florida by Proctor, Lennon and others; as such, there was interest in any methods to map out the location of lightning channels in the cloud (e.g. *Lennon*, 1975; *Proctor*, 1981). With only a single baseline to work with, the interferometer operated by Warwick was
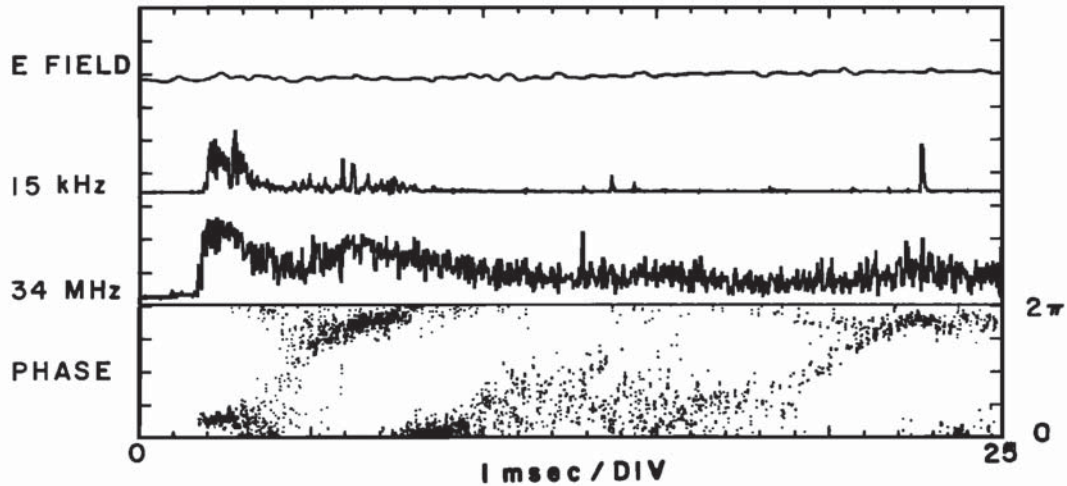
Figure 1.1: First published interferometric observation of lightning. The 25-ms segment (0-25 ms) of event 144504 showing phase (position) information in the breakdown phase. Figure adapted from *Warwick et al.* (1979)

not capable of producing images or maps of lightning. Instead, as a lightning source passed by, the fringes recorded by the instrument would move in an organized fashion. The fringes seen by Warwick were crude when compared to maps being produced by contemporary time of arrival systems in Florida. Specifically the interferometer did not actually produce locations for lightning sources like the TOA system did. However, the interferometric techniques held the promise of being able to locate a larger portion of the radiation emitted by lightning since they could locate very faint, continuously radiating sources. In addition, methods of improving the interferometers maps were discussed but not implemented. Figure 1.1 shows the fringes seen by Warwick, along with the electric field record of a lightning flash. The diagonal striations in the phase indicate a moving source.

Warwick's work was greatly extended by his graduate student, Craig Hayenga. He continued operating at 34 MHz, but implemented perpendicular crossed baselines so that 2D azimuth-elevation locations could be determined (*Hayenga and Warwick*, 1981). These were the first 2D interferometric maps of lightning made. As is the case with all narrow band lightning interferometers, the system developed by Hayenga was susceptible to a phase ambiguity. A baseline of length d operating at wavelength λ will have $2d/\lambda$ fringes, where each fringe represents a possible incident angle of the source. As a result, if the baseline between the antennas is longer than $\lambda/2$, a given measurement can be produced by a source from a discrete number of different directions. However, the phase difference measurement had a constant error (in radians), so longer baselines could locate a lightning source with greater accuracy. Hayenga employed baselines that
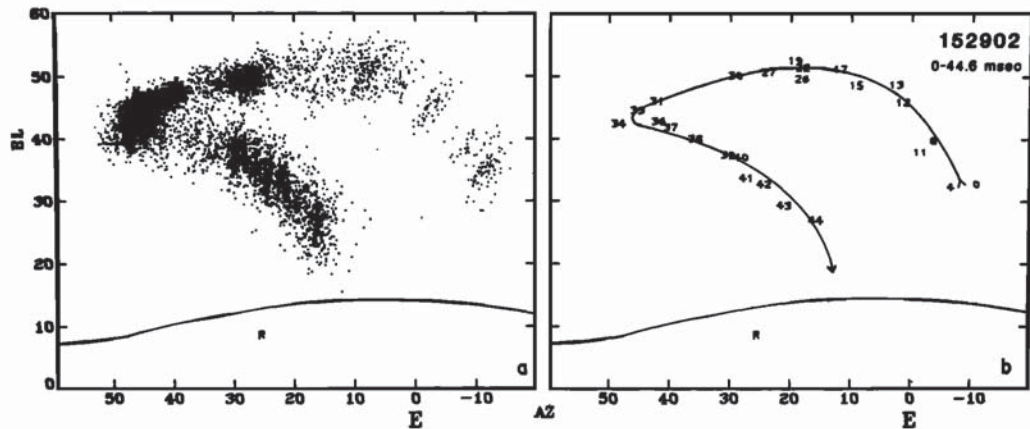
Figure 1.2: First published 2-D interferometric map of lightning. Azimuth and elevation in degrees for the initial portion of 152902. The horizon is shown. The "R" is the position of the phase reference. (a) Each point corresponds to a separately derived position. (b) Millisecond average positions. The line indicates the slower drift motion of the source of 1–5×10^5 m/s. Figure adapted from *Hayenga and Warwick* (1981)

were 2λ in length, which was a compromise between fringe ambiguity and angular uncertainty of the location. In this case there are 16 locations in the sky from which any source could have originated from. The ambiguities in location were resolved by hand by assuming the fringes formed a singled continuous map. Figure 1.2 shows the first published 2-D interferometric map of lightning. While the map is fuzzy, the result clearly shows the progression of breakdown during a lightning flash.

After graduating in 1984, Hayenga went to build an improved version of the interferometer at Langmuir Laboratory in Socorro, New Mexico. Unfortunately (but maybe not surprisingly) Socorro and Hayenga were not a good match and Hayenga never completed the improved interferometer he had planned. The study was continued by a graduate student named Charley Rhodes with the help of Paul Krehbiel (*Rhodes*, 1989). In Rhodes' interferometer, the frequency was increased from 34 MHz to 274 MHz, making for more compact baselines and allowing for more cycles per integration period. To improve the angular uncertainty without fringe ambiguity, instead of using just 1 pair of crossed baselines, 2 pairs of different lengths were used: a short baseline of $1/2\lambda$ and a long baseline of $8/2\lambda$, referred to as the $8 - 1$ configuration. The long baseline gave high accuracy results; the short baseline determined which portion of the sky the source was in. The system still used narrowband analog mixers and quadrature phase detection, therefore to record the signal of 4 baselines in quadrature required an 8 channel 1 MS/s digitizer that wrote to digital tape, a state of the art acquisition system at the time. The technique worked; however, removing the phase
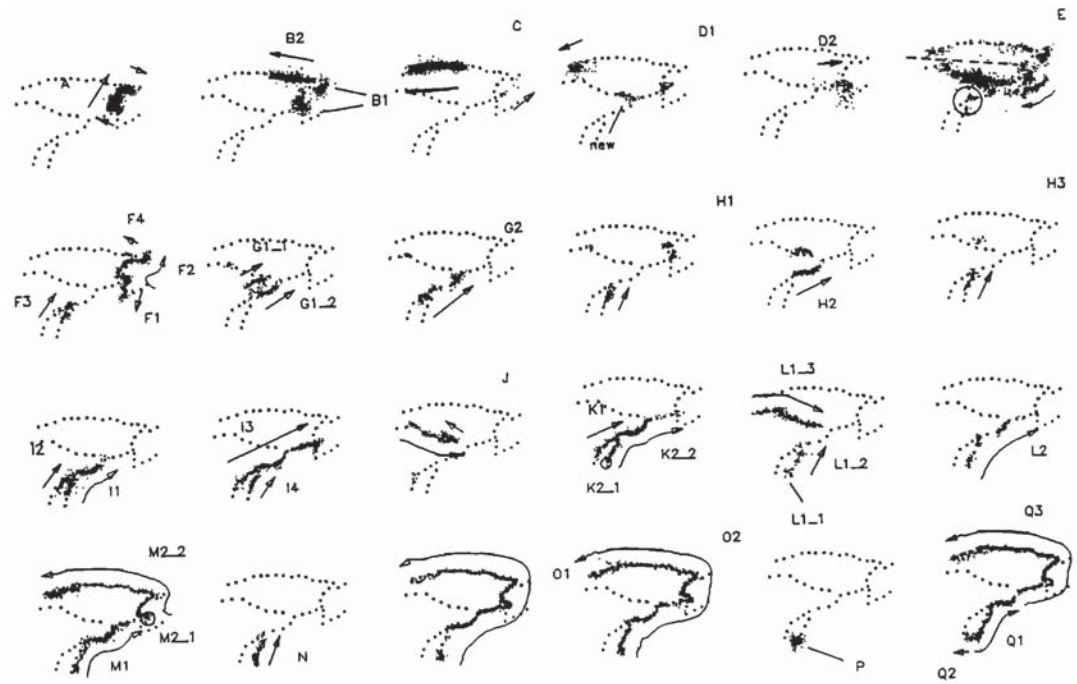
Figure 1.3: NMT Narrowband interferometer map of a lightning discharge. Spatial and temporal development of all the radiation sources for an intracloud flash on August 23, 1992 at 16:30:57 UT during the first 500 ms of the flash. Figure adapted from *Shao and Krehbiel* (1996)

ambiguity was a manual process that could only be completed reliably for cloud-to-ground flashes which had a well defined ground strike location.

Further development of the interferometer was picked Xuan-Min Shao. Shao cleverly changed the baseline lengths from $1/2\lambda$ and $8/2\lambda$ to $2/2\lambda$ and $9/2\lambda$. By using baselines which were not integer multiples of each other, the fringe ambiguity could be resolved using an automated process for both cloud-to-ground and intracloud flashes. This allowed, among other things, a real time display of the lightning locations. Two papers were published from this study, *Shao et al.* (1995) about cloud-to-ground development and *Shao and Krehbiel* (1996) about intracloud development. Even today, these papers represent the most complete descriptions of flashes ever made. Figure 1.3 shows the development of an intracloud flash as mapped by the NMT narrowband interferometer as a sequence of 24 images in chronological order (but not equally spaced in time). In each image, the overall development of the flash is shown as a dotted line, and the interferometer map for the period are overlaid as small black dots. The maps provided the direction of motion for various processes in the lightning flash. When combined with fast electric field change records at the interferometer site, it was possible to determine the sign of the charge moving in many of these processes.

This concluded the initial involvement of New Mexico Tech in the development of lightning interferometry. Lightning location research at New Mexico Tech shifted away from interferometric techniques and towards time of arrival techniques with the development of the Lightning Mapping Array which was capable of locating lightning sources in 3-dimensions (*Rison et al.*, 1999; *Thomas et al.*, 2004). Development of narrowband interferometers continued in France (e.g. *Bondiou et al.*, 1990; *Laroche et al.*, 1994; *Lang et al.*, 2000; *Defer et al.*, 2001), however, of more relevance to this dissertation is the development of broadband digital interferometers. If the signals from two antennas are measured over a narrow band, the correlation can be done by simply multiplying the signals together. If the signal from two antennas is measured over a broad band, computing the correlation needs to be done using digital Fourier techniques. The complication of implementing a broadband interferometer is that the sampling rate of the digitizer must be increased substantially. For a narrowband system, one must sample faster than the integration time of the instrument; 1–2 MS s^{-1} for the 1–2 μs integration times typically used for studying lightning. For a broadband system, one must sample faster than twice the highest frequency of operation; 68 MS s^{-1} in the case of Warwick and Hayenga's interferometer, and 548 MS s^{-1} in the case of the NMT narrowband interferometer used by Rhodes and Shao[1].

There were two perceived advantages of broadband interferometers over their narrowband counterparts. First, correlating the signals at multiple frequencies is equivalent to using multiple baseline lengths at a single frequency; therefore broadband interferometers are not susceptible to fringe ambiguity and can be operated with fewer baselines. Second, because the impulse response of a bandpass filter scales inversely with bandwidth, better time resolution is obtained, and it was thought that broadband interferometers would be less susceptible to smearing of locations during heavily branched processes. This second point will be discussed more in Section 4.1. For these reasons, in the mid 1990's two research groups were actively pursuing the development of a broadband interferometer: Shao, Holden and Rhodes at Los Alamos National Laboratory (LANL), and Kawasaki and Ushio at the Osaka University. By the mid 1990's, technology had advanced to the point where such high digitization rates were not only possible, but practical using a digital sampling oscilloscope (DSO). The DSO could sample very quickly (around 1 GS/s), but had very limited memory to record the data.

The first to publish was *Shao et al.* (1996), followed 6 months later by *Ushio et al.* (1997). The *Shao et al.* (1996) study was a proof of concept that outlined a method of determining the time difference between antennas (and therefore the

---

[1] For a norrowband interferometer, actually sampling fast enough to satisfy the Nyquist criteria would be highly inefficient. If the bandwidth is small, signal can be shifted to a lower frequency band and digitized at a slower rate.

angle of incidence of the incoming signal) by using a linear fit to the change in phase difference with frequency, which will be referred to as "phase fitting". Only a single vertical baseline was implemented, and the data were recorded continuously for short durations just prior to return strokes. The vertical baseline was used in an attempt to get more detailed measurements of the descent of a leader towards the ground. After this proof of concept, there were no published follow up studies on the topic of lightning interferometry produced by the LANL group. Their research moved towards more programmatic topics and the development of the Los Alamos Sferic Array. The *Ushio et al.* (1997) study used the same phase fitting technique introduced by *Shao et al.* (1996), but extended the observations to a pair of orthogonal horizontal baselines. Two baselines allowed lightning to be mapped in azimuth and elevation, with results similar to the narrowband interferometer studies described above. To overcome the short recording duration of the DSO, the recording memory was split into 50 separate 2 μs chunks. Each chunk would produce only a single direction to a lightning source, so at most 50 locations could be determined over the duration of a lightning flash. In practice, this meant that the measurements made of upward triggered positive and negative leaders were limited to the first several milliseconds. Ushio's instrument would eventually develop into the 'VHF Broadband Digital Interferometer', or DITF for short.

Development of broadband interferometry techniques at Osaka University have continued until present day *Ushio et al.* (1997); *Kawasaki et al.* (2000, 2002); *Morimoto et al.* (2004, 2005); *Akita et al.* (2010). The interferometer system evolved from using DSOs to PC-based digitizer cards with longer, but still limited, recording time, allowing up to 2048 sources to be located in a lightning flash. Additional research into broadband digital lightning interferometers was taken up in China at the Chinese Academy of Science, which frequently used similar triggering methods (referred to as sequential triggering) (*Dong et al.*, 2001; *Qiu et al.*, 2009; *Cao et al.*, 2010; *Liu et al.*, 2012; *Sun et al.*, 2012). The Chinese broadband interferometer systems use what is referred to as a 'short-baseline time-of-arrival' algorithm, where the time difference between antennas is obtained using cross correlation. While the name of the technique implies these are TOA systems (like the LMA), the measurement correlates both the amplitude and phase of the signal received by pairs of antennas, and so the instruments are interferometers.

Zen Kawasaki of Osaka University had a sequence of graduate students who worked with the Broadband DITF, with observations made of storms in Darwin, Australia. The most recent of these students was Manabu Akita, who used two interferometer systems to measure the location of lightning flashes in 3-D in 2010. For 3-D observations, two interferometric mapping systems are deployed approximately 5 km apart, and then the 3-D location of sources recorded by both systems can be reconstructed (*Laroche et al.*, 1994; *Akita*, 2011). The measurements
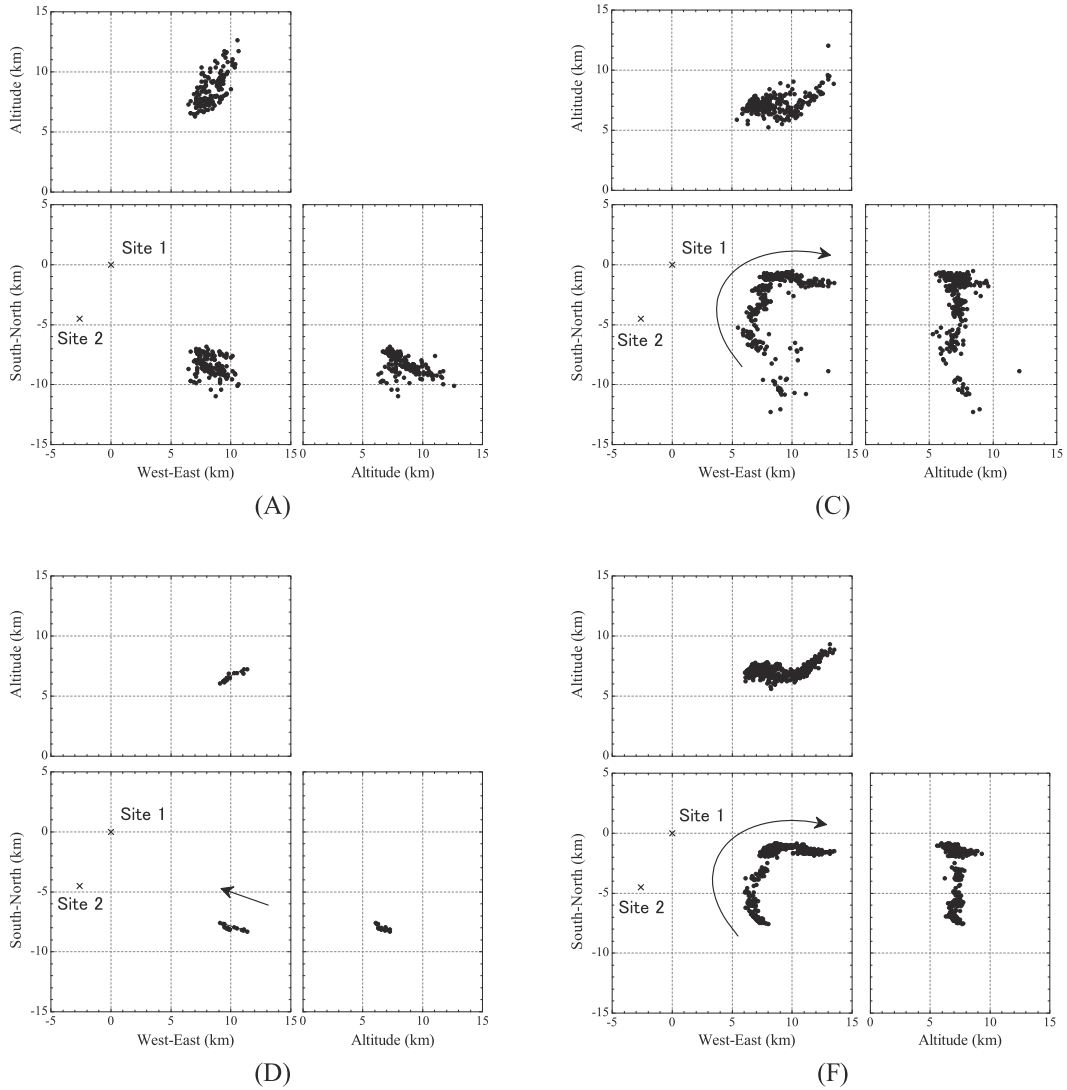
Figure 1.4: Osaka 3-D DITF map of a lightning discharge. Panels show the plan, and vertical projection of the 3D locations of individual VHF lightning sources. The letters refers to named time periods of the flash; no interferometer map was obtained from periods B and E of the flash. Figure adapted from *Akita et al.* (2010)

were combined with electric field records on the ground to estimate the charge distribution inside the cloud (*Akita*, 2011). Akita was also able to measure the 3-D propagation speeds of fast moving ionization waves called K-changes (*Akita et al.*, 2010), a topic which will be discussed in more detail in Section 7.1. Figure 1.4 shows a 3-D map produced by two DITF arrays located a few kilometers apart, showing K-changes in an intracloud lightning flash.

While the 3-D DITF worked very well for the measurements described above, the maps it produced were not as good as those made by the LMA. There are several reasons for this, but the largest contributing factor was that the 3-D DITF was still using a triggering system capable of locating at most 2048 solutions during a lightning flash. In practice, the number of located sources was lower than this because the two interferometer systems operated independently of one another; a source seen by one system may not be seen by the other. Regardless of how many sources were detected by both interferometers, a bigger problem was that the majority of the sources at each site would be located in a handful of clusters produced by millisecond duration bursts of continuous VHF radiation (caused by, for example, K-changes and dart leaders). The result was spotty maps of lightning. The lightning research group in Osaka was aware that the 3-D maps made by the LMA were better; however, they did not understand why. So in 2011, Manabu Akita came to New Mexico Tech with two full DITF systems to compare 3-D interferometric observations of lightning with those made by the LMA. This brings us to the study which is the topic of this thesis.

1.3   Broadband Interferometer Study at New Mexico Tech

What follows is an informal summary of the operations undertaken with the broadband digital interferometer at New Mexico Tech. The intent here is to not only lay out what did and did not work, but also to outline the original motivation behind each portion of the study. It is important to keep in mind that before the DITF arrived in Socorro, there was no plan to resume interferometric study of lightning. Frequently the reason something is done has little or no relation to the scientific results that eventually come about.

The basic platform for the sensor used for this thesis is the Osaka University DITF *Ushio et al.* (1997); *Kawasaki et al.* (2000). The Osaka University Digital Interferometer consists of three resistively coupled flat plate antennas arranged to form two equal-length orthogonal baselines. A fourth antenna is used to provide triggers for recording the time series data only, and could be placed anywhere near the interferometer site. The antenna design consisted of a 10" circular plate, whose signal was fed into a radio amplifier of 50 Ω impedance, depicted
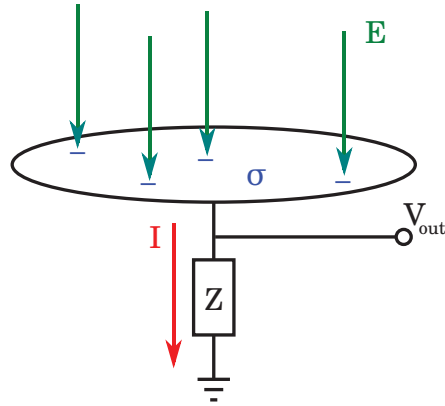
Figure 1.5: VHF Antenna Schematic.

in Figure 1.5. While a detailed response of the antenna is not available, it can be crudely modeled as a circular plate connected by a resister (Z) to ground. An electric field (E) will produce a surface charge (σ) on the plate, which in tern will cause a current (I) to flow in the resister. The signal, measured above the resister, is proportional to the current flowing through the resister, and so is proportional to dE/dt. This response partially compensates for the fall-off of lightning's VHF spectrum with increasing frequency, making it particularly convenient for the study of lightning. Because the antenna geometry was known to work for the study of lightning, when the antennas were redesigned in 2013, the same basic geometry was used.

Manabu Akita arrived in Socorro in June of 2011 with two complete interferometer systems to make 3-D measurements of lighting, and I was tasked with assisting him during the summer observations. Shortly after Akita's arrival, it became clear that the Osaka triggering system would heavily limit the quality of any data recorded by their system. As luck would have it, a better digitizing system had just been developed by NMT for observing radio frequency emissions produced by aircraft and explosions, which was easily adapted for use with the digital interferometer. Both the Osaka digitizer and the NMT digitizer were software controlled PC cards, and had similar bandwidth and sampling rates. A comparison of the Osaka and NMT digitizers is given in Table 1.1. The primary advantage of the NMT digitizer was that it could stream the digital signal over the PCIe bus continuously into PC memory, something the Osaka digitizer was incapable of doing due to being earlier technology. A PC mainboard can support substantially more memory than a typical digitizer card, and the memory modules for a PC are also relatively inexpensive. As a result, the maximum record length was increased from 1 MS (about 5 ms) on the Osaka system to 4 GS (about

	Osaka	NMT
Bandwidth	100 MHz	80 MHz
Sampling Rate	200 MS s^{-1}	180 MS s^{-1}
Channels	3	4
Record Length	1 MS	4 GS
Bit Depth	10 bits	16 bits

Table 1.1: Comparison of Osaka and NMT digitizer capabilities.

23 seconds) on the NMT system. The NMT system was fully capable of continuously sampling the entire duration of a lightning flash; the sequential triggering techniques used in the Osaka interferometer system was not needed.

It quickly became clear that the continuous sampling capabilities offered by the NMT digitizer were worth pursuing and refining, and after 2012 only the NMT digitizer was used. The planned 3-D measurements were never made, largely because a suitable second interferometer site 4–10 km distant from the first could never be located. Instead, a single continuous sampling digital interferometer was deployed in a number of different configurations to achieve various goals. The various configurations are summarized in Table 1.2.

In 2011, the first year of operation, the NMT digitizer was untested and so the Osaka and NMT digitizers were operated in parallel. The signal from a single analog front end set of antennas and amplifiers was sent to both digital back ends using a power splitter. Both systems shared the same triggering signal, which would trigger numerous times during a flash. The Osaka system would record a short (2 μs) chunk of data for each trigger, while the NMT system would begin recording after the first trigger pulse and continue recording for 2 seconds. The software running the NMT system was rudimentary, having been quickly adapted from the software used for recording RF emission from explosions. It was incapable of any pretrigger recording, and there was a large dead time of about 30 seconds between triggers as the data was written to disk. The lack of pretrigger data meant that the trigger threshold needed to be set very low, and false triggers occurred regularly; only about 1 in 10 triggers contained a lightning flash.

The majority of the time spent during the first storm season was expended deploying the interferometer antennas. The initial antenna configuration had a lot of noise pickup at one of the antennas. It was never determined what precisely caused the noise, but moving the antennas away from the back of the trailer reduced the interference. In order to move the affected antenna, the baselines had to be shortened from 13 meters to 10 meters. Through experimentation, a reasonably quiet configuration was eventually found.

2011		
Number Antennas	3	
Baselines	10.2	m
Bandwidth	105*	MHz
Sampling Rate	180	MS s^{-1}
Antenna Diameter	10	inches
Record Length	2	seconds
Pretrigger	0	samples
2012		
Number Antennas	3	
Baselines	10.2	m
Bandwidth	60	MHz
Sampling Rate	180	MS s^{-1}
Antenna Diameter	10	inches
Record Length	2	seconds
Pretrigger	0	samples
2013		
Number Antennas	4	
Baselines	16–32	m
Bandwidth	60	MHz
Sampling Rate	180	MS s^{-1}
Antenna Diameter	10	inches
Record Length	5	seconds
Pretrigger	5	seconds
2014		
Number Antennas	3	
Baselines	24	m
Bandwidth	60	MHz
Sampling Rate	180	MS s^{-1}
Antenna Diameter	13	inches
Record Length	3	seconds
Pretrigger	2	seconds

Table 1.2: Interferometer configuration for each year of deployment.
* The analog bandwith of this configuration exceeded the Nyquist criteria of the digitizer, resulting in aliasing problems.

Towards the end of the 2011 season, I began work on developing a processing algorithm as a way to better understand the data. During the initial deployment of the DITF, Manabu Akita was asked why the data was processed phase fitting instead of using a cross correlation. Partially due to the language barrier, the answer was not clearly definitive. For this reason, the new processing algorithm was implemented using cross correlation instead. My assumption was that eventually it would become clear that using a fit to the phase difference versus frequency would work better, and that in getting to this point a lot would be learned about the instrument. However, the reality is the opposite, cross correlation works as well or better than phase fitting, and the resulting algorithms are the topic of the first part of this dissertation. Work on the algorithm started with no knowledge of other broadband interferometer processing algorithms, although the final result bears close resemblance to the 'short-baseline time-of-arrival' techniques developed at the Chinese Academy of Science (*Sun et al.*, 2012).

The results of the initial cross correlation algorithm showed the solutions clumping in specific locations in azimuth and elevation, causing an artificial pattern to be seen in the lightning maps. The first working assumption was that the pattern was a side effect and limitation of processing the data using cross correlation; this turned out not to be the case. The pattern was more easily identified on maps produced by the cross correlation algorithm simply due to specifics of the visualization, and because many more sources were located. However, once it became known what to look for, the same pattern could also be seen in the data processed using Akita's algorithm, as well as data recorded with the Osaka digitizer. Regardless of the algorithm used to process the data, or the digitizer used to record the data, the artificial pattern was present. It was not until early 2012, during Akita's trip back to Japan, that Akita determined that aliasing effects (discussed in detail in Section 2.2) produced the clumping, caused by an oversight in the bandpass filter used in the antenna. Figure 1.6 shows an example map of the 2011 data showing the clustering effect. The unfortunate conclusion was that all data recorded in 2011 was contaminated by aliasing, and because there is no way to remove the contamination after the data are recorded, the data from 2011 are largely not useful for scientific pursuits. This said, tracking down the problem resulted in a better understanding of how the interferometer functioned.

Manabu Akita was able to remain in Socorro for a second year to continue development of the continuous sampling digital interferometer. Both Osaka DITF systems had to return to Japan in June 2012 for inventory and customs reasons. One set of antennas and amplifiers, as well as the triggering system, were returned to Socorro, while the Osaka digitizer was abandoned in lieu of the now tested NMT continuously sampling digitizer. The 20-125 MHz bandpass filters inside the antennas were replaced with units which pass 20–80 MHz, and additional 20–80 MHz bandpass filters were installed inside the trailer just before the
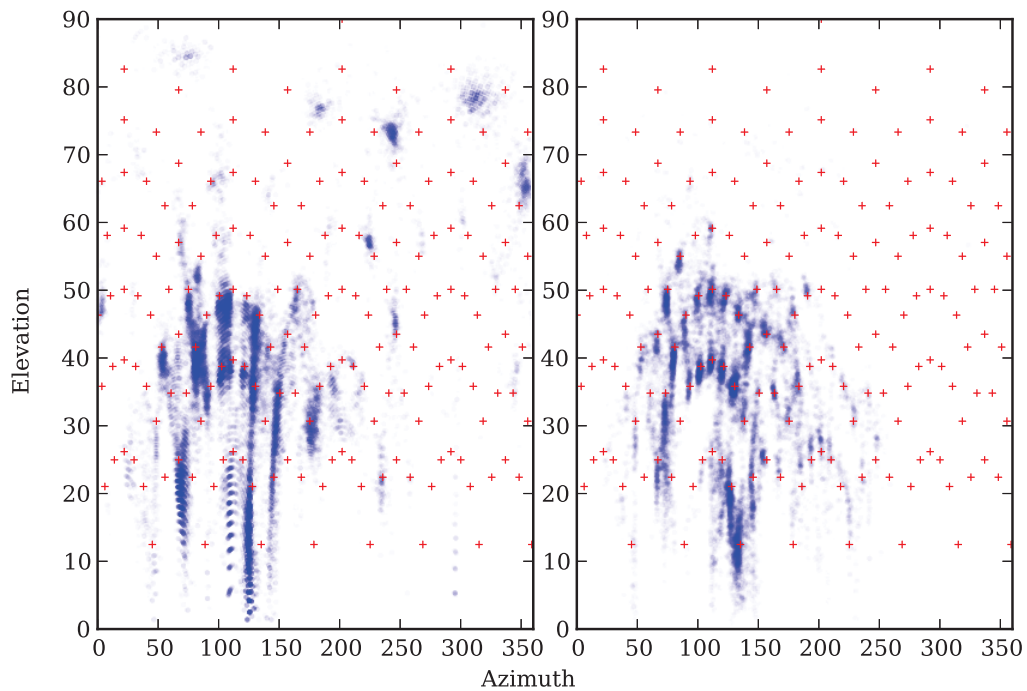
Figure 1.6: Boadband Interferometric map of a cloud-to-ground flash on Semptember 7, 2011. On the left is the early output of the cross correlation processing routine; on the right is the output of Akita's phase fitting algorithm. The red + show the directions determined using integer multiples of the sampling period. While Akita's map is superior, it still preferentially locates sources near the red +'s.

digitizers to ensure the digitized signal would not be contaminated by aliasing. Also, the fourth channel of the digitizer was used to sample the serial output of a GPS, so that accurate absolute timing of the interferometer signals could be determined. Mark Stanley was contracted to write a more advanced version of the software which operated the digitizer, allowing pretrigger data to be recorded. Unfortuately, the software was not ready until late in the 2012 season, and was used only for a few storms in September of that year.

For the 2012 storm season, there was a big push to record data for a triggered lightning flash. The long dead time of the rudimentary digitizer software (about 30 seconds) necessitated stopping automatic triggering and starting manual triggering whenever a triggered flash was likely. While some triggered flashes were recorded, none of them extended very far into the cloud and the interferometer maps are concentrated near the ground and the channels are not very well defined. Unfortunately, because the interferometer was not triggering on natural lightning during triggering operations, there is no record during many good close thunderstorms. In addition, in order to record as much of a lightning flash as possible, the trigger threshold had to be set very sensitive. This produced an excessive number of false triggers, which would then cause a real lightning flash to not be recorded. In all, only 3 natural flashes of exceptional quality were recorded, one intracloud flash on June 22, and an intracloud and cloud-to-ground flash on July 23. One of these flashes is shown in Figure 1.7, with the top panel showing the elevation vs. time for the flash, and the bottom panels showing the development of a number of K-changes in the flash (each indicated by a vertical line on the top panel). The sources of each K-change are shown colored by time, so that the direction of propagation can be seen. The flash shown in Figure 1.7 is the topic of two publications (*Akita et al.*, 2013; *Stock et al.*, 2014), and is also flash A in this dissertation (discussed in Section 5.6).

The 2012 season also saw the start of a friendly competition between Manabu Akita and myself to see who could produce the 'best' processing algorithm, where one algorithm was based on cross correlation and the other on phase fitting. The working assumption was that if one of us could implement a feature, the other could as well. In this way, the algorithms both quickly iterated from being something very basic in 2011 to producing some of the best interferometric maps of lightning ever made by the end of the 2012 storm season. Figure 1.7 shows a map made of a lightning flash in 2012 that was made for a conference poster in December, by which time both the phase fitting and cross correlation algorithms were well developed. In this particular case, the map was made using Akita's phase fitting algorithm, and then plotted using my visualization techniques.

At the end of 2012, Manabu Akita accepted a position at the University of Electro-Communications in Tokyo, Japan. Jeff Lapierre (another graduate student
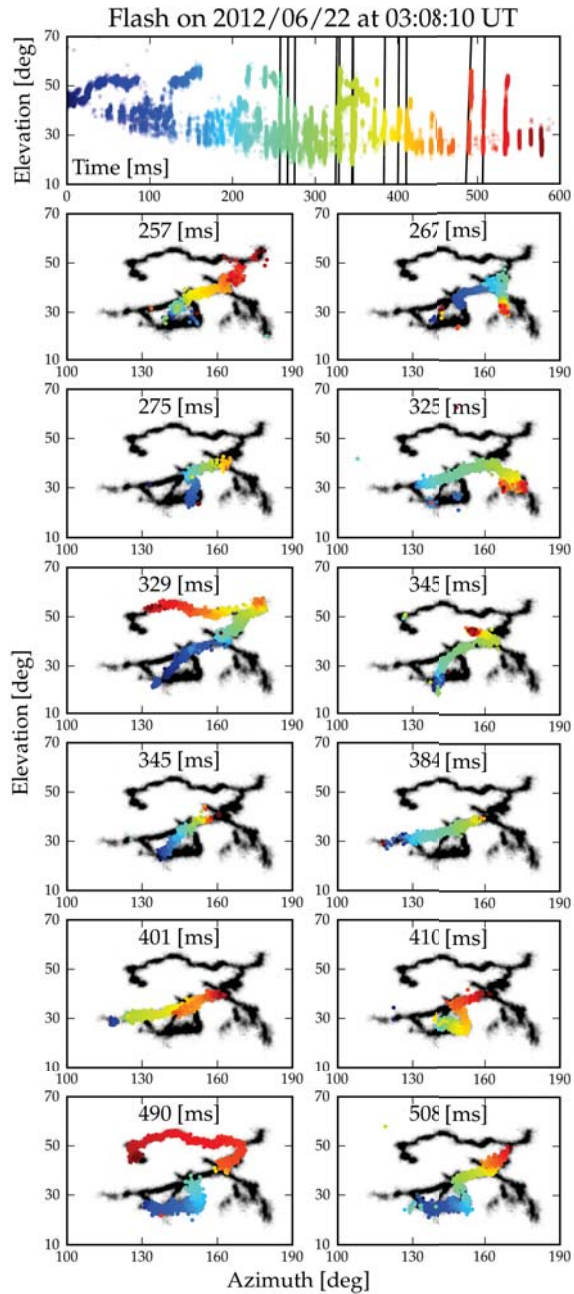
Figure 1.7: Broadband Interferometer observations of a bilevel intracloud flash on June 22, 2012. The flash occurred at 03:08:10 UTC, 8-10 km distant from the interferometer site. The top panel shows the elevation vs. time of the flash. The lower panels show the development of a number of K-changes, each colored by time so that the direction of progression can be seen. Figure adapted from a poster presented by Manabu Akita at the 2012 AGU Fall Meeting.

at NMT) helped with the operation of the interferometer over the 2013 summer storm season. The entire analog front end was redesigned so that the Osaka antennas could be returned, and hopefully to somewhat improve the sensitivity of the instrument. The new antenna design used the same basic antenna geometry, but allowed more flexible placement of the antennas by requiring only a single cable going to each antenna. This allowed the antennas to be moved farther from the (noise generating) trailer housing the digitizer, and also for the baselines to be extended from 10 meters to about 16 meters. The software developed by Mark Stanley was now fully functional, allowing for long pretriggers to be recorded, and completely removing the dead time between triggers.

Another change for the 2013 season was the addition of a fourth data channel. In 2012, this channel was used to record timing information off a GPS; however the interferometer data agrees so well with LMA data that absolute timing accurate to better than 1 μs (see Section 4.2) can be determined just by aligning the LMA and interferometer solutions in time. Early in the season, the fourth channel was used to record the output of another VHF interferometer antenna for the development of multiple baseline techniques (see Chapter 3). Later in the season, the fourth channel was used to record the output of a fast electric field change antenna.

While the antennas worked flawlessly[2], developing a new trigger for the system proved more problematic. The Osaka system used power detectors at 3 VHF bands to provide the trigger. The first attempted triggering system functioned similar to this, but the trigger pulses it produced tended to be very short, and Stanley's software required the trigger to stay high for 1 ms for reliable triggering. The final solution was to trigger off of the DC field mill data, which is streamed over Ethernet to all computers on the Langmuir network. This system worked remarkably well, as distant flashes (even if they were large) did not produce large DC field deflections over the interferometer. There is a long delay between data being recorded by a field mill, and that data arriving at the interferometer site, as much as 100 ms. The ability to trigger on field mill data was enabled by the long pretrigger records now capable with Stanley's improved software. The improved triggering scheme and the addition of pretrigger recording between the 2012 and 2013 storm season greatly increased the number of natural flashes recorded. In almost all cases in which the interferometer system automatically triggered, there was a lightning flash in the record. As a result, the total number of flashes recorded increased from 3 during the 2012 storm season to over 1000 in the 2013 storm season, providing a data set of exceptional quality.

The 2014 storm season has not yet (at the time of this writing) occurred, however some additional changes have been planned. A resonance in the antenna circuitry caused the driving amplifier on all the antennas to saturate in

---

[2] At least they appeared to work flawlessly.

a narrow band around 900 MHz. The result was that the gain of the antennas was lower than expected, although apparently the phase information of the signal was retained since interferometric mapping worked. The issue was corrected with a slight redesign of the antenna front ends. Also, only the fast electric field change meter will be deployed, a fourth VHF antenna will not be used.

1.4 Terminology and Definitions

While some effort has been made to avoid jargon, each field of study has its own terminology to describe various pertinent processes. To complicate issues, some of these terms are not well defined even within the community. A complete glossary of terms is not possible included here are only the handful of terms which are important to this study.

1.4.1 Tri-Polar Charge Structure

For a thundercloud to produce lightning, it must first physically separate charge in the cloud. This process is driven by the updraft of the storm as different types of water particles (ice, water, grauple, etc.) collide and bounce off each other. In the small isolated storms of New Mexico, this process predictably and repeatedly produces a **tri-polar charge structure** in the cloud, as depicted in Figures 1.8 and 1.9. At the bottom of the cloud, there is the smaller **lower positive charge layer**, in the middle is the **main negative charge layer**, and at the top is the sometimes very extensive **upper positive charge layer**. Because the top of the cloud has a net positive charge, electrons are drawn down from the air above the cloud to produce a **screening layer**, which causes the DC electric field to quickly drop to 0 above the cloud.

The charge structure of the type of storms common in New Mexico are very consistent, almost always showing this **tri-polar structure**. Because these storms are also common in the regions of the world in which early studies of lightning happened (New Mexico, Florida and South Africa), the **tri-polar charge structure** is also referred to as a normal polarity storm. Thunderstorms in other areas (such as Colorado, Texas and Oklahoma) can be significantly more complicated, and include storms with the opposite charge configuration. Such storms are referred to as **anomalously charged**, or **inverted polarity**.

IC   CG   BFB
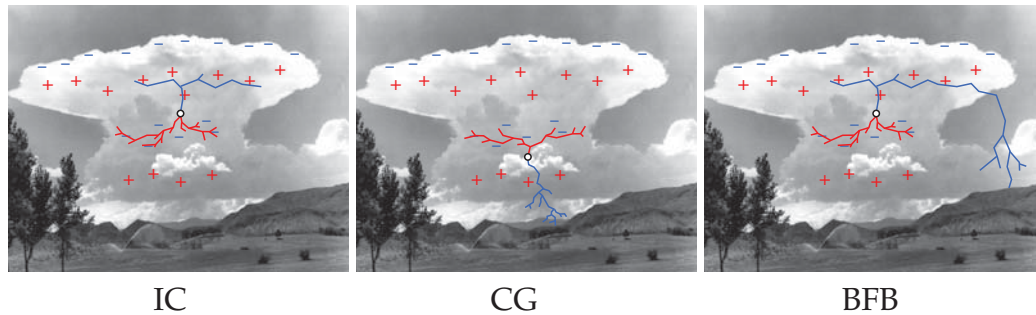
Figure 1.8: Schematic diagrams of New Mexico lightning flashes.

1.4.2 Streamers and Leaders

A **streamer** is a cold plasma which occurs whenever an electric field exceeds the breakdown field of air. In the lightning, there are **streamer zones** at the positively or negatively charged tip of any channel which is still extending, and possibly also on channels which are not extending. **Streamers** come in two varieties, those in which electrons stream out of (**negative streamers**), and those which electrons stream into (**positive streamers**).

A **leader** is a hot, conducting filamentary plasma which is formed when many streamers converge on a small region of air. Formally, a leader occurs when the temperature of the air is high enough that electrons will be stripped from air molecules through thermal processes; this happens at around 1500 K. However, if a leader is actively growing, the temperature of the air can be as high as 10,000 K or more (e.g. *Orville*, 1968). As with streamers, leaders come in two varieties, those carrying negative charge (colored blue in Figure 1.8), and those carrying positive charge (colored red in Figure 1.8).

In older texts on lightning, frequently the term **streamer** includes both **leaders** and **streamers** as described above.

1.4.3 Intracloud, Cloud-to-Ground, and Bolt from the Blue Flashes

There are three common types of lightning flashes in New Mexico thunderstorms: intracloud (IC), cloud-to-ground (CG), and hybrid IC-CG flashes called bolts from the blue (BFB), all depicted in Figure 1.8.

IC flashes include any flash wholly contained inside the thundercloud, with the possible exception of small sections of the channel. They comprise the

vast majority of all lightning (around 90%) both globally and locally in New Mexico. Figure 1.8 shows the most common type of IC flash, which initiates between the main negative and upper positive charge layers (shown with a white circle). The red color channels are transporting positive charge into the main negative charge layer, and the blue colored channels are transporting negative charge into the upper positive charge layer. IC flashes can also initiate between the lower positive and main negative charge layers, the upper positive and screening charge layers, and in anomalously charged storms.

CG flashes include all flashes which touch the ground and come in two main varieties: -CG flashes which transfer negative charge to ground, and +CG flashes which transfer positive charge to ground. In New Mexico, +CG flashes are much less common than -CG flashes. Figure 1.8 shows the most common variety of -CG flash which initiates between the lower positive and main negative charge layers. The red colored channels are transporting positive charge into the main negative charge layer, and the blue colored channels are transporting negative charge through the lower positive charge layer to the ground.

BFB flashes begin as normal IC flashes, but the channel carrying negative charge (the negative leader) for one reason or another exits the cloud at high altitude and continues towards the ground. These flashes have exceptionally long negative leaders which can touch ground more than 20 km away from the edge of the cloud.

1.4.4   Return Strokes and K-Cchanges

The potential difference between a thundercloud and the ground is around 100 MV. If one of the lightning channels bridges this gap, a potential wave travels from the ground and into the cloud at approximately a third the speed of light; this potential wave is the **return stroke**. As the **return stroke** propagates, it heats the already quite hot lightning channel, causing a bright optical flash all along the channel, shown in yellow in Figure 1.9. The return stroke also removes a significant amount of charge from the thunder cloud, producing a large electric field change on the ground. Figure 1.10 shows the electric field record for a cloud to ground flash; the top trace is the fast electric field change, and the bottom trace is the slow electric field change. Each **return stroke** is marked with an R. The return strokes produce the largest field deflections during the flash. The sign of the electric field deflection is dependent on the sign of the charge transferred. -CG and +CG flashes produce sferics[3] with opposite polarity.

---

[3] Sferic is short for 'atomospheric', and refers to the electric field waveform produced by a lightning flash.

| Return Stroke | K-change |
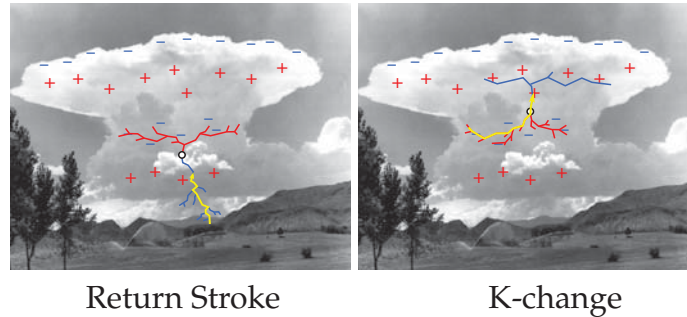
Figure 1.9: Schematic diagrams of K-changes and return strokes.

K-changes occur when a lightning channel cools to below 1500 K, and stops conducting. When this occurs, the potential of the channels on either side of the non-conducting gap diverge. Eventually an ionization wave carrying negative charge initiates which reconnects the two portions of the channel structure. In almost all cases the connection breaks near the tip of the positive leader, causing the positive leader tip to be cut off from the rest of the channel structure. The nature of the process was first discussed by *Ogawa and Brook* (1964) as transferring negative charge from the positive leader tip towards the origin of the flash.

K-changes are named after their characteristic electric field sferic, which is a small step deflection with a very fast leading edge (*Kitagawa*, 1957). Figure 1.10 is an excerpt from *Kitagawa and Brook* (1960), in which **K-changes** were first named, showing the electric field record for a cloud-to-ground flash. The **K-changes** in this flash are marked with K, and the **return strokes** R. In principal, 'K' has the meaning 'klein vernderung' or 'small change' in German, but in practice today 'K' is for 'Kitagawa' who discovered them. Since their discovery, **K-changes** have been an active topic of study nearly continuously.

The terminology for **K-changes** is somewhat murky; the same basic process is referred to as **K-changes**, **K-events**, **K-leaders**, **K-processes**, **recoil leaders**, **recoil streamers**, and more. Some of these terms have subtle distinctions between them, some do not. In addition, if the **K-change** follows a channel all the way to the ground, it is referred to as a **dart leader**, or **attempted dart leader** if it does not quite make it to the ground. Not all **K-changes** in a cloud-to-ground flash are **dart leaders**, but it is not clear when a **K-change** in the cloud becomes a **dart leader** traveling towards the ground. All of these processes are included in the somewhat more broad term **retrograde negative breakdown**, which refers to any negative breakdown on a pre-existing lightning channel which travels towards the flash origin.
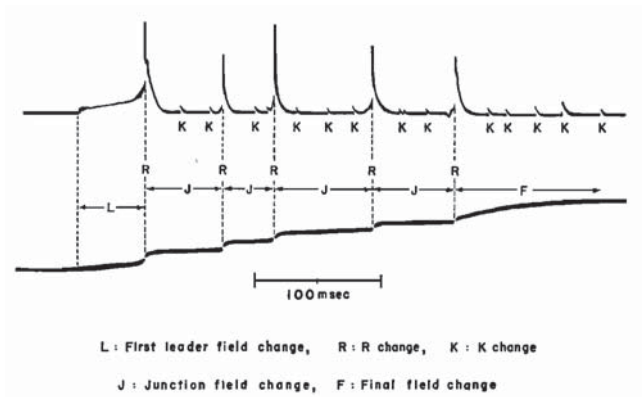
Figure 1.10: Diagram of a K-change Sferic. In cloud-to-ground flashes, K-changes were seen in the periods between return strokes (marked R), which for historical reasons was called the 'Junction' or J phase. Each K-change shows as a spike in the fast antenna record (top), and a small step in the slow antenna record (bottom). Figure adapted from *Kitagawa and Brook* (1960).

1.4.5   2-Dimensional Projections

In this dissertation, interferometer maps are frequently drawn in one of two projection, the **azimuth–elevation projection**, and the **cosine projection**. The **azimuth–elevation projection** is fairly intuitive, with azimuth increasing clockwise from the north, and elevation increasing from the horizon. The **cosine projection** is less intuitive, in this projection, the elevation angle is shown radially increasing inward from a unit circle, and the azimuth angle increasing clockwise from north, as shown in Figure 1.11.

There are a number of advantages to the **cosine projection**, versus presenting the maps or images in terms of angle: First, sources at the zenith have well defined coordinates, making flashes which travel directly overhead of the interferometer much easier to analyze in this projection. Second, and more importantly, given a constant baseline, a change in time delay is linearly related to a change in position in this projection. This has the very desirable side effect that the location uncertainty and resolution is constant over the entire **cosine projection** plane. This is not so in the **azimuth–elevation projection**, where the error in elevation increases as one approaches the horizon, and the error in azimuth increases towards the zenith.

The major drawback of displaying maps in the cosine projection is that a change in the radial coordinate is linearly related to the cosine of the elevation angle, and not to the elevation angle directly. As a result, sources located near the

22
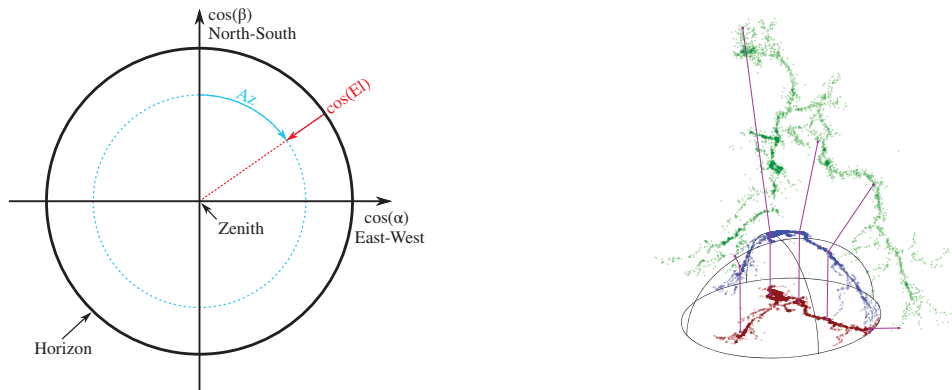
Figure 1.11: The cosine projection. The axes are the direction cosines, $\cos\alpha$ is the angle between a radial vector and the x or East axis, and $\cos\beta$ is the angle between a radial vector and the y or North axis. The cosine projection is the projection of the spherical angles onto a Cartesian coordinate system.

horizon will tend to compress and blur together. However, this is a real effect; at the horizon the error in elevation angle is infinite (see Section 4.1). The compression effect is illustrated in the right panel of Figure 1.11. Here a 3D map of a lightning flash is shown in green. Ideally an interferometer would determine the angular position of a source direction, displayed on a unit hemisphere in blue. Instead, the interferometer determines the projection of the angular position onto a plane, shown in red. This plane is the direction or angle **cosine projection**, or **image plane**.

1.4.6 Azimuth, Elevation, and Altitude

The **azimuth** angle is the angle clockwise from North, as opposed to the spherical azimuthal angle, which is defined counter clockwise from East. The **elevation** angle is the angle increasing from the horizon, again as opposed to the spherical polar angle which increases from the zenith. In this text, **elevation** always refers to an angle and never a distance. The vertical distance above the sea level is always referred to as **altitude**.

1.4.7   Maps and Images

To differentiate between traditional lightning location techniques and Fourier imaging techniques, a somewhat arbitrary distinction is made between **maps** and **images**. A **map** is defined as a sequence of point locations with time, where the point locations can be either 2-D (azimuth and elevation, as produced by the interferometer) or 3-D (x,y,z as produced by the LMA). An **image** is defined as an instantaneous grid of pixels, where each pixel has an amplitude (e.g., luminosity) and perhaps a color, as is produced by a digital camera. From a sequence of **images** a **map** can be produced, however the reverse is not so.

1.4.8   Phase Fitting and Cross Correlation

There are two dominate computational methods at the heart of lightning interferometers: **phase fitting** which fits a linear trend to the phase difference versus frequency, and **cross correlation** which is mathematically well defined. Ultimately, both computational methods coherently measure the time delay between antennas in the interferometer array, and so the two techniques are equivalent. However, there are subtle differences in the details of algorithms which can cause the resulting solutions to not match exactly. It is beyond the scope of this dissertation to discuss the differences, however which technique works better is still an open question in the field.

1.5   Scope of Study

This dissertation is split into two large parts. Part I covers the processing algorithms needed to take raw time series waveforms and convert them into interferometric maps and images of lightning. Part II covers observations of a number of flashes, showing much improved measurement of several processes occurring in lightning. A major part of this study was the design and implementation of a broadband interferometer. While the interferometer discussed was based on the Osaka DITF, by the 2013 storm season no hardware or software was shared between NMT and Osaka interferometer systems.

Part I

Processing

CHAPTER 2

THE CROSS CORRELATION TECHNIQUE

The content in this chapter was published in a Journal of Geophysical Research (JGR) article *Stock et al.* (2014), and has been reproduced here, with some sections expanded and additional figures. The cross correlation technique covers the 'traditional' way to take two crossed baselines (consisting of three antennas) and determine the direction to a correlated VHF source. The basic concepts of the cross correlation technique are not new, and several previous studies have implemented similar algorithms to produce maps of lightning (e.g. *Dong et al.*, 2001; *Qie et al.*, 2005; *Tantisattayakul et al.*, 2005; *Qiu et al.*, 2009; *Cao et al.*, 2010; *Qiu et al.*, 2012; *Sun et al.*, 2012). Here the techniques are extended to continuously sampled data. The implemenation itself included a number of challenges, some of which are common to FFT based cross correlation, and some of which are specific to the application. Because this chapter was originally written for journal publication, many of these challenges are unfortunately glossed over, and have not been expanded upon in this text.

In developing the algorithm, a major oversight in the initial deployment of the interferometer was discovered: the effects of aliasing. Aliasing has a crippling effect on the data, and can not be corrected after the data are recorded. As a result, all of the data recorded in 2011 were irreparably contaminated, and rendered useless for scientific purposes. In the original JGR article, the effects of aliasing comprise two sentences of the text. Here, the discussion is expanded to a section including figures illustrating the effects.

2.0.1 Primary Novel Techniques/Findings

Almost all of the content in this chapter has been implemented before, either for lightning or for some other purpose. That said, this chapter is needed to lay the ground work for Chapter 4, which introduces the novel noise filtration techniques that make quality maps possible. In addition, some of the techniques

had either never been applied to lightning, or been applied but never discussed in publications.

The following findings are novel:

- Equations 2.5 for azimuth and elevation solutions using non-perpendicular baselines.

- Description of the effects of aliasing.

- Heavily overlapped windows to reduce errors in the solution.

- Use of the closure delay to identify poorly located solutions.

2.1   Basic Algorithm

For a distant signal arriving at two antennas separated by a distance d, and from the simple geometry of Figure 2.1, the time difference of arrival τ_d and the phase difference $\Delta\phi$ are related to each other and to the angle of incident radiation α according to

$$d\cos\alpha = c\tau_d = \left(\frac{\Delta\phi}{2\pi}\right)\lambda ,$$
(2.1)

where λ is the wavelength of the radiation and c is the speed of light in air. Measuring the time delay τ_d or the phase difference $\Delta\phi$ determines the direction cosine, $\cos\alpha$, of the source from
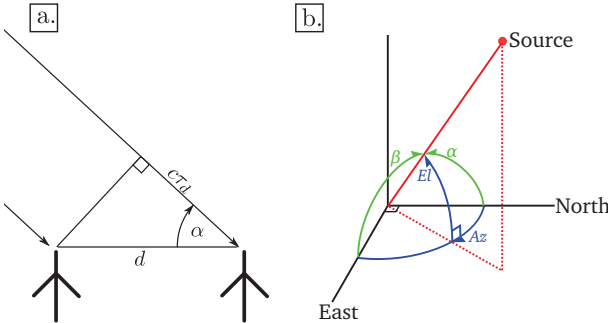
Figure 2.1: Basic geometry of the interferometer measurements.

27

$$\cos\alpha = \frac{c\tau_d}{d} = \left(\frac{\Delta\phi}{2\pi}\right)\frac{\lambda}{d}\ . \tag{2.2}$$

Whereas the direction cosine can be determined directly from correlation measurements of τ_d, its determination from phase values is more complicated due to the 2π ambiguity of phase measurements, necessitating that the phase values versus frequency be 'unwrapped' for baselines of length $d > \lambda/2$. In both cases, however, the estimated value of τ_d cannot exceed the transit time $\tau_{transit} = (d/c)$ between the two antennas. This physical constraint ensures that the value of $\cos\alpha$ lies in the range ± 1 and is useful in distinguishing between actual sources and random noise events in the correlation measurements.

For sources in located in two spatial dimensions, two angles are needed to specify the direction, requiring an additional measurement for their determination. Equations (2.1) and (2.2) still apply, but with the plane tilted to pass through the source location. The second measurement can be obtained from an orthogonal horizontal baseline, which similarly determines the arrival angle β relative to its axis. Letting the two baselines correspond to east and north directions, respectively, and defining the azimuthal angle to increase clockwise from north, we have from spherical trigonometry (e.g. *Rhodes et al.*, 1994) that

$$\begin{aligned} \cos\alpha &= \sin(Az)\cos(El) \\ \cos\beta &= \cos(Az)\cos(El)\ , \end{aligned} \tag{2.3}$$

where $\cos\alpha$ and $\cos\beta$ are the direction cosines. Geometrically, the above equations correspond to the transformation between unit-radius spherical and Cartesian coordinates, with the spherical angles (θ, ϕ) replaced by their complements (El, Az). The resulting (x, y) coordinates correspond to the direction cosine values $(\cos\alpha, \cos\beta)$. The direction cosines thus represent the projection of the sources from a unit celestial hemisphere down onto the horizontal plane of the antennas (e.g., (*Rhodes et al.*, 1994)). The transit time constraint corresponds to $(\cos\alpha)^2 + (\cos\beta)^2 \leq 1$, namely to a unit radius circle in the direction cosine plane (e.g., Figure 1.11).

The above equations can be inverted to obtain the azimuth and elevation in terms of the two time differences of arrivals, τ_{d1} and τ_{d2}, giving

$$\begin{aligned} Az &= \arctan\left(\frac{\tau_{d1}}{\tau_{d2}}\right) \\ El &= \arccos\left(\frac{c}{d}\sqrt{\tau_{d1}^2 + \tau_{d2}^2}\right)\ . \end{aligned} \tag{2.4}$$

For the case of non-perpendicular baselines that may or may not have a baseline in the north-south direction, these projections can be generalized to
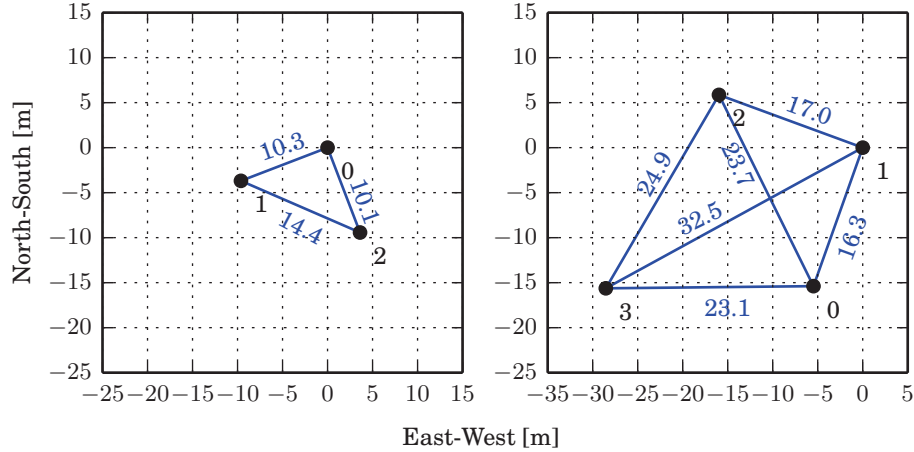
Figure 2.2: 2012 and 2013 antenna configurations. Left, configuration for the 2012 storm season. The three antennas for a traditional pair of orthogonal baselines. Right, configuration for the 2013 storm season. Antennas 0, 1 and 2 still form a traditional pair of orthogonal baselines. Antenna 3 was added for experimentation with multiple baseline techniques.

$$
\begin{aligned}
Az &= Az_1 + \arctan\left(\frac{\tau_{d1}\cos(\Delta\theta) - \tau_{d2}}{\tau_{d1}\sin(\Delta\theta)}\right) \\
El &= \arccos\left(\frac{c}{d}\sqrt{\frac{\tau_{d1}^2 + \tau_{d2}^2 - 2\tau_{d1}\tau_{d2}\cos(\Delta\theta)}{\sin^2(\Delta\theta)}}\right)\ ,
\end{aligned}
\tag{2.5}
$$

where Az_1 is the azimuth angle of baseline 1 and $\Delta\theta = Az_1 - Az_2$ is the angle between the baselines.

The $1/\sin(\Delta\theta)$ term in the equations for both Az and El show that the best solutions will occur when the baselines are oriented perpendicular to each other. Equation 2.5 is really only suitable for correcting deviations from perpendicularity which occur during deployment. Methods for effectively utilizing fully non-perpendicular baselines is presented in Chapter 3.

Estimates of the time delay values can be obtained using the generalized cross correlation. The measured signals at each antenna, x_1 and x_2, are assumed to be band-limited and of the form

$$
\begin{aligned}
x_1(t) &= v(t) + n_1(t) \\
x_2(t) &= v(t - \tau_d) + n_2(t)\ ,
\end{aligned}
\tag{2.6}
$$

where v is the signal from the coherent source and n_1 and n_2 are uncorrelated noise sources.

29

If $X_1(f)$ and $X_2(f)$ are the Fourier transforms of x_1 and x_2, then the time delay estimate $\hat{\tau}_d$ can be determined from the maximum value of the cross correlation. The generalized cross correlation differs from a non-generalized cross correlation by making use of a windowing function in the frequency domain, $W(f)$, which tailors the cross correlation for different purposes. The generalized cross correlation $R_g(\tau)$ with windowing function $W(f)$ can be found in the following way:

$$x_1(t), x_2(t) \xleftrightarrow[\mathcal{F}]{\quad\quad} X_1(f), X_2(f)$$
$$\downarrow$$
$$R_g(\tau) \xleftrightarrow[\mathcal{F}]{\quad\quad} X_1(f)X_2^*(f)W(f) .$$

Note that a non-generalized cross-correlation function R_{12} can be determined directly in the time domain by convolving x_1 and x_2, but the computations are prohibitively intensive, and windowing is also more complicated. It is both faster and simpler to utilize FFTs to transform into the frequency domain, where the convolution becomes simple multiplication, and then transform back to the time domain.

Numerous windowing functions have been described in the literature. For this study only three windows are considered: no windowing ($W = 1$), the smoothed coherence window (SCOT), and the W_I function described by *Hassab and Boucher* (1979). The SCOT window is widely used, and generally does a good job of both equally weighting portions of the spectra with good signal to noise ratio, and reducing contributions from noisy portions of the spectra. SCOT has the added benefit that it requires no knowledge of either the signal or noise spectra, but is not capable of removing narrow bands contaminated by correlated noise, such as carriers. The SCOT windowing function is defined as:

$$W_{SCOT}(\omega) = \frac{1}{\sqrt{\Phi_1(\omega)\Phi_2(\omega)}} , \tag{2.7}$$

where Φ_i are the real valued power spectra recorded at each antenna. Ideally, W_{SCOT} would be calculated using an ensemble average, however this is usually not practical to do. Instead, the ensemble average can be estimated by smoothing W_{SCOT} over frequency, although one must take care not to move the peaks of the spectra by using a 0-phase filter.

The W_I function is a more complex filter requiring knowledge of the signal spectra of the source.

$$W_I(\omega) = \frac{\Phi_v(\omega)}{\Phi_{n_1}(\omega)\Phi_{n_2}(\omega) + \Phi_v(\omega)\left(\Phi_{n_1}(\omega) + \Phi_{n_2}(\omega)\right)} , \tag{2.8}$$

where Φ_v is the signal power spectra and Φ_n is the noise power spectra. The effect of W_I is to emphasize frequency components that have good signal to noise ratio, thereby improving the time delay estimation. The noise spectrum is readily obtained from portions of the record that contain no signal from lightning. The signal spectrum is estimated by differencing the cross-spectrum of the current window and the cross-spectrum of noise. Again, to emulate an ensemble average, the signal spectrum is smoothed over frequency. Estimating Φ_v in this way allows the W_I function to exclude frequency bands contaminated by correlated noise sources.

An estimate of the time difference of a signal arriving at two antennas, $\hat{\tau}_d$, is obtained from the maximum value of the generalized cross correlation R_g. Because the cross correlation is computed discretely, the maximum of the correlation function is an integer multiple of the sampling period (5.6 ns in this study). To obtain a more accurate value of $\hat{\tau}_d$, the cross spectrum is upsampled before transforming back to the time domain, and a parabola is fit to three upsampled values about the peak (e.g. *Boucher and Hassab*, 1981).

2.2   Effects of Aliasing

It is particularly important that the signal be band-limited consistent with the Nyquist frequency before digitization to eliminate aliasing effects. Otherwise, the time delay estimate ($\hat{\tau}_d$) determined using cross correlation for contaminated sources will tend to be an integer multiple of the sampling period (*Moddemeijer*, 1991). The result is that the location of sources contaminated by aliasing will appear to cluster on a square grid in the cosine projection. Once a source is recorded, there is no post processing technique which can remove the contamination caused by aliasing.

The effect of aliasing on interferometric maps is illustrated in Figure 2.3 using synthetic data. The figure is made by choosing a location in the sky, and then applying the appropriate time delays for this location to a synthetic, band limited waveform. The bandwidth of the waveform is shown in the right hand plot, with the vertical axis representing the analog input frequency, and the horizontal axis showing the apparent frequency after sampling. Any portions of the band that undergo aliasing are shown in red. The synthetic waveform is then run through the processing algorithm; the 60 MHz bandwidth which contributes to the cross correlation is denoted by the vertical blue lines. The location provided by the algorithm can then be compared with known true location.

The top set of plots show the case where none of the signal is aliased. The solution provided by the cross correlation algorithm (center) almost perfectly
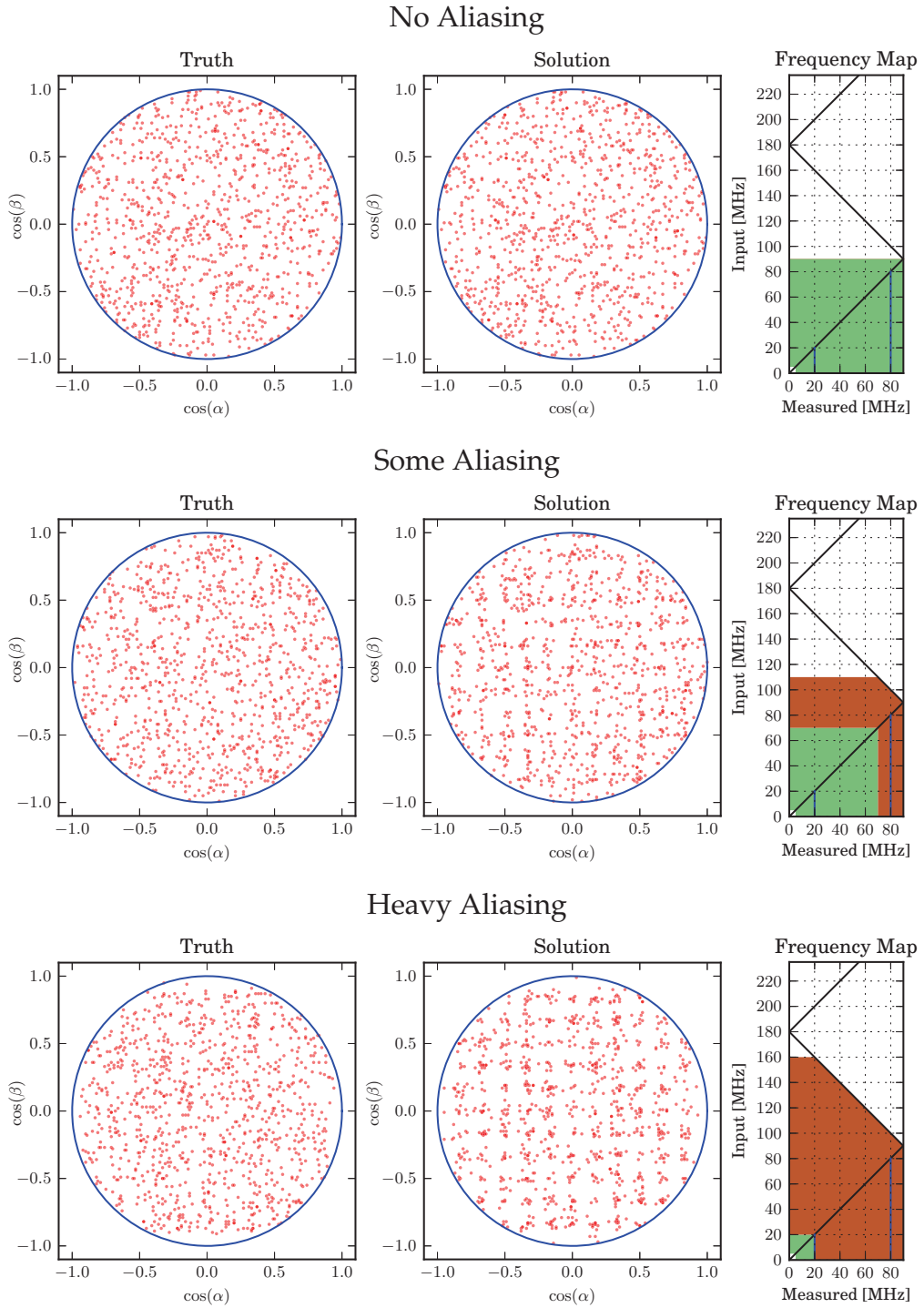
Figure 2.3: Effects of aliasing. Left, the locations of randomly distributed synthetic sources. Middle, the resulting solutions using the processing algorithm. Right hand plot shows the bandwidth used for the synthetic source, regions shaded in red undergo aliasing.

matches the known source locations (left). If even a little of the band used for the cross correlation is contaminated by aliasing, the solution provided by the cross correlation begins to deviate from the known source locations, shown in the center set of plots. In this case, the analog bandwidth is 110 MHz, and the high frequency portions alias down to 70 MHz. Of the 60 MHz band contributing to the cross correlation, only 10 MHz is contaminated, however a solutions are already beginning to cluster on a grid. The bottom case shows the effects of heavy aliasing contamination, which shows the grid even more clearly.

The only way to avoid the effect is to properly filter the analog signal from the antennas before the signal is digitized, such that no portion of the bandwidth which contributes to the cross correlation is contaminated by aliasing.

2.3   Implementation

The signals from the antennas are band-limited to 20–80 MHz and sampled by a 16 bit, 180 MS s^{-1} PC digitizer that streams the digitized signals into PC memory, allowing for long record lengths. Even though the PC digitizer is capable of streaming the digitized signal into memory indefinitely, the data rates are too fast to transfer selected data segments to hard disk continuously. For this reason the recording is triggered on a flash-by-flash basis, with each trigger making a continuous multi-second record of the VHF time series data (2 seconds long in 2012, increased to 5 seconds in 2013). During post-processing the records are divided into 256 sample (1.42 μs) windows. Successive windows are overlapped by an adjustable amount so that the location of a given source can be based on the centroid of the solutions from a number of windows.

The process of determining $\hat{\tau}_d$ for a single window is depicted in Figure 2.4 for an impulsive radiation event at the beginning of the flash discussed in Section 5.6. Figure 2.4a shows a 256 sample window of the recorded waveforms for two of the receiving channels, with the vertical scale representing normalized amplitude after digital filtering was used to further attenuate noise sources outside the 20–80 MHz band. Close examination shows that the channel 1 signal (blue) is slightly advanced relative to channel 2 (red). The oscillatory nature of the waveforms is due to the bandpass filter being excited by an impulse by a relatively short duration, impulsive radiation event. An impulsive excitation causes the bandpass filter to ring at its center frequency $f_c = 50$ MHz, corresponding to $\simeq 4$ samples of the digitized waveform. For a receiver of bandwidth $B = 60$ MHz, the ringing dies out in a time Δt approximately equal to 2-4 times the inverse bandwidth, or about 33-66 ns (6-12 digitizer samples).
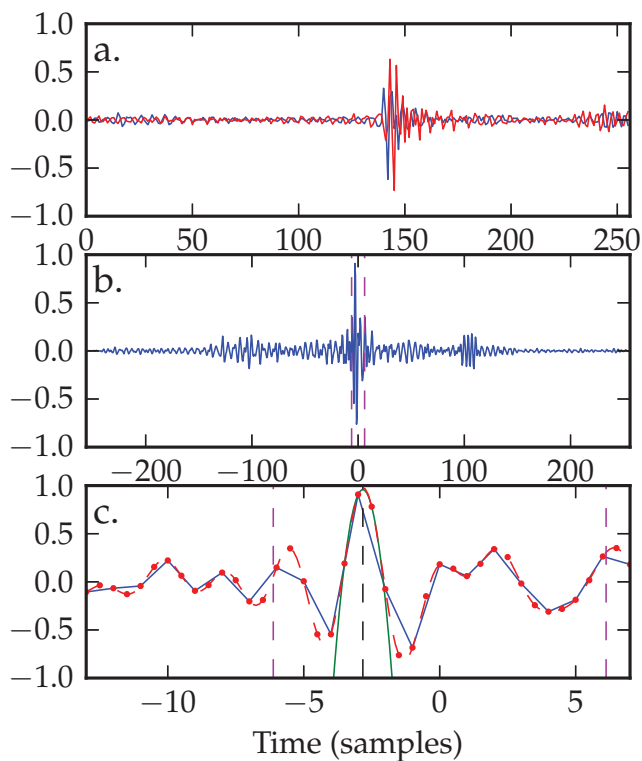
Figure 2.4: Example window showing the cross correlation technique. A temporally isolated radiation event at the beginning of the flash of Section 5.6, illustrating the processing technique used to determine the time difference τ_d of arrival at two antennas. a) Normalized waveforms from the two channels for a 256 sample (1.42 μs) window, after digital filtering to remove signals outside the 20-80 MHz bandwidth; b) cross-correlation of the two signals; c) expanded view of the cross-correlation around its peak, illustrating how the sampled data (blue lines) are upsampled (red dots). Three points around the peak are then parabolically fitted (green curve) to accurately determine the arrival time difference τ_d (black dashed line), allowing τ_d to be determined to a small fraction of the sampling period. The red dashed lines indicate the maximum physically possible τ_d for 10.2 m baselines (± 6 samples about zero lag.

Figure 2.4b shows the full cross-correlation of the two signals, with a peak near zero offset. The horizontal axis indicates the time lag of the correlation, which extends over ± 256 samples. The vertical axis is the normalized correlation coefficient with maximum limits of ± 1. Figure 2.4c shows a zoomed-in plot of the correlation peak. The piecewise-linear blue line connects the sampled points at time intervals $T_s = 1/180$ MHz $\simeq 5.6$ ns. The cross-correlation oscillates at the same frequency as the ringing which, because the recorded spectrum is roughly constant across the 20-80 MHz band, corresponds to the center frequency of the band (50 MHz), or $\simeq 4$ samples per period, as above. In addition, significant correlation dies out beyond about a 6-sample interval, consistent with the inverse bandwidth estimates given above.

Although the sampling fully satisfied the Nyquist criterion (i.e., 2 or more samples per period), it is a bit too coarse for parabolic fitting to accurately estimate the peak. To rectify this, the waveform is up-sampled by a factor of 2 or more, in a manner that does not alter the frequency content of the waveform (for example, by zero-padding the two $X_i(f)$ spectra used in determining the cross-spectrum). The red points show the cross-correlation when the individual waveforms are up-sampled by a factor of 2. While it is possible to up-sample the waveforms with arbitrarily fine precision to determine the cross-correlation peak, doing so would be much more computationally intensive than fitting a parabola to 3 up-sampled points about the maximum. If the waveform is not up-sampled at all, the parabolic fit would introduce error and cause the peak to be mis-located. Up-sampling by a factor of 4 results in the difference between the peak determined with a parabolic fit and that obtained by excessive up-sampling being much less than the timing uncertainty fundamental to the measurement (see section 4.1). The green curve in Figure 2.4c shows the parabolic fit to three points about the maximum. The cross correlation quickly deviates from the parabolic fit, but near the maximum the fit is good. The black dashed line is the resulting time delay estimate, and does not fall on a sample boundary.

The 256 sample windows are purposely overlapped so that the location of a single emission source can be based on the weighted centroid of the solutions from successive overlapping windows. Increasing the fractional overlap improves the quality and number of solutions at the expense of processing time. In this dissertation, generally two levels of overlapping are shown, a 75% medium overlap (all but 64 digitizer samples overlapping, up to 4 windows contributing to a solution), and a 98% heavy overlap (all but 4 samples overlapping, up to 64 windows contributing to a solution). As the amount of overlap is increased, the detection efficiency (and so the number of solutions) increases at the expense of processing time. The medium overlap is a good compromise between processing time and map quality, and has been applied to all the flashes on most of the storm days recorded. The heavy overlapping is reserved for flashes which are singled out for detailed analysis.

The overlap procedure requires a method for determining if the solution from a given window corresponds to the same emission as the solution from a previous window. Two windows are considered to contain the same emission if the time between the peak value of successive windows is less than half the window length (0.71 μs), as depicted in Figure 2.5. Here, the waveforms for three channels from successive windows in a flash are shown. Each successive window is shown vertically, with the time limits of the window denoted in green. The time of the window is taken to be the time of the time of the largest voltage within it, shown with a cyan line. The time of the maximum sample tends to move abruptly, as in the figure, when the emission from lightning is impulsive. For continuously radiating sources, the transition is more gradual. Regardless, a new 'event' is said defined whenever the time of the maximum sample moves more than half a window length. This criterion has the effect that 2 sources can be located in a single window, particularly in the case of continuously radiating source, but does not otherwise significantly affect the results of the calculation.

The weights for the centroid calculation are based on the closure delay, defined as

$$\tau_{123} = \tau_{12} + \tau_{23} - \tau_{13} \tag{2.9}$$

where the indices indicate the antennas involved in the time difference. The closure delay is closely related to the closure phase used in astronomical interferometers. If the emission is from a distant point source the expected closure delay is zero. The closure delay from a non-symmetric distributed source will deviate from zero. In addition, because the time delay measurement is imperfect, the measured closure delay will vary on the same order as the time delay uncertainty (see Section 4.1 below). Typical values of the closure delay are much less than the sampling period of the digitizer, however if the wrong peak was chosen from the cross correlation due to noise effects, the closure delay greatly deviates from zero. The weighting used is such that solutions with large closure delay are excluded from the mean, while those with reasonable closure delay are weighted roughly equally.

Finally, it should be noted that the actual time resolution of the observations is substantially better than that of the 256 sample (1.42 μs) window approach described above. In particular, as can be seen from Figures 2.4 and 2.5, a given time window could contain the responses to multiple impulsive events, but only one power weighted mean location is determined for the relatively long window. More detailed observations could be obtained by shortening the window length, or by examining the raw waveform data.

A given window could also be completely filled by continuously radiating events such as stepped and dart leaders to ground, or analogous breakdown during intracloud discharges, in which case the radiation centroid (again weighted
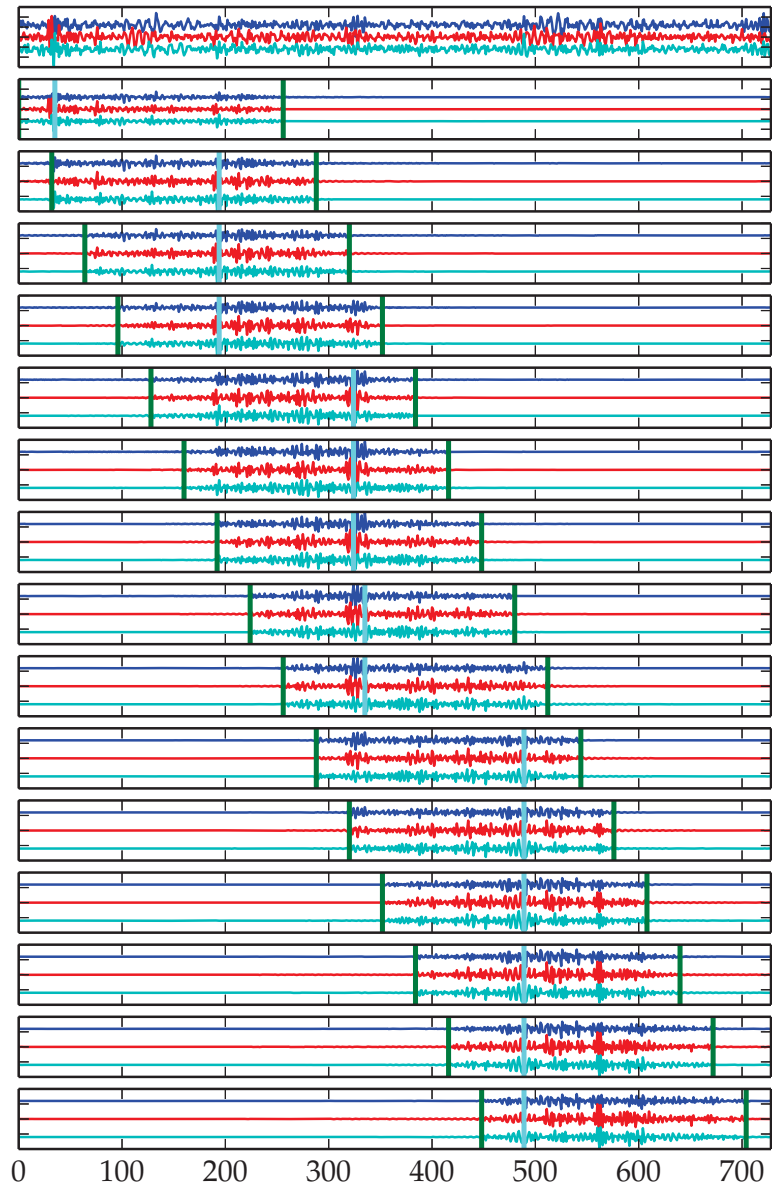
Figure 2.5: Separating overlapping windows in time. The time of the sample with the maximum voltage (denoted by the cyan line) is used for the time of a window (denoted with green lines). Once the time of the maximum value moved by more than half of the integration period, a new event is formed, seen by the sudden shift in the cyan line. The horizontal axis is samples, and each iteration shifts the window by 32 samples.

by the strongest activity) will be located as a function of time in the successive overlapping windows, again with correspondingly higher time resolution. The ability to locate both continuously radiating as well as impulsive events is one of the major advantages of interferometric vs. time-of-arrival measurements. Another advantage is that interferometric measurements can be processed to generate spatial *images* of simultaneously radiating events during each time window, rather than just a centroid location. These interferometric imaging techniques have been well developed for radio astronomy, and will be applied to lightning in Chapter 3.

2.4   Example Lightning Map

The net result of mapping lightning as outlined in this chapter is very good. Sources can be, and routinely are, located down to the thermal noise floor at the first stage amplifier. And, while the location provided for each window is a single dot on the sky, the time resolution is such that when all the sources are combined, the map resembles an image. An example map is shown in Figure 2.6 of a flash occurring on July 8, 2013 at 20:07:22 UT. This flash has been chosen because it covers a large portion of the sky, and the interferometer was operating with 4 antennas at the time, making it a good example for multiple baseline techniques as well. The flash will be discussed in more detail in Section 5.2, and is here only used as an example of the output.
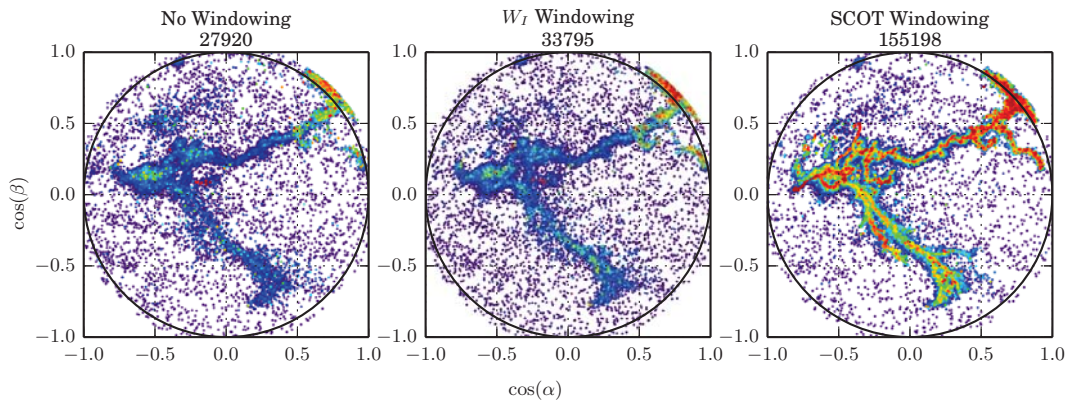
Figure 2.6: Example map of a lightning flash using various weighting functions

CHAPTER 3

MULTIPLE BASELINES

The two-baseline technique discussed in Chapter 2 leaves a lot to be desired. While the astronomical community has regularly and vigorously sought to increase the number of baselines used in radio interferometers whenever possible, lightning interferometers have persisted in using only two perpendicular baselines since the original *Hayenga and Warwick* (1981) two-dimensional study. The narrow band interferometer employed at New Mexico Tech used 5 antennas; however, still only two perpendicular directions were used for the baselines. It is instructive to note that in the literature on broadband lightning interferometers, the equation used to determine the azimuth and elevation of a source is in all cases in close resemblance to equation 2.4, and interferometer arrays always used perpendicular baselines as a correction for imperfect antenna placement was only recently published in *Stock et al.* (2014).

In this chapter, the two-baseline technique will be greatly extended to not just correct for imperfectly deployed arrays, but to utilize an arbitrary number of antennas deployed in an arbitrary configuration to improve the resulting solutions. There are numerous benefits which might be obtained through use of more baselines: If The majority of noise sources are not correlated at different antennas (for example, thermal noise), recording the emission from lightning at more antennas will improve the signal-to-noise ratio of the measurement. This in turn should improve minimum locatable signal, and the uncertainty in the location, especially for faint sources. Additional antennas also offer a natural way to increase the baseline lengths to improve angular resolution, without risking possible complications due to aperture size or lack of short baseline sampling. Finally, multiple baseline measurements hold promise in being capable of locating multiple sources in a single integration window, or even sources radiating in an extended volume, something which current lightning interferometers are incapable of doing.

Implementing multiple baseline techniques and imaging has been a long time coming. The first multiple baseline algorithm implemented for non-synthetic lightning data applied the algorithm discussed in Chapter 2 to all possible

permutations of 3 antennas in the array. An array of 4 antennas has 12 unique permutations of 3 antennas, even though it offers only 6 baselines. This algorithm met with limited success. The variance of the solutions obtained with different permutations of antennas for a single integration window was greater than the jitter in the solutions from a single 3 antenna permutation from window to window. While valid solutions were produced, the number of solutions decreased and there was no evidence of improved accuracy or sensitivity.

There is a short discussion of Fourier synthesis imaging techniques given in *Stock et al.* (2014), however the example presented (Figure 3.1) was made only as a proof of concept. The baselines were required to be purely in the north-south and east-west directions (contributions from diagonal baselines could not be computed), and the image took several minutes to render for a single 1.4 μs window. The algorithm was far too slow to be applied to an entire lightning flash.

The imaging algorithm presented in this chapter was not developed until early in 2014. Here, the cross correlations of a signal arriving at each baseline are projected onto the image plane directly. For broadband data with a small number of baselines (3–30 or so), this turns out to be a very efficient technique; the processing time for imaging is only slightly slower than for the traditional algorithm presented in Chapter 2. Unfortunately, not all the benefits listed above have yet been realized. For the 4 antenna solutions, there is a small but noticeable increase in the detection efficiency of faint sources, resulting in a 15% increase in the total number of sources located, but no improvement to the minimum locatable signal. More importantly, the uncertainty in the location of faint sources is improved by around 30%. However, multiple source location in a single integration window is still not possible. Images with multiple sources can sometimes be identified by hand, but the second source has always been fainter than the side lobes of the primary source. Multiple sources are also detected if the image is run through a deconvolution algorithm, though unfortunately deconvolution is as likely to locate a residual side lobe as a true second source. In short, multi-baseline techniques are a promising work in progress.

3.0.1 Primary Novel Techniques/Findings

Fourier synthesis imaging as it relates to lightning has not been well explored in the literature. Jake Hartman imaged lightning using narrowband LWA data (*Hartman et al.*, 2012), however this was done by simply applying astronomical interferometer techniques to lightning without alteration. The data were also recorded using an extremely narrow bandwidth (100 kHz), and as a result the time resolution is not high enough to observe fast processes during the flash.

While not related to lightning, it is likely that the techniques used to image cosmic rays by the ANITA project are similar to those presented in Section 3.2 (*Gorham et al.*, 2010). While the receiver used in the ANITA project operates at a higher frequency (UHF), it was also designed to detect and locate impulsive radio sources. In all of the cases above, no scholarly articles have been published detailing the techniques.

Time of arrival lightning mapping systems (such as the LMA) make heavy use of as many baselines as possible to improve the accuracy of the resulting maps. However, lightning interferometer systems all normally use only 2 orthogonal baselines. As a result, at least in the context of lightning, the majority of this chapter is novel.

The following findings are novel:

- Formulations of Fourier synthesis imaging for broadband lightning data.

- Extension of the cross correlation mapping algorithm to an arbitrary number of antennas in any configuration.

3.1 Fourier Imaging

As is the case for other lightning interferometer studies, the interferometry algorithm presented in Chapter 2 treats the instrument as a short-baseline time-of-arrival system for determining the directions of the source centroids. The time delays are determined using a cross correlation, and then a single direction to a source can be determined for each integration window. By applying the algorithm to many windows, a map can be made of the lightning-produced VHF source locations with time. The broadband interferometer has such high time resolution that enough point source locations are found over the duration of a lightning flash that, when combined, the map can appear to be a continuous image.

By simply changing the processing algorithm, the same data can be used to produce actual *images* of the radiation activity of multiple or distributed sources within each (1.42 μs) time window. The basis for doing this are the fundamental ideas of Fourier optics. The image of a 2-dimensional pattern of radiation sources is the Fourier transform of the diffraction pattern of the sources incident upon the observer. At optical frequencies, the Fourier transformation is produced by the eye or other lenses. At radio frequencies, the incident diffraction pattern is sampled by an array of antennas, the Fourier transform of which is the source image in the direction cosine plane.
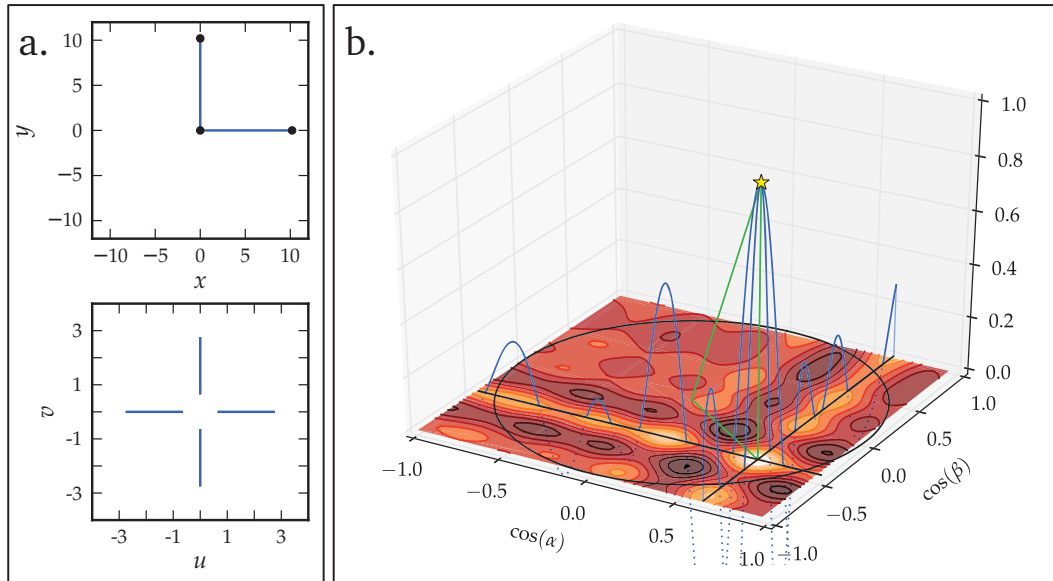
Figure 3.1: Fourier synthesis imaging for an example window. Example illustrating how the broadband data can be used to instantaneously image the lightning activity within a given 1.42 μs time window, as opposed to locating only the strongest source. The blue lines extending both above and below the direction cosine plane are the cross-correlation results from each orthogonal baseline, whose peak intersection (yellow star) is the centroid of the strongest source. The radiation intensity can be determined over the entire direction cosine plane, as indicated by the diffraction pattern associated with a minimal 3-antenna array.

Techniques for obtaining images have been fully developed and applied by the radio astronomy community, utilizing large arrays of receiving antennas (e.g. *Taylor et al.*, 1999). Correlations between all possible pairs of antennas sample the diffraction pattern over a variety of baseline lengths and directions, which is related to the radio image in the sky by a 2-dimensional Fourier transformation. For narrowband systems, a general baseline corresponds to a single location in the spatial frequency or u,v diffraction plane. Many sets of antennas and baselines are required to sample the diffraction pattern sufficiently to produce a quality image. For broadband systems, data from a given pair of antennas corresponds to a range of baseline distances in terms of wavelengths, greatly increasing the extent to which the diffraction pattern is sampled[1]. As result, broadband systems can produce quality images with fewer antennas.

An example of a simple image from the data of this study is shown in Figure 3.1. In this simple example, the $\cos(\alpha)$ and $\cos(\beta)$ directions are assumed to be aligned with the perpendicular baselines, even though in truth the baselines are rotated with respect to north. The data come from a 256 sample (1.4 μs) window from Flash A (described in Section 5.6). For the interferometer configuration at this time, the baselines vary from $(2/3)\lambda$ to $(8/3)\lambda$. The antenna locations in the x,y measurement plane are shown in Figure 3.1a, along with the corresponding sampling in terms of wavelengths in the u,v plane. The third baseline, corresponding to the diagonally displaced outlying antennas, has been omitted to simplify the figure, but could be used to further improve the sampling. The one-dimensional cross-correlation obtained from the cross-spectrum of each baseline corresponds to the image values in orthogonal directions in the direction cosine plane (blue lines in Figure 3.1b). The intersection of the correlation peaks corresponds to the centroid value obtained in Chapter 2.

3.1.1   Preliminaries

Before delving too far into the implementation of Fourier synthesis, a number of definitions are needed. There are three planes that are frequently referred to when doing image synthesis, and have already been referenced above. Figure 3.2 shows an example of these three planes. First is the measurement plane, defined by x pointing East and y pointing North with units of length (meters). The measurement plane defines where the antennas are physically located. The left panel of Figure 3.2 shows the measurement plane for the 2013 antenna configuration.

---

[1] Wide bandwidths can be used to extend the sampling of the diffraction pattern only if the frequency spectrum does not have any structure, such as emission lines. In the case of lightning, the spectrum in the radio frequencies is smooth and continuous.

Next is the image plane, which is synonymous with the cosine projection, and defined by l pointing East, and m pointing North,

$$l = \cos(\alpha)$$
$$m = \cos(\beta) \, ,$$

(3.1)

where α is the angle between the radius vector to the source and the x axis, and similar for β and the y axis. l and m vary from -1 to 1 and are unitless. The horizon (assuming a flat Earth) is defined by $l^2 + m^2 = 1$. The image plane is the same as the cosine projection used for many of the lightning maps, and discussed in detail in Section 1.4. It is important to note that the image plane is not defined in terms of angle, although there is a non-linear one-to-one transform between a source's angular location and its location on the image plane. The center panel of Figure 3.2 shows the image plane with some synthetic Guassian sources placed in it.

Finally, the diffraction plane, which is the Fourier transform of the image plane, is defined using u and v which can be thought of as 'spatial frequencies'. u and v are unitless, but can be found from the baseline length and the frequency of measure[2]:

$$u = \frac{\Delta x}{\lambda} = \frac{\Delta x \nu}{c}$$
$$v = \frac{\Delta y}{\lambda} = \frac{\Delta y \nu}{c} \, .$$

(3.2)

Here, Δx is the distance between 2 antennas in the x direction, and Δy is the distance between 2 antennas in the y direction, and ν is the radio frequency. The right panel of Figure 3.2 shows the diffraction plane, including the diffraction pattern of the image in the center panel of the figure. The diffraction pattern cannot be fully sampled; instead measurements are made in only a few locations. The measurements that would be made by the antenna configuration in the left panel at 50 MHz (the center frequency of the interferometer in this study) are overlaid in black dots. If an image were produced based on these very sparse measurements, the image in the center panel would be poorly reproduced.

Since the image plane and the diffraction plane are related by a Fourier transform, the basic goal of Fourier synthesis is to compute

---

[2] Note, this is a simplification. In addition to u and v, there is also a vertically oriented spatial frequency w. However, if the array is planar, and w is defined to be perpendicular to the plane (pointing at the zenith), then $w = 0$. If the field of view of the interferometer were narrow, as is the case with parabolic reflectors, the interferometer is not usually centered on the zenith, in which case w usually is not perpendicular to the plane of the array, and the extra term must be taken into account.
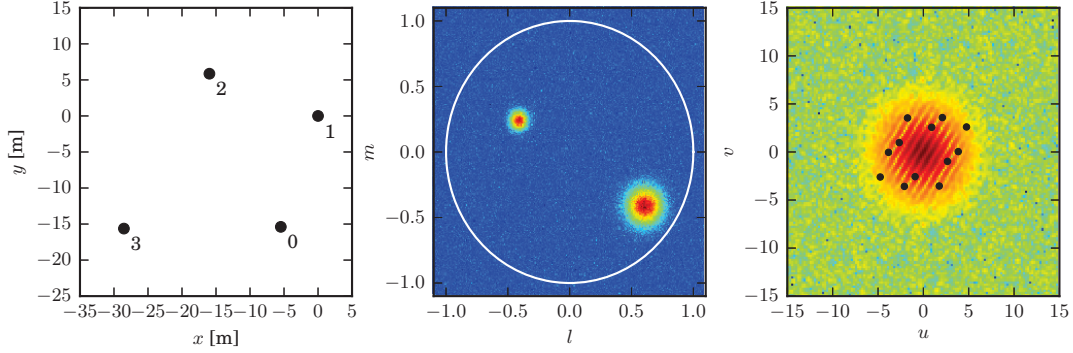
Figure 3.2: Measurement, image, and diffraction planes used in imaging. Left, is the measurement plane showing the location of the 4 VHF antennas as deployed in 2012. Center, is the image plane with two Guassian sources in the sky, color represents amplitude. The white circle shows the location of the horizon. Right is the diffraction plane of the center image, color represents spectral power in arbitrary units. Black dots show where the diffraction plane would be sampled at 50 MHz by the 4 antennas.

$$f(l, m) = \int \int F(u, v) e^{2\pi i u l} e^{2\pi i v m} du dv .$$ (3.3)

The diffraction pattern, $F(u, v)$, is sampled by each baseline (each pair of antennas) in the interferometer array. In astronomical circles, $F(u, v)$ is referred to as the complex visibility, and is found by multiplying and averaging the narrow-band signal arriving at two antennas[3]. By having many different antennas, or by allowing the Earth to rotate, several different u,v locations are sampled.

With broadband data, $F(u, v)$ for one baseline is the cross spectra, $G(\nu)$, of the signal coming in at two antennas. The cross spectra can be found by implementing the FFT in 1-dimension,

$$G_{ij}(\nu) = \mathcal{F}(s_i(t)) \mathcal{F}^*(s_j(t)) ,$$ (3.4)

where i and j are the indexes for the antennas, and s is the voltage signal received at the antenna. The trick then is to relate the frequency ν of the cross spectra to the u,v coordinates of the diffraction plane, which has already been done in equations 3.2.

By rearranging and combining the terms in equations 3.2, we see that

---

[3]This is also a simplification, what is described is the simplest form of correlator which only works properly on narrow bandwidth measurements. Modern astronomical interferometers are utilizing ever increasing amount of bandwidth, and utilize more sophisticated correlating techniques.
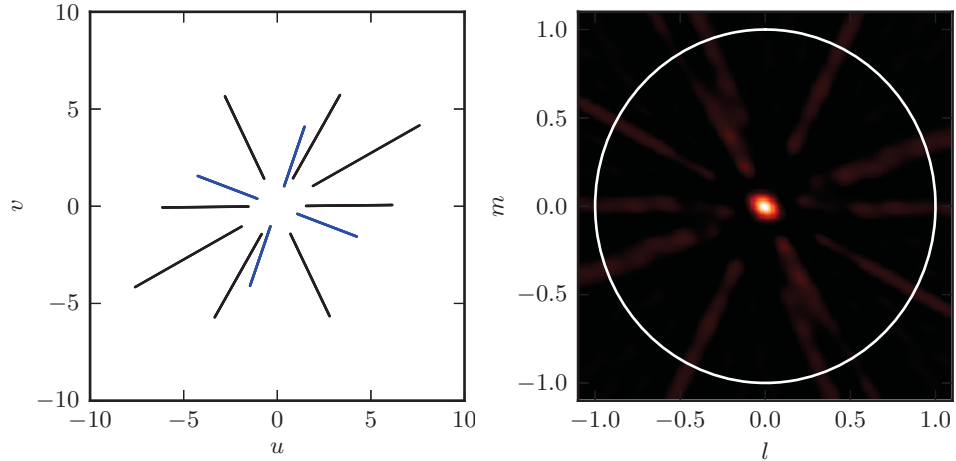
Figure 3.3: *u,v* coverage and point spread function. Left, the *u-v* coverage, or sampling function, including all 6 baselines from the 2013 4 antenna configuration. The blue lines are contributed by the 1-0 and 1-2 baselines used in the two-baseline algorithms. Right, the ideal point spread function, found by taking the Fourier inverse of the sampling function.

$$\sqrt{u^2 + v^2} = \frac{d\nu}{c} ,\qquad(3.5)$$

where d is the baseline distance. A change in ν causes a radial change in the u,v coordinates. Figure 3.3 shows the sampling function of the diffraction plane produced by measuring 20-80 MHz signals at the antenna locations shown in Figure 3.2. This sampling function is referred to as the *u-v* coverage of the interferometer. In astronomical interferometers, which use the Earth's rotation to increase the *u-v* coverage, a given baseline at a given frequency will produce an ellipse in the sampling function. For broadband interferometers taking snapshots of the sky, the sampling function is made up of radial lines.

If a perfect point source were observed at the zenith, the antennas would sample the Fourier transform of a delta function, which is unity for all frequencies. An interferometer observing such a source would produce a diffraction plane with ones in all sampled locations and zeros elsewhere. The Fourier inverse of this sampling is called the point spread function, and describes the response of the interferometer to a perfect point source. The point spread function for the 2013 4 antenna configuration is shown in the right panel of Figure 3.3. The central bright peak describes the maximum angular resolution of the interferometer, and the radial pattern are the side lobes of the interferometer.

3.1.2 Implementation without FFTs

Because the diffraction pattern is sampled in a discrete manner, the integrals in equation 3.3 become sums, and the image is given by:

$$f(l,m) = \sum_u \sum_v G_{ij}(\nu_{uv})e^{2\pi i(ul+vm)} \ .$$
(3.6)

Computing the sum in this way will produce an image, but the computation is far from efficient. The size of the u,v space may be rather large, and many u,v values covered by the sums are not sampled by the u-v coverage of the array, and therefore do not contribute to the final image. Because the measurements are broadband, the measurements always fall on lines in the diffraction plane (as shown in Figure 3.3). Therefore the sums can be reordered to go along each line in the point spread function,

$$f(l,m) = \sum_{ij} \sum_v G_{ij}(\nu)e^{2\pi i(u_\nu l+v_\nu m)} \ ,$$
(3.7)

where the first sum is a sum over the baselines, and the second is a sum over the frequencies. Not all u,v values of the diffraction plane are covered by the summation; those excluded in equation 3.7 are not sampled and do not contribute to the result.

Frequently, the delay time from the antenna to the digitizer is not the same for all antennas, arising, for example, from different cable lengths. In this case, the delay can be corrected by adding a term to the transform,

$$f(l,m) = \sum_{ij} \sum_v G_{ij}(\nu)e^{2\pi i\nu\Delta\tau_{ij}}e^{2\pi i(u_\nu l+v_\nu m)} \ ,$$
(3.8)

where $\Delta\tau_{ij}$ is the relative delay time between the ith and j^{th} antennas.

The last step in implementing the Fourier image is to remove the complex exponential computation and treat the argument of the sum as real. This is done only to reduce the computation time, which tends to be larger for complex numbers.

$$f(l,m) = \sum_{ij} \sum_{v>0} \left(2\Re(G_{ij}(\nu))\cos(\theta) - 2\Im(G_{ij}(\nu))\sin(\theta) \right) \ ,$$
(3.9)

where θ is the argument to the complex exponential in equation 3.8.

During this study, much more emphasis has been placed on the quality of the results rather than on the speed at which they can be produced. However, the
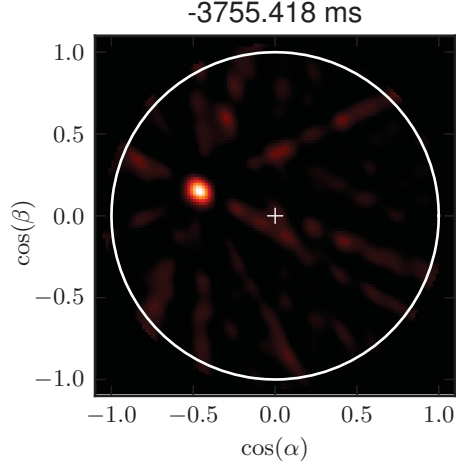
Figure 3.4: Fourier image of a source computed without FFTs. Image computed using a single 256 sample (1.4 μs) time window of data taken from a lightning flash on 2013/07/08 at 20:07:22 UT. The white circle shows the horizon, and the white + the zenith. Color of the image shows correlation amplitude, increasing from black through red to white, and correlations below 0 shown in black.

computations still need to be completed in a reasonable amount of time (a day or so per flash). For this reason, a rough approximation of the computation scaling is presented here. Table **??** gives more practical estimates of the time needed to process 1 window of data, as well as an entire flash. The algorithms are all implemented in Cython, or with numpy vector computations, neither of which are particularly high performance programming languages. Additional performance gains may be found by migrating to another language, however the table values do give good relative comparisons.

Regardless of how the image is computed, first the cross spectra are needed. If there are S samples in each integration time window, and $N_B = N_A(N_A - 1)/2$ baselines, then the time to compute the cross spectra scales as:

$$\mathcal{O}(\text{cross spectra}) \propto N_B \cdot S \log_2 S . \tag{3.10}$$

The image is computed pixel by pixel, and for each pixel one must loop through the baselines and frequencies. The summation is over ν, and the number of frequencies is proportional to the number of samples in the window, so:

$$\mathcal{O}(f(l,m)_{\text{Fourier}}) \propto M \cdot N_B \cdot S , \tag{3.11}$$

where M is the number of pixels in the image. In the case that one dimension of the image is proportional to the number of samples in the integration, $M \sim S^2$.

Algorithm	Compute Time (Window)	Compute Time (Flash)
Cross Spectra	2.615 ms	--
Fourier Image	1361.541 ms	11 days
FFT Image	Not Implemented	Not Implemented
Projection Image	2.787 ms	1 hour

Table 3.1: Computation times for different imaging algorithms. All algorithms produce a 128×128 pixel image of the entire sky, using 4 antennas arranged as in Figure 3.2. The last column extends the computation out to 700,000 windows, the approximate length of a typical flash. All algorithms were implemented in Cython or with numpy array computations. While some effort has been made to optimize each algorithm, these numbers should be considered in comparison to one another only.

In almost every practical case, computing the image in this manner takes much much longer than computing the cross spectra. However, the processing time can be dramatically shortened.

3.1.3 Implementation with FFTs

The way in which imaging is usually done is with FFTs, as they give a much needed reduction in implementation time. The complication with using FFTs is that the diffraction plane must be placed on a square grid, and the locations of the u,v sampling function rarely happen to fall exactly on a grid location. Placing the measured cross spectra values on the u,v grid is referred to as 'gridding'.

If we want to produce a 128×128 pixel image of the $\cos(\alpha)$ and $\cos(\beta)$ in the range of $[-1.1, 1.1]$ (as shown in Figure 3.4), then the smallest interval in the image plane is 0.0172. This corresponds to a maximum u and v value of 29.1, which is quite a lot larger than the maximum value seen in Figure 3.3 of the u-v coverage of about 9. The result is that each pixel of the diffraction pattern will have contributions from numerous frequencies. This problem is illustrated in Figure 3.5. The blue 'lines' in this figure are actually a sequence of points – the measurement locations for a standard 256 (1.4 μs) time window. Each 'line' contains 172 measurement locations.

FFT computation of the image has not yet been implemented, and due to the above complications, may not be. However, we can still discuss how the computation scales, for comparison with the other algorithms:
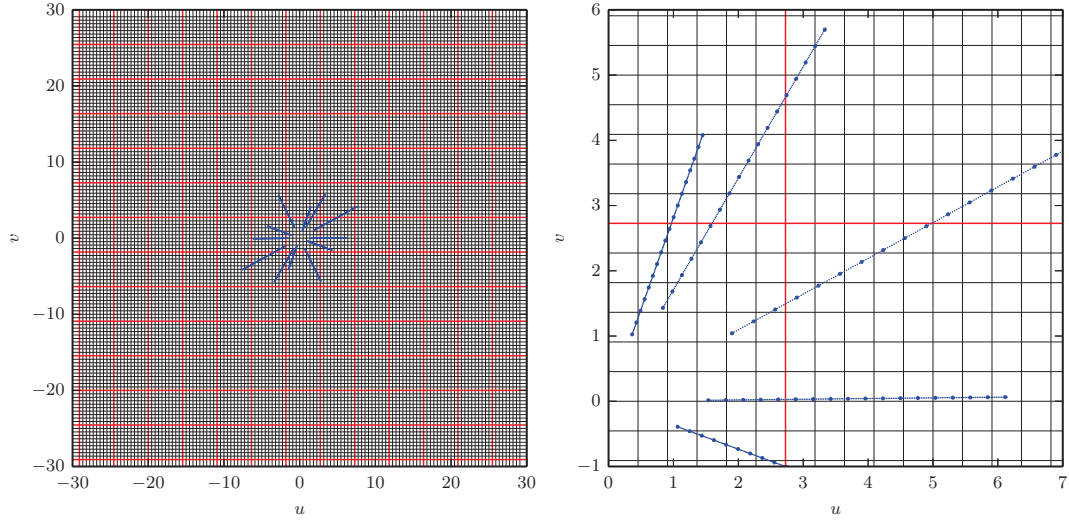
Figure 3.5: Gridding broadband data onto the diffraction plane. The black lines show the boundaries of a 128×128 pixel grid of the diffraction plane designed to see the entire sky, with red lines every 10 grids. The blue points overlaid are the measurement locations of the sampling function. The left panel shows the entire diffraction, and the right zooms in on a region with large dots every 10 measurement locations.

$$\mathcal{O}(f(l,m)) \propto N_B \cdot S + M(\log_2 M)^2 \ . \tag{3.12}$$

The first term is needed for gridding the cross spectra (complex visibility) on the diffraction plane; the second term accounts for the inverse Fourier transform in two-dimensions. This is clearly faster than the Fourier synthesis algorithm implemented without FFTs. Depending on the number of pixels in the image, producing an image using FFTs is frequently faster than computing the cross spectra.

3.2   Projection Imaging

The goal of projection imaging is to produce an image in a short amount of time at the possible expense of image accuracy. Looking at Figure 3.1, it is clear that there is a strong relationship between the cross correlation and the resulting image. Where the cross correlation is high, the image is bright, and vice versa. An image can be produced by projecting the cross correlation of each baseline on the sky. Producing an image in this way is fully equivalent to Fourier synthesis imaging using the techniques described in Section 3.1, if the cross correlation is perfect. However, with a discretely sampled cross correlation, deviations will occur due to differences in the way the measurements are interpolated.
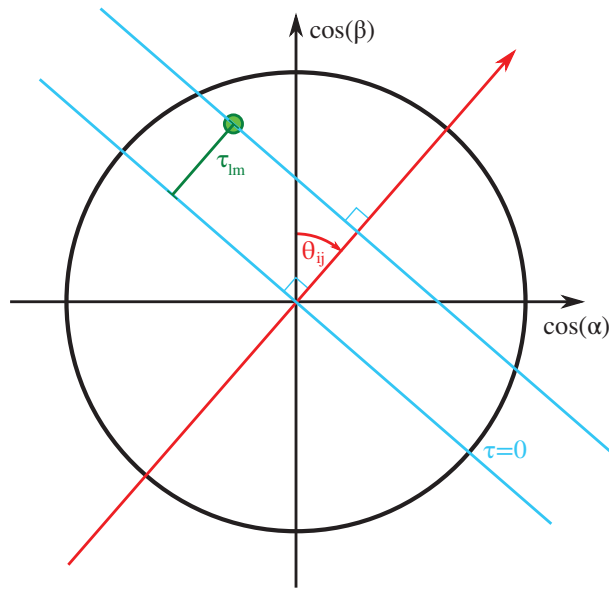
Figure 3.6: Geometry used to determine projection imaging time delay. The red line shows the orientation of the baseline. Each time delay defines a line perpendicular to the baseline orientation (blue), with $\tau = 0$ running through the zenith. Any location in the cosine image plane has a unique time delay associated with it (green).

Computing the image in this way is equivalent to taking several 1-dimensional inverse Fourier transforms from the diffraction plane to the image plane, and then combining them. However, the cross correlation has an independent variable of time, whereas the image plane has coordinates related to angles. The time of the cross correlation is related to a location on the image plane in much the same way as frequency of the cross spectra is related to a location on the diffraction plane.

When producing an image by projecting the cross correlation on the sky, each pixel has an amplitude given by

$$f(l, m) = \sum_{ij} X_{ij}(\tau_{lm} - \Delta\tau_{ij}) , \tag{3.13}$$

where i,j are the antenna indices (so the sum is over baselines), X is the cross correlation, τ_{lm} is the delay corresponding to the l,m pixel, and $\Delta\tau_{ij}$ corrects for differing cable lengths to the antennas. This is equivalent to equation 3.8 with the last sum (over ν) being replaced by an FFT. The speed increase occurs because the FFT can be computed outside the sum over baselines for each pixel! For the 4 antenna interferometer being discussed, the sum over baselines loops 6 times ($N(N-1)/2$), whereas the sum over frequency loops 174 times for a 256 sample window. Not only is one of the sums removed, it is the bigger sum that is removed.

τ_{lm} can be found using the geometry depicted in Figure 3.6. Here, the red line shows the orientation of the baseline. The angle is defined clockwise from north to be consistent with the azimuth angle used in Chapter 2:

$$\theta_{ij} = \arctan(\Delta x / \Delta y) . \tag{3.14}$$

Each time delay corresponds to an angle of incidence,

$$\cos\phi = \frac{c\tau_d}{d} , \tag{3.15}$$

where ϕ is the angle of incidence, and d is the baseline length. Each location in the image plane corresponds to a specific time delay (although the reverse is not so):

$$\tau_{lm} = \frac{d}{c}(l\sin\theta_{ij} + m\cos\theta_{ij}) . \tag{3.16}$$

In this way, each location in the image plane can be assigned an amplitude from the cross correlation of each baseline. By adding up all the amplitudes, an image is formed.
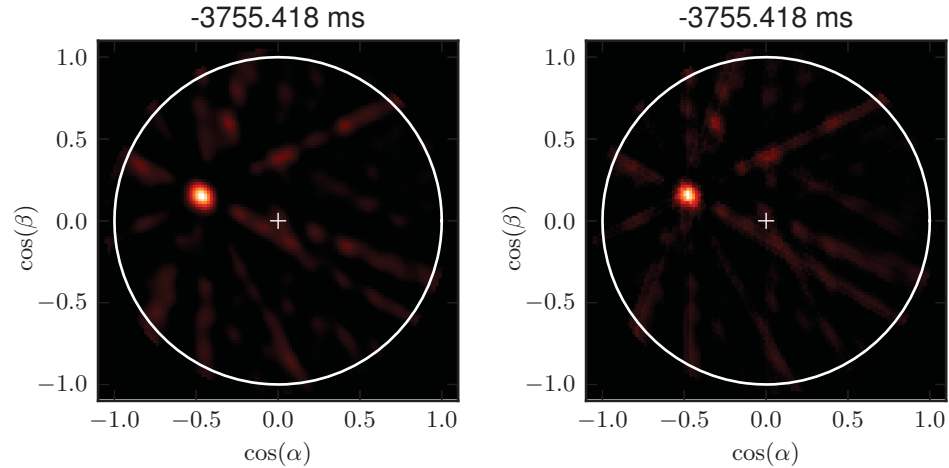
Figure 3.7: Image of a source computed using projection imaging. Left, image produced by Fourier synthesis (Section 3.1). Right, image produced by projection imaging. The cross correlations used for the projection image were interpolated by a factor of 2.

Figure 3.8 shows an example of imaging a bright source seen in a lightning discharge. In principle, the image produced by projection imaging should be identical to that produced by Fourier synthesis, however the images seen in Figure 3.8 differ. The difference in the image arises from how the image is interpolated. With Fourier synthesis, the pixels in the image are guaranteed to be interpolated in a frequency-consistent manner. However, with projection imaging, the cross correlation is finitely sampled, and the amplitude at each pixel contributed by each baseline is discrete. The artifacts that are produced are illustrated in Figure 3.8, which shows the projection image produced by varying amounts of interpolation implemented in the cross correlation. Interpolation of the cross correlation is implemented by zero padding the cross spectra (frequency domain) at high frequencies. Such padding produces interpolation in the time domain such that the frequencies in the signal are held constant. This is different than linear interpolation, and is a fundamental aspect of sampling theorem. As the cross correlation is interpolated more and more, the effects of mismatch between pixel and time delay locations should lessen, which is seen in the right hand panels of the figure. The top pair of plots show the projection image using no interpolation, and the bottom set of plots interpolate the cross correlation by a factor of 4. The right hand set of plots are the differences of the projection image with the image produced by Fourier synthesis, using the same color scale for each plot. White represents no difference between the Fourier synthesis and projection images.

The high interpolation projection images are indeed much closer to the Fourier synthesis images than the low interpolation plots. If the interpolation

53
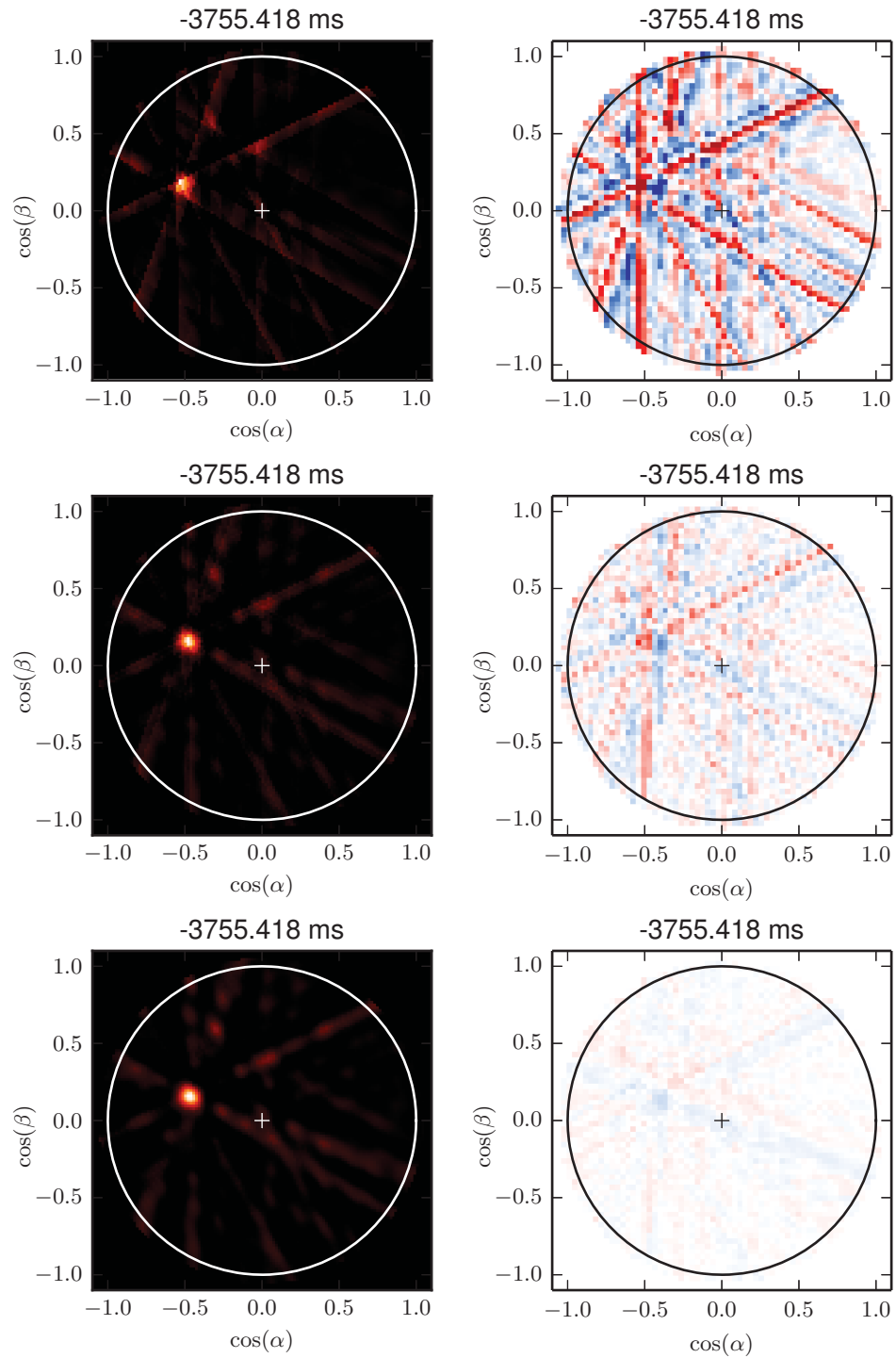
Figure 3.8: Effects of interpolation on the projection image. Left, projection image. Right, difference between projection image and Fourier synthesis image (Figure 3.4). Red regions indicate where the projection image overestimates the value. Top, no interpolation; middle, by a factor of 2; bottom, by a factor of 4.

is high enough, there is no measurable difference between the Fourier synthesis image and the projection image. However, interpolation comes at the cost of processing time.

One of the other benefits of projection imaging is that the frequency weighting techniques developed in Chapter 2 are particularly easy to implement. In addition, to produce the same correlation amplitudes as seen in Chapter 2, the image amplitudes need only be divided by the number of baselines. Both these techniques can be applied to Fourier synthesis imaging as well, however, their application is not as straightforward.

Finally, the computation time for the projection image is particularly short. The computation time scales as:

$$\mathcal{O}(f(l,m)) \propto M \cdot N_B + N_B \cdot S \log_2 S . \tag{3.17}$$

As in the case with the FFT implementation, there are two terms to the computation time. The first covers the computation of the image itself, and the second the extra cycles needed to compute the cross correlation. However, in this case, the second term was already being computed for use with the mapping technique of Chapter 2. In addition, the second term scales exactly as the computation time needed to compute the cross spectra. Depending on the amount of frequency interpolation needed in the cross correlation to produce the desired quality of image, the time to compute the projection image is comparable to the time needed to compute the cross spectra.

3.3   Least Squares Location

In this section, the mapping techniques of Chapter 2 will be combined with the projection imaging techniques developed in the previous section. The result will be maps (instead of images) of lightning, which utilize the added information contained by all the baselines. There are a number of reasons to convert from images to maps. First, maps are oftentimes more convenient to work with because the time axis can easily be expanded or compressed. In comparison, it is difficult to present many frames of imaging data in a manner which is easily visualized. The frames can be animated in a video, however 256 sample windows correspond to a recorded frame rate of 7×10^5 fps. If a 500 ms flash were played back at 60 fps, the video would take over 3 hours to complete, at which point it is hard to identify motion of slowly propagating processes within the lightning flash. Second, an imaged point source shows up as a fuzzy blob due to the angular resolution of the interferometer. However, it is possible to locate to the point
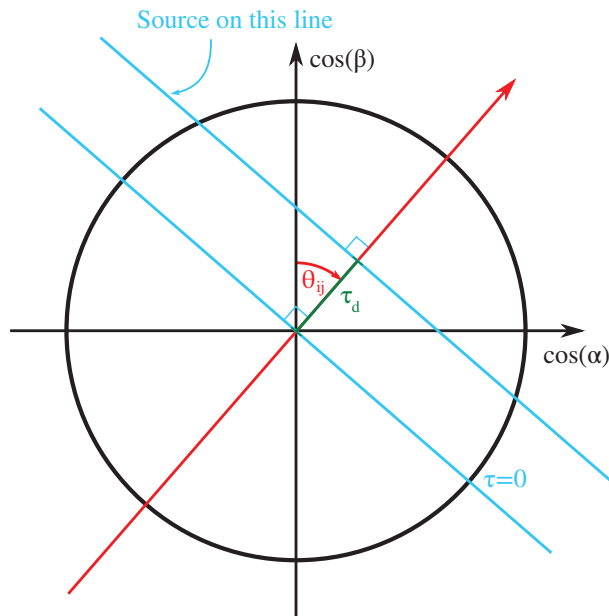
Figure 3.9: Geometry used to determine least squares location. The red line shows the orientation of the baseline. Each time delay defines a line perpendicular to the baseline orientation (blue), with $\tau = 0$ running through the zenith. If the time delay is known, then the source must lie on the corresponding line.

-3755.418 ms
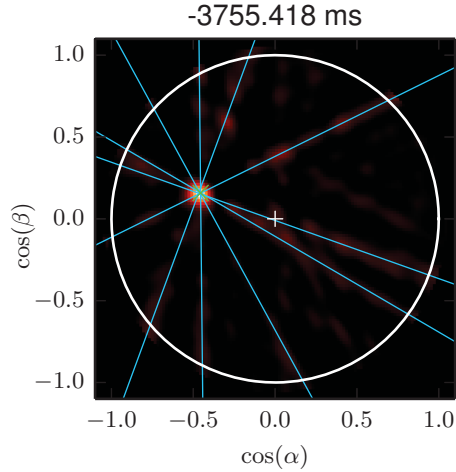
Figure 3.10: Least Squares solution for a high amplitude source. This is the same source used to illustrate imaging in Figures 3.4, 3.7 and 3.8. The blue lines are the lines perpendicular to each baseline orientation, offset by the appropriate time delay. The green $\times$ marks the least squares solution.

source much more accurately than the apparent size of the fuzzy blob (see Section 4.1). By mapping, the precise location of the peak of the blob is visualized, making small movements easier to identify.

In Figure 3.6, it was shown that a given location on the image plane corresponds to a single time delay for each baseline. The reverse of this statement is: if the time delay of arrival at one baseline is known, then the source must lie on a line in the image plane. This is illustrated in Figure 3.9. Again, the red line shows the orientation of the baseline. The known time delay, τ_d, gives a distance from the zenith parallel to the baseline orientation, shown in green. Then the source lies on the blue line perpendicular to the baseline orientation. The equation of the line the source falls on is

$$l \sin(\theta_{ij}) + m \cos(\theta_{ij}) = \frac{c\tau_{ij}}{d_{ij}} , \qquad (3.18)$$

where θ_{ij} is the angle of the baseline relative to north, d_{ij} is the baseline length, and τ_{ij} is the time difference of arrival determined for the baseline. The time delay, τ_{ij}, can be determined from the maximum value of the cross correlation using the techniques outlined in Chapter 2. However, the specific method used to find the time delay doesn't matter, so long as it is accurate.

If there are multiple baselines, the source can be located by determining where the lines intersect. In this case, there are N_B equations with 2 unknowns, l and m. The least squared solution is found by solving

-3755.643 ms
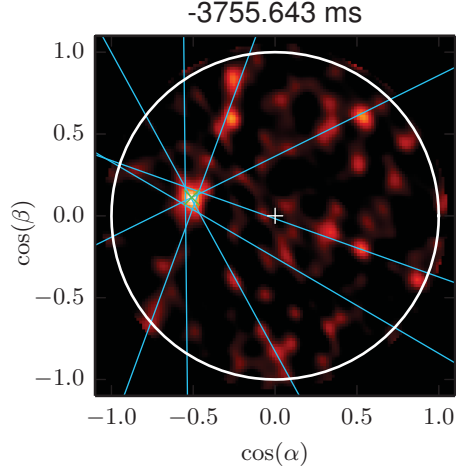
Figure 3.11: Least Squares solution for a low amplitude source. The blue lines are the lines perpendicular to each baseline orientation, offset by the appropriate time delay. The green × marks the least squares solution. The coloration has been scaled to the highest correlation value, making the side lobes more apparent.

$$A\vec{x} = \vec{b}\,, \tag{3.19}$$

where A is a matrix of the antenna orientations, $\vec{b}$ is a column vector of the cosine of the incident angle determined by the time delays (right hand side of equation 3.18), and $\vec{x} = [l, m]$ is the solution. This can be solved for $\vec{x}$ as:

$$\vec{x} = (A^T A)^{-1} A^T \vec{b}\,. \tag{3.20}$$

This technique works very well for high amplitude sources, illustrated in Figure 3.10. The lines determined from each baseline meet in a well defined point, and the least square algorithm has no trouble determining a good solution. Unfortunately, not all sources are bright.

For low amplitude sources, while there is a well defined bright spot in the image, there is much more jitter in the time delays determined from the cross correlation. The result is that the lines do not cross at a well defined location, as illustrated in Figure 3.11. The solution is particularly damaged if only a single cross correlation is off. In this case, the solution is heavily weighted towards the outlying time delay by the least squares algorithm. One correction to this problem is utilization of a weighted least squares solution

$$\vec{x} = (A^T W A)^{-1} A^T W \vec{b}\,, \tag{3.21}$$
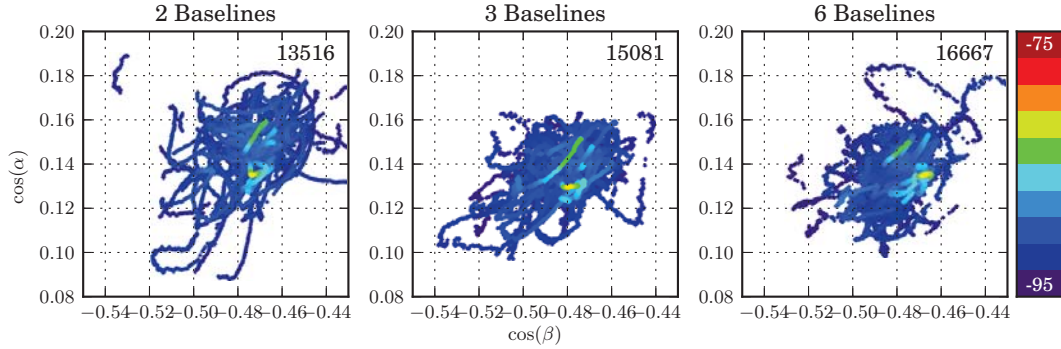
Figure 3.12: Scribble plot showing source stability. Left panel shows the directions to a dim source determined using the traditional, 2 baseline cross correlation algorithm. The center and right panels show the same source, but using locations provided by the least squares algorithm using 3 baselines (3 antennas) and 6 baselines (4 antennas) respectively. Color for all images is based on received power over a narrow, 20 dB, range indicated by the color bar on the right.

Algorithm	Solutions	std (l)	std (m)	Time
2 Baseline	13516	0.015	0.015	–
3 Baseline lsq	15081	0.012	0.014	42.39 s
6 Baseline lsq	16667	0.011	0.011	65.19 s

Table 3.2: Number of solutions and standard deviation for the scribble plots shown in Figure 3.12. Total processing time for 100 μs of data is also quoted for the least squares algorithms. The 3 and 6 baseline algorithms use parallel processing techniques, and the 2 baseline algorithm does not; therefore, the processing time of the 2 baseline algorithm is omitted.

where W is an $N_B \times N_B$ diagonal matrix of weights. The weights can be determined from the residual of the line to an approximate solution, and can also be weighted by the correlation amplitude. An appropriate approximate solution is the location of the maximum brightness pixel of the projection image of the window. Weighting in this way dramatically reduces, but does not eliminate, the number of mis-located sources.

Figure 3.12 shows what I have termed a scribble plot of a faint, stationary source generated from locations produced using three different algorithms. To make a scribble plot, a single 256 sample (1.4 μs) window is processed, then the window is incremented by 1 sample and the next source is located. No averaging occurs over the very heavily overlapped windows; instead, all sources are plotted. Because the sources from each window are not independent, the locations tend to drift in the image. If the emission is produced by a compact source, as is generally the case, the determined source locations will drift over a small region

of the sky. In Figure 3.12, each algorithm processed the same 100 μs time period, using the same frequency weighting for the correlation, and are colored using the same power scale. The sample rate of the digitzer is 180 MS/s, so a maximum of 18,000 solutions could have been located during the time period. The actual number of solutions located is shown in the upper right hand corner of each plot and in Table 3.2.

Scribble plots are a good way to evaluate the stability of sources located by an algorithm, and have been heavily used to tune the parameters of the algorithms developed in this dissertation. In the example shown in Figure 3.12, the source chosen is a continuously radiating, dim source near the beginning of the flash C (Section 5.2). The source is likely moving as part of the initial extension of the negative leader into the upper positive charge region, but does not include the bright emission associated with the leader step. Average negative leader velocity during this portion of most flashes is approximately 10^5 m/s, so the leader tip should move less than 10 meters during the time interval. However, the emission may also be from negative streamers extending from the leader tip, in which case the volume of air producing VHF emission could be very large.

The left hand plot shows the output of the traditional cross correlation algorithm using only 2 baselines (which still requires 3 antennas). This algorithm finds 75% of the total possible number of locatable windows, with a standard deviation of 0.015 ($\sim 0.86°$) in both the l and m directions. This is very good performance for a dim source such as this. The middle plot shows the results for the least squares location algorithm using 3 antennas (3 baselines). The number of located sources increases to 84% of the total possible, and the standard deviation in both directions improves, but improves more in the vertical direction. The right hand plot shows the results for the least squares algorithm using 4 antennas (6 baselines). The processing time increases about 50% over the 3 baseline algorithm, but nearly all (93%) possible windows are located within the bounds of the plot. The stability of the solutions is also improved in both directions, showing a standard deviation of 0.011 ($\sim 0.63°$) both vertically and horizontally. These statistics are detailed in Table 3.2.

Scribble plots will be discussed again in more detail in Section 4.1 to investigate the uncertainty of the interferometry measurements.

3.4 Example Lightning Map

Figure 3.13 shows example maps made using the least squares multiple baseline techniques for both 3 and 4 antenna configurations. For each map, the
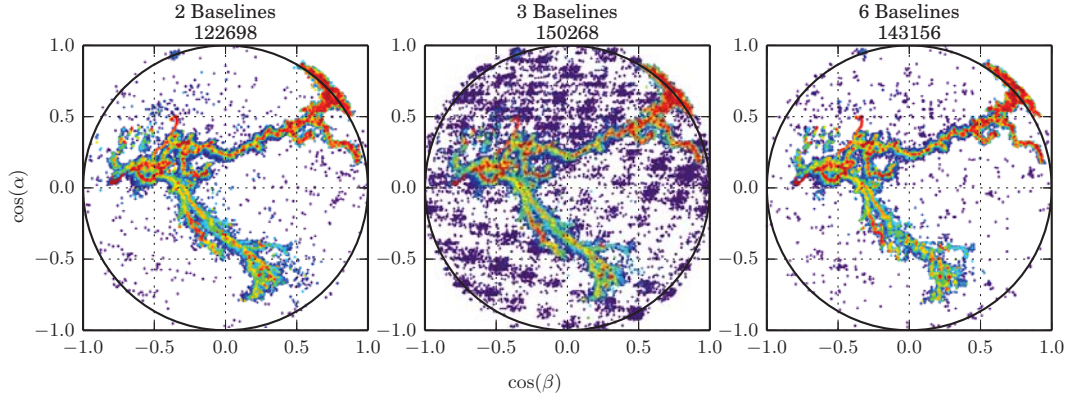
Figure 3.13: Lightning flash mapped with multiple baseline techniques. Left, map of lightning using traditional orthogonal baseline cross correlation technique (Chapter 2). Center, map made using 3 antennas (3 baselines) using the least squares location technique. Right, map made using 4 antennas (6 baselines) using the least squares location technique. All solutions are colored by received power on the same color scale.

same window lengths, window overlap, and frequency weighting were used, outlined in Table 3.3. The medium level of overlap was used to expedite producing the figure, and at this point only the SCOT filter has been implemented for the multiple baseline algorithms. Also, unlike Figures 2.6, noise reduction has been applied to the maps. Based solely on these maps, the positive results are not immediately apparent. The 3 baseline map locates a many more noise contaminated sources which lay the grid expected from aliasing effects. The additional solutions are an unintended consequence of searching for the solution over a narrow range of values in the cross correlation. The noise contaminated solutions can be removed with additional filtering, and the resulting maps have a similar number of total solutions and noise solutions of 2 baseline maps with less noise filtering. The 6 baseline map has 16% more solutions, and similar or slightly reduced noise (seen in the purple sources away from the channels), compared to the traditional 2 baseline map. The additional solutions are in the low received amplitude portions of the power distribution, but the minimum detectable signal is about the same. Overall, this is a net positive change.

Conversely, in the 3 baseline map, while the number of solutions increases, almost all of the additional solutions are noise and contained on the grid corresponding to the sample period of the digitizer (see Section 2.2). The reason for the additional noise sources is that, unlike the traditional algorithm, the least squares multiple baseline algorithm only searches for a solution over time delays which could produce a source on the sky. The result is that almost every window of data produces a valid solution somewhere on the sky, even if no signal from lightning is present. A satisfactory solution to this problem has not yet been found.

Parameter			Baselines	Solutions
Window Length	256	samples	2	122698
Window Overlap	192	samples	3	150268
Weighting	SCOT		6	142189

Table 3.3: Parameters for multiple baseline example map.

Looking at the maps in Figure 3.13, it is difficult to see small differences between the source locations in the flash. To better illustrate these differences, Figure 3.14 overlays the 2 baseline and 6 baseline solutions. This is done by calculating the total received power from the entire flash in each pixel over the region covering the sky, producing a VHF luminosity image. The luminosity images from each algorithm are placed in different color channels, such that where both algorithms produce similar total luminosity, the image show up in shades of white. Regions of the sky where the 2 baseline algorithm located sources, but the 6 baseline algorithm did not, show up as shades of red; the reverse case shows up as shades of green.

The two algorithms generally agree on the location of the lightning channel structure, but there are some differences. The low amplitude noise sources surrounding the flash show little correlation between the 2 and 6 baseline solutions, indicated by the general lack of white pixels in this region. Portions of the channel near the horizon in the north-east (the ground strike location) show a small red halo. The halo indicates that the green pixels are more tightly located in the white portion of the channel, showing that the 6 baseline solutions have more tightly located sources in this region. Some portions of the channel show a location shift. In the image this is seen as one side of the channel being colored red, and the other colored green. The effect is quite noticeable in the long channel extending south-east, but also occurs in other locations. A likely cause for the shift is inaccuracy in the location of the antennas, although a substantial effort has been made to ensure the locations are as accurate as possible. A small inaccuracy in the location of the antennas for the 2 baseline solutions causes a slight skew in the resulting map. For the 6 baseline solutions, small antenna location errors cause correlations that do not perfectly overlap, producing rotation and blurring effects in the maps.

The multi-baseline techniques are still a work in progress. Currently, multi-baseline algorithms offer only a slight, but real, improvement over the traditional 2 baseline cross correlation algorithm. 4 antenna solutions do improve the uncertainty of the sources which are located; however the improvement is at least partially due to the inclusion of longer baselines. 4 antenna solutions also show a small increase in the number of low amplitude sources located. At this point,
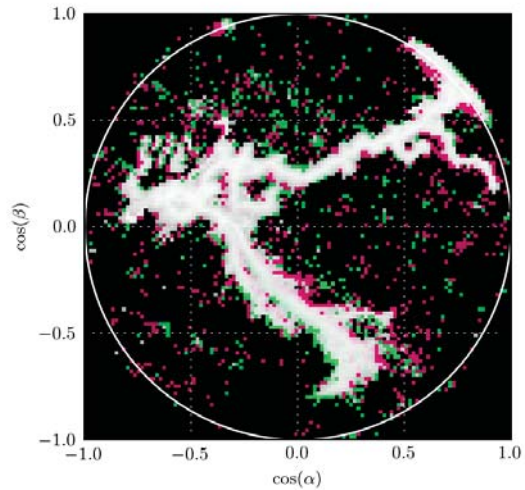
Figure 3.14: Overlay of 2 and 6 baseline interferometer maps. Shown as a colored luminosity image. Locations where both algorithms give similar results are colored white. Reddish pixels were located only in the 2 baseline algorithm, and greenish pixels only in the 6 baseline algorithm.

multiple baseline algorithms are still in their infancy. While not covered in this thesis, deconvolution of the images greatly improves their accuracy, and can be used to directly produce images of lightning integrated over several time windows. Also, the inclusion of a handful of very long baselines can be used to calculate the curvature of the wave-front incident on the interferometer array, which can be used to focus the images and determine the range to the source. It is quite reasonable to expect that multi-baseline techniques will improve greatly in the near future.

CHAPTER 4

SPECIAL TECHNIQUES AND METRICS

This chapter is a collection of short, not fully related, topics on characterizing or improving the solutions provided by the algorithms in Chapters 2 and 3, concluding discussion of how the data are processed.

Section 4.1 covers theoretical and measured estimates of the angular uncertainty of the lightning interferometer. Estimates of angular accuracy of broadband lightning interferometers in the literature are surprisingly sparse. Hayenga and Rhodes developed analytic equations describing the expected error in phase estimation by their equipment, as well as how the phase errors related to position errors in the maps (*Hayenga*, 1984; *Rhodes*, 1989). Unfortunately, the narrowband formulations are not directly applicable to broadband interferometers, especially in the case when all frequency components do not have the same amplitude. *Kawasaki et al.* (2000) noted that broadband interferometers appeared better able to locate heavily branched lightning structures than their narrowband counterparts, but did not quantify the result. Later, *Tantisattayakul et al.* (2005) correctly determined that two sources could be independently located if their times of arrival at the interferometer were greater than the width of the cross correlation peak, but did not relate this to an angular separation or to array size. In *Qiu et al.* (2009), a stationary radiation source was used to directly measure the accuracy of the location provided by a handful of algorithms. This is the ideal way to measure accuracy. However, it does not describe how location uncertainty varies with elevation or signal-to-noise ratio, both of which evolve during a lightning flash. The formulations presented in Section 4.1 were published in *Stock et al.* (2014), but have been greatly expanded.

Section 4.2 compares the minimum detectable signals of the interferometer and LMA. The reason for carefully determining the interferometer sensitivity concerns observations of triggered lightning reported in similar detail by *Edens et al.* (2012). The LMA data of this study showed clear evidence of radiation from upward positive breakdown from triggered lightning, whose source power values were between about 10 and 20 dBW. The sensitivity analysis was done to

confirm that the interferometer could detect such weak signals in natural lightning flashes. The analysis was published in *Stock et al.* (2014), however the flash studied in this paper occurred early in the storm season when the LMA was in a sub-optimal configuration. Here, the analysis has been re-applied to a different flash which occurred when the LMA was fully operational.

Section 4.3 presents a robust way to identify and remove noise contaminated events from interferometric maps of lightning. The noise reduction technique was modeled after the way LMA data is handled. For LMA data, two metrics (reduced χ^2 and number of stations contributing to the solution) are used to filter noisy locations from the data. In addition, the filtration is not applied during processing, instead the metrics are only computed and stored. Filtration occurs during data analysis, allowing the researcher to tailor the noise reduction to the data at hand. For the interferometer, the filtration is based on 4 different metrics, none of which are directly related to the received power at the interferometer. The resulting noise reduction technique does a good job of identifying noise contaminated events without removing events with low received power.

The last few sections describe useful ways to manipulate or transform the data to improve or enable scientific measurements. Section 4.4 discusses how to project the 2D interferometric maps of lightning onto the 3D structures provided by the LMA. The resulting quasi-3D maps can be prone to distortion, and cannot be applied to every flash. That said, the technique results in surprisingly good 3D maps of lightning for most well oriented flashes, and provides a direct way of measuring 3D velocity of processes which are not well mapped by the LMA. Section 4.5 describes methods for investigating the raw VHF waveforms recorded by the interferometer, leveraging the positional information the instrument provides.

4.0.1 Primary Novel Techniques/Findings

The majority of this chapter was published in *Stock et al.* (2014) as new scientific results.

The following findings are novel:

- Theoretical formulations of the location uncertainty for broadband interferometer measurements.

- Sensitivity comparison of the LMA and interferometer.

- Post processing noise reduction without using an amplitude based threshold.

- 3D conversion of 2D interferometer maps.

4.1 Angular Resolution and Angular Uncertainty

The uncertainty of the time delay estimation governs the angular uncertainty of the interferometer. The variance of the time delay estimation can be found from the Cramer-Rao Lower Bound. The minimum variance of any time delay estimator with constant signal-to-noise power spectra is given by (e.g., *Carter*, 1987):

$$\sigma_\tau^2 \geq \frac{1}{2T \int_{f_1}^{f_2} (2\pi)^2 \frac{1+2 \cdot SNR}{SNR^2} f^2 df} \tag{4.1}$$

where T is the integration time, f_1 and f_2 are the lower and upper frequency bounds, and SNR is the linear signal-to-noise ratio. The SNR is the ratio of the RMS amplitude of the signal over the RMS amplitude of the noise floor. The variance in the time delay can be rewritten in terms of the center frequency f_c and bandwidth B as

$$\sigma_\tau^2 \geq \frac{3}{8\pi^2} \frac{1+2 \cdot SNR}{SNR^2} \frac{1}{BT(3f_c^2 + B^2/4)} . \tag{4.2}$$

This uncertainty is a lower bound; the actual uncertainty may be greater than this, especially in situations with low SNR (*Carter*, 1987). The variance in the location of a source in the cosine projection is linearly related to the variance in the time delay, since

$$\cos(\alpha) = \frac{c\tau_d}{d} . \tag{4.3}$$

In general, there is not a single baseline length, d, which can be used to compute the uncertainty. In this case, an average baseline length can be used. The location of the source in the azimuth–elevation projection is not linearly related to the time delays. An error analysis of equations 2.4 for determining the azimuth and elevation from the measured time delays gives

$$\sigma_{Az} = \frac{c}{d} \frac{1}{\cos(El)} \sigma_\tau \tag{4.4}$$

$$\sigma_{El} = \frac{c}{d} \frac{1}{\sin(El)} \sigma_\tau . \tag{4.5}$$

For the parameters of this study (Table 1.2), the rms timing uncertainty of the interferometer is $\sigma_\tau \simeq 0.11$ ns for signals with an SNR of 10 dB. The resulting uncertainty in location is summarized in Table 4.1. The effects of changing SNR and elevation angle are depicted in Figure 4.1.

66
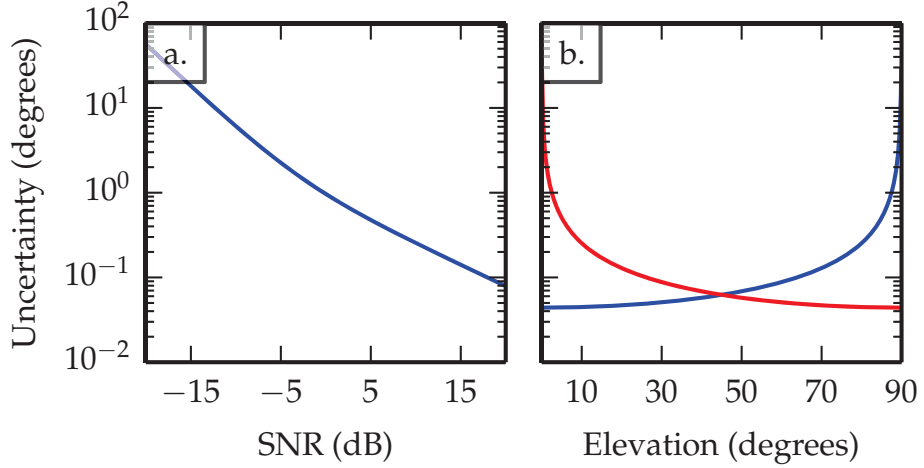
Figure 4.1: Effect of SNR and elevation angle on the angular uncertainty. a) Angular uncertainty vs. SNR for an elevation angle of $45°$. b) Angular uncertainty of the elevation angle (red) and azimuthal uncertainty (blue) vs. elevation angle for SNR = 3 dB. Plots based on the 2012 antenna configuration (10.2 m baselines).

We note that the timing uncertainty σ_τ (0.11 ns) is much smaller than the sampling period of the digitizer, $1/f_s = 5.5$ ns. The reason such a small timing uncertainty is possible is because the time delay is calculated by coherently comparing (i.e., 'interfering') the signals from pairs of antennas. Achieving this small of a timing uncertainty requires that the sampling rates of the digitizers are synchronized to better than the expected timing uncertainty.

In addition to the angular uncertainty, the interferometer also has an angular resolution related to its overall aperture size. From classical diffraction theory, the angular resolution (i.e., the ability to distinguish between two adjacent sources) is approximately $\Delta\theta = \lambda/d$. Interferometers frequently have a collection of different baseline lengths, and broadband interferometers are sensitive to a wide range of frequencies. The resolution pattern is not an Airy disk because the aperture is not filled. Instead, as discussed in detail in Chapter 3, the array of antennas forms a complex point spread function with large side lobe patterns. Still, the resolution for a broadband system can be estimated by λ as the shortest wavelength and d as the longest baseline. For the 2013 antenna configuration, this gives a maximum resolution of $\lambda/d \sim 0.11$ in the image plane (i.e. the cosine projection). A more accurate way of determining the resolution is to fit a Gaussian function to the central maximum of the point spread function, as has been done in Figure 4.2. Here, contours of the Gaussian fit are shown in cyan; the best fit was obtained for a Gaussian function with major $\sigma = 0.0575$, and minor $\sigma = 0.0418$, and a rotation of $31.9°$ clockwise from the l axis. In good agreement with the
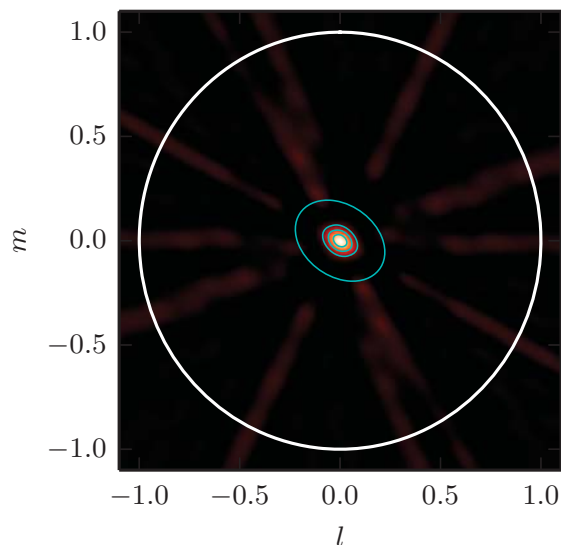
Figure 4.2: Point spread function and the maximum resolution. The background color shows the point spread function (Chapter 3). Overlaid in cyan are contours of a Gaussian fit to the central maximum, showing the smallest region on the sky which can be resolved.

simple λ/d estimate above, the Gaussian fit gives a full-width-half-maximum (FWHM) of the interferometer beam pattern of between 0.098 and 0.135.

Two sources arriving at the interferometer simultaneously which are closer together than the angular resolution element will be indistinguishable. In these cases, the algorithms presented in Chapters 2 and 3 will determine an intermediate location between the two sources. In practice, because the integration time is very short, it is very uncommon for two bright sources to arrive at the interferometer simultaneously (within a single processing window). As a result, effects of limiting angular resolution are only seen in a handful of situations: during heavily branched negative leaders, and when a recoil leader makes a sharp turn during its propagation. The angular resolution element is constant in the cosine projection, but varies in the azimuth–elevation projection. In the azimuth–elevation projection, the angular resolution gets progressively worse towards the horizon. As a result, angular resolution smearing is more common in cloud-to-ground strikes as the initial leader approaches the ground.

The resolution of the interferometer also determines the largest structures that will be detected by the interferometer. In this case, the longest wavelength and shortest baseline are of interest. For both the 2012 and 2013 antenna configurations, structures as large as $\lambda/d \sim 1$ can be detected, or the continuous emission over the entire sky. This is a much larger structure than any lightning

Year	Resolution		Angular Uncertainty		Spatial Uncertainty
2012	0.36	28.9°	0.00302	0.244°	42 m
2013	0.11	8.9°	0.00127	0.103°	18 m

Table 4.1: Theoretical resolution and uncertainty for the 2012 and 2013 antenna configurations. The resolution is first calculated in the cosine projection, then converted to degrees assuming an elevation angle of 45°. The uncertainty assumes an SNR of 10, and is shown for the cosine projection first, and then is converted to degrees assuming an elevation angle of 45°. Spatial uncertainty assumes a range of 10 km.

flash is expected to produce during the short integration time (1.4 μs) of the interferometer. A more realistic (but still conservative) estimate of the largest scale of emission from lightning is about 5°. An interferometer with the same bandwidth which meets this criteria would have a shortest baselines of about 170 m. The broadband lightning interferometer used in this study would greatly benefit from having all baselines extended.

The theoretical treatment provided above for location uncertainty and resolution is broadly applicable. The assumptions made to arrive at the lower bound are that the measured signal is coherent, stationary and Gaussian, and that the noise in each channel is uncorrelated. The lower bound timing uncertainty works equally well for any method that estimates time delay and meets these criteria, including narrowband and broadband interferometry using phase fitting. It should be noted that the VHF emission from lightning in a single window tends to be impulsive rather than continuous. The noise over the window is still fully uncorrelated, but the correlation will not increase as fast as expected with integration time (window length). The result of the signal from lightning not completely filling an integration window should be an increase in the measured uncertainty of the interferometer.

The point spread function has already been observed to be very similar to the Fourier images of real lightning signals arriving at the interferometer (Chapter 3). Using a Gaussian fit to model the central maximum of the point spread function (referred to as the clean beam) is a well accepted technique of radio interferometry.

4.1.1 Measured Uncertainty.

The effects of the angular uncertainty relations described above can be seen in the maps of lightning flashes. From equation 4.2 it is expected that the
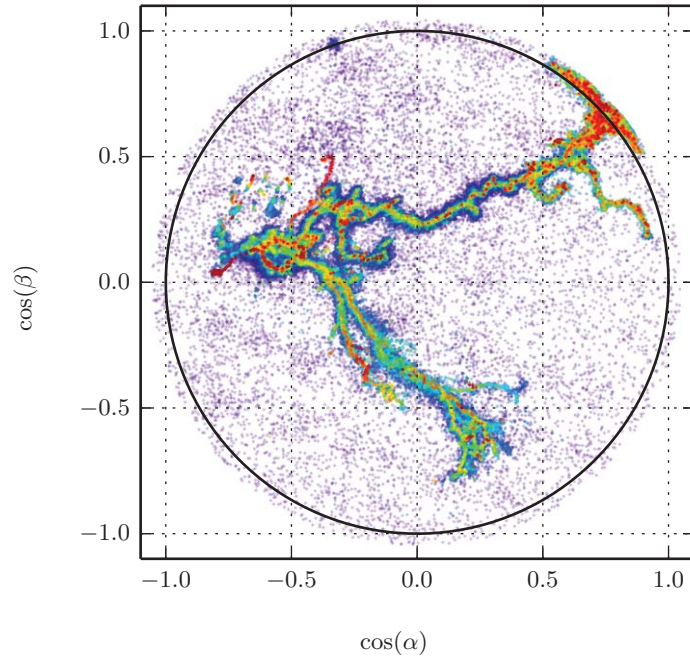
Figure 4.3: Example flash showing the effects of location uncertainty. In the flash, brighter sources are better located than dim sources, and so better define the narrow lightning channels.

angular uncertainty of strong sources will be less than that for weaker sources. Indeed, and not surprisingly, Figure 4.3, in which the sources are colored by received amplitude/power, shows that the stronger amplitude (red or light green) sources more clearly define the breakdown channels in both the positive and negative breakdown regions than the low amplitude (blue/dark green) sources.

An estimate of the actual angular uncertainty can be made from the data in two ways: one, by examining the scatter in scribble plots, and two, by examining clusters of events over the entire duration of the flash. Scribble plots are made by heavily overlapping time windows during processing so that all but one sample is shared between adjacent windows. Instead of combining the overlapping windows into an event, the solution from all windows are plotted. Due to the heavy overlap, the windows are not all independent, and so the source appears to slowly drift over a small region in the sky. A set of scribble plots for two different sources which covers three received power ranges is shown in Figure 4.4. The left hand panel shows a dim source during the initial leader extension between leader steps. The two right hand panels show the negative leader during a step
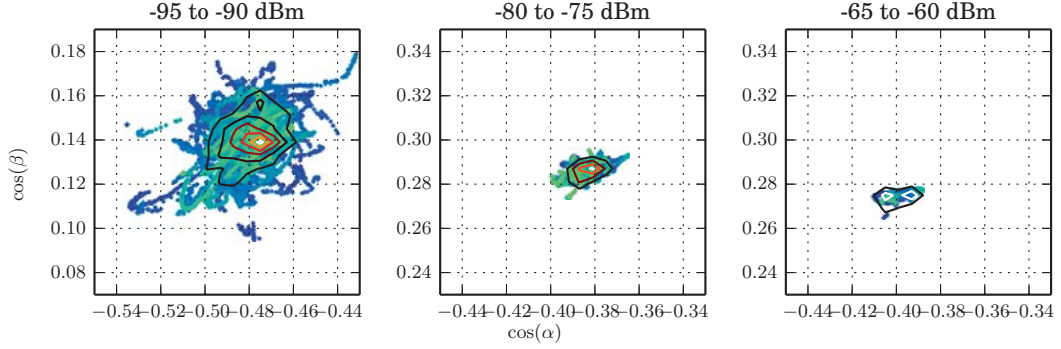
Figure 4.4: Scribble plots for stationary sources of varying amplitudes. The left hand panel is the scribble plot of a 100 μs period of weak emission between negative leader steps. The two right hand panels are of a different 100 μs period which includes a step leader extension. Contours show the density of sources.

extension, at which time the VHF emission is much brighter. Colored contours show the density of located events, which for the two left hand panels is symmetric in the $\cos(\alpha)$ and $\cos(\beta)$ directions. The symmetric distribution of sources indicates a single, stationary source of VHF emission. The right hand panel shows a bi-modal distribution in the $\cos(\alpha)$ direction, indicating the source was moving in this direction during the 100 μs period the scribble plot was produced.

A comparison of the standard deviation of the scribble plots about their mean is shown in Figure 4.5. Here, the solid blue line is the theoretical minimum uncertainty assuming a noise floor of -95 dBm (the expected thermal noise from 60 MHz bandwidth and 50 Ohms impedance). The interferometer only measured the received power, which is the sum of the signal and noise. For small signals, this must be taken into account when computing the SNR by inverting:

$$10 \log_{10} \left(SNR^2 + 1 \right) = P_{received} - P_{noise} \tag{4.6}$$

where the powers are measured in dB[1]. The green and red dots are the measured standard deviations in the $\cos(\alpha)$ and $\cos(\beta)$ directions, respectively. The very high standard deviation of the scribble at -62 dBm is expected since, as noted above, the source appeared to be moving in the $\cos(\alpha)$ direction. While not evident from the contours of $\cos(\alpha)$ in Figure 4.4, the high error seen in the -77 dBm source is also likely due to the emission moving in the $\cos(\alpha)$ direction. The measured uncertainty in the scribble plots is between a factor of 2 and 4 worse than the theoretical minimum uncertainty, as shown by the dotted blue lines.

---

[1] This is a rather crude method of estimating SNR, which breaks down for $SNR < 1$. It would be good to revisit this with a more robust technique.
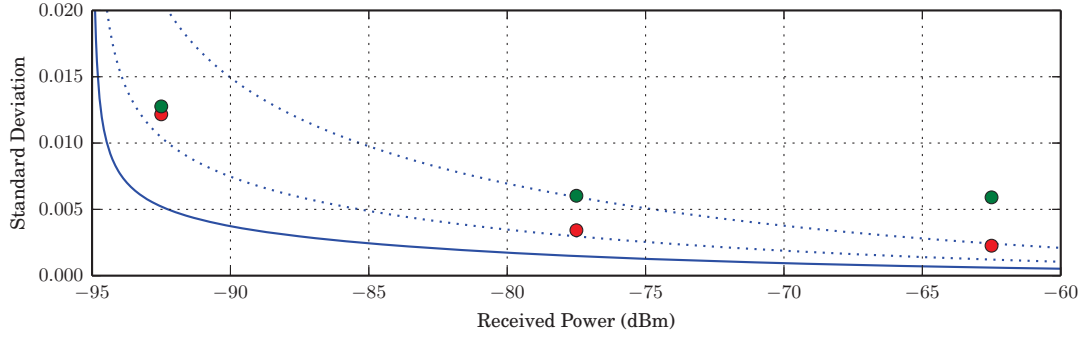
Figure 4.5: Measured amplitude dependence of location uncertainty. The solid blue line is the Cramer-Rao Lower Bound as a function of received power, the dotted blue lines are a factor of 2 and 4 above the lower bound. The dots show the standard deviation of the cosine of the incident angle, as seen in the scribble plots (Figure 4.4) in the $\cos(\alpha)$ (green) and $\cos(\beta)$ (red) directions.

The second method of estimating the angular uncertainty is to examine clusters of solutions. A cluster is broadly defined as a 25 μs window having ten or more sources, and where at least half of the sources are contained within a 0.2 by 0.2 box in the cosine projection. Such clusters are produced, for example, at the tip of propagating negative leaders, and as localized, stationary activity prior to the onset of negative leaders. The angular uncertainty is calculated by subtracting the mean location of each cluster and then examining the scatter of the sources about their mean.

In all, 115,375 sources in 6,130 clusters were found over the duration of flash C (Section 5.2), with standard deviation of 0.0163 and 0.0164 in the $\cos(\alpha)$ and $\cos(\beta)$ directions, respectively. A histogram of the deviation of the location of the sources about the mean location of the clusters is shown in Figure 4.6. The red line in each panel shows the Normal probability density function corresponding to the standard deviations above. The distribution of sources is not normal; instead it follows a Cauchy-Lorentz distribution:

$$P(x) = \frac{1}{\pi} \frac{\gamma}{x^2 + \gamma^2} dx \, , \tag{4.7}$$

where x is either $\cos(\alpha)$ or $\cos(\beta)$, and γ is a parameter of the distribution. The Cauchy-Lorentz distribution does not have well defined moments higher than 1, which means there is no defined standard deviation. What this means in practice is that the wide tails cause any estimate of the standard deviation to depend on the sample size and the search region. There is a well defined FWHM of 2γ. A fit of the Cauchy-Lorentz distribution is shown in Figure 4.6 as the black line.
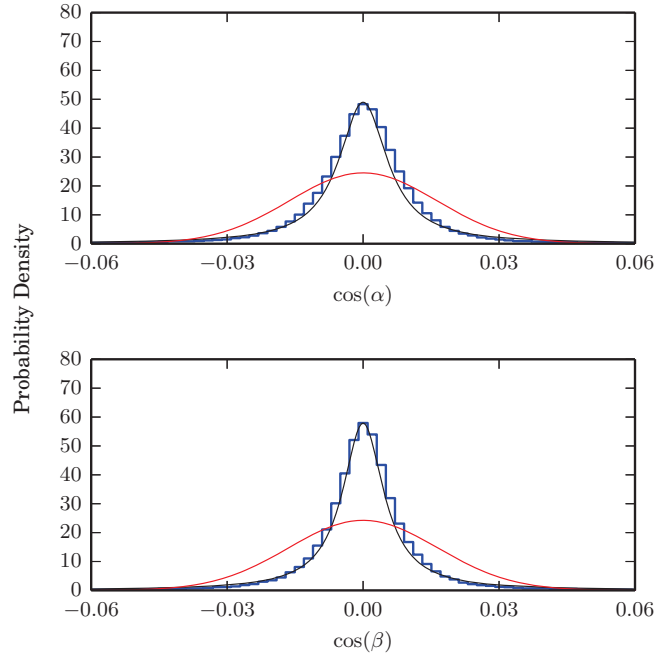
Figure 4.6: Location uncertainty as measured by clustering. (Blue) histogram of the deviations from the mean of 115,375 events found in 6,130 clusters. (Red) the Normal probability distribution with the same standard deviation as the above histogram. (Black) a fit of the Cauchy-Lorentz distribution to the data.

The $\cos(\alpha)$ and $\cos(\beta)$ distributions have FWHM's of 0.013 and 0.011, respectively. These FWHM values correspond to Gaussian distributions with standard deviations of 0.0055 and 0.0047, respectively, about a factor of 3 smaller than if the standard deviation is computed discretely for all sources included in the histogram. In other words, discretely computing the standard deviation of the location scatter implies a larger uncertainty than what is actually observed. The wide tail effect is also present to a lesser extent in the distribution of sources about the mode of the scribble plots discussed above.

Regardless of the method used to estimate the uncertainty, the agreement between the theoretically predicted and the measured error is very good. The theoretical model correctly predicts the behavior of the uncertainty as a function of amplitude. The observed uncertainties are within a faction of 4 of the theoretical minimum uncertainty, and frequently better. Significant deviation from the theoretical minimum is expected since the signal usually is shorter in duration than the 1.4 μs integration window. Given these conditions, the measured angular uncertainty indicates the interferometer system is operating well within the expected parameters and operating properly.

4.2   Sensitivity

An important factor in determining what types of breakdown processes can be detected by the interferometer is its ultimate sensitivity. Some processes, like negative leader steps and recoil leaders, are very bright and easily detectable. Other processes, such as negative streamer emission, are very dim. A single network of interferometer receivers locates the source only in 2 dimensions and can determine only the received signal powers, either from the computed powers at each of the antennas or from the peak of the cross-correlations between antenna pairs. The results are expressed as power levels at the receiver input, in dBm units (decibels relative to 1 mW reference power; 0 dBm = -30 dBW). The LMA, on the other hand, locates sources in 3 spatial dimensions and can determine the power radiated by a source (*Thomas et al.*, 2004, 2001), corresponding to the source power in dBW units (decibels relative to 1 W reference power) over the 6 MHz bandwidth of its measurements. What follows is a detailed comparison and calibration between the LMA calculated source power, and the received power at the interferometer.

The LMA has a minimum detectable power limited which is limited by environmental noise levels and approached -90 to -95 dBm in quiet locations. The Interferometer antenna is much less efficient at converting incoming signal into voltage, and so when deployed at Langmuir Laboratory the minimum detectable power is limited by thermal noise at the pre-amplifier (about -95 dBm for the 60 MHz bandwidth). Whereas the LMA stations utilize tuned VHF dipole antennas and power-detecting logarithmic amplifiers to measure the peak arrival times and received powers of impulsive events over a wide (100 dB) dynamic range, the interferometer receivers use less-sensitive flat plate antennas, linear amplifiers, and deep 16 bit fast digitizers to record the coherent raw time series data over a wide bandwidth. The increased bandwidth of the interferometer when compared to the LMA (20–80 MHz compared to 60-66 MHz) improves the sensitivity of the interferometer, however, the improvement offered by increased bandwidth is offset by the insensitive antenna design.

We begin by referring to the histograms of the powers for located radiation events from the two systems, shown in Figure 4.7. Both are plotted over a 70 dB range of power values: -35 to -105 dBm received power values for the interferometer and -35 to $+35$ dBW source power for the LMA. From the width of the histograms, it is evident that the interferometer and LMA observations have roughly the same wide dynamic range of about 50 dB. If it is assumed that the highest power events are the same in both histograms, it follows that the interferometer can detect and locate sources as weak as -25 dBW.

The shape of the interferometer and LMA power distribution is quite different. The number of sources located by the LMA increases towards lower
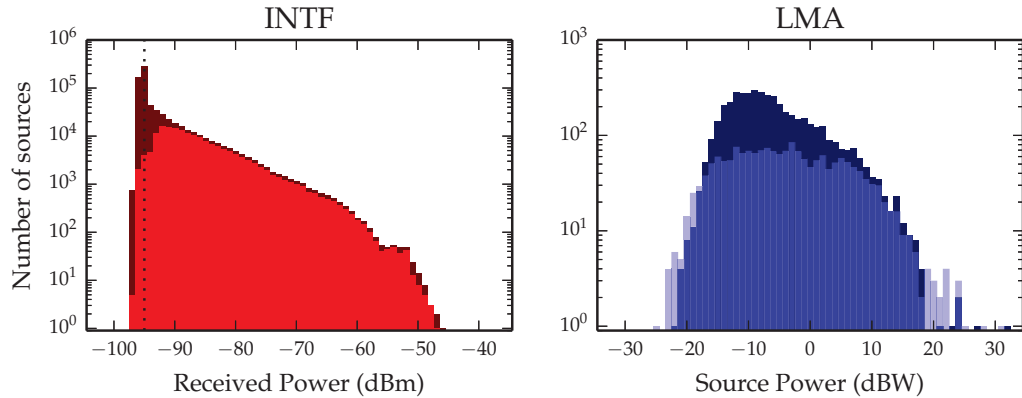
Figure 4.7: Power distributions of the interferometer and LMA. (Left) power distribution of the interferometer after phase 0 filtering (dark red) and phase 2 filtering (bright red). (Right) power distribution of the LMA using 10 μs windows and improved processing (dark blue) and 80 μs windows and standard processing (bright blue).

source powers, but plateaus at about 5 dBW. Conversely, the power spectrum for the received power at the interferometer continues increasing until the thermal noise floor is reached (denoted by the black dotted line). Part of the difference in the power distribution is due to the 80 μs time windows used for normal LMA processing (shown in bright blue). If the data are processed with 10 μs windows (shown in dark blue), the situation improves but still does not follow the trend seen by the interferometer.

The effects of metric-based filtering (Section 4.3) is also shown in the interferometer power distribution (left panel of Figure 4.7). The histogram of powers after phase 0 filtering is shown in dark red, and after phase 2 filtering (leaving ∼ 2% noise) is shown in bright red. Many of the sources removed by the filtering were produced by lightning, but poorly located. This is even true of the very low power sources in the −95 dBm range of the distribution. The usefulness of these mislocated sources is questionable, but they do show that improving the minimum detectable signal of the interferometer is a worthwhile undertaking.

Both the interferometer and the LMA record the VHF emission from lighting and so both instruments frequently see the same processes. But, to be able to directly compare the interferometer record with the LMA record, the maps from both systems must be aligned in time. While the LMA uses a GPS for very accurate absolute timing, the clock on the interferometer can be in error by as much as 100 ms. The alignment is done by adding a constant time offset to all the sources located by the interferometer. This is first done by eye by plotting the elevation versus time of the LMA sources on top of the interferometer sources. Once the maps are aligned within about 10 μs, it becomes efficient to plot a histogram of
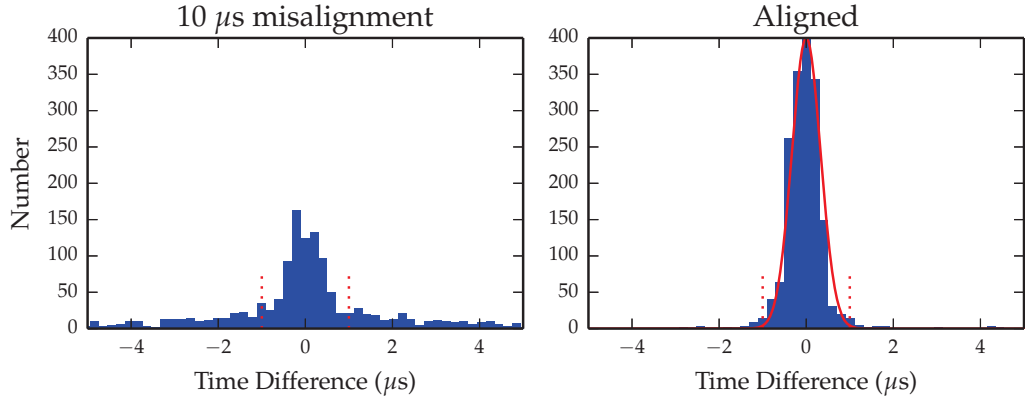
Figure 4.8: Absolute timing alignment for the interferometer. Histograms of time differences for sources seen by the LMA and interferometer after a constant time offset is added to the interferometer times. If the alignment is imperfect (left), the distribution does not show a strong peak. Once the data are well aligned (right), the distribution follows a Gaussian distribution with standard deviation of 0.33 μs.

the time difference between LMA and interferometer sources, as in Figure 4.8. When there is even a small mis-alignment in timing, the peak of the time difference histogram is greatly reduced in number, and the distribution is broadened (as shown in the left panel). Once the absolute times are aligned, the time difference histogram peaks sharply at 0 (as shown in the right panel). The absolute timing uncertainty after alignment is shown by the red Gaussian fit which has a standard deviation of 0.33 μs.

After the alignment process is complete, a subset of interferometer located events, which are space and time correlated with LMA sources, can be compared to determine the relative sensitivity. Ideally, this should be done by using the LMA determined emitted source power to compute an estimated received power at the interferometer. This is not easy to do, as the bandwidths of the two systems are different and the efficiency of the interferometer antenna is unknown. However, we can and should correct for propagation effects since the sources can be at highly varying distances from the interferometer. This is done simply by defining a range corrected power:

$$P_{corected} = P_{source} - 20 \log_{10}(R) \, , \tag{4.8}$$

where R is the range in meters from the interferometer to the source.

The subset of sources used for the comparison was found by looking for LMA and interferometer sources which were close in time and space. Two sources are said to be correlated if their absolute timing is within 1 μs of each other, and their separation in the cosine projection is less than 0.05. Out of the 1824 LMA
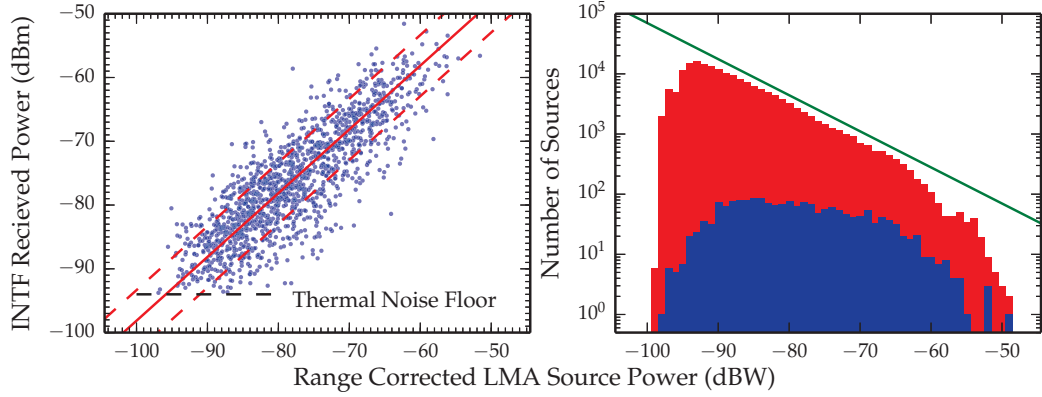
Figure 4.9: Power calibration of the interferometer. Left a scatter plot of the received power at the interferometer vs. the range corrected source power detected by the LMA. The linear trend gives the conversion factor to allow source powers to be estimated by the interferometer. Right is the range corrected power distribution for the interferometer (red) and LMA (blue). The green line is a power law fit to the interferometer distribution with exponent −0.6.

sources in flash C (Section 5.2), 1401 were well correlated with interferometer events. The left panel of Figure 4.9 shows a scatter plot of the range corrected LMA source power versus the interferometer received power. These powers should be related by a linear trend with unity slope. The median offset between the LMA and interferometer powers is shown with the solid red line and has a value of -1.86 dB. The standard deviation of the powers about this offset is 4.8 dB, shown by the red dashed line. The right hand panel of Figure 4.9 shows the interferometer and LMA range corrected power distribution. The two distributions overlap very nicely, but (as mentioned above) the shapes of the distributions are different.

If the range to a source is known, the power received by the interferometer can be used to determine the source power (in the 60-66 MHz band) using:

$$P_{source} = P_{received} + 20log_{10}(R) + 1.86 \, \text{dB} \,, \tag{4.9}$$

where R is the range in meters. Section 4.4 discusses a method of converting the 2-dimensional interferometer locations into quasi-3D maps, in which case this equation can be applied directly. Alternatively, the range can simply be estimated as a constant value for all sources, but the error in the resulting source power will be higher. The overall sensitivity of the interferometer and LMA are roughly equal. Sources which radiate more than about 20 mW are routinely detected by both the LMA and interferometer if the source is reasonably close, although the interferometer will locate substantially more of such sources. For flashes directly

over Langmuir Laboratory, the sensitivity of the LMA is slightly better than that of the interferometer, and in these situations the LMA will locate VHF emission before the interferometer will. This leaves both instruments just capable of locating emission from very faint but very interesting sources, including streamer emission and emission from positive breakdown.

Currently, the sensitivity of the interferometer is being limited by the thermal noise seen at the first stage of amplification. Improving the sensitivity of the interferometer requires an alteration of the antenna design, either by increasing the collecting area of the sensing plate, or transitioning to a resonant design such as a disc-cone antenna. Looking at the power distributions presented in this section, the number of sources found at each power level follows a power law with exponent -0.6 (the green line in Figure 4.9). This indicates that improving the sensitivity of the interferometer by 3 dB would increase the number of sources located by about 50%. Future concentrated investigation of very low power sources is attainable and promises to produce some interesting results.

4.3   Noise Reduction

Continuous recording of the radiation signals, coupled with the coherent nature of the measurements, substantially increases the sensitivity and number of locatable events during a discharge. However, it also produces numerous solutions that are either contaminated by or entirely produced by noise. The noise comes from a number of different sources: thermal receiver noise, transmitters, reflections, local power transients, etc. Because the time delays are determined by correlating the signals, the processing is rubust against all uncorrelated noise and narrowband correlated signals, but broad correlated noise exists that can significantly degrade the solutions.

The magnitude of the noise problem becomes evident by noting that the digitizing goes well into the ambient noise levels of each receiving channel, and that correlation peaks are obtained for all windows of the data record. One second's worth of data contains $1/(1.42\ \mu s) \simeq 700,000$ non-overlapping windows, each of which gives a correlation peak. For heavily overlapped windows, the number of solutions is larger by a substantial factor. Correlation peaks produced by noise only will be randomly distributed over the $\pm 1.42\ \mu s$ (± 256 sample) time interval. Emission from lightning at the relatively short (10–33 m) baselines produces very small (33–110 ns) time delays. This allows the 2-baseline algorithm (Chapter 2) to exclude many of the noise produced solutions as unphysical. Even so, as shown in Figure 2.6, many noise sources persist. Even worse, the multi-baseline algorithms use the sky as a constraint for the initial guess for the least squares solution. As a result, it is much more likely that correlation peaks for noise contaminated windows will have physically possible relative time delays.

Contamination by noise predominently affects weak emission with low signal-to-noise ratio (SNR). The power spectrum of the VHF emission from lightning also peaks at the low powers (see Section 4.2). Of all the possible time windows which could be located, the 2 and 6 baseline algorithms produce a solution (which may be noise contaminated) for 35% and 80% of the windows respectively. But, of all these located windows, only 17% of them have an SNR of 5 or more above the thermal noise floor. The number of solutions contaminated by noise is likely to be very high.

Sequentially triggered interferometers avoid the complication of noise contaminated solutions by only recording VHF emission if the power rises above a certain threshold. As a result, the SNR of the data is always very high, and the solution can be determined with relative certainty. The continuously sampled data can be filtered in a similar way using a criterion based on the rms or peak-to-peak amplitude of the emission. But, as shown in Section 4.2, there are a large number

of solutions in the very low power region. Therefore, there is a strong desire to keep as many of these solutions as possible.

The basic goal of noise reduction is to identify noise contaminated solutions so that these locations can be removed. This is done using metric based filtering. The metric used to identify noise contaminated solutions should have the following properties:

- It should not be based on amplitude or power of the signal.

- It should be relatively easy to calculate.

- It should have some physical basis and meaning.

- It should identify noise and noise contaminated solutions.

After considerable experimentation, the following four metrics have been found to provide a basis for good-quality filtering:

1. Mean closure delay.

2. Standard deviation about the centroid.

3. Multiplicity of contributing windows.

4. Normalized correlation amplitude.

The first three metrics are made possible by the overlap analysis procedure, which provides a distribution of solutions weighted by the closure delay (as described in Chapter 2).

4.3.1 Definition of Metrics

Before giving the details of each metric, some discussion is needed of the processed data to which the metrics apply. Each 1.42 μs window correlates the recorded VHF emission to produce an instantaneous direction to a source on the sky – a window solution. Because the windows are allowed to overlap heavily, several windows are combined to produce a single event. In this study, 256 sample (1.42 μs) windows are used, where all but 4 samples overlap between windows. In this case as many as 64 windows can contribute to a event. Even though the event contains several window solutions, only one mean location is reported – the event solution. It is these event solutions that are shown in all of the maps of this dissertation.

Closure Delay (ecls)   The closure delay metric was used in Chapter 2 to weight the solutions from several overlapping windows. It is defined in equation 2.9 as:

$$\tau_{123} = |\tau_{12} + \tau_{23} - \tau_{13}| \ .$$

In the absence of noise, the window solution of a point source will produce a closure delay of 0, but due to errors in the measurement, there is usually deviation of much less than half the sampling period of the digitizer (5.5 ns). If the noise is high, sometimes a side lobe of the cross correlation will be larger than the correct central maxima. In this case, the closure delay is almost always larger than the sampling period of the digitizer. For processing algorithms using four or more antennas, there are multiple combinations of antennas which will produce a closure delay. In this case, the smallest closure delay of the antennas which contribute to the solution is used. The closure delay is used to identify events where the time delays produced by the algorithm are likely in error.

Standard Deviation (estd)   The standard deviation metric is the standard deviation of all window solutions in a given event. As seen in the scribble plots (Section 3.3 and 4.1), heavily overlapping windows containing emission from lightning produce solutions which slowly drift in the sky because the windows are not independent. Solutions due to noise alone tend to shift large distances across the sky because the windows are closer to being independent. In addition, if there are two sources separated by a large angular distance, the window solutions frequently will alternate between one and the other. In this way, the standard deviation metric is used to identify events produced by noise alone, and events where the windows may be contaminated by a second source. Events for which only a single window contributes to the solution are excluded from the results. Such events do not have a defined standard devation, and are always due to noise. This is referred to as phase 0 filtering.

Multiplicity (emlt)   The multiplicity metric is simply the number of windows contributing to a single event. So that the multiplicity metric does not vary greatly with different amounts of overlap, the metric is normalized so that it varies from 0 to 1,

$$\text{emlt} = \frac{N_{contributing}}{N_{possible}} \ , \tag{4.10}$$

where N is the number of windows in an event. The multiplicity is a measure of how much brighter a source is than the surrounding emission. This is not exactly a measure of SNR since the surrounding emission may be produced by another source. A source which is isolated in time, and whose amplitude is higher than the noise will have a multiplicity close to 1. A source buried in the noise will have a very low multiplicity.

Solutions using Constant Metrics

No Windowing						
Baselines	Phase 0		Phase 1		Phase 2	
2	25,372	6,464	21,973	639	21,336	217
3	25,802	15,508	22,116	5,166	20,581	176
6	25,028	16,209	21,770	5,146	19,316	36

W_I **Windowing**						
Baselines	Phase 0		Phase 1		Phase 2	
2	24,951	6,568	22,145	612	21,245	169
3	25,468	16,617	21,778	4,806	20,331	117
6	24,941	21,657	20,707	1,928	19,871	57

SCOT Windowing						
Baselines	Phase 0		Phase 1		Phase 2	
2	24,325	6,098	21,738	483	19,586	60
3	25,028	16,209	21,770	5,146	19,316	36
6	25,232	21,077	21,256	2,483	19,356	19

Solutions and Metrics for Constant Noise Ratio

	None			W_I			SCOT		
Baselines	Events	Mlt	Xpk	Events	Mlt	Xpk	Events	Mlt	Xpk
2	21,876	0.59	0.29	21,973	0.59	0.29	21,713	0.52	0.22
3	21,165	0.60	0.30	20,871	0.61	0.31	20,830	0.54	0.24
6	20,830	0.54	0.24	20,505	0.55	0.25	20,970	0.51	0.21

Table 4.2: Solution counts for metric based filtering. The constant metric table uses ecls=2.0, estd=2.0, emlt=0.65, and expk=0.35 for all iterations. The constant noise ratio changes the emlt and expk metrics proportionally until the ratio of solutions inside and outside the flash region is 2%.

Correlation Amplitude (expk) The correlation amplitude metric is the maximum value of the normalized cross correlations for all windows contributing to an event. This usually occurs when the source is centered in the window. The correlation amplitude is a direct measure of the SNR of the source. Of all the metrics, the correlation amplitude is also the most affected by the amplitude of the signal; a bright source will almost always have a high correlation amplitude. Strong filtering based on the correlation amplitude will remove many low amplitude events.

The metric based filtering proceeds in two steps: first, damaged solutions are removed from the data based on closure delay and standard deviation (ecls and estd); next, a more subjective filtering occurs based on multiplicity and correlation amplitude (emlt and expk). To determine reasonable thresholds, the event solutions for a 40 ms portion of flash C (Section 5.2) are partitioned into two regions using a polygon. The noise region excludes the flash; solutions in this region are due to noise only, or badly contaminated by noise. The signal region is the inverse, and contains the flash; solutions in this region are due to a mixture of noise and signal. The 40 ms portion of the flash chosen occurs near the beginning, during the initial negative leader extension. During this time, the emission from the lightning flash is fairly compact in space, allowing the pattern of the noise sources to be easily seen.

The density of sources in each region can then be plotted in metric space to determine reasonable decision lines to distinguish between noise and signal. What follows are a set of 9 figures, one for each windowing function (none, SCOT, and W_I) for each antenna configuration (2, 3, and 6 baselines), showing the density of sources in metric space and the effects of filtering. Panels a. and b. show contours of the density of sources, first in the estd–ecls plane, and then in the expk–emlt plane. The filled blue–green contours show the density of solutions in the signal region, and the open red contours show the density of solutions in the noise region. Panels c.–f. show maps of the solutions colored by power after various stages of filtration. The red polygon defines the signal region, and at the top of each map are the number of solutions inside the signal region (and inside the noise region). Numerical results are summarized in Table 4.2, although the numbers do not tell a complete story of the effects of filtering.
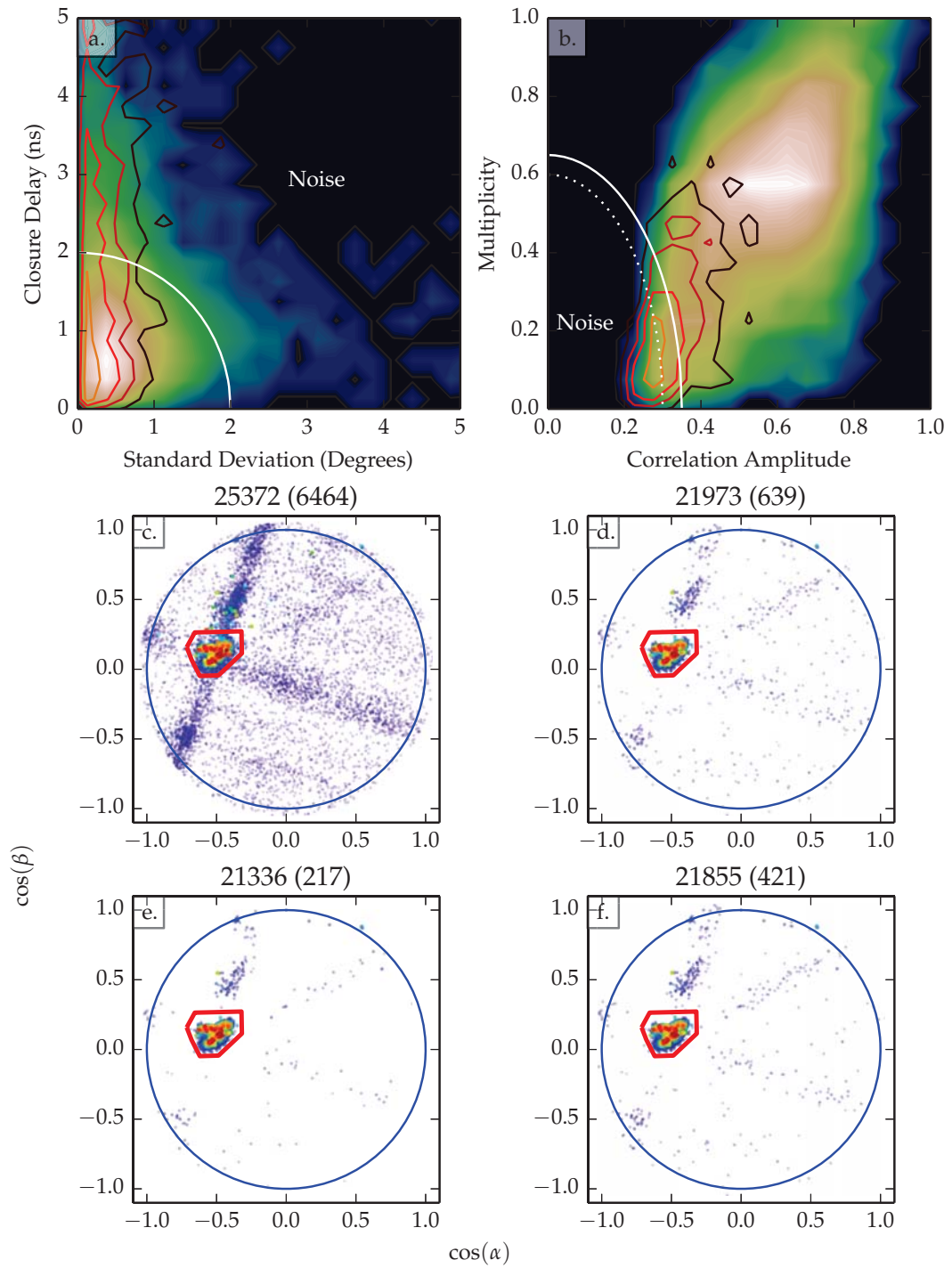
Figure 4.10: Metric space for 2 baseline solutions using no windowing function. The top panels (a. and b.) show the solutions plotted in metric space. The bottom panels (c.–f.) show the resulting maps after each phase of the filtering.
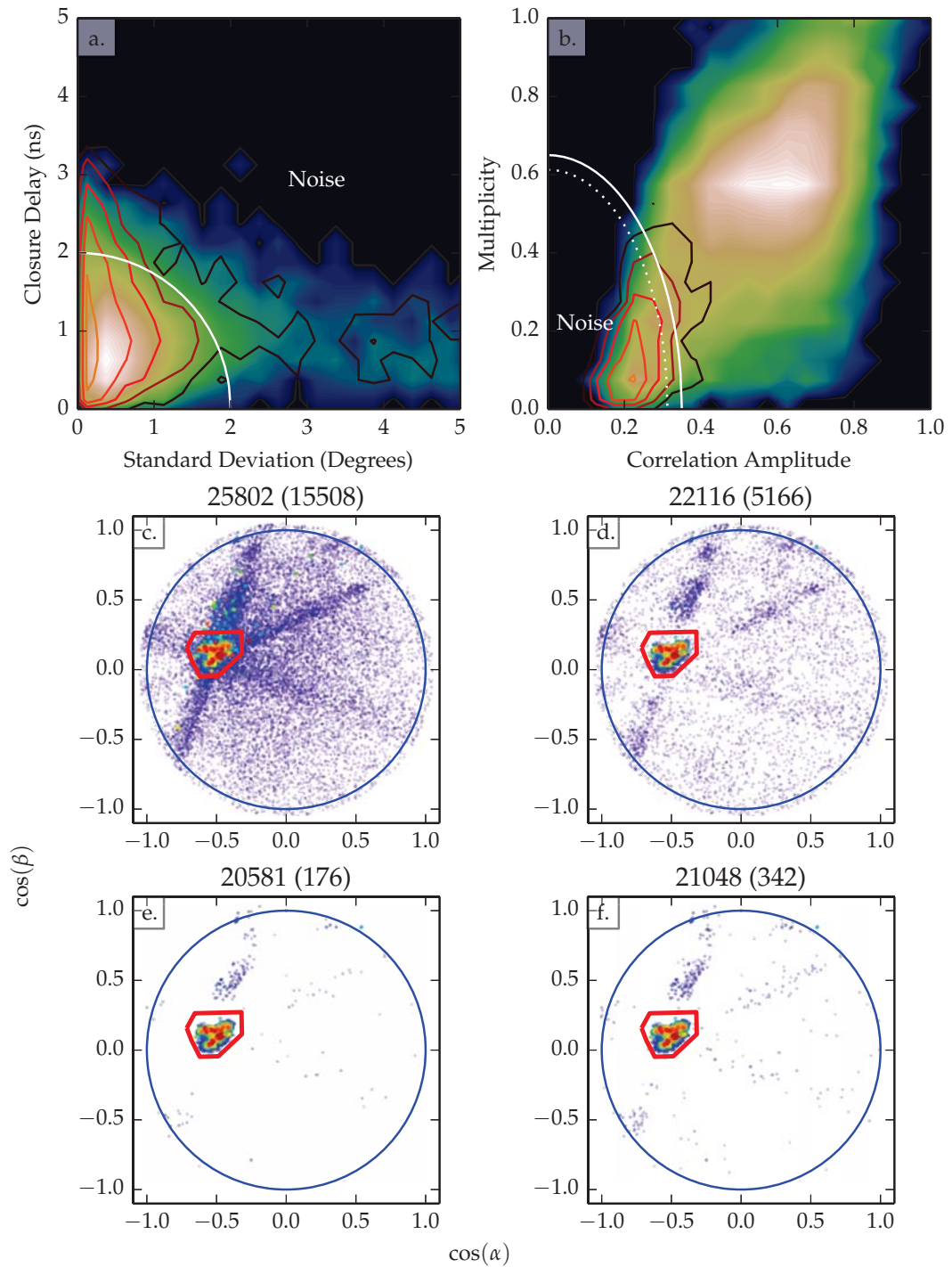
Figure 4.11: Metric space for 3 baseline solutions using no windowing function. The top panels (a. and b.) show the solutions plotted in metric space. The bottom panels (c.–f.) show the resulting maps after each phase of the filtering.
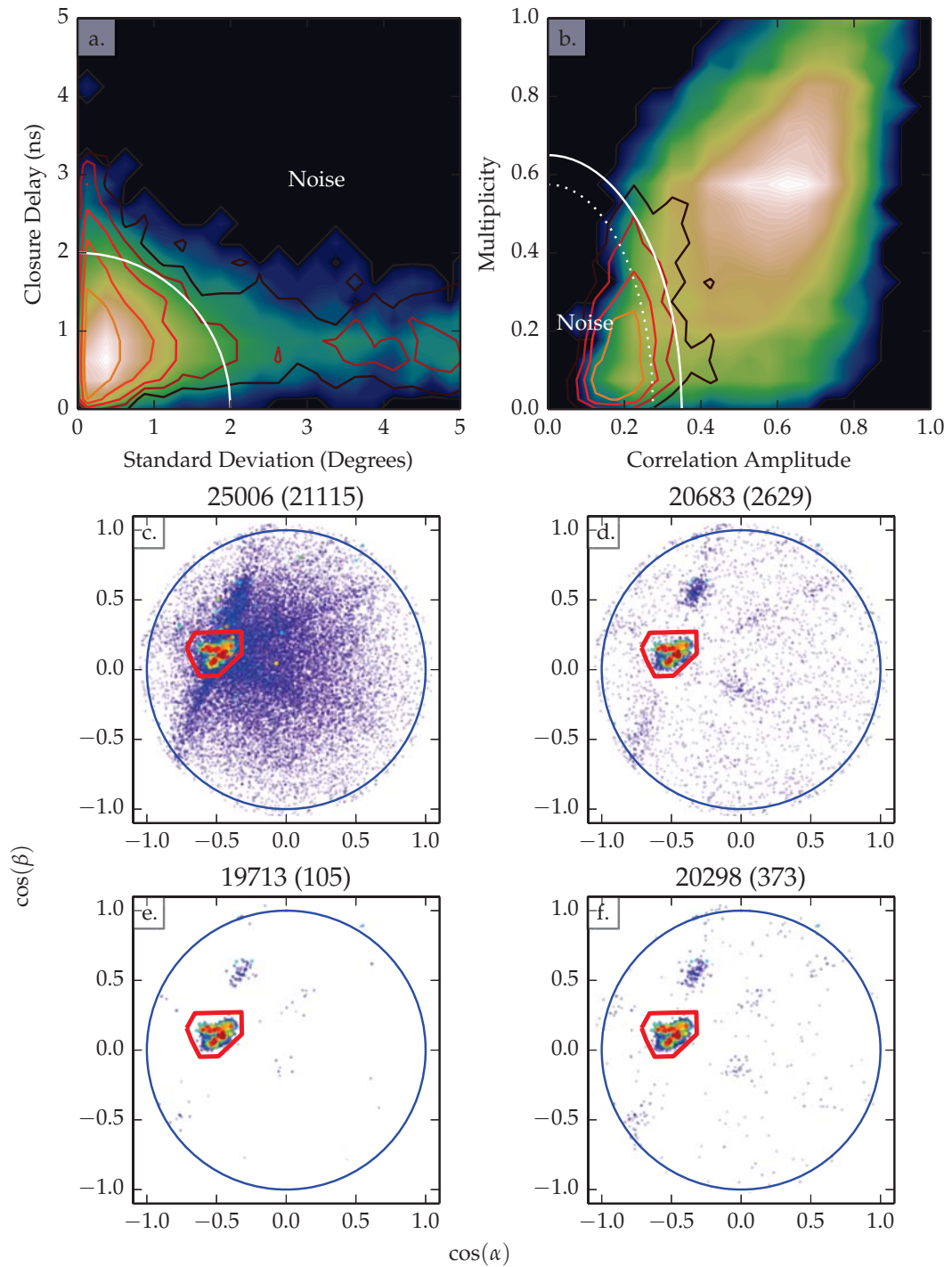
Figure 4.12: Metric space for 6 baseline solutions no windowing function. The top panels (a. and b.) show the solutions plotted in metric space. The bottom panels (c.–f.) show the resulting maps after each phase of the filtering.

2 Baselines, W_I
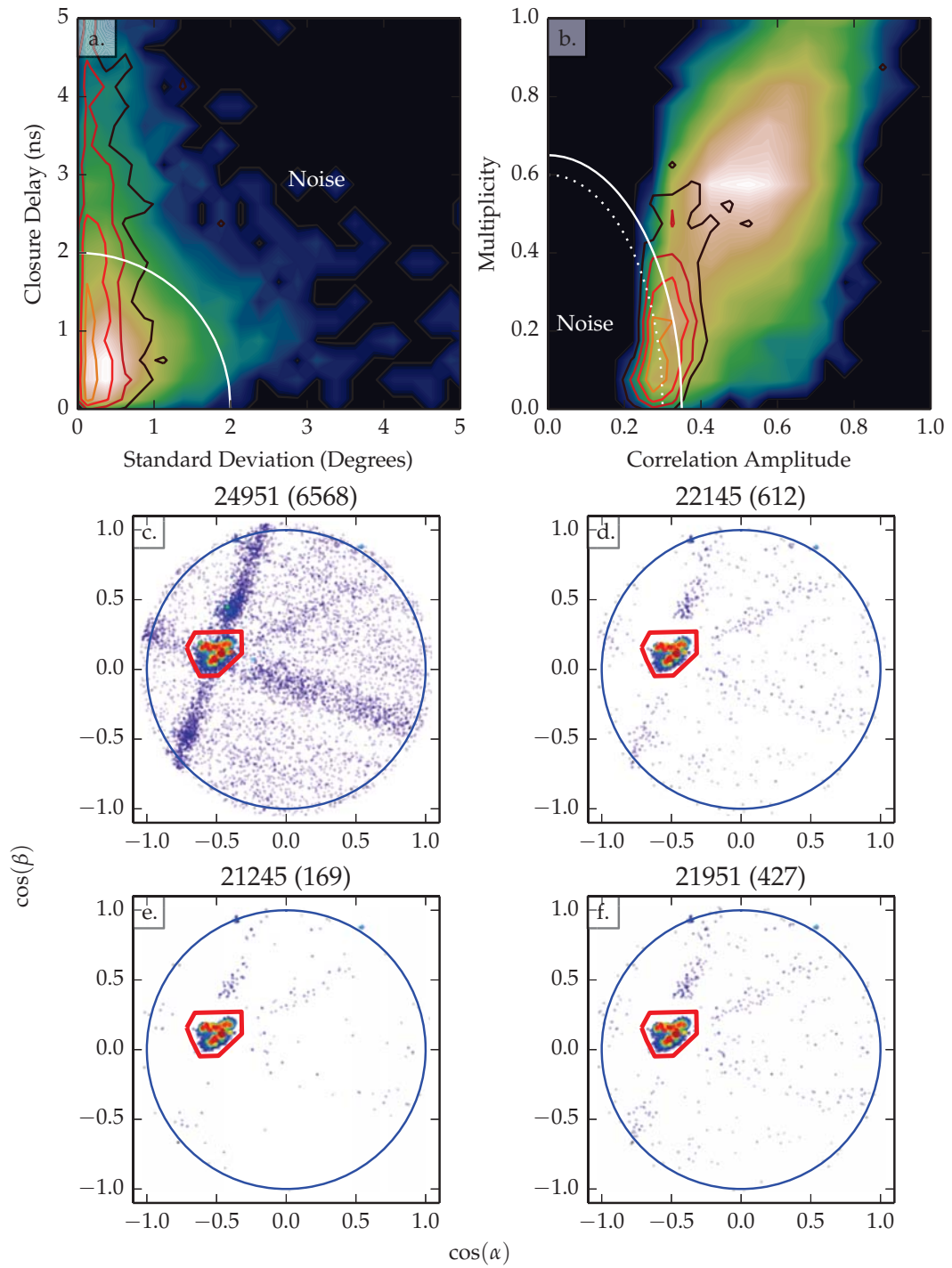
Figure 4.13: Metric space for 2 baseline solutions using W_I. The top panels (a. and b.) show the solutions plotted in metric space. The bottom panels (c.–f.) show the resulting maps after each phase of the filtering.
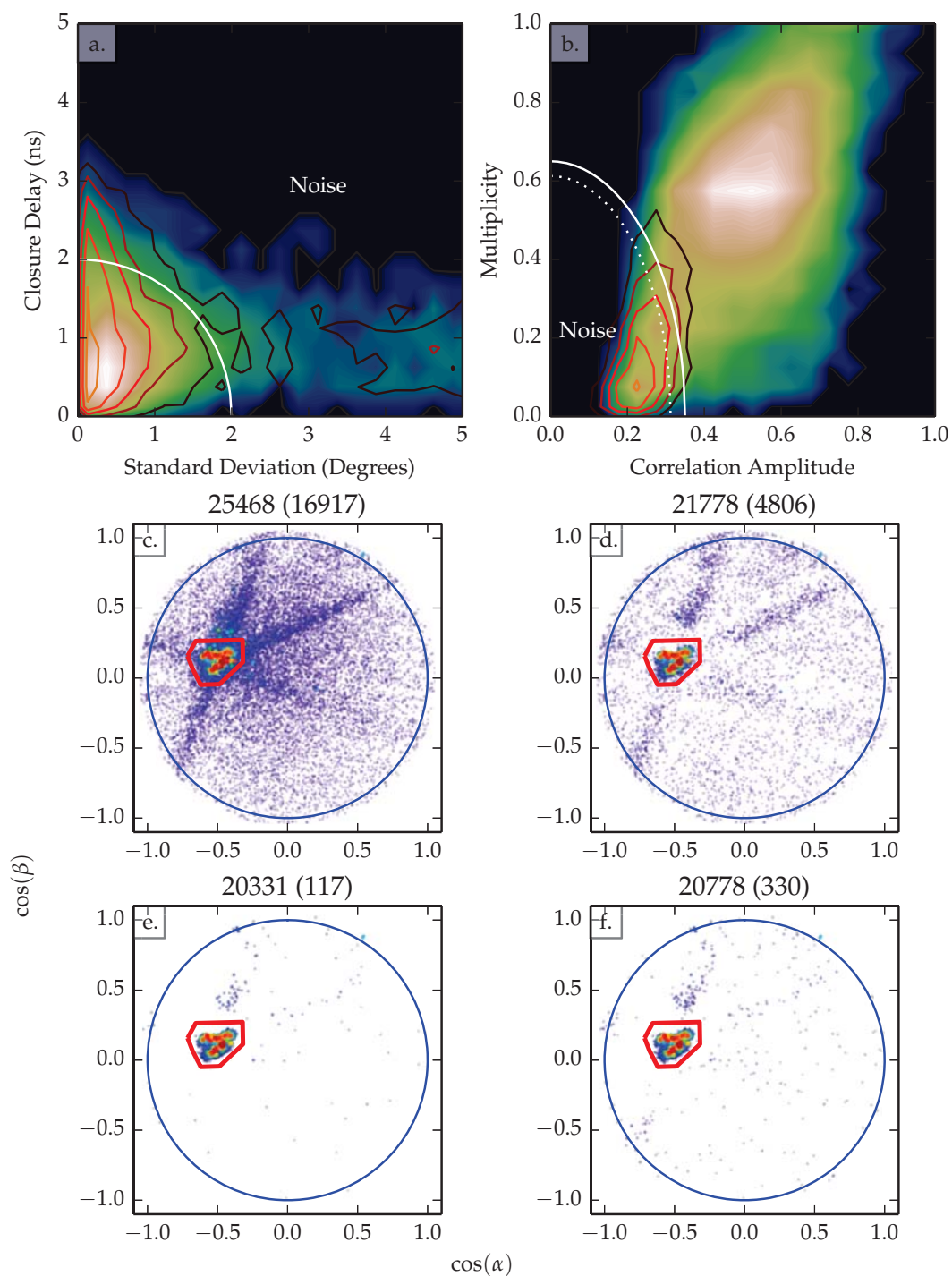
Figure 4.14: Metric space for 3 baseline solutions using W_I. The top panels (a. and b.) show the solutions plotted in metric space. The bottom panels (c.–f.) show the resulting maps after each phase of the filtering.
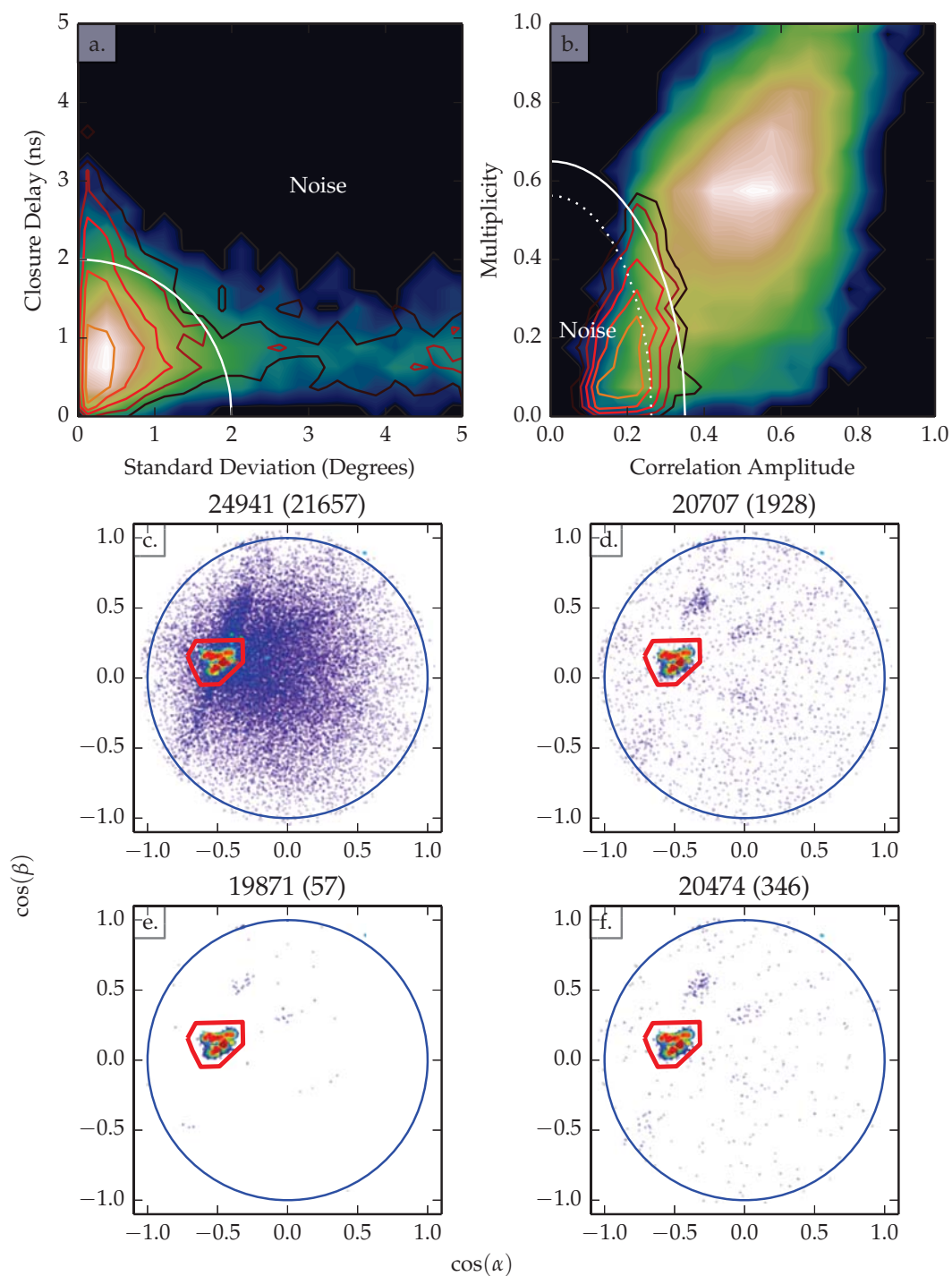
Figure 4.15: Metric space for 6 baseline solutions using W_I. The top panels (a. and b.) show the solutions plotted in metric space. The bottom panels (c.–f.) show the resulting maps after each phase of the filtering.

Figure 4.16: Metric space for 2 baseline solutions using SCOT. The top panels (a. and b.) show the solutions plotted in metric space. The bottom panels (c.–f.) show the resulting maps after each phase of the filtering.
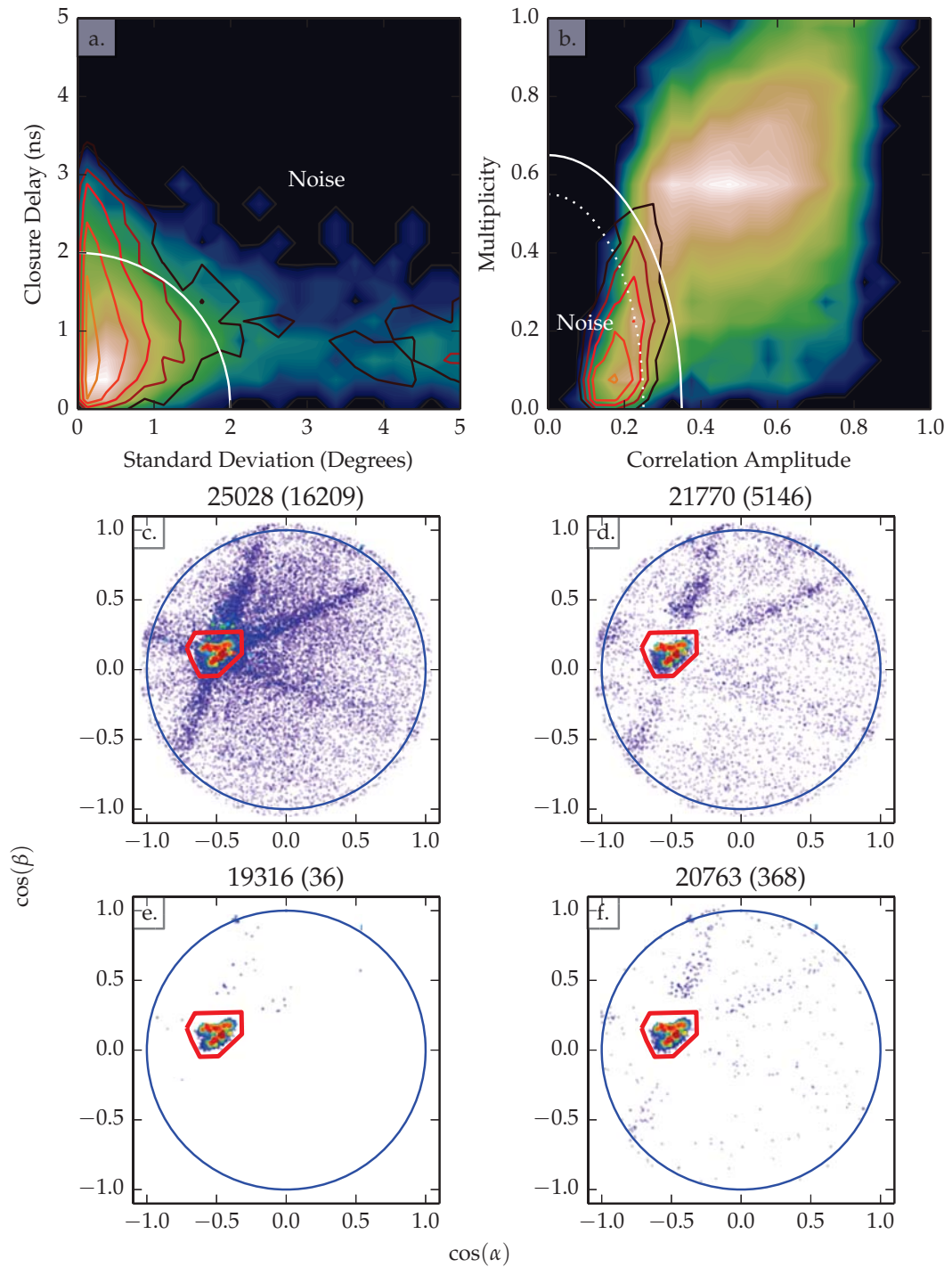
Figure 4.17: Metric space for 3 baseline solutions using SCOT. The top panels (a. and b.) show the solutions plotted in metric space. The bottom panels (c.–f.) show the resulting maps after each phase of the filtering.
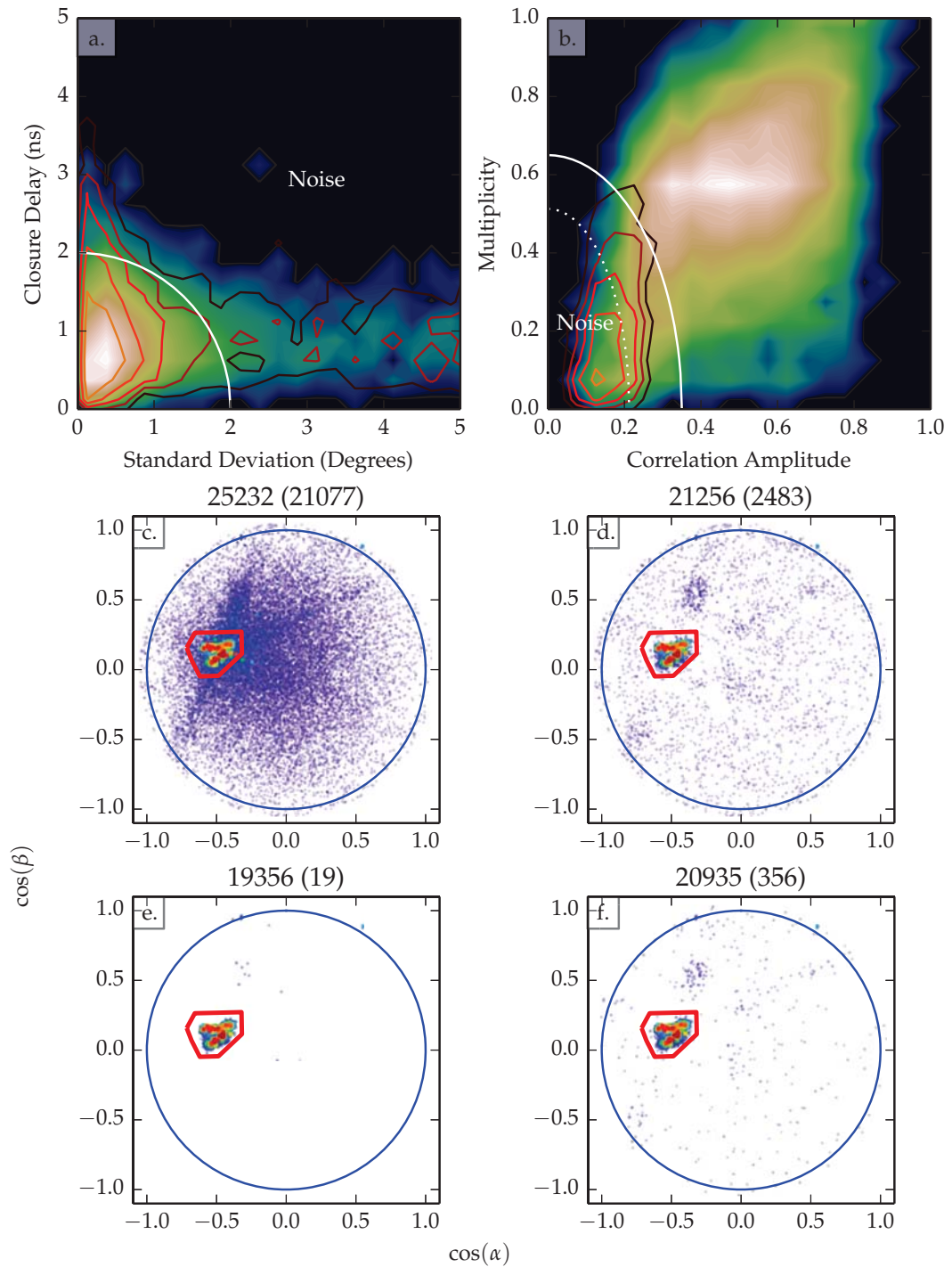
Figure 4.18: Metric space for 6 baseline solutions using SCOT. The top panels (a. and b.) show the solutions plotted in metric space. The bottom panels (c.–f.) show the resulting maps after each phase of the filtering.

4.3.2 Phases of Filtering

Phase 0   Panel c. in each figure shows a map of the solutions colored by power after only phase 0 filtering (removing events with only one contributing window) has been applied. The cloud of low amplitude sources outside the red polygon is noise contaminated. These weak, noise contaminated solutions predominantly fall in rays around the central cluster of bright sources. The rays follow the side lobes of the point spread function of the interferometer (see Section 3.1). Sources located off these rays are likely chance correlations of pure noise, and show a near uniform random distribution on the sky. Sources located on the side lobes are from low amplitude emission from lightning which has been noise contaminated. That is to say that even the noisiest sources detected by the interferometer are produced by lightning. The signals which produce noise sources are just of such low amplitude that they are easily contaminated by noise, which is manifested by the algorithm locating a side lobe of the correlation instead of the central peak. The number of sources located outside the red polygonal region by the 3 and 6 baseline algorithms far exceeds that of the 2 baseline algorithm. This is a side effect of these algorithms using the brightest pixel of the Fourier image as the initial guess for the window solution.

Phase 1   Panel a. shows the density of sources in the estd–ecls metric space (the absolute value of the closure delay is shown in the vertical axis). Here, the blue–green filled contours show the density of event solutions in the signal region (inside the red polygon), and the open red contours show the density of events in the noise region (outside the red polygon). Large values of either the closure delay or the standard deviation indicate a noise contaminated solution. Specifically, for solutions due to the emission from a single point source, the closure is expected to be much smaller than half the sampling period of the digitizer (5.5 ns). Therefore, the closure delay for sources produced by lightning should be less than ± 2 ns. The peak of the density of solutions in the signal region (shown in light browns) is roughly circular, so a circular decision line is used (shown in white). Sources falling outside this region are likely to be noise contaminated, and removed; this is referred to as phase 1 filtering. The distribution of events in the noise region also peaks near 0 closure delay and standard deviation. Using phase 1 filtering alone will not be able to remove all of the noise contaminated solutions.

The effect of removing the events identified by the estd–ecls decision line is shown in panel d. of the figures. For the 2 baseline algorithms, almost all of the sources in the noise region falling off the side lobes are removed. Most of the sources on the side lobes are also removed, but clusters of sources remain. For

the tight cluster of sources used in this example, the side lobes are quite obvious. However, in more complex cases the side lobes can appear to be real sources, or look like the fringe ambiguities seen in narrowband interferometers. For the 3 baseline algorithm, the number of sources remaining after phase 1 filtration is much larger, with many sources remaining both on and off the side lobes. As before, the increased noise is a side effect of requiring the initial guess of the solution to be on the sky. The number of sources in the noise region of the 6 baseline algorithms is much reduced when compared to the 3 baseline algorithm. Even better, the remaining sources are much less concentrated on the side lobes, meaning they are less likely to be confused with well located emission from lightning.

Phase 2   For many applications, just filtering based on the estd–ecls criteria removes enough noise sources to produce a high quality map, especially when working with solutions produced by the 2 or 6 baseline algorithms. If a less noisy image is required, further filtering based on correlation amplitude and multiplicity can be employed, referred to as phase 2 filtering. Where phase 1 filtering removes mostly noise contaminated sources, phase 2 filtering will also remove well located weaker sources. For this reason, the placement of the decision line is much more subjective for phase 2 filtering. There are 2 white lines in panel b. of the figures: the solid line represents a constant decision line which has been seen to produce very maps of lightning in the past; the dotted line is determined by moving the decision line for expk and emlt until $\sim$ 2% of the solutions in the signal region are located in the noise region. Where the relative magnitude of the density distribution in the estd–ecls metric plane was roughly equal, the noise distribution in the expk–emlt metric plane extends further in the multiplicity direction than the correlation amplitude direction. For this reason, the decision line is elliptical instead of circular[2].

Looking at the density contours of the sources located in the noise region in panel b. of the figures, it can be seen that the 3 and 6 baseline algorithms better separate noise from signal than the 2 baseline algorithms. The 6 baseline algorithms do a particularly good job at separating the noise from the signal; the peak of the noise distribution (open red contours) is shifted farther to the left in this metric space, and the fraction of sources in the signal region (blue–green filled contours) is smaller. The separation also improves when one of the frequency weighting windowing functions is used (either SCOT or W_I), although not as noticeably.

The results of phase 2 filtering are shown in panel e. (constant threshold, solid white line) and panel f. (constant noise fraction, dotted white line). Again,

---

[2] The decision lines for both the estd–ecls and expk–emlt metric spaces are implemented as ellipses with varying semi-axes.

the number of sources located in the noise region is dramatically reduced. Ideally, no sources would be located in the noise region, or at least those that are should be uniformly distributed. Unfortunately, the remaining sources still cluster on side lobes of the main bright emission. This is especially true of the 2 and 3 baseline algorithms. In maps produced by the 6 baseline algorithms, the sources located in the noise region are more uniformly distributed, but still preferentially lie on the side lobes.

4.3.3   Effects of windowing functions and antenna configuration

In general, applying a windowing function produces better results than not. There is a set of moderately bright (cyan and green) events seen to the north, just outside the red polygon defining the signal region when no windowing function is used. These events disappear when one of the two windowing functions is used, presumably having moved into the signal region. However, the number of sources located in the signal region is not dramatically affected by the windowing function used. Determining which windowing function works better, W_I or SCOT, is much harder. In the current implementation, the results of the W_I and SCOT windowing functions look nearly identical for the 2 and 3 baseline configurations, and SCOT shows slightly better noise behavior for the 6 baseline configuration. However, the W_I function is very sensitive to the estimation of the signal spectra, and in an attempt to equalize how the windowing functions were applied on all baseline configurations, the manner in which the signal spectra was computed was recently changed. The result was that W_I was rendered a little less effective on the 2 and 3 baseline configurations, and was not improved for the 6 baseline configuration.

There are indications that the 6 baseline algorithm is less affected by noise than the 2 and 3 baseline solutions. For example, the moderately bright sources discussed above are greatly reduced in the 6 baseline map made using no windowing function (Figure 4.12 vs. Figures 4.10 and 4.11). There is also a reduced tendency for noise contaminated events to cluster tightly on the side lobes of the interferometer's point spread function.

Overall, the metric based filtering described above removes about 20% of the solutions in the signal region, and nearly all of the solutions in the noise region. This very good performance of metric based filtering has persisted through numerous alterations to the processing code, and with every frequency weighting windowing function used.

4.4 Quasi 3-Dimensional Conversion

The LMA and interferometer maps of a lightning flash agree exceptionally well. Shown in Chapter 5 are several examples of LMA maps converted into the interferometer projection and overlaid on interferometer data (Figures 5.2, 5.6, 5.10, 5.15, 5.20). In addition to projecting the LMA data onto the azimuth vs. elevation framework of the interferometer observations, the inverse can be done – namely using the LMA data to infer the radial distance of individual interferometer sources. In this way one is able to construct quasi-3D maps of the interferometer data. The conversion is best done using spatial correlations alone and not considering their relative timing. The structure of the lightning channels is better determined in the complete LMA data for a flash rather than from its temporal components.

The 3D conversion is an iterative process that proceeds in the following manner. First, the LMA data are converted into azimuth, elevation and range from the interferometer. Second, a crude first approximation of the 3D projection is made for the range of each interferometer source by averaging the range values to the LMA sources that have similar azimuth and elevation values. The first conversion tends to have strong radial artifacts because there are often multiple channels in the direction of a given interferometer source. Radial smearing is also produced by asymmetric spreading in the range of the LMA sources even for single channels. The radial artifacts are removed with an iterative process that uses weighting to determine which LMA sources determine the range values. The weighting factor is the distance of the LMA sources to the iterated 3D interferometer locations shortly before and after the source of interest. LMA sources closest to the previous and subsequent converted interferometer locations are given the most weight. In this way, a propagating event that appears to intersect with another channel in 2D will continue on the same 3D channel. After each iteration step, the converted 3D interferometer locations shift, causing the weights to change. Although there is no guarantee that such an iteration will converge, in practice it converges quickly if the interferometer data is in good agreement with the LMA locations.

Additionally and optionally, a piecewise linear fit can be made to the LMA sources to more completely define each channel. This allows gaps in the LMA sources to be filled in for a given channel, which both better defines and extends the channel. The piecewise-linear fits to the LMA sources are combined with the actual LMA source locations such that both have roughly equal weight in determining the range of a given interferometer location. Overall, the weighting procedures work well to keep a moving source of emission on the correct channel when the emission passes an apparent intersection in the 2D projection. However, if the emission begins near an intersection (such as for the K-event starting
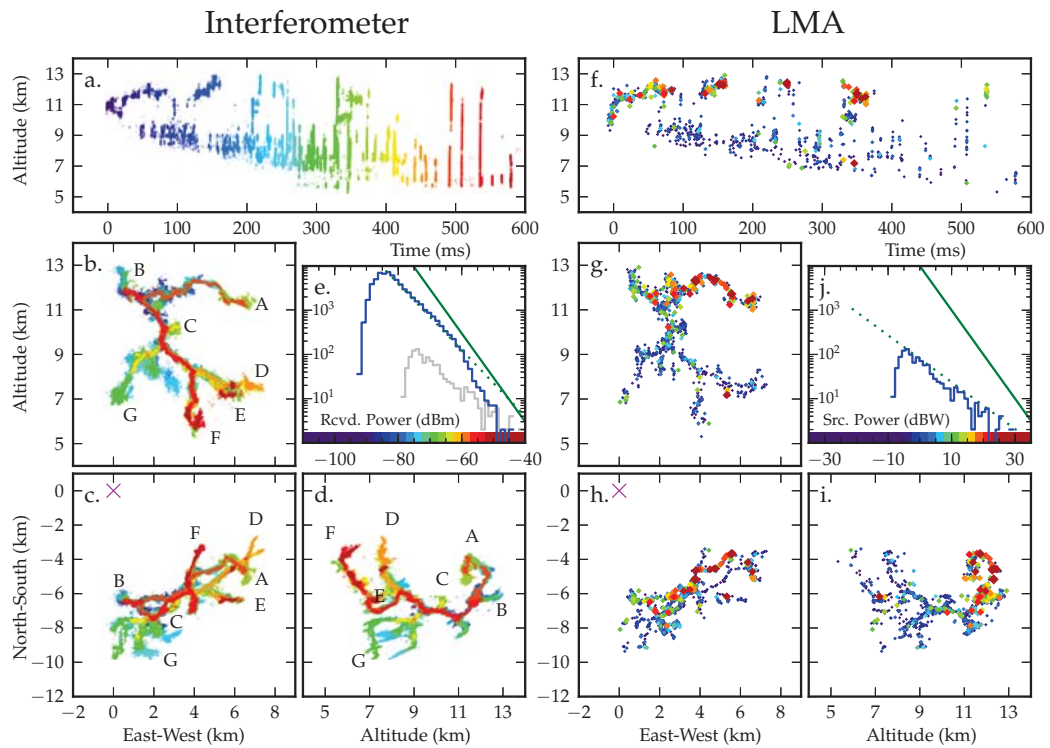
Figure 4.19: Quasi-3D reconstruction. Colored by time (left) compared with LMA observations colored by power (right), illustrating how the quasi-3D conversion works well to reproduce the LMA structure and adds substantial detail to the structure. The histograms show the distribution of measured power values P from the two systems and are retained from the original publication where they referred to the relative sensitivity of the interferometer and LMA.

at 577 ms flash A), the algorithm can guess the wrong channel for the beginning of the emission, in which case it needs to be manually corrected. The quasi-3D projection works best when the flash is oriented face-on to the interferometer, which reduces the number of apparent intersections. Channels that are oriented radially will tend to have distorted quasi-3D projections.

Figure 4.19a-d shows the quasi-3D interferometer images of a flash in the same format as for the LMA data. In particular, the panels show altitude vs. time as well as vertical and plan projections of the inferred source locations. The channels identified in the 2D observations of Figure 5.25 are correspondingly labelled. The quasi-3D projections obviously rely on the availability of LMA data, but the LMA data do not need to be fully complete, as piecewise linear fitting helps with the reconstruction. By examining where each added piecewise linear fit falls in the interferometer projection, one can be reasonably certain that the added channels are placed in the correct 3D location. Partial manual reconstruction was required to obtain good quasi-3D projection results for channel G.

Panels d. and j. are vestigial plots retained from the original publication, and similar histograms are shown in Figure 4.7 for a different flash. Here these panels have been retained for simplicity. The solid green lines correspond to a P^{-1} distribution and the dotted green lines correspond to -0.75 (interferometer) and -0.53 (LMA) power laws. The color bar shown applies to the sources shown in Figures 4.19, 4.20 and 5.26 only.

The results of the quasi-3D conversion for this flash are very good. Ambiguities in elevation between vertical and radial development normally associated with 2D interferometer maps are completely removed. As will be shown in Chapter 7.1, the length and velocity of features of the flash not well mapped by the LMA, such as K-leaders, can be measured in the quasi-3D constructions with a reasonable amount of confidence.

4.5   Waveform Separation

If the flash is oriented in such a way that the positive and negative breakdown regions are well-spaced, it is relatively easy to identity and separate out VHF waveforms for the two regions. Figure 4.20 shows the results of doing this for the first 200 ms of the flash discussed in Section 5.6. During this time interval there were two distinct episodes of upper-level negative channel development, each followed by relatively long (tens of millisecond) periods of no apparent growth or VHF activity. The overall state of the flash development after 200 ms is seen in Figure 5.25b.
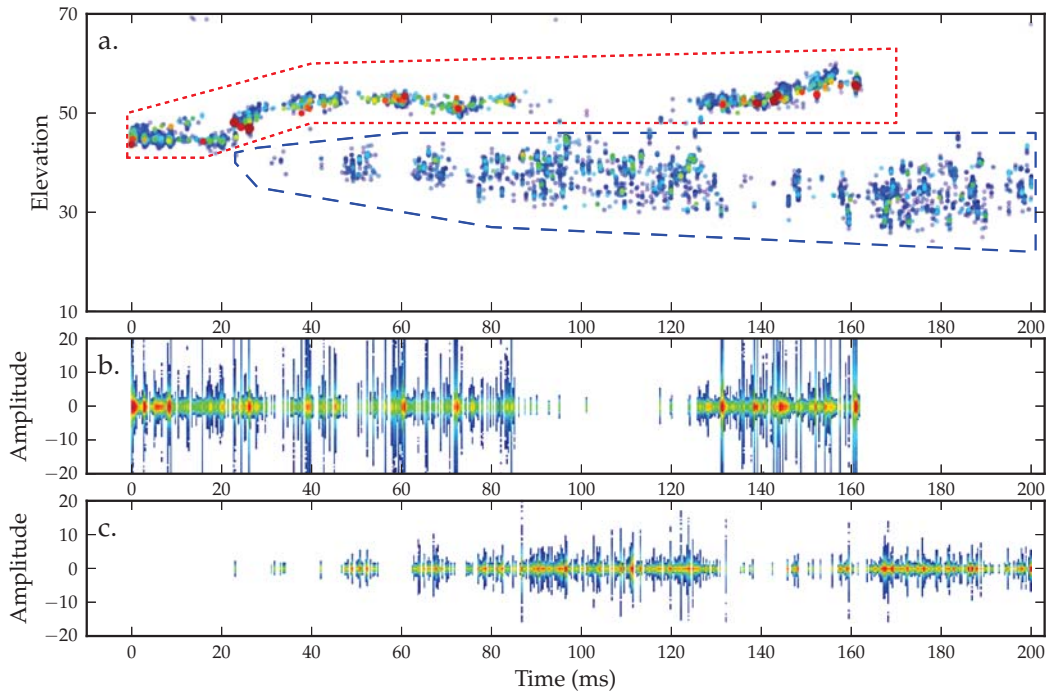
Figure 4.20: Waveform separation of flash A. Partitioning of the raw time series waveforms into emissions associated with the upper-level negative breakdown (panel b and red dotted box in panel a), and lower-level positive breakdown (panel c and dashed blue box in a), plotted with the same amplitude scales to illustrate the differences in emission intensity for the two types of activity. Color indicates radiation intensity in a) and the density of emission events in b). The time between large amplitude pulses in the negative waveforms may indicate stepping intervals of the leader.

The upper-level sources enclosed by the dotted red box in panel a) of Figure 4.20 correspond to negative polarity breakdown within the storm's upper positive charge – almost entirely through virgin air. The dashed blue box encloses sources associated with positive breakdown in the mid-level negative charge region. The coloring of the points indicates the peak amplitude of each source.

Panels b) and c) of Figure 4.20 show raw time series data for the upper and lower sources, respectively. The coloring indicates the density of events. For purposes of comparison the two sets of waveforms are plotted on the same vertical scale (corresponding to ± 20 mV at the digitizer input, equivalent to -63 dBm received power out of the flat plate sensing antenna). With this scaling, the waveforms from large amplitude negative breakdown events frequently exceeds the plot limits.

It is evident that the emission from negative breakdown events has higher peak amplitudes than the emission associated with positive breakdown. The larger negative leader emissions are typically 10 dB stronger (a factor of $\sqrt{10} \simeq 3$ times larger voltage-wise) than those of the positive breakdown. Occasionally the voltage waveform from negative breakdown region is 20–30 dB stronger (10–30 times larger voltage-wise) than that from the positive breakdown region. The relative weakness of the emissions in the positive breakdown region occurs not only for the flickering emissions but also for the retrograde negative breakdown events in the region. The same results are seen in the LMA data for IC flashes (Figure 4.19e ; *Thomas et al.* (2001)). A detailed analysis of the amplitude distributions of different types of emissions is provided in a companion paper (*Akita et al.*, 2013).

There are two time period regimes seen in the negative breakdown which may be related to negative leader stepping. First are short duration, high-amplitude pulses that are separated by 600 μs on average, and a slower cyclic build up in intensity over the course of 5-10 ms which then reverts to a lower activity level. Given a propagation speed of $\simeq 10^5$ m/s, the short duration pulses correspond to spatial scales of $\simeq 60$ m, and the slower build up corresponds to $\simeq 100 - 500$ m spatial scales. Negative leader step lengths will be covered in more detail in Chapter 6.

The emission from the positive breakdown region is lower in amplitude, but is still impulsive. This is clearly seen in animations; in part it is caused by inclusion of the largest, brightest flickers, which are produced by short bursts of retrograde negative breakdown. However, if these bright clusters are eliminated, the residual emission is lower in amplitude but the remaining events continue to be intermittent and impulsive in nature.

Both the negative and positive breakdown regions experienced periods of enhanced and diminished activity. When the negative breakdown region was

very active, the positive breakdown region shows diminished activity and vice versa. This is at least partially because the processing approach located only one emission source in each 256 sample (1.42 μs) window. If both the negative and positive breakdown regions are active in a given window, the emission from the negative breakdown region will usually overwhelm the positive breakdown activity. This causes ongoing negative breakdown to 'mask' any weaker positive activity. However, even when the negative breakdown was very active, not all windows contained the activity. It would thus be expected that occasional sources associated with positive breakdown would be detected, in particular during the early stages of a flash. The fact that they are not seen in the early stages indicates that the breakdown is either too weak to produce detectable VHF radiation or that it is not yet occurring.

Part II

Observations

CHAPTER 5

DESCRIPTION OF LIGHTNING FLASHES

In this chapter, the reader is introduced to the flashes which contribute data to the detailed observations in Chapters 6–7. The descriptions provided in this section are not intended to cover all of the processes which occur during each flash. The interferometer maps contain an incredible amount of detail, and providing complete descriptions for all the flashes would be both repetitive and exceedingly lengthy. Instead, a brief overview of the development is given, including unusual portions of the flash. The overview figures are also not detailed enough to see all of the processes described in this chapter. More detailed figures of various processes will be provided in later chapters.

Animations of the interferometer data are particularly useful for getting a feel for what is going on in the flash. While animations for the flashes could not be included in this text, they can be obtained from the author by request.

The flashes presented were sampled from a wide variety of storms over Langmuir Laboratory during the 2012 and 2013 storm seasons. The interferometer is particularly well suited for studying the in cloud portion of the lightning flash, and so the majority of the flashes are the intracloud variety. There is one flash that touches the ground, but it is a bolt from the blue type flash, which is not representative of normal cloud-to-ground flashes.

Because the flashes were selected from several years of operation, they were recorded by different configurations of the interferometer. The measurements available for each flash are summarized in Table 5.1, and are discussed in more detail in the corresponding section.

As a final note, the description for flash A was published in *Stock et al.* (2014), and is substantially more detailed than the descriptions for the other flashes. For this reason, even though flash A occurs first chronologically, its description appears at the end of the chapter.

	A	B	C	D	E	F
3 VHF antennas	✓	✓		✓	✓	✓
4 VHF antennas			✓			
Fast Antenna				✓	✓	✓
LMA Observations		✓	✓	✓	✓	✓
Pretrigger				✓	✓	✓
Uncertainty [deg]	.25	.25	.10	.10	.10	.10

Table 5.1: Summary of the measurements available for each flash. The top two rows show how many antennas were in the interferometer array. The bottom rows show supporting observations and summary interferometer capabilities.

5.1 Flash B, IC 18:44:29 UT on July 23, 2012

Flash B is featured in Section 7.1 about K-changes.

Flash B occurred on July 23, 2012 at 18:44:29.7156 (based on the first located LMA source) initiating 5 km east of the interferometer site. Because the flash occurred in 2012, when there was no pretrigger capability for the interferometer, the interferometer record begins 0.4 ms later at 18:44:29.7160. This particular flash immediately initiated with bright VHF radiation, which is why the interferometer record began so soon after the first located LMA source. This is not typically the case, flash A (for example) begins 7.8 ms after the first located LMA source. There were also no fast or slow antenna records available for the 2012 storm season. By this time in the storm season, the LMA was fully operational and provided high quality maps for the flash and for the storm. In addition, the LMA data for the flash itself was reprocessed using 10 μs windows and the highest quality processing settings by Harald Edens. These very high quality processing settings are extremely computationally expensive (one flash requires one month to reduce), and so not every flash in this study has been processed this way.

Flash B is a classic example of a well developed, ordinary intracloud discharge between the main negative and upper positive charge regions of the storm. This can be seen in Figure 5.1, which gives the storm context for the flash. The top and right panels are vertical cross sections of 10 minutes of LMA data around flash B. Each flash in these 10 minutes was analyzed by hand to determine which regions of the storm carries positive and negative charge, a process referred to as charge analysis (*Rust et al.*, 2005)[1]. The results are displayed in the colored regions of the storm of the figure; red (blue) regions carry positive (negative) charge. A

---

[1] Charge analysis is at this point well accepted in the lightning scientific community, and the results of charge analysis have been included in a number of publications including *Marshall et al.* (2005), *Krehbiel et al.* (2008) and *Edens et al.* (2012). A good description of the analysis method is presented in *Trueblood* (2013).
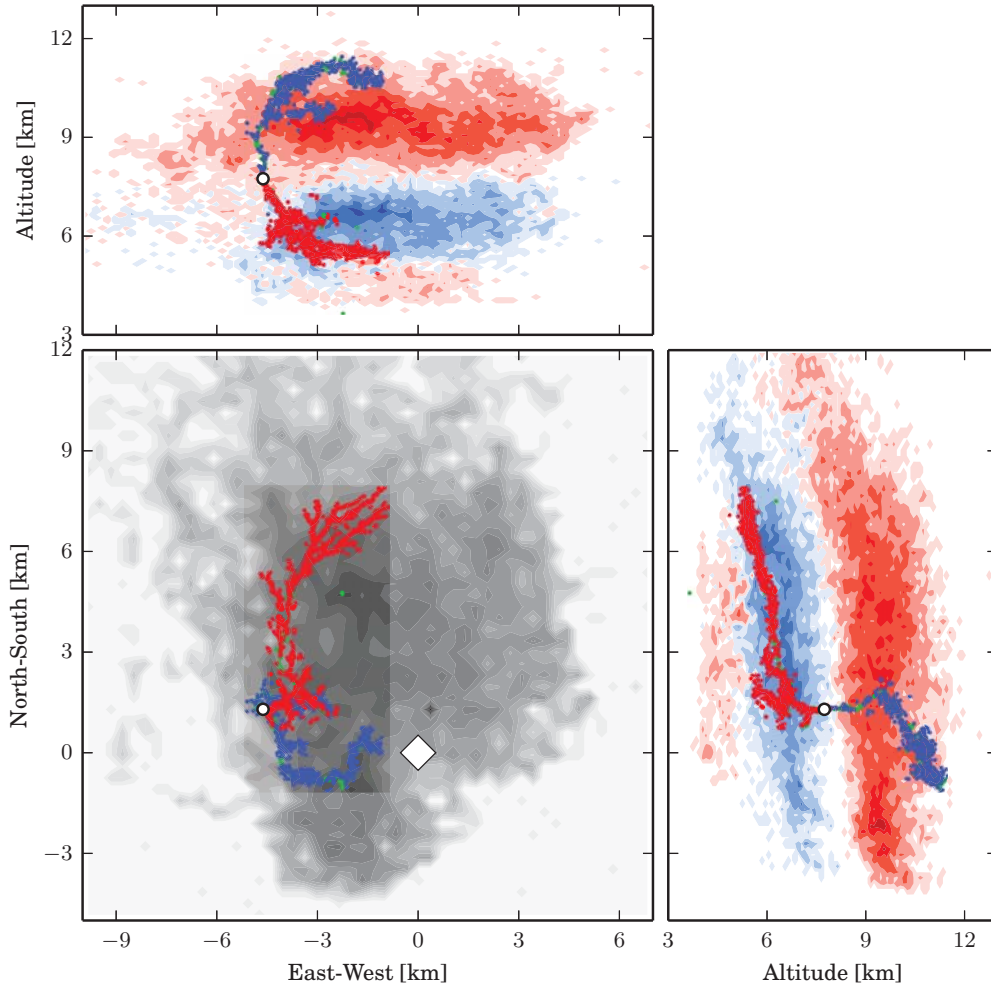
Figure 5.1: Flash B, LMA map of LMA map of storm context. Vertical cross sections show charge structure of the storm with red (blue) showing regions of positive (negative) charge. The plan view shows the LMA source density for the storm in grey-scale. The channels of the flash are colored by charge, those carrying positive (negative) charge are colored red (blue). The white circle marks the origin of the flash, and the white diamond marks the location of the interferometer.

similar analysis was applied to flash B by itself, but in reference to which sign of charge channel carries; with negative leaders colored blue, positive leaders colored red, and K-changes colored green. The lower left panel shows a plan view of the flash. The charge regions largely overlap in the plan view, so instead the total VHF source density is shown for the storm in shades of grey. The channels of the flash are still colored by charge, so that channels seen in the vertical cross sections and the plan view can be compared.

The interferometer site is located at the origin of the plan view, indicated by the large white diamond. Flash B initiated between the upper positive and main negative charge regions of the storm 5 km east of the interferometer, indicated by the small white circle. From the origin of the flash eminate two channels: one carrying positive charge (red) and the other carrying negative charge (blue). The channel carrying negative charge (the negative leader) propagates upward into the positive charge region of the storm. The channel carrying positive charge (the positive leader) propagates down in to the main negative charge layer, and then horizontally to the north away from the interferometer.

The interferometer map for this flash is compared to the LMA map in Figure 5.2. The grey-scale shows the integrated VHF luminosity of the interferometer map. Overlaid on top are the LMA locations, converted into the interferometer projection and colored by charge as above: red (blue) channels carry positive (negative) charge. As with all flashes, the agreement between the LMA and interferometer is very good, but worsen as the sources approach the horizon. The disagreement near the horizon is a systematic error in the interferometer map which currently can not be corrected, although work on developing a correction is underway. In this particular flash, the positive and negative breakdown regions of the flash are particularly easy to identify, as denoted by the sharp red–blue transition at about 41° elevation angle. The clear separation of the breakdown regions, and lack of crossing channels makes Flash B a particularly good candidate for quasi-3D conversion.

Colored in green in Figure 5.2 are numerous K-changes which occur during the flash. Each of these K-changes starts near the tip of the positive leader (red channel) and propagates backwards along a previously ionized channel, towards and sometimes past the flash origin; this is classic K-change behavior (e.g. *Shao and Krehbiel*, 1996). Likely due to the simple channel geometry of flash B, with a single main positive leader, none of the K-changes in the flash deviate from the classic behavior. Due to the high quality settings of the LMA processing, the K-changes of this flash are mapped particularly well by the LMA.

Flash B starts with a negative leader propagating upwards into the positive charge layer. The initial negative leader was exceptionally active, and for the
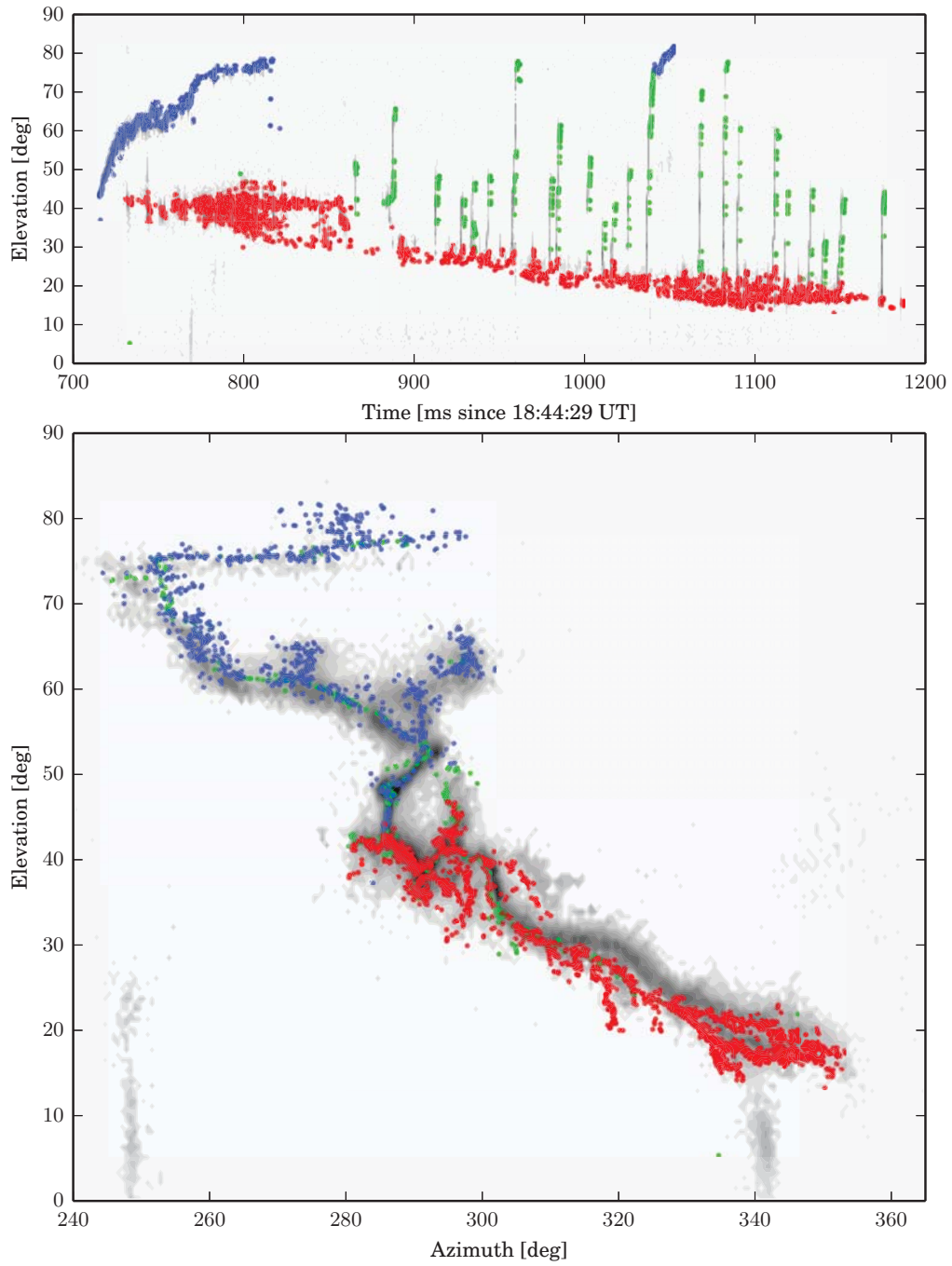
Figure 5.2: Flash B, LMA–interferometer overlay. LMA sources (colored by charge) are overlaid on the interferometer map (shaded by integrated VHF luminosity).

first 7 ms of the flash all possible interferometer windows produced a valid location. The negative leader continues propagating without pause until 18:44:29.8178 (102 ms after initiation), at which point the negative leader abruptly stops propagating. During this phase, the negative channel propagates into a null in the interferometer antenna pattern, which causes the sources to fade away in the interferometer, but not the LMA, map (this can be seen in Figure 5.4.

Breakdown is first located on the positive leader at 18:44:29.7276 (12 ms after initiation) and was located by both the LMA and interferometer. While the negative leader propagates up into the positive charge region, activity in the positive breakdown region increases. A K-change can be identified starting at 18:44:29.7442 (28 ms after initiation) that is not well mapped by the LMA. While small scale K-processes are frequently observed during this stage of a lightning flash, large scale K-changes which travel into the negative breakdown region of the flash are much less common.

After the negative leader stops propagating, there is an associated decrease in activity seen in the positive breakdown region. At 18:44:29.8568 (150.2 ms after initiation), there is a K-change and then activity in the positive breakdown almost completely stops. Activity resumes at 18:44:29.8872 (171 ms after initiation). From this point on, activity in the flash is characterized by dim emission at the tip of the positive leader, and repeated K-changes retracing the previously ionized channel. The repeated K-changes continue for approximately 300 ms, at which point the flash ends at 18:44:30.1870.

For reference, included with each flash are side by side comparisons of the inteferometer (bottom) and LMA (top) maps, colored by time (Figure 5.3) and power (Figure 5.4). The LMA panels for these plots are in the normal format used to display LMA data. The top panel shows altitude versus time for the flash, and the bottom three panels show the vertical cross sections and plan view of the flash. The limits on Figures 5.3 and 5.4 are identical to those in Figures 5.1 and 5.2 for easy comparison.
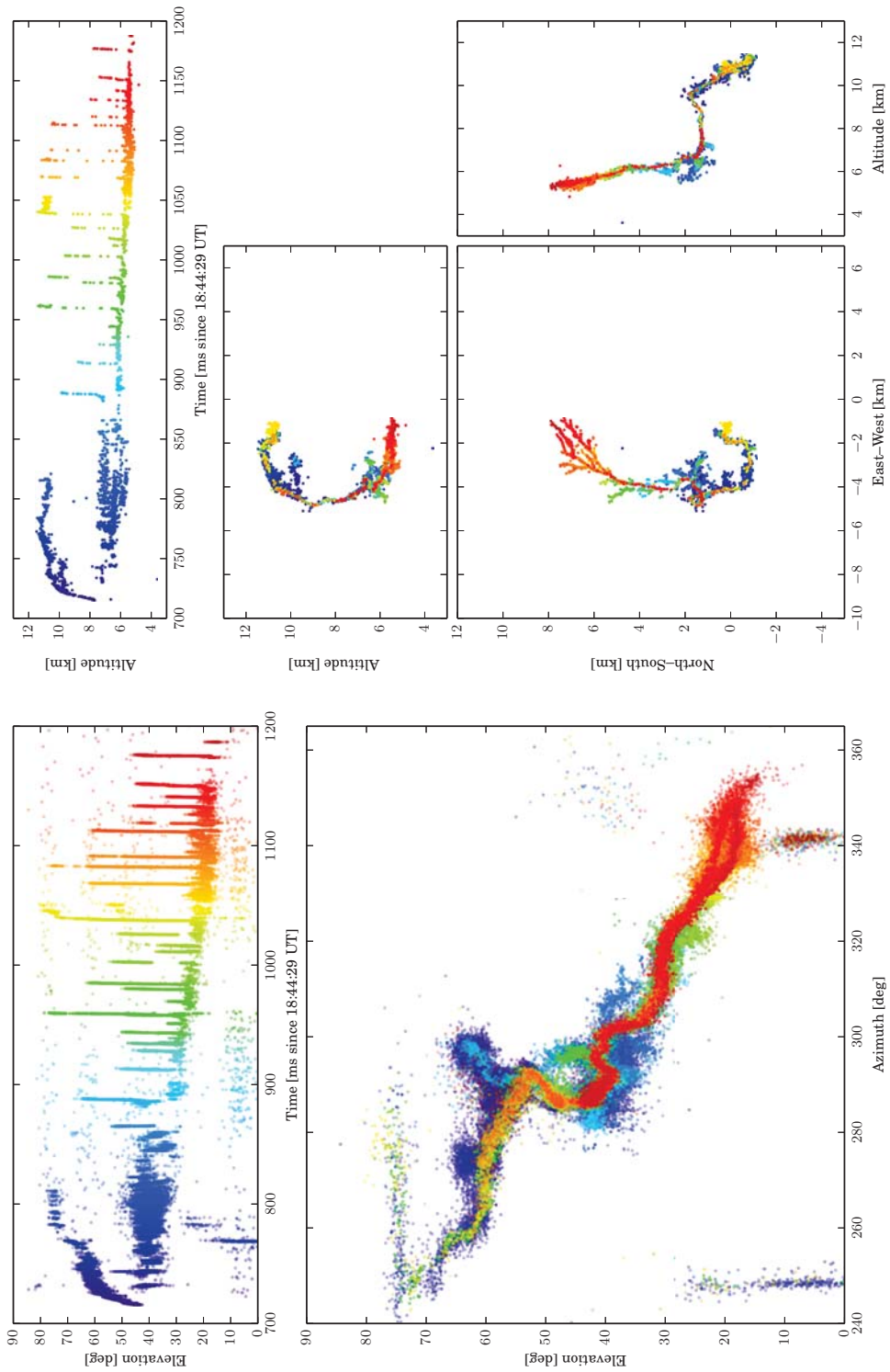
Figure 5.3: Flash B, overview colored by time. Top: LMA map with the same limits as Fig. 5.1. Bottom: Interferometer map.
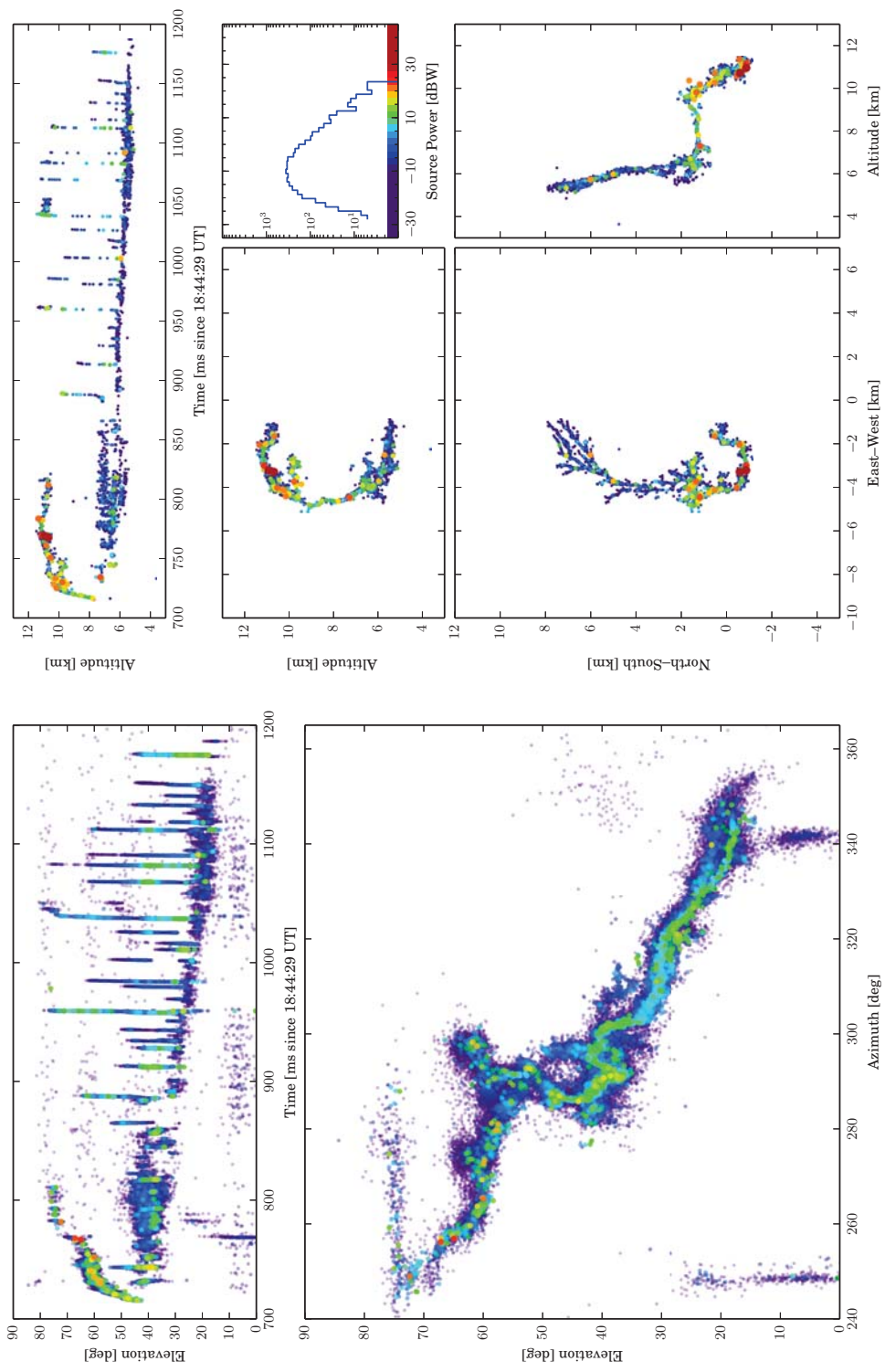
Figure 5.4: Flash B, colored by power.

5.2 Flash C, BFB 20:07:22 UT on July 08, 2013

Flash C was used as the example flash for developing multi-baseline location techniques, and is also featured in Section 6.2 about positive leaders, and Section 7.2 about fast positive breakdown.

Flash C occurred on July 8, 2013 at 20:07:19.0547 UT (based on the first located LMA source). By 2013, an upgrade to the software used to record data from the digitizers allowed for long pretrigger records to be recorded. For this flash, the interferometer record begins over a second before the flash initiated, and nothing was missed. At this time, the interferometer was being operated with 4 VHF antennas for an exploratory study into possible benefits of multi-baseline location techniques (see Chapter 3). As a result, no fast antenna record is available for this flash. The LMA data for this flash was processed using 10 μs windows using high quality settings.

Flash C is a hybrid cloud-to-ground, bolt from the blue (BFB) flash. While the flash initiated between the upper positive and main negative charge layers, like a normal intracloud flash, the negative leader left the storm and connected to the ground. In this particular example, the negative leader traveled 9 km horizontally before touching ground. However, negative leaders from this type of flash have been observed to travel much farther and touch ground well outside of the cloud, hence the name bolt from the blue (*Edens*, 2011). When the lightning channel touches ground, negative charge is transferred from the cloud to the ground, and so this is classified as a negative cloud-to-ground flash. But, the flash is not representative of typical negative cloud-to-ground flashes, which normally initiate between the main negative and lower positive charge regions.

Figure 5.5 shows the context of the flash which initiated at 9 km altitude, between the upper positive and main negative charge regions, indicated by the small white circle. The flash begins with an upward propagating negative leader, which turns horizontally west in the positive charge layer. In the interferometer projection (Figure 5.6), the initial negative leader development appears to twist around itself. This is an effect of the 2-dimensional projection of the interferometer. In Figure 5.7 and 5.8, the LMA map of the flash shows clear separation between the positive and negative breakdown regions, and fairly little branching in the initial negative leader.

Flash C initiates some distance to the west of the interferometer site, but has channels which propagate east and pass very nearly overhead. With two lightning channels flanking the interferometer site, the flash fills nearly the entire sky when viewed from the interferometer site. As a result, the interferometer map shows the map in the cosine, rather than azimuth-elevation, projection.
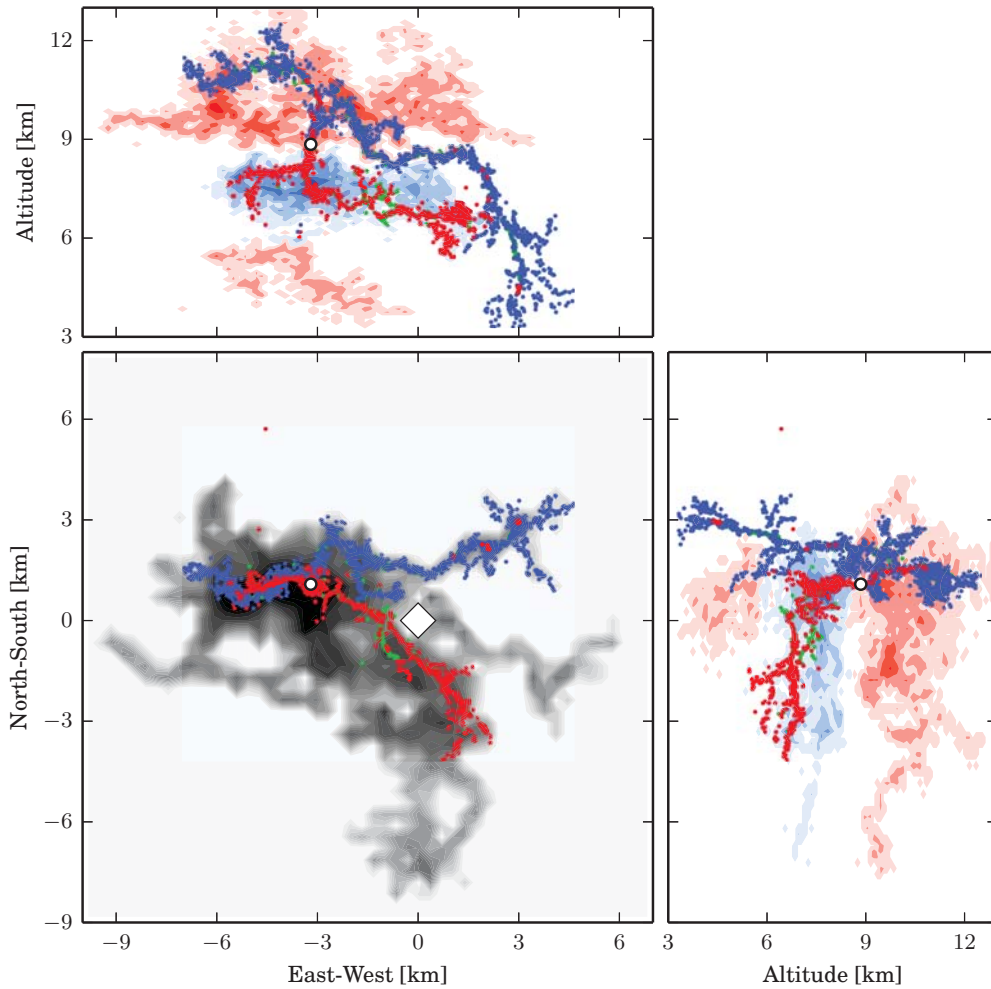
Figure 5.5: Flash C, LMA map of storm context. Vertical cross sections show charge structure of the storm with red (blue) showing regions of positive (negative) charge. The plan view shows the LMA source density for the storm in grey-scale. The channels of the flash are colored by charge, those carrying positive (negative) charge are colored red (blue). The white circle marks the origin of the flash, and the white diamond marks the location of the interferometer.
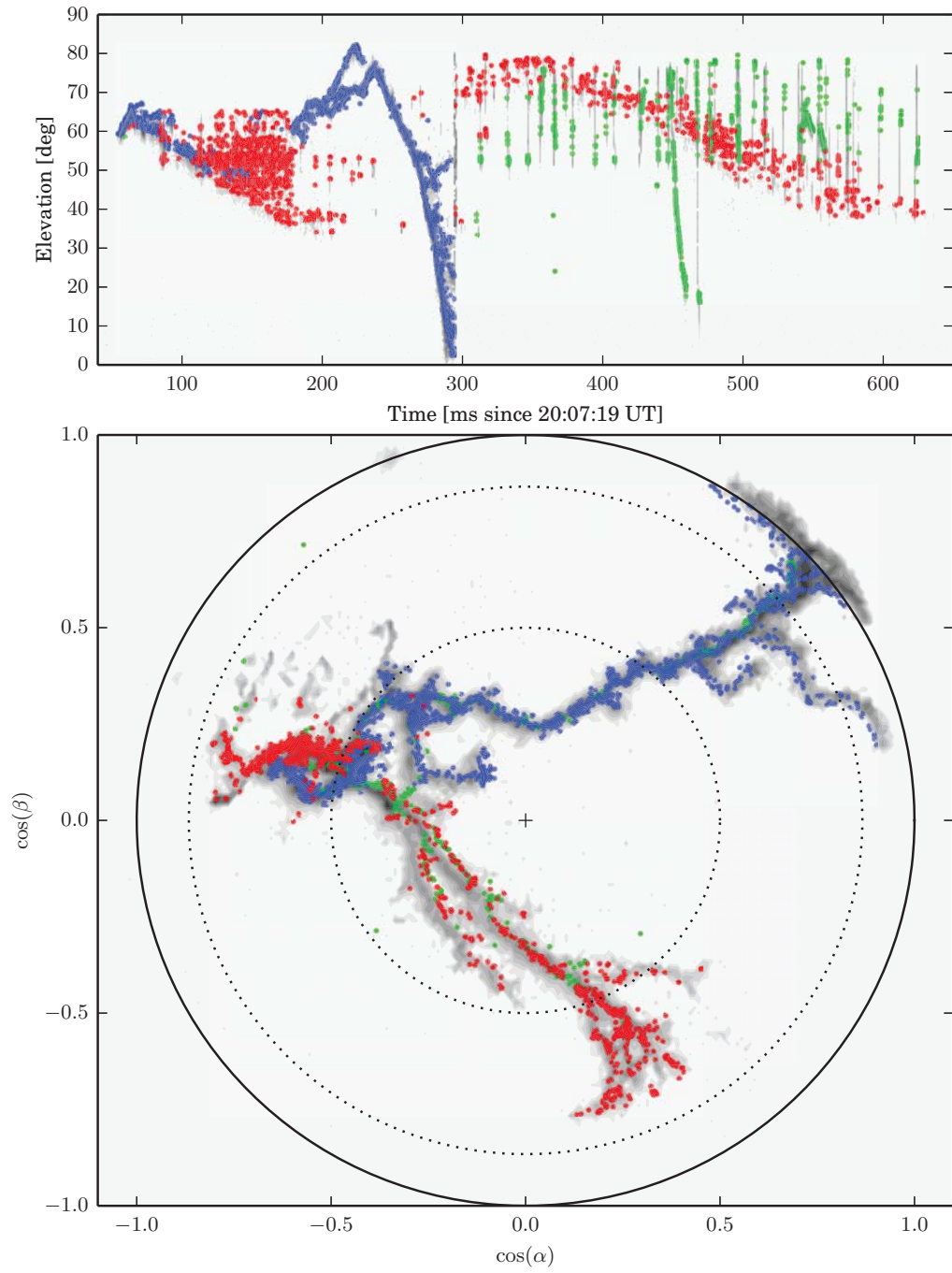
Figure 5.6: Flash C, LMA–interferometer overlay. LMA sources (colored by charge) are overlaid on the interferometer map (shaded by integrated VHF luminosity).

At 20:07:19.1783 UT (123.6 ms after initiation), a new negative leader initiates approximately midway up the central vertical channel of the flash, and begins propagating to the east. This is the negative leader that will eventually propagate to the edge of the storm, and then to ground. When the new negative leader initiates, activity in the positive breakdown is seen to dramatically reduce, and concentrate on just a single channel to the south of the interferometer site and propagating southeast.

The negative leader touches ground at 20:07:19.2947 (240.0 ms after initiation), producing a large positive current traveling into the cloud, the return stroke. The stroke itself is not located by the interferometer, however when it reaches the end of the existing ionized channel, it produces a burst of bright, fast propagating, positive breakdown. As will be also seen in other flashes, the fast positive breakdown is almost completely un-mapped by the LMA, even though the LMA data was processed using maximum quality settings and 10 μs windows. The fast positive breakdown propagates into a region of the cloud in which no other sources had been detected, indicating a region of previously un-ionized air. After the burst of positive breakdown, no emission is seen in this region of the sky for the remainder of the flash.

After the return stroke, the positive leader continues propagating southeast. Numerous K-changes are seen propagating from near the tip of the positive breakdown, and towards the flash origin. Some of these K-changes propagate beyond the flash origin and onto the negative channel to ground, but none of them reaches the ground to produce another stroke[2]. The positive leader continues propagating, with repeated K-changes, until it reaches the edge of the cloud and the flash ends at 20:07:19.6316 UT (576.9 ms total duration).

---

[2] For historical reasons, K-changes which reach the ground are called dart leaders, even though the physical process is the same. Similarly, K-changes which travel on the negative channel to ground, but do not reach the ground, are called attempted dart leaders.
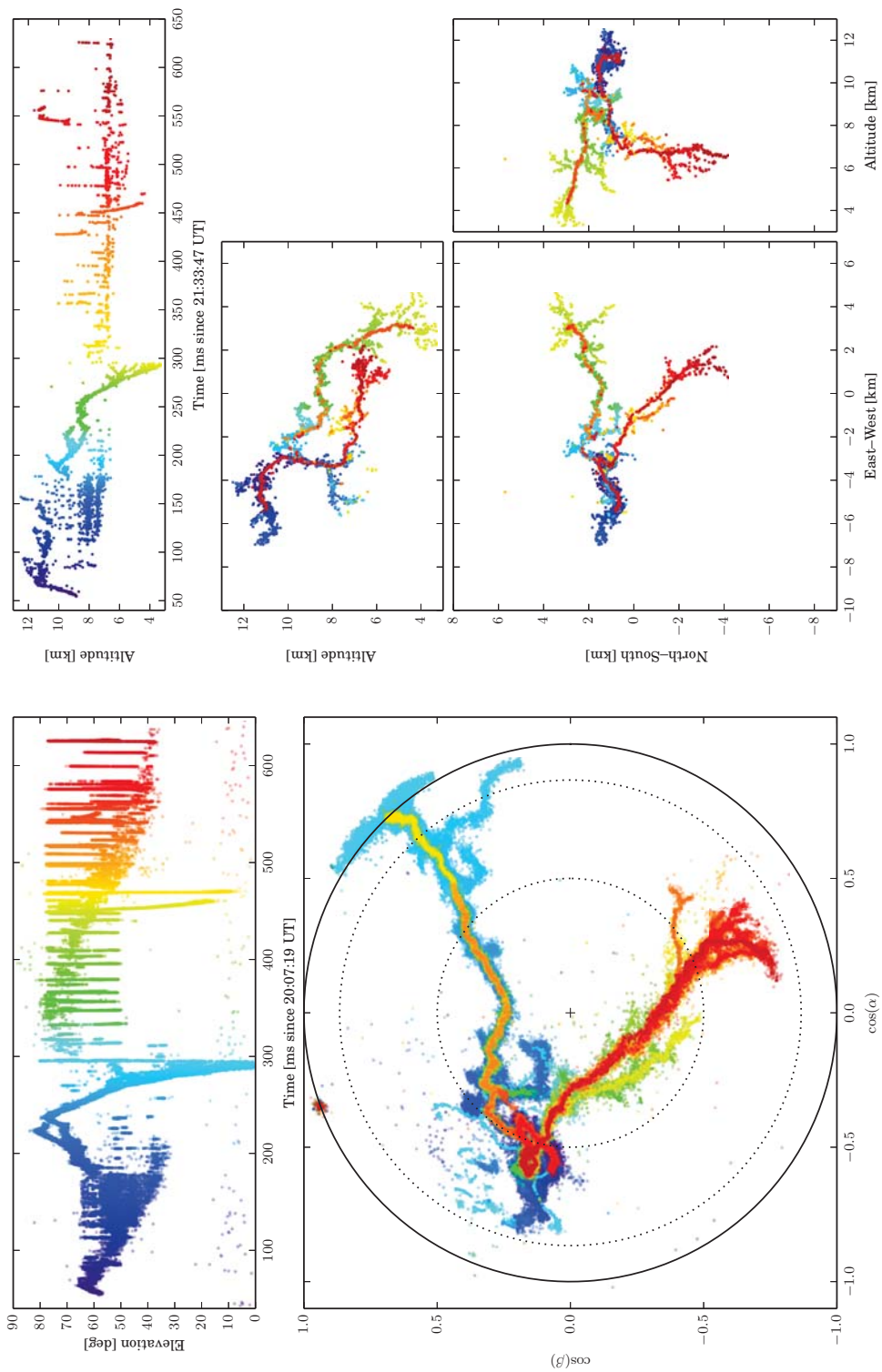
Figure 5.7: Flash C, overview colored by time. Top: LMA map with the same limits as Fig. 5.5. Bottom: Interferometer map.
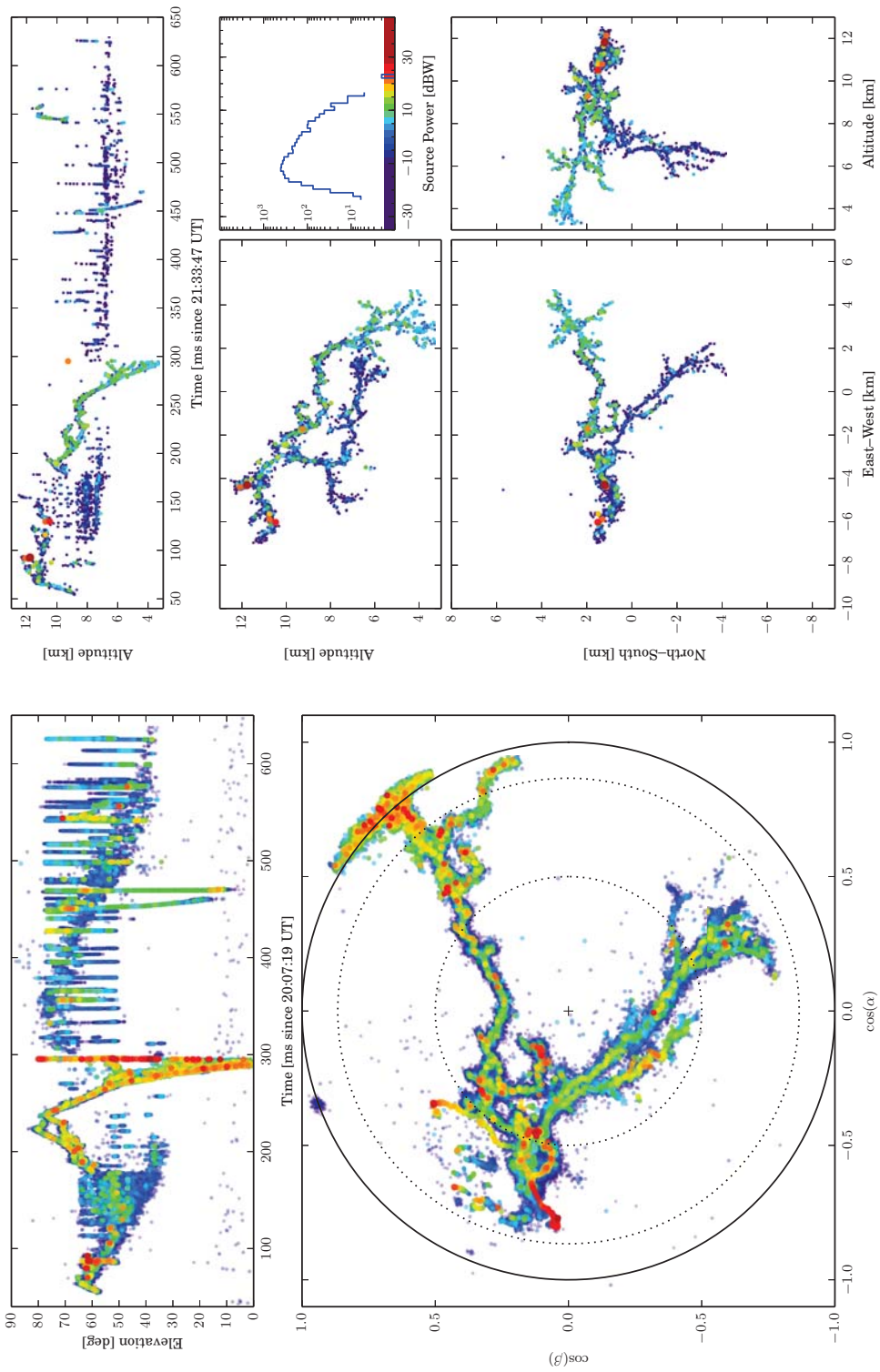
Figure 5.8: Flash C, overview colored by power. Top: LMA map with the same limits as Fig. 5.5. Bottom: Interferometer map.

5.3 Flash D, IC 21:33:47 UT on July 24, 2013

Flash D is featured in Section 6.1 about negative leader steps.

Flash D occurred on July 24, 2013 at 21:33:47.7645 UT (based on the first located LMA source). The fourth VHF antenna of the interferometer was replaced with a fast electric field change meter (fast antenna), which was sampled time synchronously with the VHF data. The LMA was fully functional during this storm, but all the data (including the data for the flash) was processed using normal quality settings and 80 μs windows.

Flash D is an example of a low altitude intracloud flash; Figure 5.9 shows the storm context of the flash colored by charge. The flash initiated between the main negative and lower positive charge layers. Normally, flashes which initiate in this region become negative cloud to ground flashes. However, if the lower positive charge layer is larger than the main negative charge layer (as is the case for this storm), the negative leaders may stay in the cloud. This charge configuration is more often observed near the beginning of the storm's life span (*Mansell et al.*, 2010). In the case of this storm, flash D occurred approximately 3 minutes after the first flash of the storm. A few minutes after flash D, the storm transitioned from producing low altitude intracloud flashes, to producing negative cloud-to-ground flashes. Low level intracloud flashes exhibit the same behavior as the initial stage of a cloud-to-ground flash. In addition, there is a very marked difference in the behavior of the negative leader in these low altitude flashes versus a normal, higher altitude intracloud flash (discussed in Section 6.1).

Figure 5.10 shows the interferometer map of flash D, with LMA sources overlaid and colored by charge. The negative leader channels of low level intracloud flashes (and the initial portion of negative cloud-to-ground flashes) are frequently seen to be more tortuous. The added tortuosity causes the channels to twist on each other when viewed from the perspective of the interferometer. The resulting maps are frequently very difficult to interpret.

In flash D, there are two main negative leader branches: the first starts at the beginning of the flash and propagates to the south away from the interferometer; the second starts at 21:33:47.8241 UT (59.6 ms after initiation) and propagates roughly to the north towards the interferometer.

Figure 5.11 shows the fast electric field change (fast antenna) record for this flash. The fast antenna measures the electric field convolved with a 150 μs exponential decay. As such, the fast antenna is not well suited for measuring the electric field produced by processes which change on time scales longer than 150 μs. The electric field change produced by the initial several negative leader
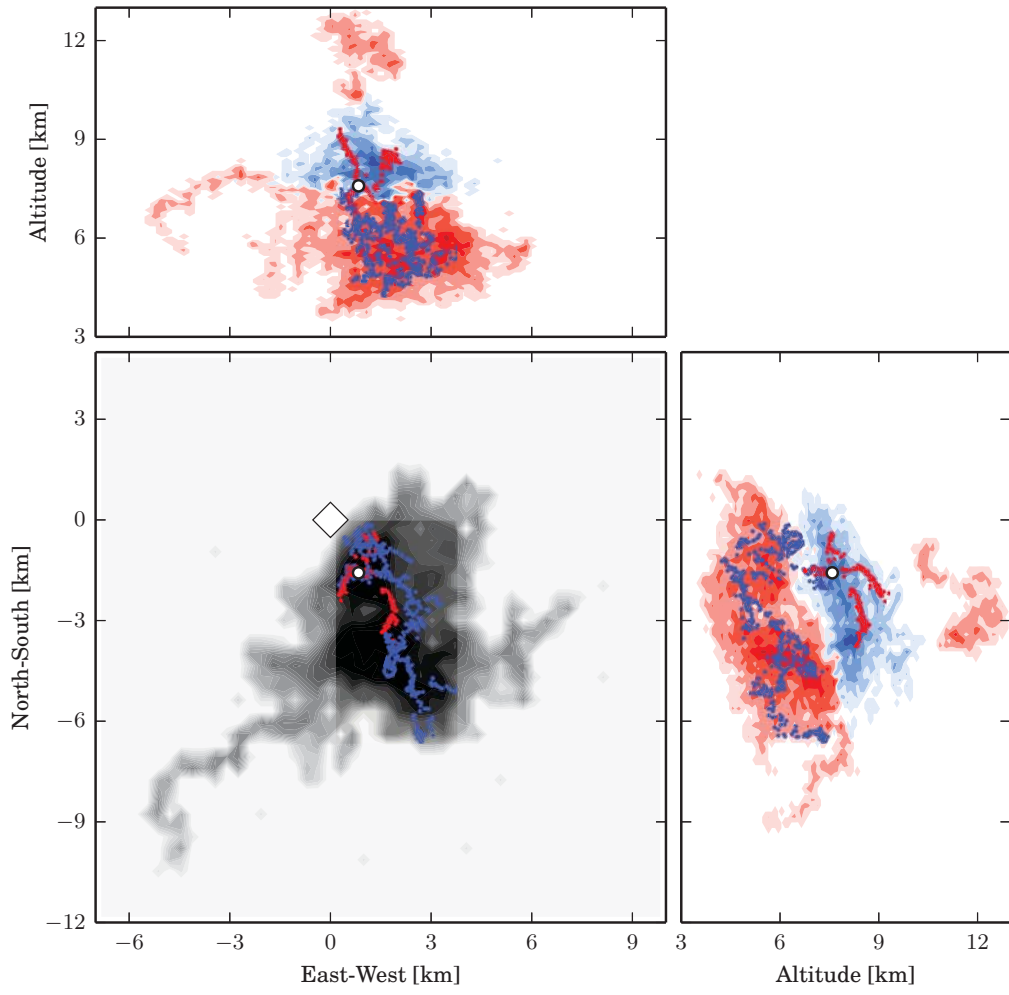
Figure 5.9: Flash D, LMA map of storm context. Vertical cross sections show charge structure of the storm with red (blue) showing regions of positive (negative) charge. The plan view shows the LMA source density for the storm. The channels of the flash are colored by charge, those carrying positive (negative) charge are colored red (blue). The white circle marks the origin of the flash, and the white diamond marks the location of the interferometer.
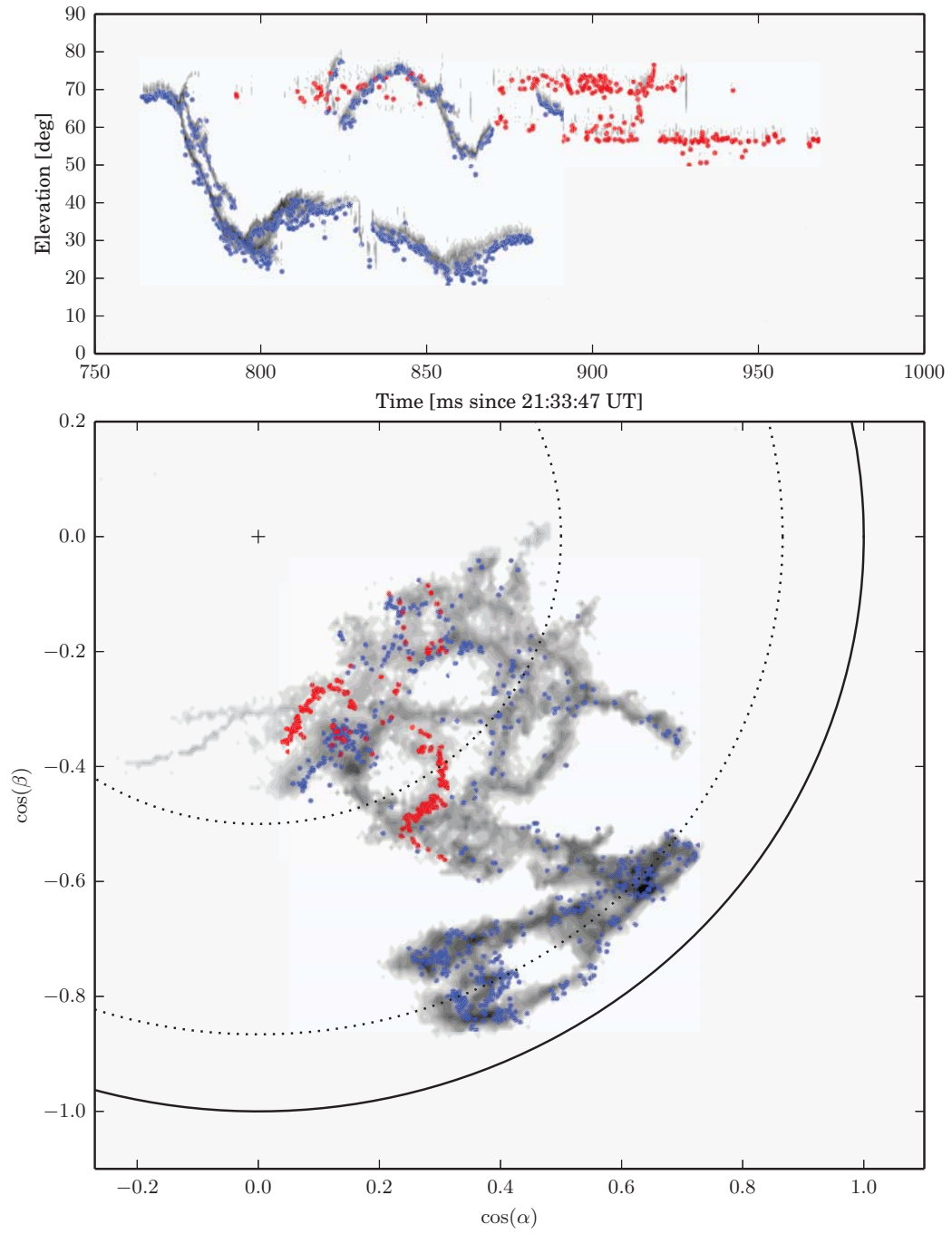
Figure 5.10: Flash D, LMA–interferometer overlay. LMA sources (colored by charge) are overlaid on the interferometer map (shaded by integrated VHF luminosity).

steps is relatively small. Each step of the negative leader shows a distinct positive deflection in the electric field record, consistent with negative charge moving towards the fast antenna. At roughly 21:33:47.773 UT (9 ms after initiation), the stepping rate and the field change from each step increase. This causes the large positive deflection seen in the field record. The change in behavior is also coincident with brighter VHF emission.

Very few sources are located in the positive breakdown region for the first 120 ms of the flash. However, the lack of located sources is not due to lack of activity in the positive breakdown region. Both the interferometer and the LMA are capable of locating only a single source during each time window. For the LMA, the time window is 10 or 80 μs, and for the interferometer the time window is 1.4 μs in duration. If emission from multiple sources separated by more than the angular resolution of the interferometer ($\sim 10°$) is present in a single time window, only the brightest source is located. The very active negative leader of flash D therefore masks the emission from the positive breakdown region.

After activity in the negative breakdown region ceases, activity in the positive breakdown region continues. The onset of positive breakdown activity is not due to the emission starting, but because the masking radiation of the negative leader ends. At 21:33:47.9284 UT (163.9 ms after initiation) there is a single large scale K-change which propagates from a previously un-mapped region towards the body of the flash. While the LMA did not locate any sources during this K-change, coincidence with the breakdown is a strong positive deflection of the electric field as seen in Figure 5.11. Shortly after the K-change, activity in the positive breakdown region also ceases and the flash is over.
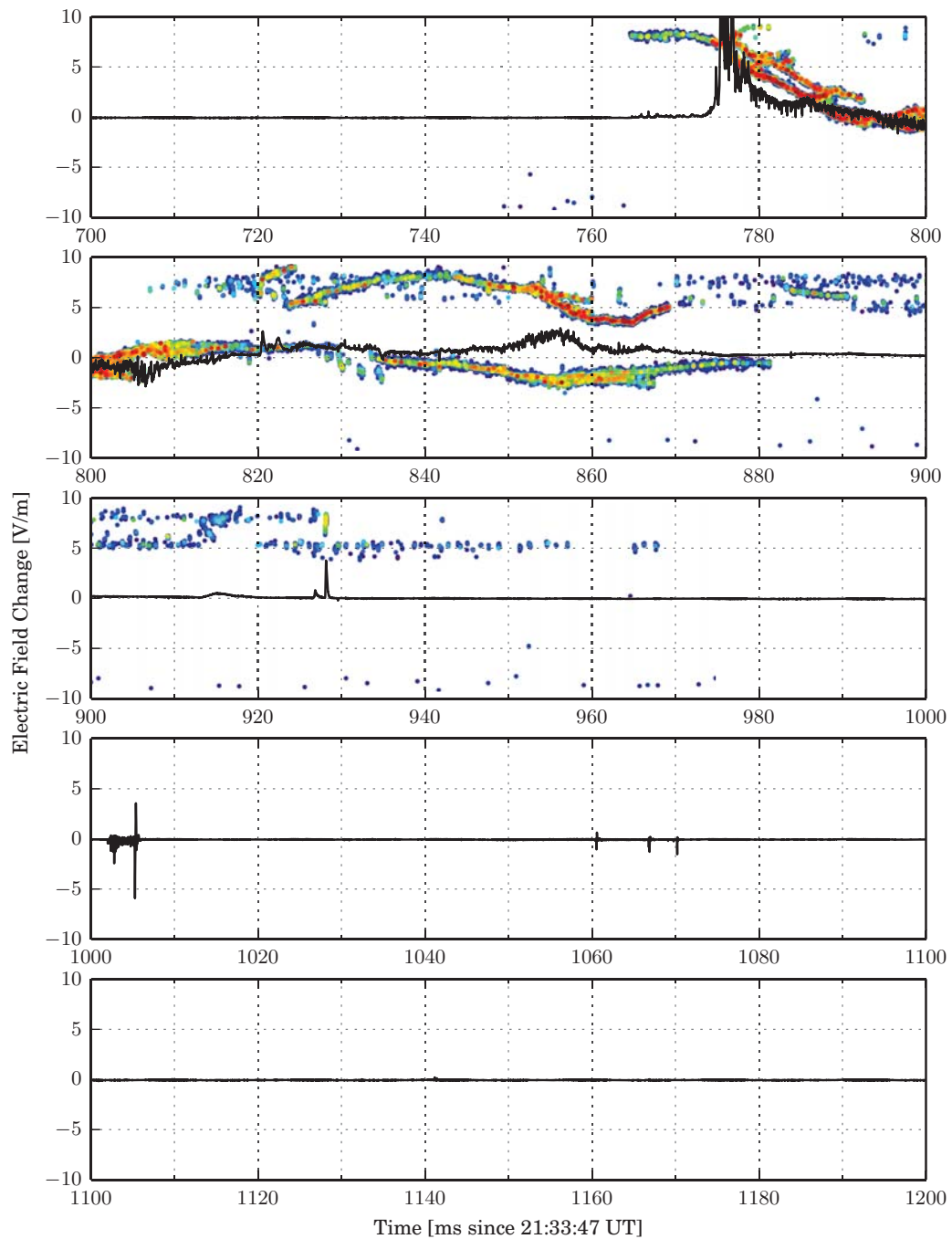
Figure 5.11: Flash D, Sferic. Fast electric field change record with 150 µs exponential decay time shown in black, with elevation of the interferometer map colored by power shown for reference.

121
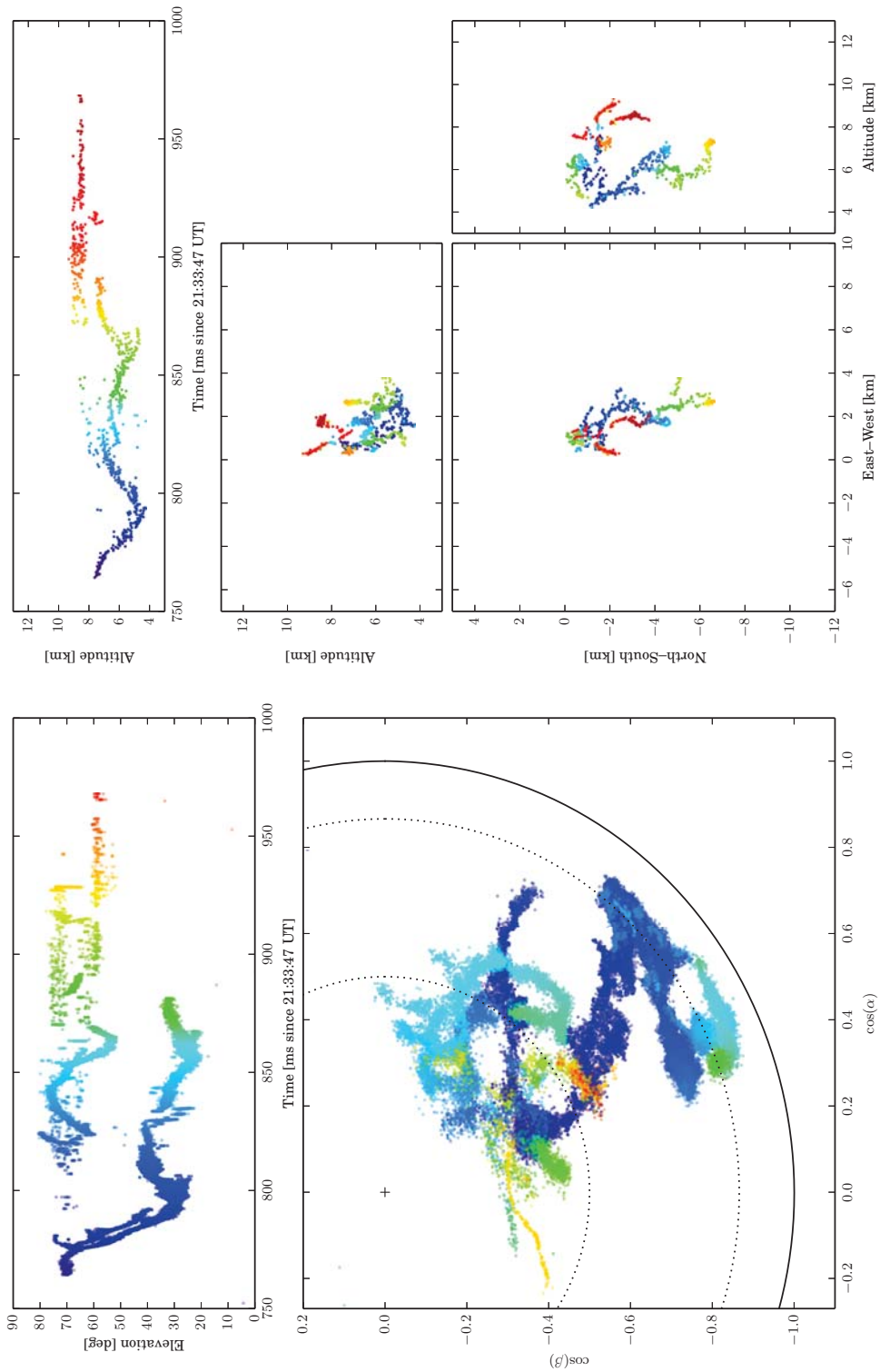
Figure 5.12: Flash D, overview colored by time. Top: LMA map with the same limits as Fig. 5.9. Bottom: Interferometer map.
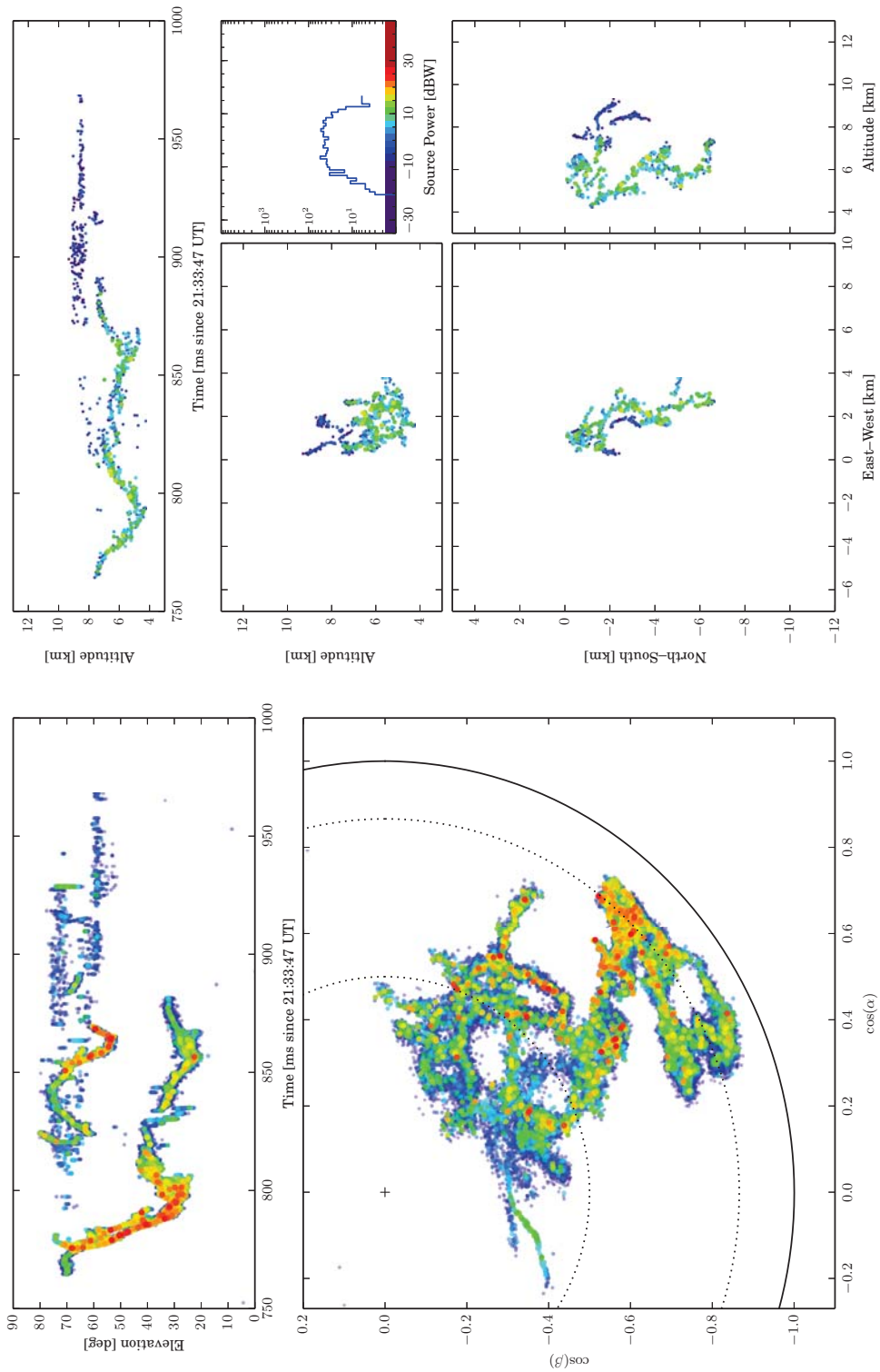
Figure 5.13: Flash D, overview colored by power. Top: LMA map with the same limits as Fig. 5.9. Bottom: Interferometer map.

5.4   Flash E, IC 20:25:10 UT on August 5, 2013

Flash E is featured in Section 6.1 about negative leader stepping, and also in Section 7.2 about fast positive breakdown.

Flash E occurred on August 5, 2013 at 20:25:10.3656 UT (based on the first located interferometer source) initiating 5.7 km northeast of the interferometer site. Flash E is a somewhat abnormal example of a intracloud discharge. The flash is considered abnormal for three reasons: it is initated by a narrow bipolar event (NBE, *Willett et al.* (1989)), the negative leader is much longer than the positive leader, and there is a cluster of fast propagating radiation in the later part of the flash which are not K-processes. All of these points will be discussed below. Figure 5.14 shows an LMA map of the storm context for this flash. This particular storm cell was adjacent to a second, larger storm to the northwest. Only a portion of the adjacent cell can be seen in Figure 5.1.

Flash E initiates with a NBE at 20:25:10.3656 UT between the upper positive and main negative charge regions (indicated by the white circle in the Figure 5.14). NBEs in general are the topic of very active research in the field, and the NBE of this particular flash is the subject of an on-going study, however NBEs will not be discussed in detail in this dissertation. NBEs are defined by a characteristic waveform seen in the electric field at distant station, seen as a short duration bipolar pulse. The sferic produced by the NBE of flash E can be seen quite clearly in the electric field record for the flash (Figure 5.16). The field change produced by the NBE extends off scale in Figure 5.16, saturating the digitizer, but not the analog circuity of the fast antenna. The interferometer sees the NBE as a bright radiation source moving vertically downward at a velocity of about 10^7 m/s over a period of about 20 μs.

The negative leader is seen to start propagating into the upper positive charge layer at 20:25:10.3671 UT (1.5 ms after the NBE). The initial several steps carry negative charge vertically away from the interferometer, and are associated with dramatic negative deflections in the electric field record. At 20:25:10.4159 UT (50.3 ms after the NBE), the negative leader turns horizontal and begins propagating southwest, towards the interferometer site, producing positive field deflections in the electric field record. Activity is first seen in the positive charge region 20:25:10.3854 UT (19.8 ms after the NBE). The positive leader propagates a short distance down into the main negative charge layer, with comparatively little branching compared to other intracloud flashes. Activity in the positive breakdown region continues for 112 ms, frequently being masked by the brighter radiation produced by the still active negative leader.

At 20:25:10.4788 UT (133.2 ms after then NBE), a new negative leader forms at the top of the vertical channel which propagates away from the interferometer to the north. The initial negative leader step shows a large negative
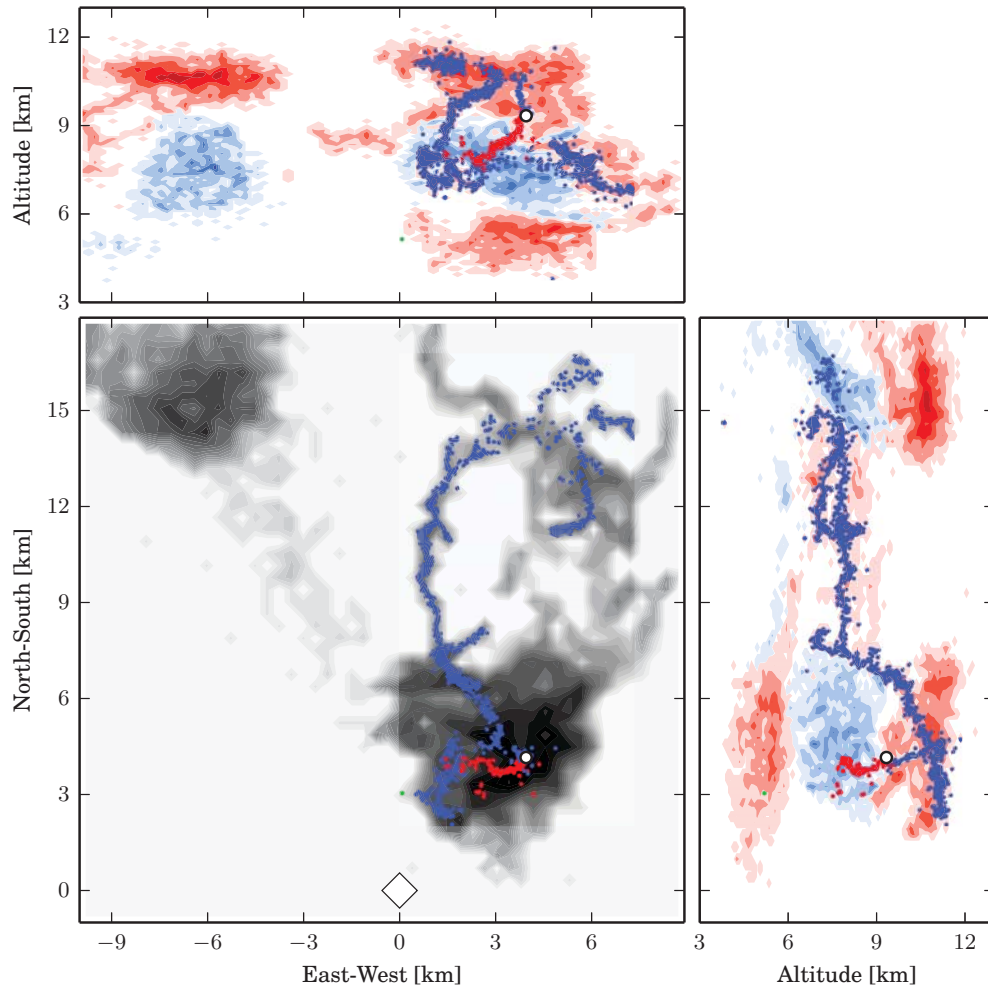
Figure 5.14: Flash E, LMA map of storm context. Vertical cross sections show charge structure of the storm with red (blue) showing regions of positive (negative) charge. The plan view shows the LMA source density for the storm. The channels of the flash are colored by charge, those carrying positive (negative) charge are colored red (blue). The white circle marks the origin of the flash, and the white diamond marks the location of the interferometer.
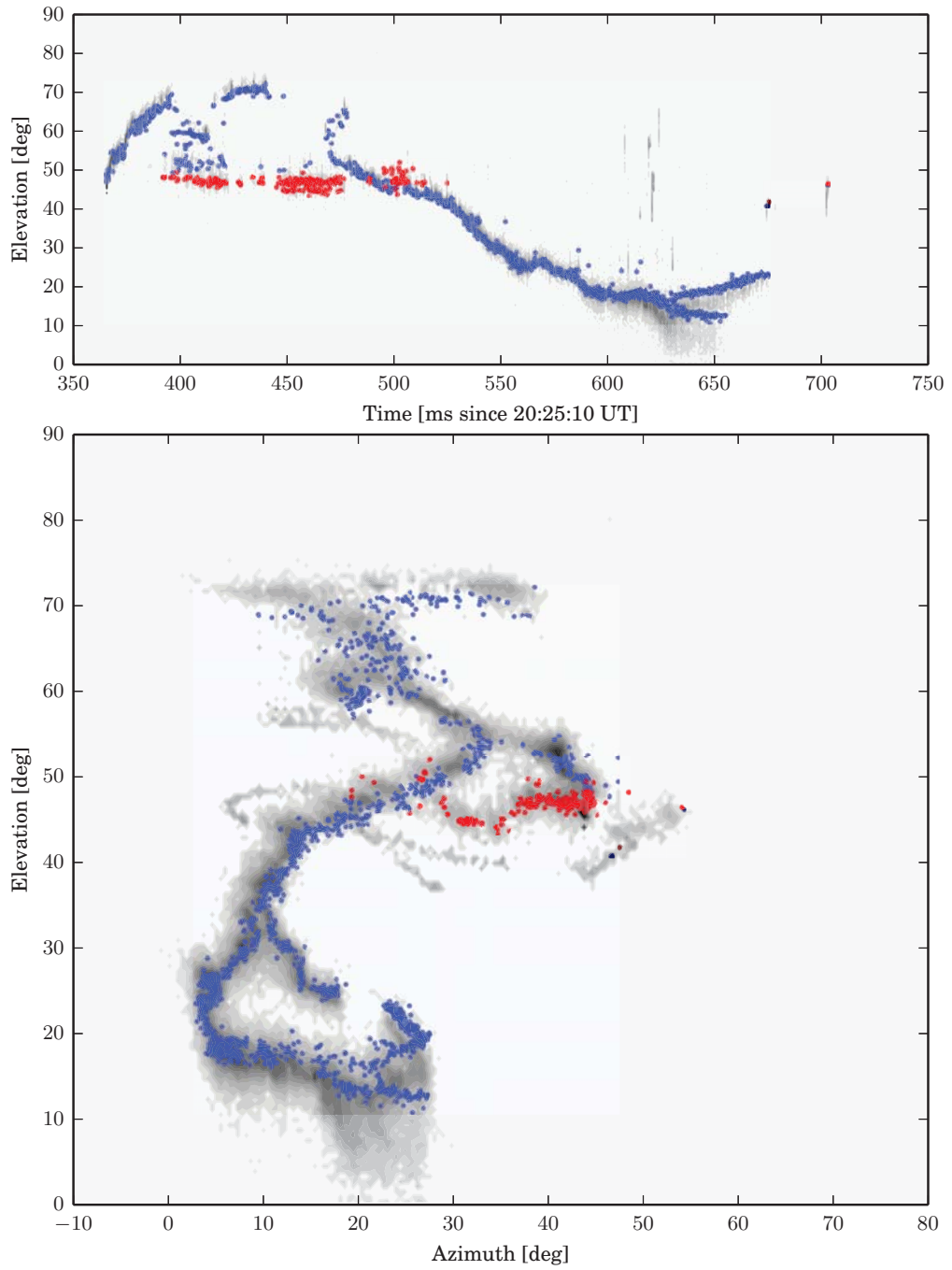
Figure 5.15: Flash E, LMA–interferometer overlay. LMA sources (colored by charge) are overlaid on the interferometer map (shaded by integrated VHF luminosity).

deflection in the field record, due to negative charge moving away from the fast antenna site. This negative leader continues propagating into the anvil region of the storm. These stratiform regions of a storm frequently carry positive charge at a lower elevation than the upper positive charge layer, and have relatively fewer (but larger) flashes as seen by the low LMA source density in Figure 5.1. intracloud flashes propagating into the stratiform region of a cloud are not uncommon, and a handful of such flashes occurred in this storm, though they are not representative of typical IC flashes. In this case, the negative leader extends over 15 km horizontally and propagates continuously for the remaining duration (196.4 ms) of the flash. In comparison, the negative leader of Flash B is propagating only for the first 100 ms of the flash.

There is an almost complete lack of K-events in flash E. The two K-events that are present can be seen in Figure 5.15 at the very end of the flash, colored in green. Starting at 20:25:10.6079 UT (242.3 ms after then NBE), a visually similar, but more unusual process is seen: a cluster of fast processes which are well mapped by the interferometer but not by the LMA. These processes start roughly at the furthest extent of the positive leader, where the positive and negative leaders are seen to cross in the interferometer map, and last for less than 100 μs each. In Figure 5.16, it can be seen that these events are associated with a negative deflection of the electric field. These events are produced by breakdown propagating into virgin air carrying positive charge, and will be discussed in much more detail in Chapter 7.
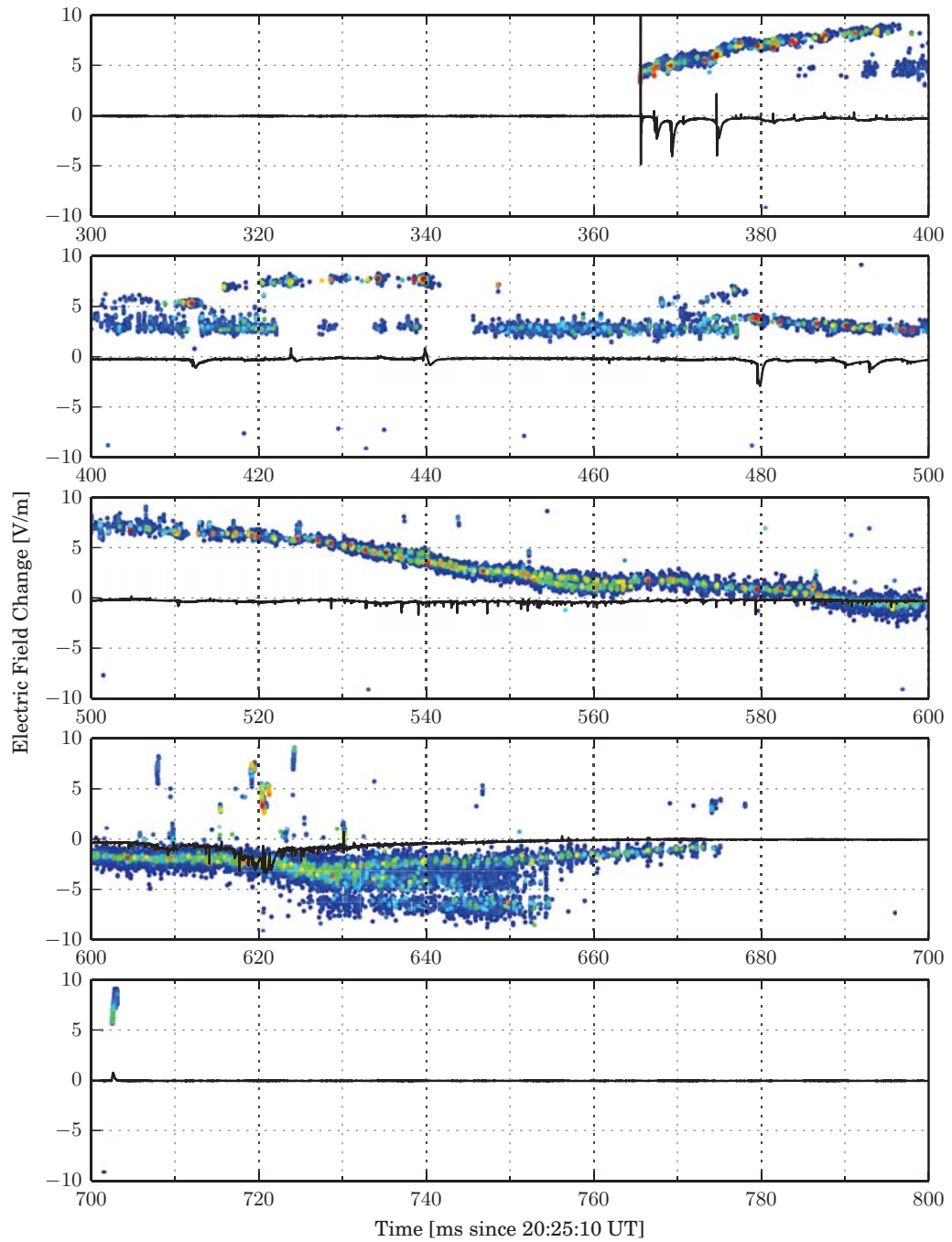
Figure 5.16: Flash E, Sferic. Fast electric field change record with 150 μs exponential decay time shown in black, with elevation of the interferometer map colored by power shown for reference.

128
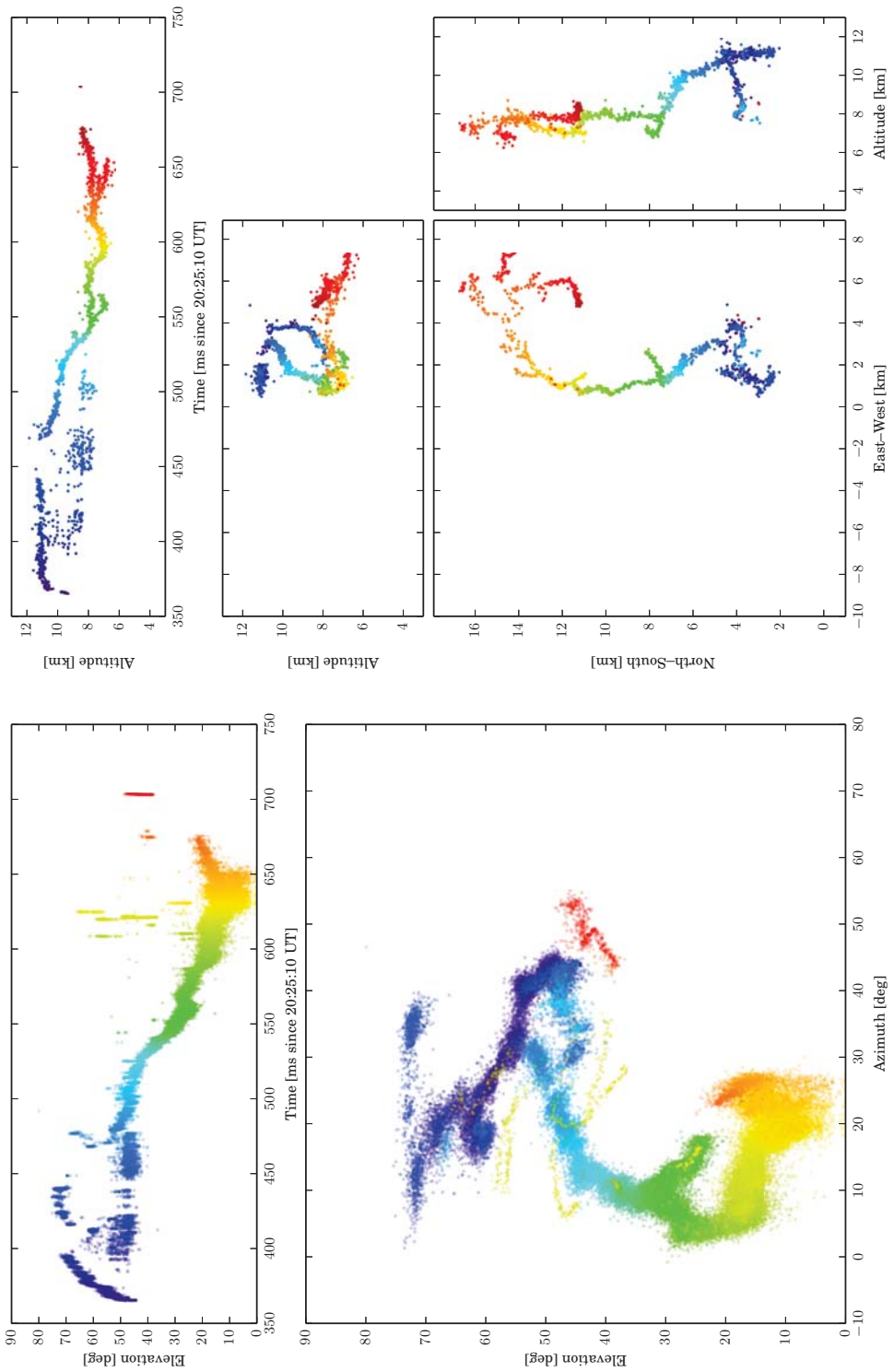
Figure 5.17: Flash E, overview colored by time. Top: LMA map with the same limits as Fig. 5.14. Bottom: Interferometer map.
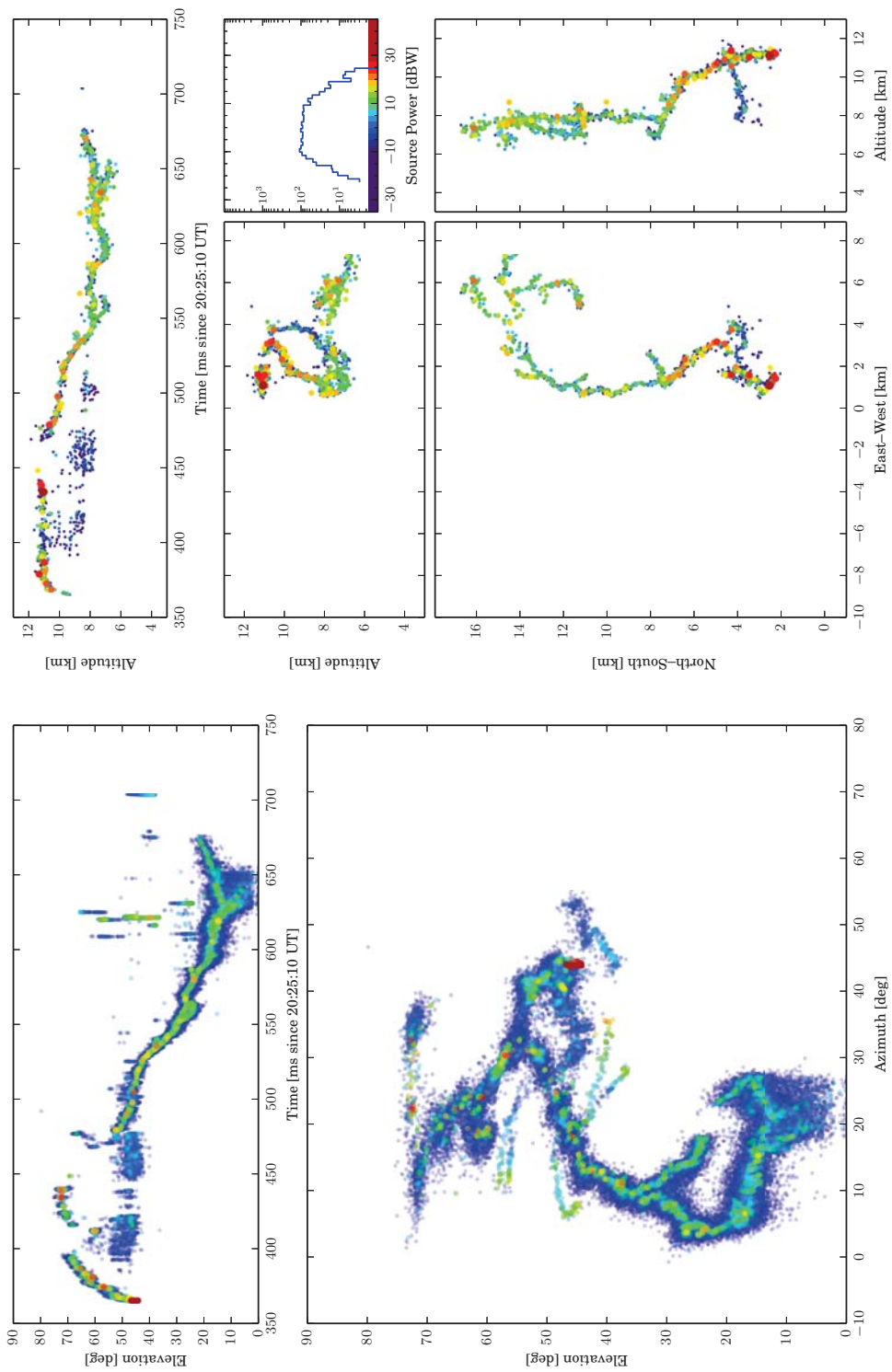
Figure 5.18: Flash E, overview colored by power. Top: LMA map with the same limits as Fig. 5.14. Bottom: Interferometer map.

130

5.5 Flash F, IC 03:11:51 UT on August 6, 2013

Flash F is featured in Section 6.1 about negative leader stepping, and in Section 6.2 about the positive leader and in Section 7.2 about fast positive breakdown.

Flash F occurred on August 6, 2013 at 03:11:51.1547 UT (based on the first located LMA source) initiating at 1100 meters east of the interferometer site. Flash F is an example of a extensive, but otherwise normal intracloud flash. The total duration of the flash is just shy of one second, which is exceptionally long for flashes observed near Langmuir Laboratory. The flash initiated almost directly overhead of the interferometer, making it a very good flash to analyze to investigate the horizontal development of natural leaders.

Figure 5.19 shows the storm context of the flash, with charge regions colored in the vertical cross sections, and density of VHF sources in the plan view. The parent storm for flash F was fairly large and exceptionally active for storms over Langmuir Laboratory[3], as expected for a storm which produced a flash of this size. The flash initiated at the top of the main negative charge layer (small white circle) with initial development typical of most intracloud storms; a negative leader is seen propagating into the upper positive charge region, and a positive leader is seen after a short delay extending horizontally into the main negative charge region.

A complication of the very close proximity of the flash is that the positive and negative breakdown regions inhabit the same portion of the sky. Figure 5.20 shows the interferometer map of the flash with LMA sources colored by charge overlaid. Most of the channels do not significantly overlap, however there is a negative leader (colored in blue) just south of the zenith which runs parallel to and overlaps a positive leader (colored in red). The negative leader steps for this channel are more difficult to identify.

Flash F has 3 primary negative leader channels. The first begins immediately at initiation and propagates upwards 4 km, slanted slightly to the north. The leader channel begins to turn horizontal towards the west at 03:11:51.1748 (17.4 ms after initiation). The negative electric field deflections for the first several leader steps are closely spaced in time, and relatively small in amplitude. As the leader develops, the steps become spaced further in time, but are also generally large in amplitude.

---

[3] Exceptionally active for Langmuir storms means a flash rate of 3–5 per minute for extended periods of time. This is not exceptionally active in Texas, Oklahoma, or Colorado, which regularly see supercell and multi-cell storms with flash rates of 100-200 per minute!
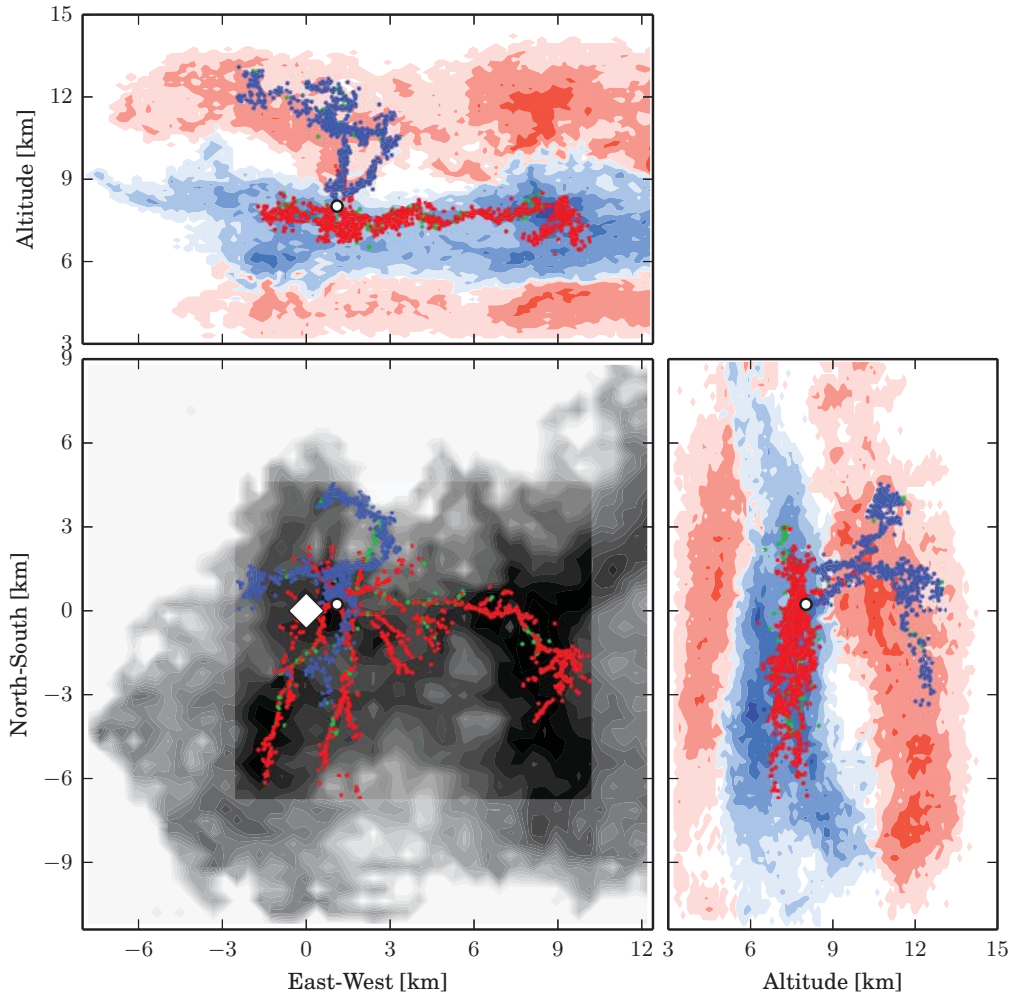
Figure 5.19: Flash F, LMA map of storm context. Vertical cross sections show charge structure of the storm with red (blue) showing regions of positive (negative) charge. The plan view shows the LMA source density for the storm. The channels of the flash are colored by charge, those carrying positive (negative) charge are colored red (blue). The white circle marks the origin of the flash, and the white diamond marks the location of the interferometer.

The second forms as a branch off of the previous negative leader at 12 km altitude in the positive charge region. The first identifiable step on this leader channel occurs at 03:11:51.2739 UT (116.5 ms after initiation) near the origin of the flash. There is evidence of a handful of small leader steps starting at 03:11:51.303, otherwise there is little activity in the negative breakdown region immediately following the first step. However, the positive breakdown region is active at this point, especially near the flash origin, making analysis of this portion of the flash somewhat difficult. The second negative leader starts propagating in earnest at 03:11:51.3264 UT (169.0 ms after initiation), moving to the southwest, parallel to and overlapping a channel in the positive breakdown region. The electric field changes produced by these later steps of the second negative leader are much more complex than those of the first negative leader. This is because there are several K-changes occurring in the positive breakdown region simultaneously with each step.

The final negative leader begins stepping late in the flash at 03:11:51.7059 UT (548.5 ms after initiation), immediately after an especially extensive K-change. This leader propagates to the north, fed by repeated K-changes originating in the only remaining active positive leader channel.

Activity in the positive charge region begins shortly after initiation at 03:11:51.178 UT (23 ms from initiation). The emission from the positive breakdown region flickers, and is not concentrated at any one point. Several miliseconds of these quasi-random source locations shows a star pattern of positive leader channels spreading horizontally into the main negative charge region.

So long as the first negative leader is active (until approximately 03:11:51.240 UT (82.6 ms after initiation), there are no K-change signatures seen in the electric field record of the flash. K-changes are identifiable in the electric field record (Figures 5.21 and 5.22) as short pulses with a leading positive deflection. That said, there are signs of retrograde negative breakdown in the interferometer record earlier in the flash which lack the classic electric field signature of a K-change.

The first identifiable K-change occurs at 03:11:51.2818 UT (124.4 ms after initiation) in a channel to the southwest of the origin. While there were no clearly identifiable K-changes during the first negative leader, there are several which occur while the second and third negative leader are propagating. The K-changes early in the flash tend to be small, traveling over relatively short sections of previously ionized channel near the furthest extent of the positive breakdown. Late in flash F, the K-changes become much more extensive, and frequently propagate into the negative breakdown region. These late, extensive K-changes produce a bipolar electric field change; first moving negative charge towards the fast antenna in the positive breakdown region, and the moving negative charge away from the fast antenna in the negative breakdown region.
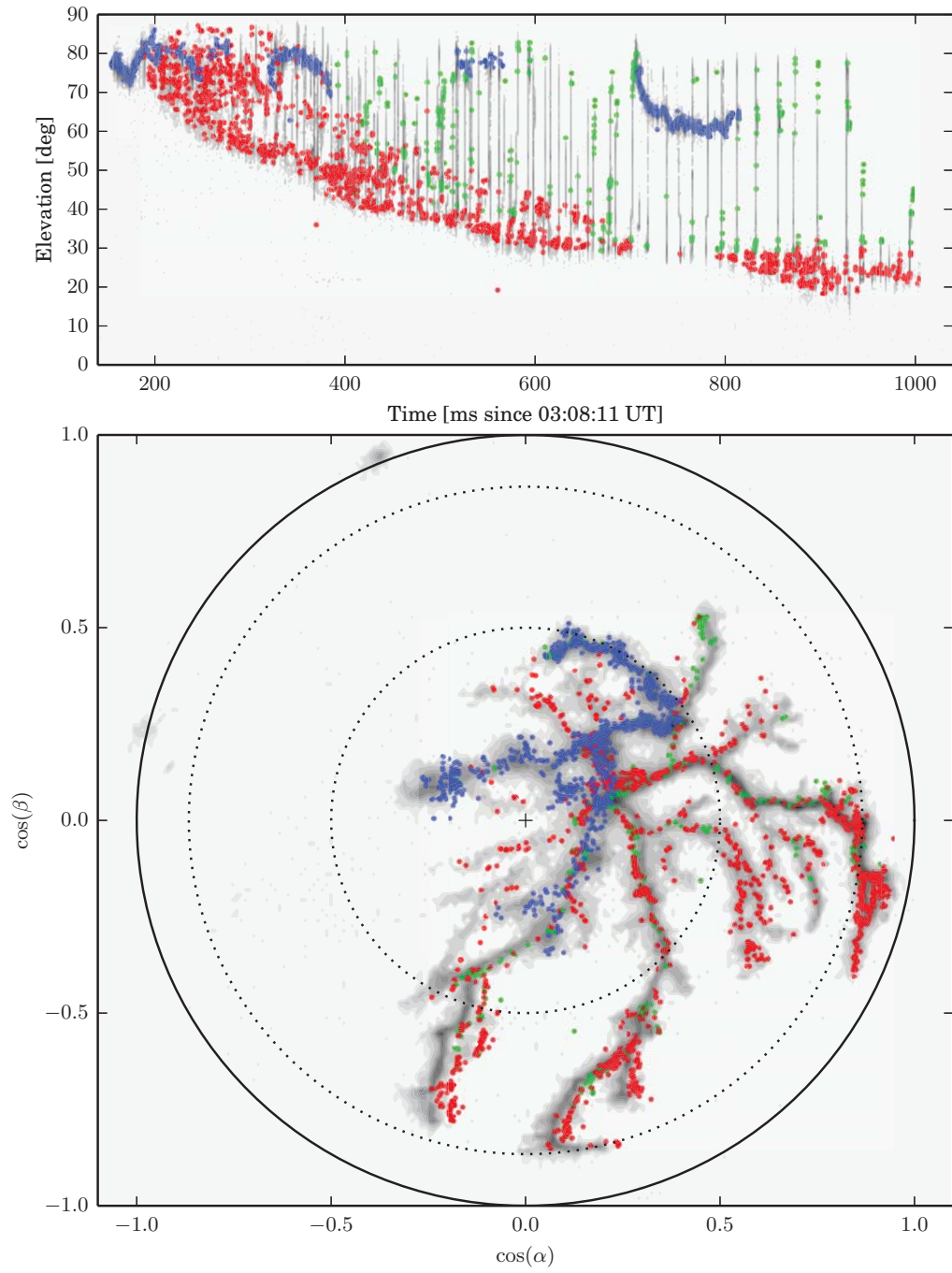
Figure 5.20: Flash F, LMA–interferometer overlay. LMA sources (colored by charge) are overlaid on the interferometer map (shaded by integrated VHF luminosity).
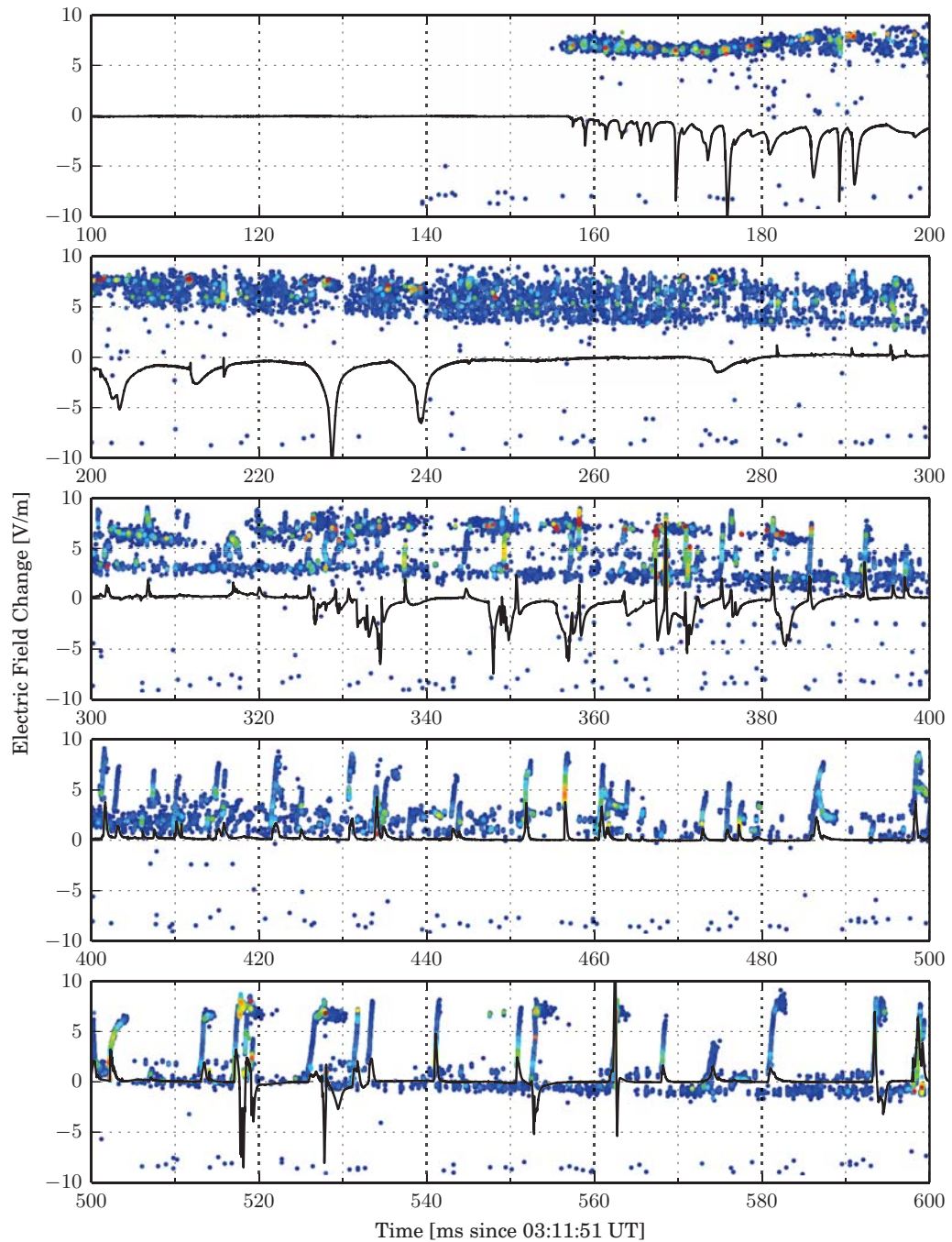
Figure 5.21: Flash F, Sferic. Part 1. Fast electric field change record with 150 μs exponential decay time shown in black, with elevation of the interferometer map colored by power shown for reference.
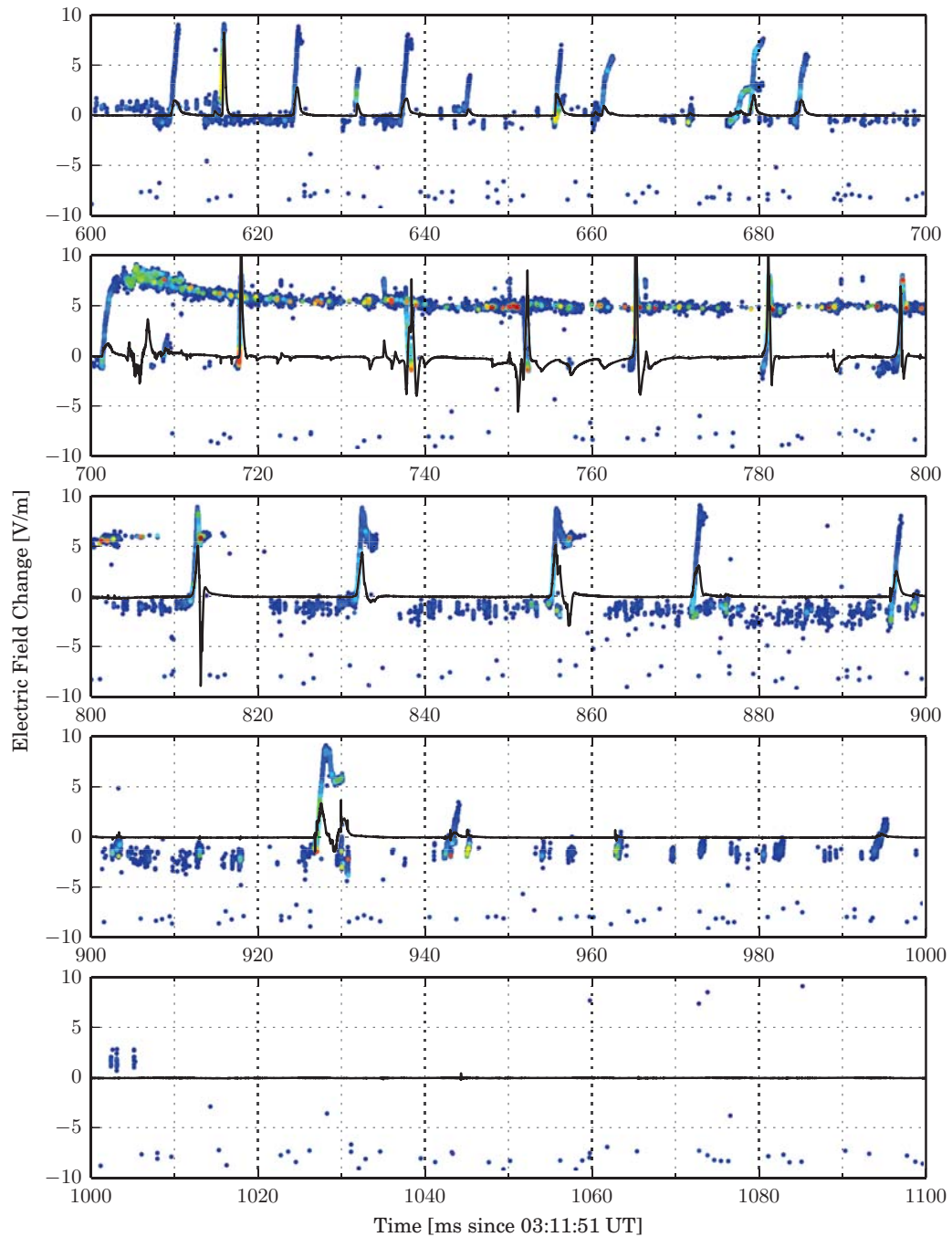
Figure 5.22: Flash F, Sferic. Part 2. Fast electric field change record with 150 μs exponential decay time shown in black, with elevation of the interferometer map colored by power shown for reference.
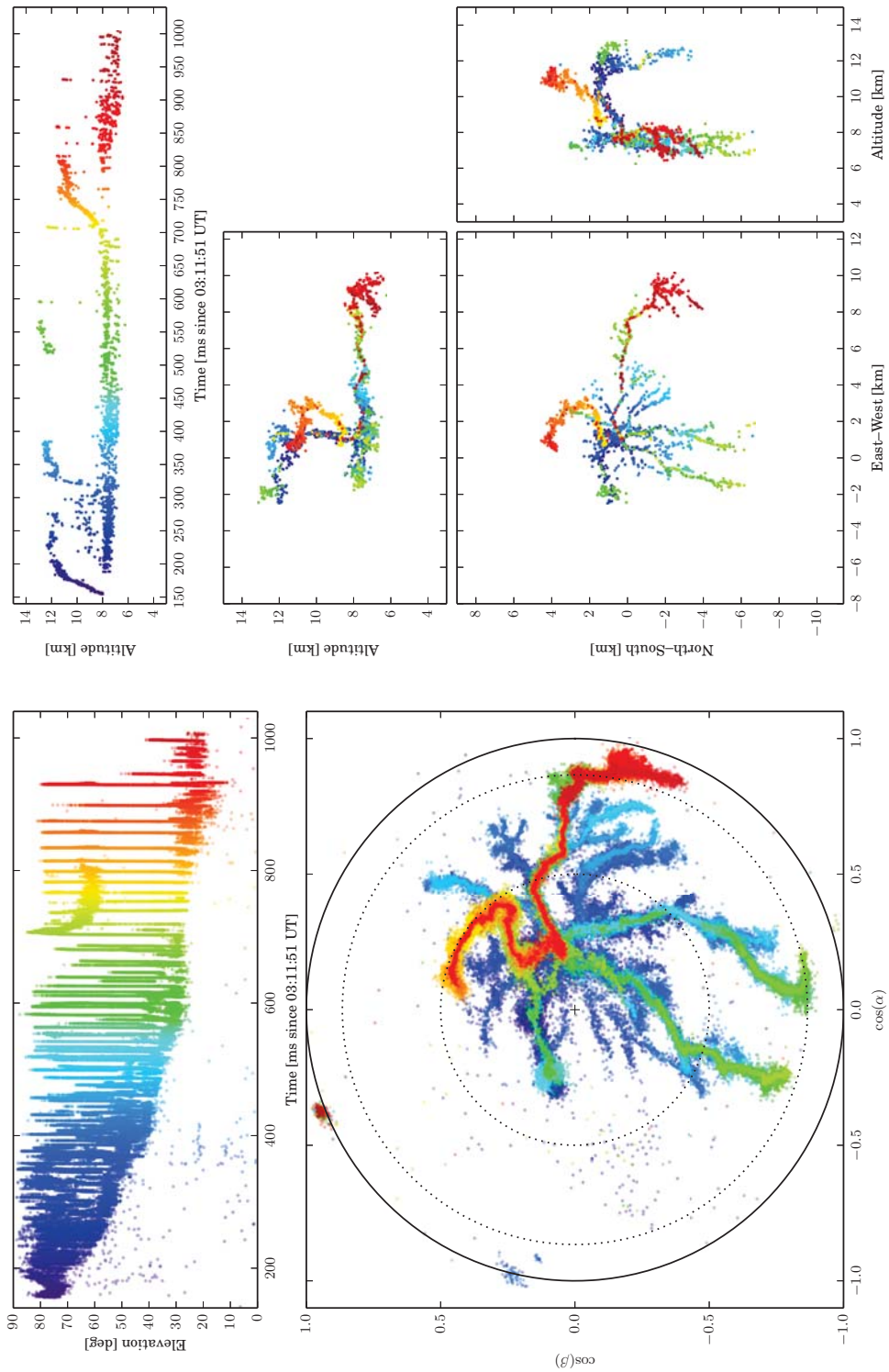
Figure 5.23: Flash F, overview colored by time. Top: LMA map with the same limits as Fig. 5.19. Bottom: Interferometer map.
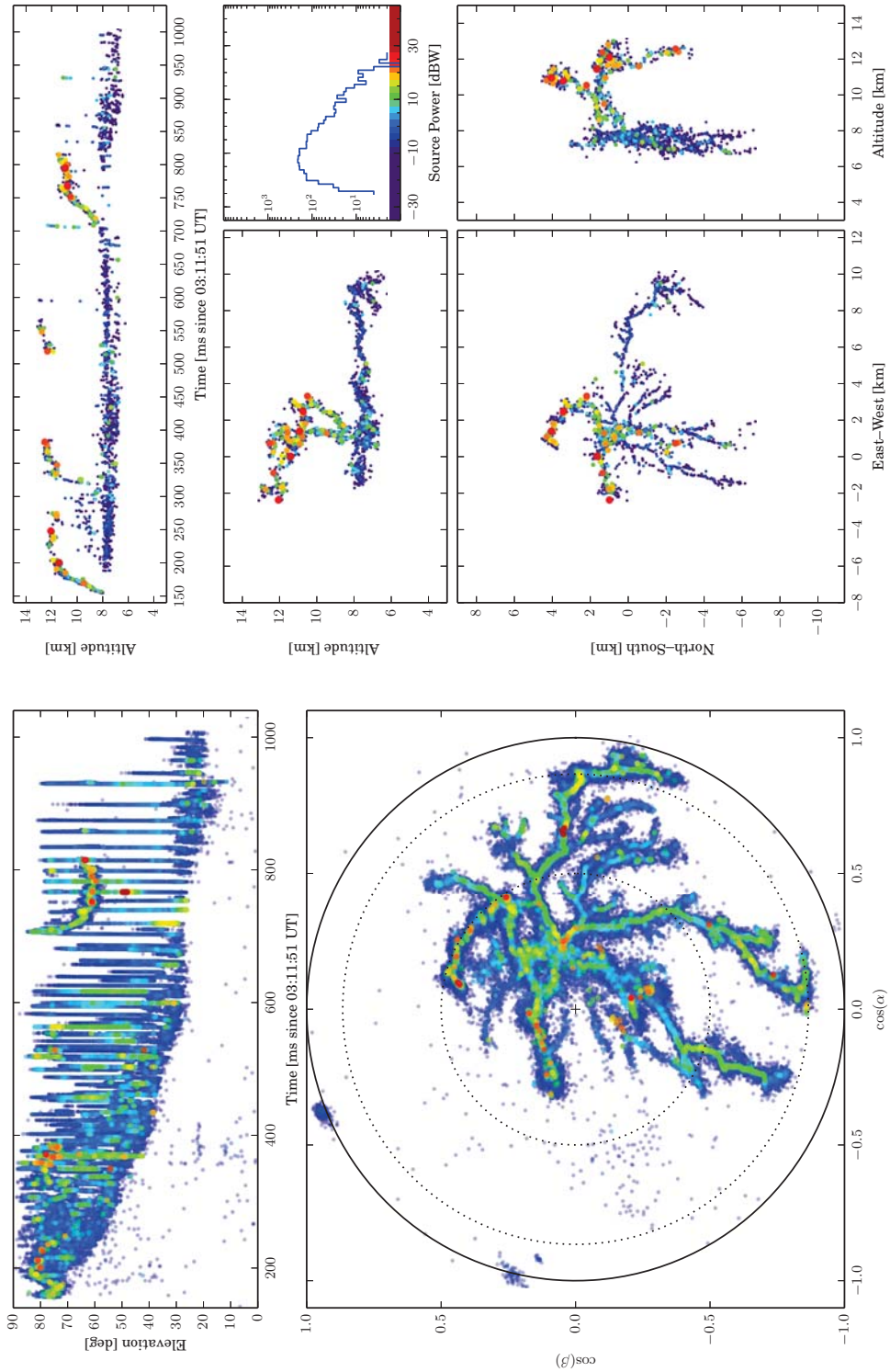
Figure 5.24: Flash F, overview colored by power. Top: LMA map with the same limits as Fig. 5.19. Bottom: Interferometer map.

5.6   Flash A, IC 03:08:11 UT on June 22, 2012

Flash A was used for the initial tuning of the 2 baseline processing technique (Chapter 2), and is featured in Section 7.1 about K-changes.

What follows is an excerpt from *Stock et al.* (2014) reproduced in its entirety, including original figures. A portion of this section refers to an animation that was included with the publication; frames of the animation referred to are included here as figures, but were not included in the original text. The animation in its entirety can be acquired by request from the author.

On June 22, 2012 a storm developed near the mountaintop laboratory from which several lightning flashes were initially recorded. We discuss here a bilevel intracloud flash that occurred at 03:08:10.390 UTC, 6–8 km south and southeast of the mountaintop observatory and interferometer site. The flash time corresponds to the time of its first located LMA source. Due to the lack of pretigger capability in the 2012 measurements, the interferometer recording started 8 ms into the flash. All times for the interferometer data are in milliseconds from the beginning of its record, at 03:08:10.398. Due to the storm occurring early in the 2012 field program, electric field change measurements were not yet being made for the observations.

Figures 5.25 and 5.26 show overviews of the interferometer observations for the flash. The 3-dimensional LMA data are shown in Figure 5.27. The top panel in each figure shows the flash development vs. time, colored according to time (Figure 5.25) and by received power (Figure 5.26). The flash lasted about 600 ms, with the initial 200 ms of activity shown in Figure 5.25b. The dashed circle indicates where the flash initiated. Figure 5.26b shows the source locations in the direction cosine measurement plane, which are projected up onto a unit-diameter hemisphere to obtain the azimuth and elevation locations (equations 2.3 in Chapter 2). The results show the flash approximately as it would be viewed from the interferometer location.

Typical of normal-polarity IC discharges, the flash began with upward negative breakdown (the green sources at the beginning of the flash in Figure 5.27a) into and then developed horizontally through the storm's upper positive charge region (channels A and B of Figure 5.25, corresponding to the red sources in Figure 5.27). This was followed after a delay by slower-developing positive breakdown downward into and through mid-level negative storm charge. The latter activity established lower-elevation branches D,E,F,G, corresponding to the blue sources in Figure 5.27. Whereas the negative breakdown produced only
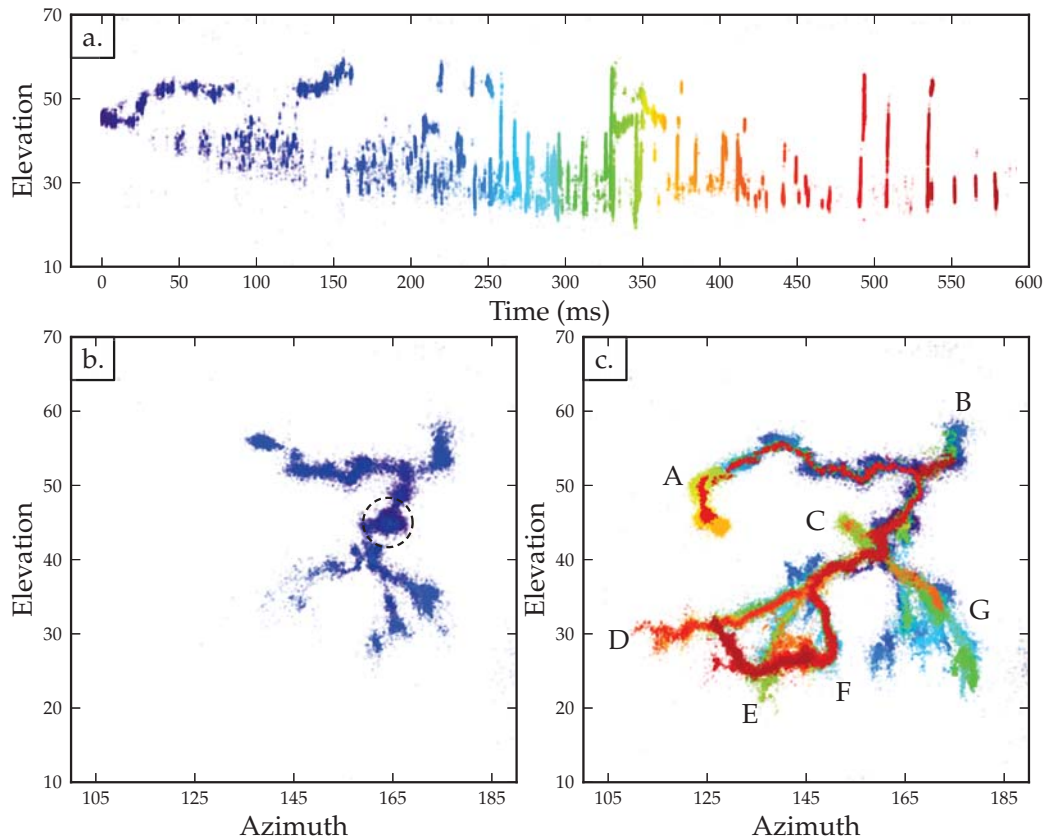
Figure 5.25: Interferometer map of flash A, colored by time. Interferometer observations of a bilevel intracloud flash on June 22, 2012 at 03:08:10 UTC, 8-10 km distant from the interferometer site. a) Elevation angle vs. time; b) azimuth vs. elevation of the sources during the first 200 ms of the interferometer record, c) sources for entire flash. The interferometer record began 8 ms into the flash, and the coloring indicates time. Because the flash was well-oriented with respect to the interferometer, elevation angle primarily indicates altitude. Upper level channels A and B correspond to negative leaders propagating into upper positive storm charge. Lower level channels D,E,F,G are formed by positive breakdown propagating into mid-level negative charge. Channel C is a negative-polarity side-channel that resulted from negative charge temporarily being unable to propagate up the vertical connecting channel, partway into the discharge. The dashed circle indicates the flash origin.

140
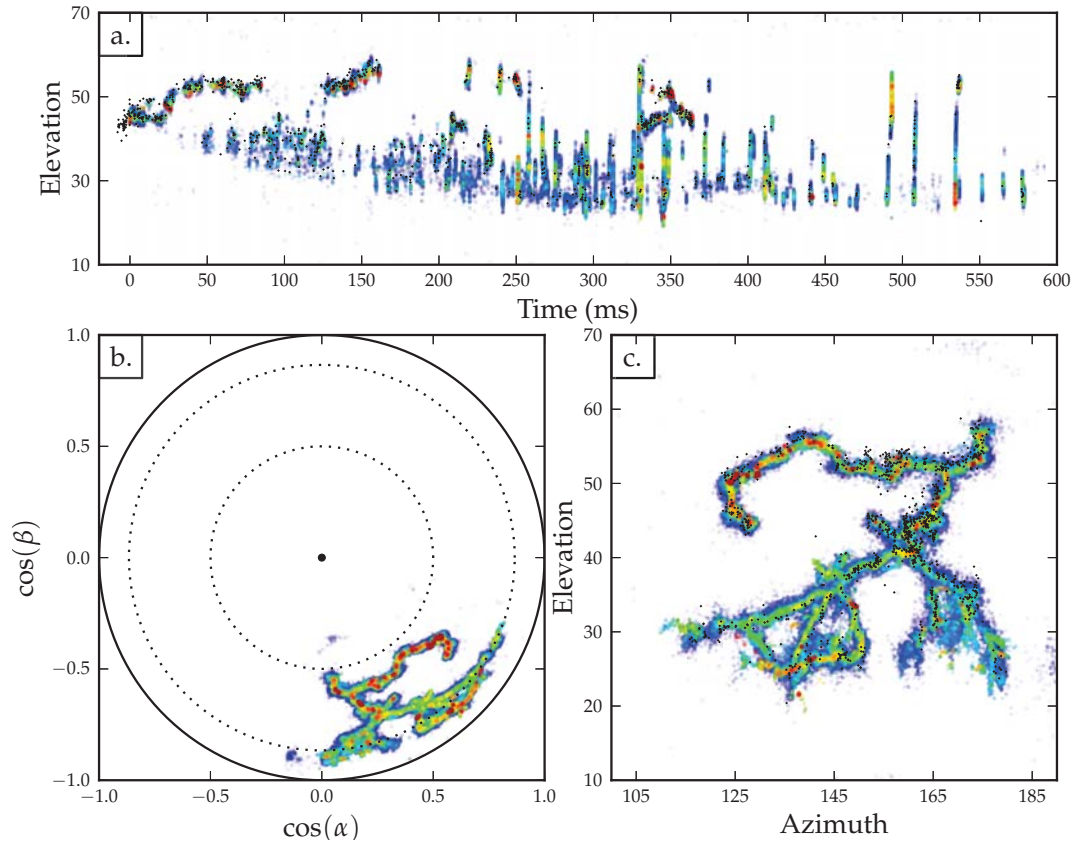
Figure 5.26: Interferometer map of flash A, colored by power. Same as Figure 5.25, except with the sources colored by peak correlation amplitude (power), and showing the sources in the direction cosine plane of the measurements (panel b). LMA observations of the flash are overlaid as small black dots in panels a) and c). The direction cosine plane is equivalent to the phase plane of narrowband measurements. Physically realizable sources lie within the unit circle, corresponding to the transit time constraint at horizontal incidence. The azimuth and elevation results are obtained by projecting the direction cosine locations up onto the unit celestial hemisphere, whose equator corresponds to the unit circle and whose zenith (black dot) is directly above the interferometer (e.g., *Rhodes et al.* (1994)). The dashed circles correspond to 30° and 60° elevation and illustrate how sources at elevation angles below about 30° are located less accurately in elevation than sources at higher elevation (Fig. 4.1b).
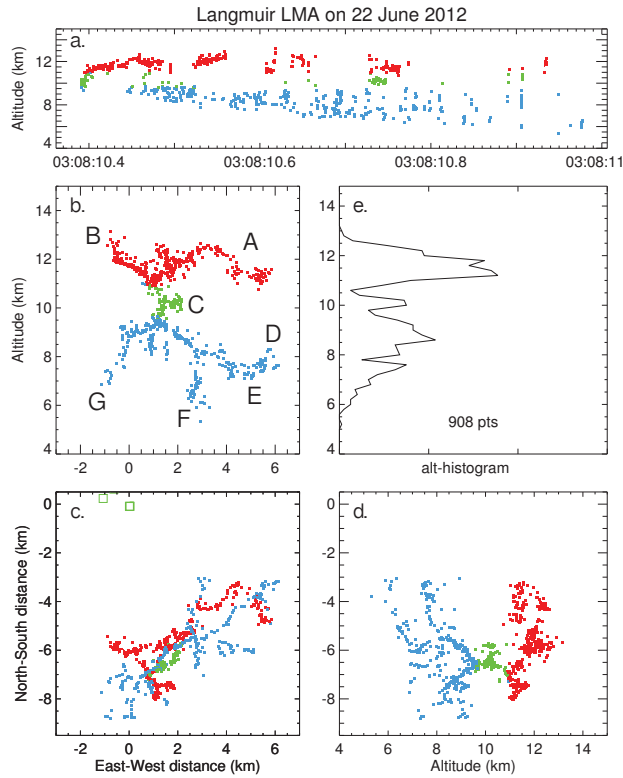
Figure 5.27: LMA map of flash A, colored by charge. Three-dimensional LMA observations of the flash of Figure 5.25. Panel a) shows the source altitudes vs. time and is very similar to the elevation angle vs. time plots of the interferometer maps. Panels c,b,d show the sources in plan view and in E-W and N-S vertical projections. The interferometer was co-located with the upper left-most LMA station (green square) in the plan projection, and viewed the flash approximatly as seen from the back side of the E-W vertical projection. The sources are colored by inferred storm charge, with the red sources being indicative of negative leaders propagating into upper positive charge, and activity associated with positive breakdown in the main negative charge region colored in blue. The green sources show the initial upward negative breakdown that connected the two charge regions. Panel e shows a histogram of the source altitudes.

three leader channels and developed intermittently with time, the positive break-down, once detected, developed continuously and simultaneously along multiple branches and sub-branches until the final stages of the flash (e.g., Figure 5.25a). A prominent feature in the positive breakdown channels are a succession of fast retrograde negative leaders ('K'-events, also referred to as 'recoil' leaders) back along inferred positive leader paths within the negative charge region. The K-events are seen as vertical lines in the elevation/height vs. time panels in both the interferometer and LMA data (figs. 5.25a and 5.27a). For much of the flash, the K activity served to supply additional negative charge into still- or partially-conducting main channels, and from there into the storm's upper positive charge. The retrograde leaders initiated along the farthest few km of the previously detected activity in the positive breakdown region, and tended to cease radiating upon entering main conducting channels. As in the study by *Shao and Krehbiel* (1996), some of the K-leaders radiated along the full extent of the channel, beginning in the middle stages of the flash, but particularly in final stage, indicating that the channel conductivity was decreasingly sustained as the flash matured and neared completion.

Figure 5.26 shows how the LMA sources (small black dots) compare with the interferometer data, both temporally and spatially. The comparison is obtained by transforming the 3D LMA data into the two-dimensional azimuth-elevation coordinates of the interferometer. Although the LMA data was obtained from a minimal number of stations (7), it imaged the lightning discharge in reasonable detail and the results agree exceedingly well between the two sets of observations. This is to be expected, given that both instruments measure the emissions in the lower VHF. Figure 5.26 also illustrates how the negative leader sources have stronger peak power values than those associated with the positive breakdown, consistent with similar findings in LMA observations (e.g. *Thomas et al.*, 2001). The source power differences are seen more clearly in Figure 4.20a.

Partly by coincidence but primarily the result of being a common type of discharge, the example flash of this study was very similar to flash 163057 studied interferometrically by *Shao* (1993) and *Shao and Krehbiel* (1996) in a Florida storm on August 23, 1992. In turn, both are similar to IC flashes during TRIP 1977 at Kennedy Space Center, whose electrical charge transfer was studied in detail by *Krehbiel* (1981). The early charge transfer and interferometer observations have been confirmed and expanded upon by numerous LMA observations since then, and are further expanded upon, substantially so, by the broadband interferometer observations.
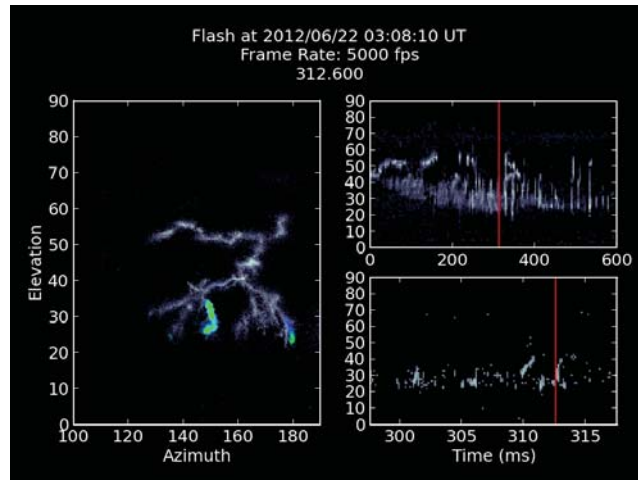
Figure 5.28: Example frame of the animation for flash A. Sample frame from an animation of the interferometer observations, 316 ms into the interferometer record. The full animation is available in the supplement. The lefthand panel shows the flash in the same azimuth-elevation view as Figure 5.25. The light gray background channels show the accumulated prior activity and the colored points indicate the radiation intensity (power) of the current activity, with approximately 10 frames of persistence. The righthand panels show elevation angle vs. time, both for the entire flash and for an expanded time period before and after the current frame. The red lines indicate the time of the current frame. The simulated frame rate (top center) alternates between slow (200 μs/frame) and fast (16 μs/frame) rates during the animation to allow the development of faster moving processes to be seen.

5.6.1 Flash Development

How the flash developed is best seen from animations of the data, an example of which is available in the supplement. Figure 5.28 shows a frame from the animation, 316 ms into the flash. By this time the flash was relatively well developed in both the negative and positive breakdown regions. The light blue-colored sources in the lefthand panel show that simultaneous K activity was occurring back along the far end of the F and G channels, with the gray background indicating the integrated VHF intensity and channel structure up to the frame time. The animation has simulated frame rates of 5,000 and 62,500 frames per second, with the higher frame rate used to show the motion of rapidly propagating events. The results are analogous to high speed video observations of developing lightning channels at optical wavelengths (e.g., *Warner et al.* (2013)), but reveal the activity inside the storm as well as outside. Detailed analyses of the observations of this and other flashes is the subject of ongoing study; in the following we describe selected results from the animation and LMA observations, in addition to the overall features mentioned in the preceding section.

Initial Activity   During the first 10 ms of the flash, the LMA data show that negative breakdown developed upward from the flash start point at 9.6 km altitude, toward and into the upper positive charge region. The leader progressed 1 km vertically to 10.6-10.7 km altitude in the first 8 ms of the flash, corresponding to a speed of 1.2×10^5 m s^{-1}. This speed is typical of the initial leaders of IC flashes (*Behnke et al.*, 2005).

The start of the interferometer record corresponds to the beginning of horizontal development within the upper positive storm charge. During the first
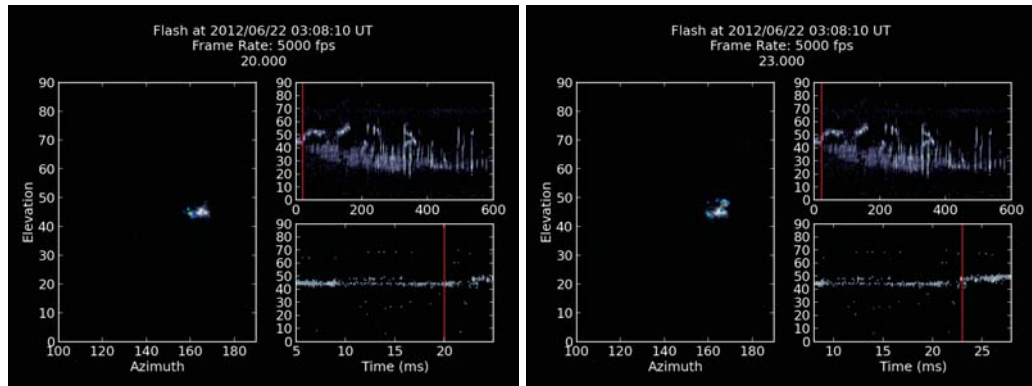
Figure 5.29: Initial development of flash A.
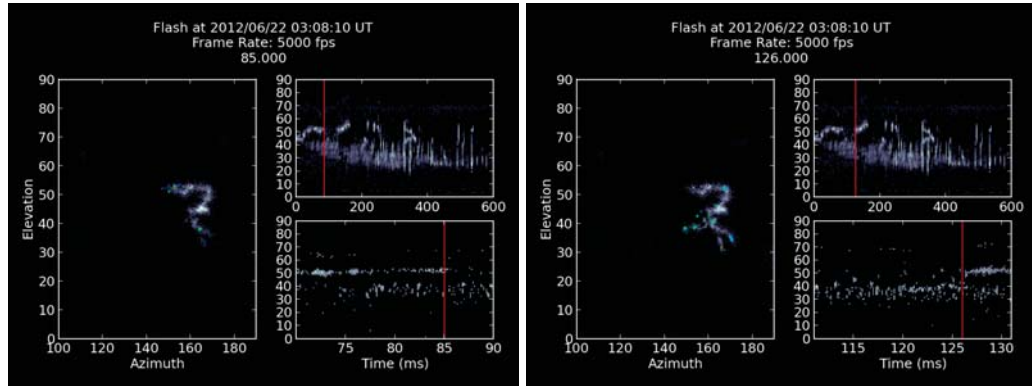
Figure 5.30: RF-quiet interval of flash A.

20 ms of the record the radiation remained localized at about $45°$ elevation and $165°$ azimuth. From the LMA data, the radiation during this time was produced by the beginning segments of two horizontal branches that developed over ~1-km distances toward and away the interferometer, causing the sources to have a stationary appearance in the 2D data. At 23 ms, the closer negative leader turned upward again, establishing the initial part of channel A. Subsequently, channel A developed horizontally, propagating ~4 km northeastward in 64 ms at an estimated average speed of 6×10^4 m s^{-1}, a factor of two slower than the initial upward leader speed. Similar speed decreases were observed in LMA observations of IC flashes by *Behnke et al.* (2005).

Also as in LMA observations of IC flashes, the interferometer data show a delayed onset of detected VHF radiation from downward positive breakdown. The first indicated VHF activity associated with the positive breakdown occurred 23 ms into the interferometer record (31 ms into the flash). The first located LMA source associated with the positive breakdown occurred 24 ms later, 55 ms into the flash. The delay is due in part at least to the weaker positive radiation being masked by stronger radiation from the developing negative breakdown, as found for example by *Edens et al.* (2012). But it may be also be due to the positive breakdown being inherently weak initially, or not immediately occurring. After being detected, the positive activity increased slowly and somewhat randomly with time, revealing a gradually lengthening breakdown path.

Eighty-five milliseconds into the animation, the negative leader temporarily stopped developing. The cessation is readily seen in the height-time panels of both the interferometer and LMA data (figs. 5.25 and 5.27), and gave rise to a relatively RF-quiet interval during which the positive activity was more readily detected. Cessations and intermittent rejuvenations of the negative breakdown are a common feature of LMA observations of IC discharges, and imply that the positive breakdown supplies insufficient charge to keep the negative breakdown
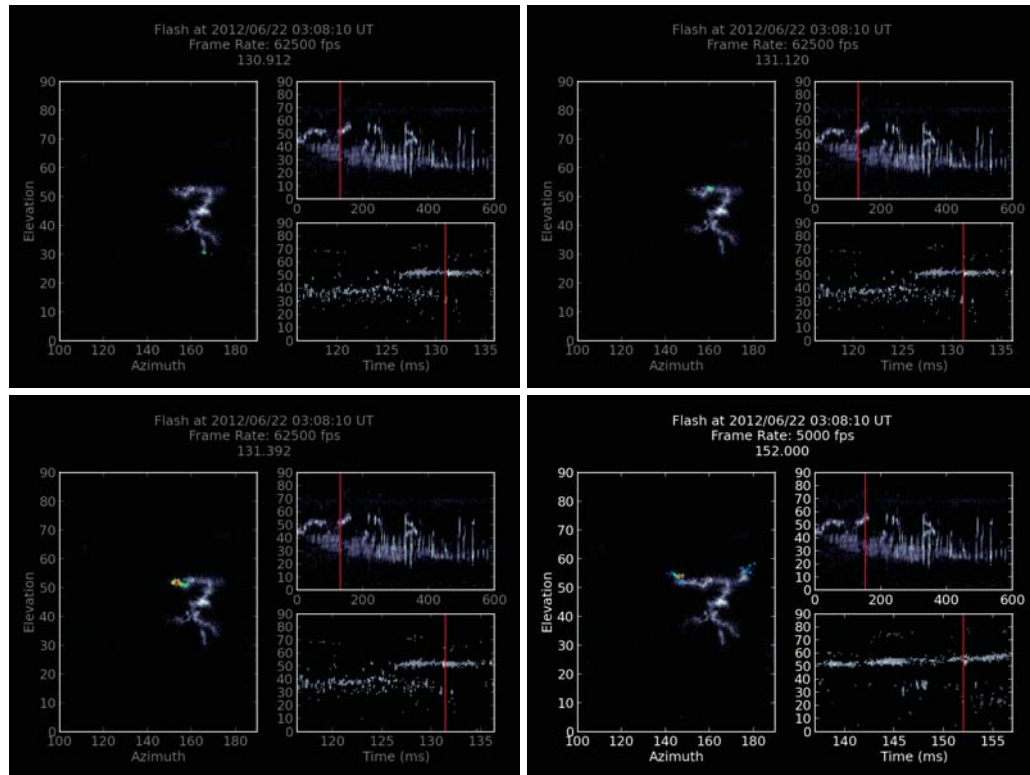
Figure 5.31: Rejuvenation of channel A in flash A.

active. (In this sense intracloud discharges are similar to multistroke negative cloud-to-ground discharges, whose positive breakdown is the same as that of normal polarity IC flashes and favors multiple discrete strokes over continuing currents.) By the time of the initial cessation the positive activity extended the vertical trunk downward and a short distance rightward into the beginning part of channel G. The RF-quiet period lasted 41 ms, up until 126 ms, during which time the positive activity advanced further downward and outward, simultaneously along three fronts – the initial parts of the two main G branches and the start of the lefthand branch D.

At 125.800 ms into the animation, renewed negative breakdown started at the top of the upward trunk in the upper part of the storm, and began establishing negative channel B. Five milliseconds later, at 131.072 ms, negative breakdown began half-way along channel A that re-activated the remainder of that channel and extended it further northeast. The rejuvenation and extension appeared to be initiated by impulsive breakdown 160 μs earlier, at 130.912 ms, at the opposite, positive breakdown end of the flash. The breakdown in question initiated at the far tip of the low-elevation sub-branch of channel G and appeared to propagate back up the branch as a retrograde negative leader and possibly a short distance downward beyond the tip as positive breakdown. Altogether, it

147

is an early instance of a K-type retrograde event rejuvenating and extending the upper level negative leaders. The ensuing extension of channel A lasted 32 ms, ending 163.000 ms into the record and beginning another RF-quiet interval where the positive activity became more detectable.

Positive Breakdown   Development of positive breakdown in the storm's mid-level negative charge region was more complex than that of negative breakdown in the upper positive charge region. Whereas the negative breakdown radiated primarily from its leading edge and advanced intermittently with time between relatively long quiet intervals, the positive breakdown was more continuous and did not have quiet periods. Rather, it produced continual 'flickering' VHF activity quasi-simultaneously along a number of developing sub-branches. The flickering continued over the first 400 ms or so of the flash, with an increasing number of stronger K-events superimposed on it, before gradually dying out in the final stages.

For the first 230 ms or so of the animation, the VHF activity in the positive breakdown region consisted primarily of flickering events that gradually revealed multiple branches and sub-branches of the positive channels. Initially, the flickering tended to be randomly distributed along the developing channels but it increasingly occurred at or ahead of the advancing tips of the detected channels (e.g., at 177.400, 205.616, 214.016, 237.208 ms and numerous other frames). A few events appeared to propagate in a forward direction as positive breakdown (e.g., at 109.400 and 130.960 ms). Superimposed upon this activity was a steadily increasing number of short-length negative retrograde events that further illuminated the developing channels.

At 239.016 ms, negative breakdown reinitated again along channel A, this time back at the beginning of its horizontal channel. The breakdown rejuvenated the extension of channel A yet a second time, in so doing producing VHF radiation along the full length of A. That the leader produced radiation indicates that the channel had become non-conductive sometime during the 76 ms interval since it last appeared to be active. The negative leader that rejuvenated the channel appeared to initiate on its own, with no precursor event detected in the positive breakdown region. Presuming that charge was continually transported into the upper part of the storm during the early stages of the flash, as found in the Florida studies, such charge transfer would have been occurring throughout the 76 ms quiet interval after channel A had died out. The rejuvenating breakdown could have been initiated simply by the increasing accumulation of negative charge at the base of A, rather than by a K event in the positive breakdown region.

148

Advancing Tip
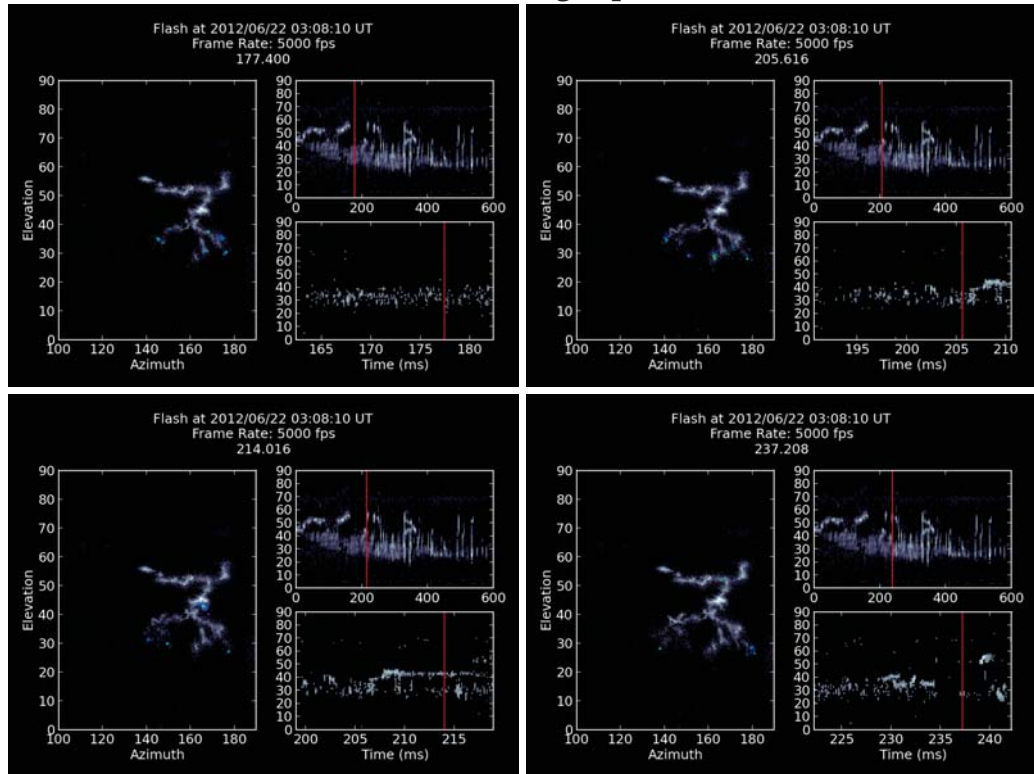
Forward Propagating
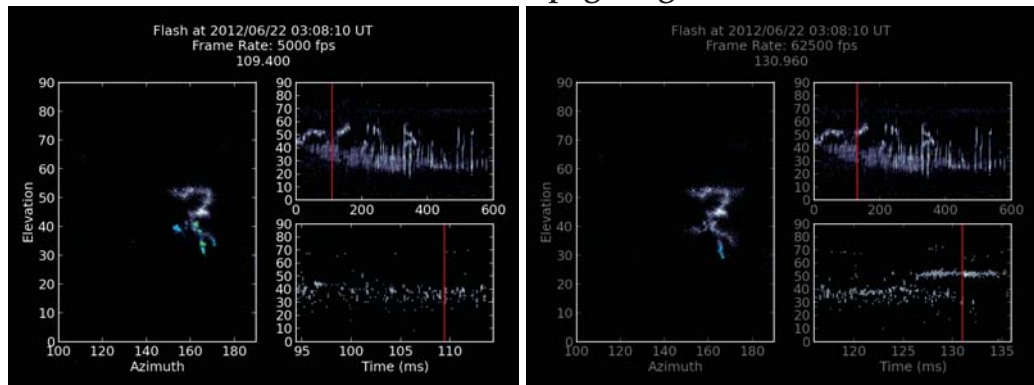
Figure 5.32: Positive breakdown in flash A.
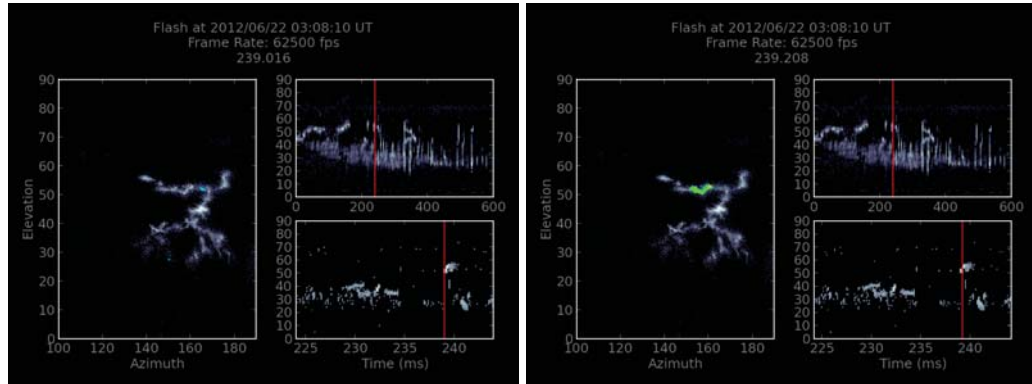
Figure 5.33: Second rejuvenation of channel A in flash A.

More pertinent to the discussion of positive breakdown, within about a millisecond following completion of the upper level rejuvenation and extension, three retrograde negative K events occurred in rapid succession along low-elevation channels at the opposite end of the discharge. The activity began at 240.608 ms in the animation and was more energetic VHF-wise than seen prior to this time. Significantly, the events occurred in branches progressively displaced from right to left within the storm, being initially along two low-elevation sub-branches of channel G and finally along the lower extent of channel F. The activity appears to have been triggered by the A-extension, possibly from a propagating potential wave initiated by effects of the channel extension. A similar apparently triggered event occurred as the extension neared completion, at 239.512 ms. In this case a burst of radiation sources suddenly appeared within a 16 μs time interval a substantial distance away from the low-level channel, where no previous activity had been detected.

Before proceeding, we note that the left-most post-extension K event in the G channel discussed above, at 240.808 ms, had the shape of an inverted 'V'. This resulted from the breakdown initially propagating as a retrograde leader up the sub-branch on the right and, upon reaching the bifurcation point with an adjacent sub-channel, sharply reversing directions and propagating in a forward, 'prograde' direction back down the adjacent channel on the left. Such V-shaped events are a common feature of high speed optical observations of positive leaders (e.g. *Saba et al.*, 2008; *Warner*, 2012). It has also been observed at VHF by *Edens et al.* (2012) in connection with LMA observations of rocket-triggered lightning. Rather than switching from negative to positive breakdown, the leader continued to be of negative polarity and therefore would have transferred negative charge from the right to the left sub-branch.
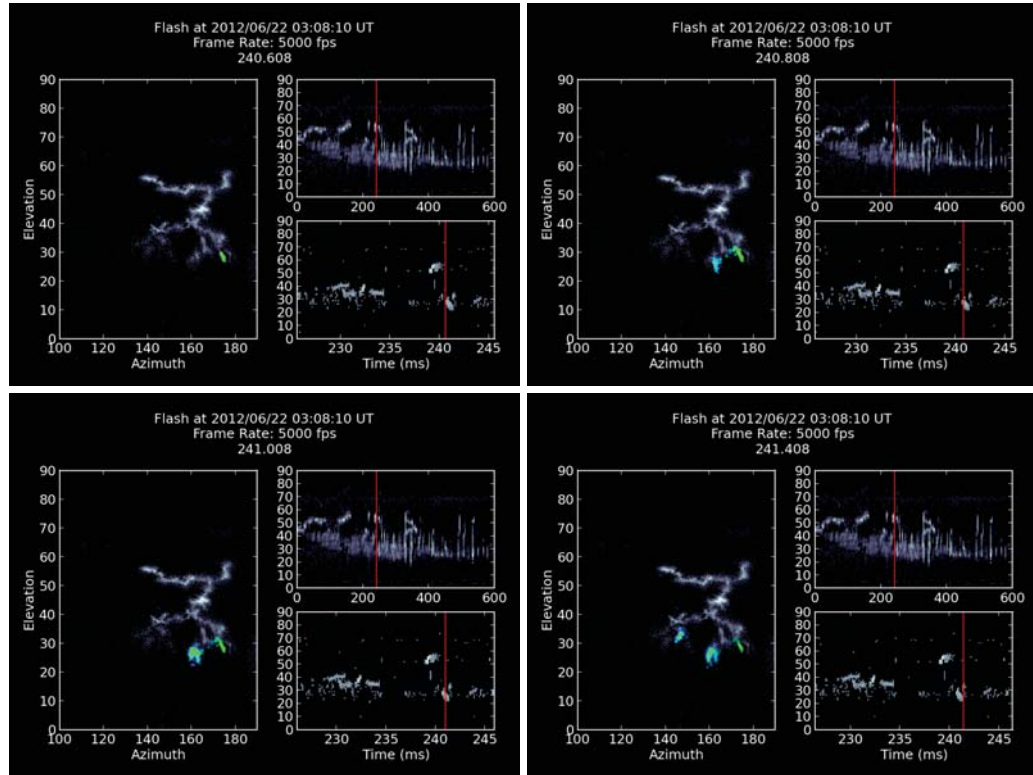
Figure 5.34: A sequence of K-changes in flash A.

Strong Positive Bursts The above activity was followed by continued flickering and channel development along the low-elevation channels, accompanied by further extension of the upper-level A channel. Then, beginning at 250.400 ms, two exceptionally bright (red-colored) VHF events occurred in quick succession off the far end of the right-most G branch, 80 μs apart in time. Each appeared to be associated with positive breakdown away from the developing channel. Another pair of bursts occurred about 1 ms later, beginning at 251.488 ms in a nearby sub-branch, that appeared to initiate positive breakdown in two different directions away from their starting point. We call these events 'strong positive bursts'. The cause of the two pairs of events is not clear, but their occurrence is indicative of some sort of strong potential disturbance.

Other positive bursts occurred at 328.840, 345.216, 348.416, 410.680, and 533.584 ms in the animation. The first two bursts occurred 17 ms apart in time in adjacent sub-branches at the far end of the low-level channel E. In both instances retrograde negative breakdown started at the bifurcation point of the two sub-branches, well back from their tips. The breakdown propagated as a retrograde negative leader back up the E channel toward and into channel D. For the first event, the positive burst occurred at the far end of the lefthand branch, within a few tens of μs of the leader appearing to reach the junction point with D. A

151
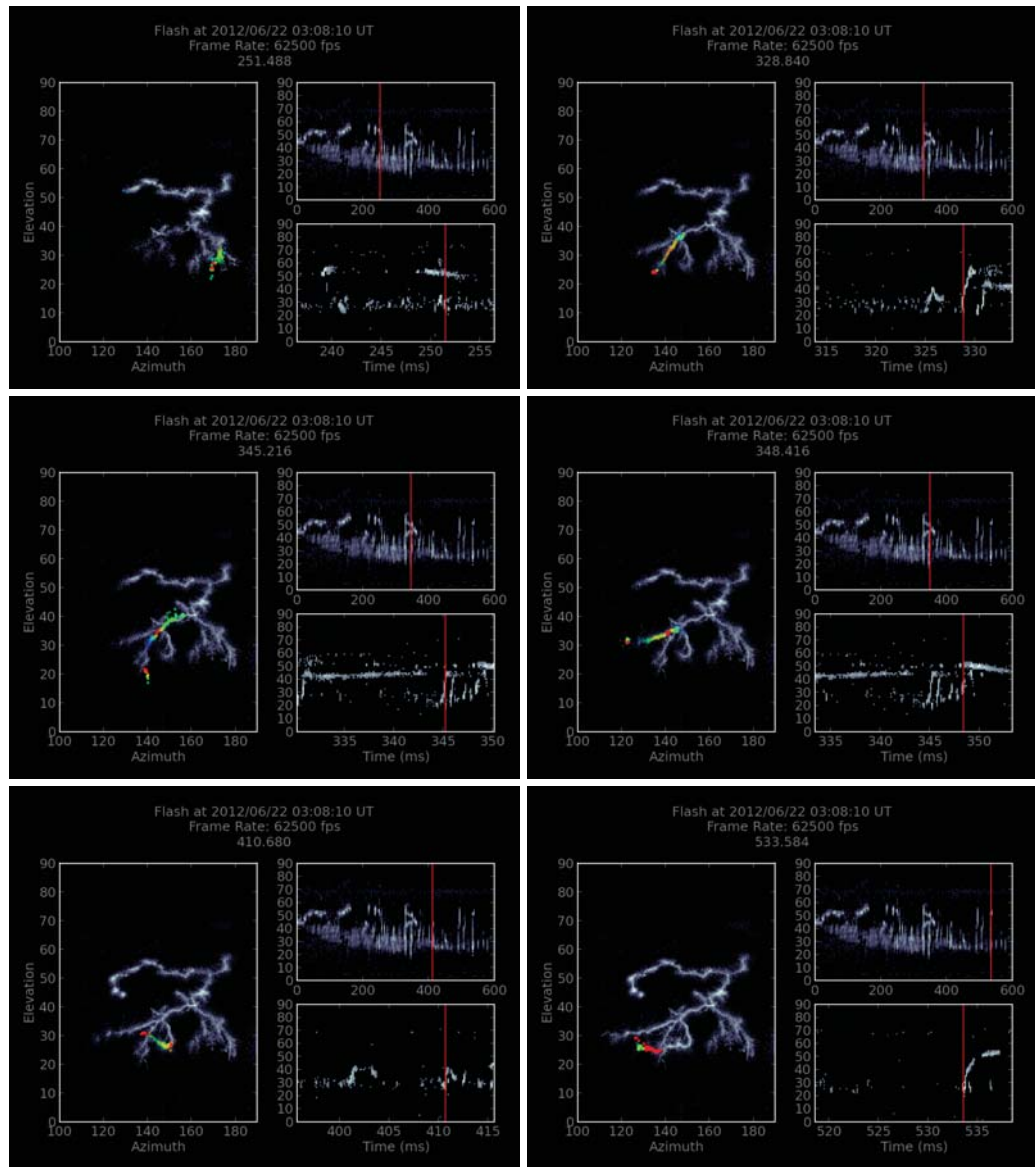
Figure 5.35: Examples of positive bursts in flash A.

similar sequence of events occurred for the second burst, except that the burst followed a sudden increase in the VHF radiation by the leader as it neared the D channel, presumed to be indicative of actually connecting with D. The positive burst occurred at the far end of the right-most sub-branch, two frames (32 μs) after the leader intensification. In both cases, the bursts appear to have occurred as a result of channel D having a significantly different electric potential than that of the retrograde leader, and that this caused a potential wave to travel in a forward direction down the respective sub-branches, producing the positive burst at their far end.

The third positive burst, at 348.416 ms, occurred off the end of the left-most D channel, again in the lower part of the storm. It was similar to the above E-bursts in that it appeared to be initiated by retrograde negative breakdown reaching a junction point on the main D channel. Like the second of the two E-events, its retrograde leader brightened substantially upon nearing the apparent branch point. The burst occurred 32-48 μs after the brightening, beyond the starting point of the retrograde leader. The event differed from the E-channel events in that the retrograde breakdown (at 348.272 and 348.304 ms) was immediately accompanied by oppositely directed, weaker breakdown laterally away from the channel tip. In addition, three distinct bright sources occurred well beyond the leader start point and burst location as the leader immediately prior to the leader intensification.

Each of the three burst events discussed above were part of a sequence of energetic K events that originated in the lower left side of the storm. In each case the leader went on to propagate into the upper or mid-storm level, along the full extent of the A, B, or C upper negative channels. The final two bursts, at 410.680 and 533.584 ms, also originated in the lower left part of the storm, at the far end of channel F. Without going into the details, it can be seen from the animation that the event at 410 ms was basically the same as the events at 325 and 348 ms, except that the positive burst occurred back at the tip of a slightly different, adjacent sub-branch rather than the branch of the retrograde inception. Upon arriving in the trunk region, a weaker positive burst was initiated along yet another slightly different sub-branch back at far start region. Again, the weaker burst was delayed by some tens of microseconds from the leader reaching the trunk base, indicating that it also resulted from a forward potential wave caused by attachment to a conducting channel.

We note that delayed VHF bursts back at the starting point of K events were also observed by *Shao et al.* (1995) (their figures 22 through 24). The K events occurred in the late stages of a negative cloud-to-ground flash, but the positive breakdown processes and K activity for $-$CG flashes are essentially the same as for normal-polarity IC flashes. The bursts occurred at a high elevation angle and relatively close to the interferometer, so that the propagation direction of
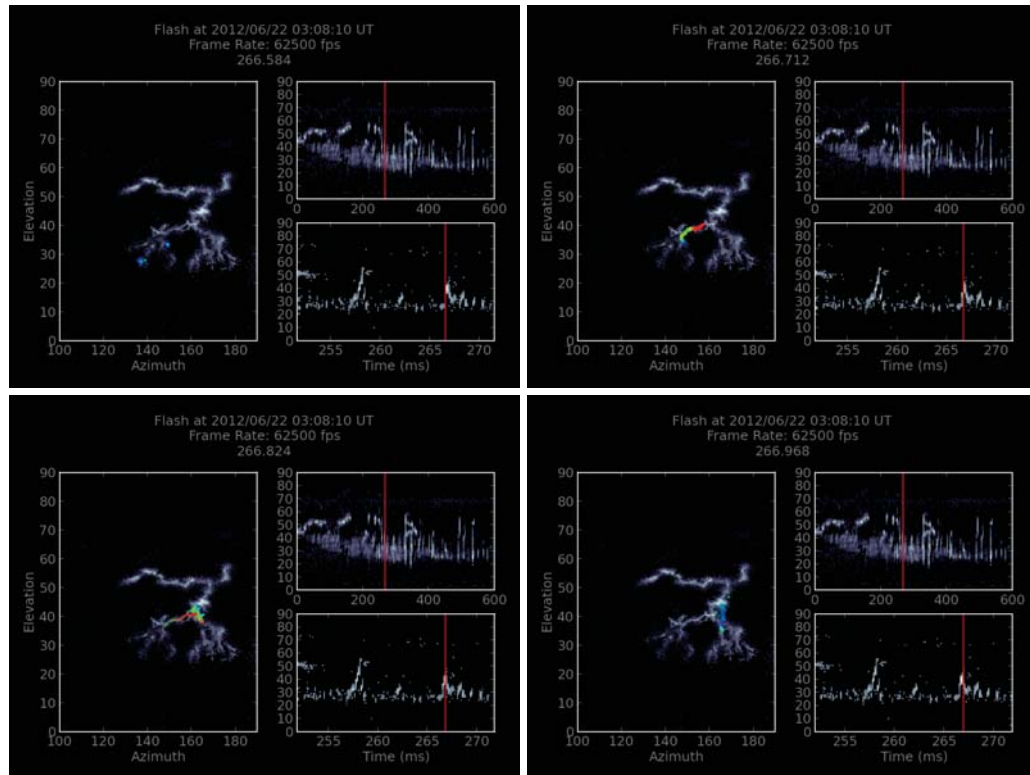
Figure 5.36: A horizontal charge transfer in flash A.

the bursts was readily detected. They were found to correspond to fast positive breakdown in the opposite direction away from the starting point of the negative K leader. Their VHF radiation was brief and also exceptionally strong, even at the upper VHF frequency of the measurements (274 MHz; events 'b' of their figures 22 and 23). The bursts occurred immediately adjacent to the K-leader inception point, rather than at a distance as in the present observations, but are otherwise similar to the present results.

Horizontal Charge Transfer Events   At 266.584 ms retrograde negative breakdown initiated partway down the beginning part of the F branch on the lefthand side of the flash. The breakdown propagated a short distance into and back up along the main D channel to its bifurcation point with channel G, whose branches connected into the righthand side of the storm. The K leader arrived at the bifurcation point 192 μs after being initiated, at 266.776 ms in the animation. From there it split in two directions, with one branch continuing upward along the trunk into the flash initiation region, and the other propagating in a forward direction down the left-most G channel on the lower right side of the storm. As in

154
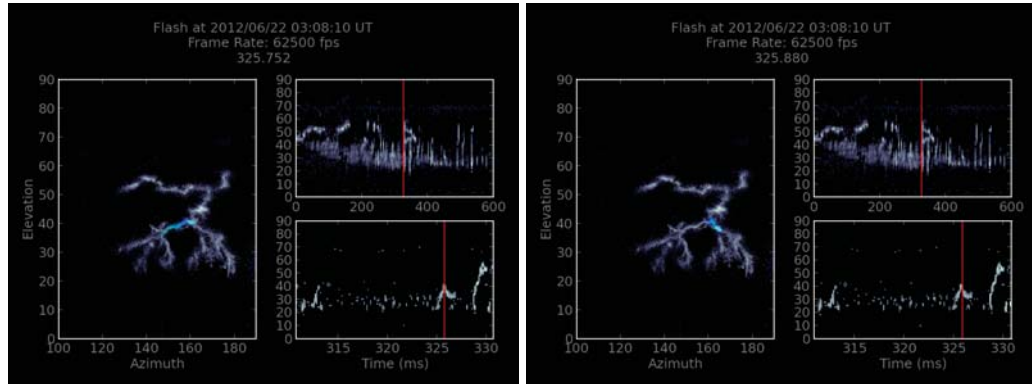
Figure 5.37: Horizontal charge transfer event K-1 of flash A.

the case of the inverted 'V' event discussed above, the downward G breakdown continued to be of negative polarity and therefore transported negative charge from the lefthand side of the storm to the righthand side, all within the storm's main negative charge region. Similar left-to-right K discharges occurred at 295, 326, 401-403, and 410 ms in the interferometer observations, along with an earlier, somewhat weaker event at 229 ms.

The occurrence of the horizontal cross-discharging is a new finding of VHF observations for otherwise vertical IC flashes. It indicates the development of a lateral charge imbalance in the storm produced by the discharge itself. In particular, the imbalance appears to result from excess positive charge being induced in the righthand side of the storm's negative charge region early in the flash, where the G channels initially produced most of the discharging, and by the excess charge subsequently being stranded there by channel cutoff processes. The D→G breakdown can thus be considered as a charge redistribution event that reduced the imbalance. The observations are consistent with charge transfer results for a similar IC flash in a Florida storm by *Krehbiel* (1981) (Flash 49), where dominant vertical charge transfer later became horizontal within the negative charge region.

Other instances of negative breakdown propagating in the forward direction along positive channels are seen in the interferometer observations, although less well-resolved than the above large scale activity. In these cases, the discharges have a characteristic, sharply-pointed 'V' or forked appearance, discussed above in connection with the K-activity at 241 ms. Other examples of this type of activity are listed in Table 5.2. The events can be considered as charge redistribution or potential equalization activity on a more local scale.

155

Name	Time (ms)	Channels	Duration (μs)	Length (km)	Velocity (m/μs)
	131.1	A	336	–	–
	202.4	D	512	–	–
	231.9	D	224	–	–
	229.0[2]	D-G	–	–	–
	239.0	A	919	6.50	7.06
	240.8[2]	G	–	–	–
	250.4[1]	G	–	–	–
	251.4[1]	G	–	–	–
	257.2	D-B	911	7.04	7.73
	261.9	G	342	4.54	13.24
	266.6[2]	F-G	737	5.61	7.60
	268.1	D	346	2.06	5.96
	275.2	F	506	4.64	9.16
	291.7	G	778	3.51	4.51
	293.4	G	478	4.05	8.46
	295.0[2]	D-G	1295	11.24	8.68
	309.9	D	849	3.46	4.07
K-1	325.3[2]	D-G	1071	8.46	7.89
K-2	328.5[1]	E-A	1401	16.71	11.92
K-3	330.2	E	176	–	–
K-4	330.7	F	160	–	–
K-5	344.7[1]	F-C	670	6.16	9.18
K-6	345.7[1]	E	265	4.76	17.89
K-7	347.0	F	206	3.67	17.76
K-8	348.3	D	335	3.82	11.41
	371.6	D	670	5.81	8.66
	383.4	D	603	5.86	9.72
	400.8[2]	D-E	688	6.05	8.78
	403.2[2]	G	462	1.56	3.37
	410.3[12]	F	608	–	–
	412.4	D	256	–	–
	439.9	F	513	4.51	8.80
	448.4	D	412	4.07	9.85
	454.8[2]	D	418	2.85	6.80
	489.6[2]	F	969	7.00	7.21
	492.2	A	897	11.97	13.33
	506.9	F-C	1550	12.01	7.75
	533.5[1]	F-C	1252	11.94	9.53
	577.0	F	1216	–	–

Table 5.2: Summary of K-leaders longer than 200 μs duration, and other activity. Length and average velocity are reported for leaders whose quasi-3D channels were well-fitted.
[1]Positive Bursts
[2]Horizontal Charge Transfer Events

K Activity   As indicated earlier, negative polarity K events were a prominent and characteristic feature in the activity in the positive breakdown region. The activity took the form of a succession of retrograde negative leaders back along the inferred paths of the positive breakdown, and were undoubtedly a controlling factor in the flash development. The K leaders connected into and rejuvenated previously conducting main channels, thereby continuing to supply negative charge into the upper positive storm levels.

Table 5.2 lists the times, durations, and channel lengths of 33 negative K leaders whose VHF radiation lasted longer than a nominal value of 200 μs. The channel lengths are estimated 3D values obtained by expanding the 2D interferometer observations to quasi-3D results utilizing the LMA observations (Section 4.4). The estimated lengths range from about 2 km to 17 km, with the lengths of five events exceeding 10 km. As can be seen from the animation, many more K events occurred that were of shorter duration, including ones whose propagation was not resolved by the observations but can be inferred from the number and strength of their radiation sources. Many of the K-leaders were physically and temporally short because they contacted a conducting main channel, whereupon the radiation weakened or ceased.

Figure 5.38 shows observations of the extensive K event that occurred between 328 and 330 ms (labeled K-2 in table 5.2), whose initiation was discussed in the previous section on positive bursts. In particular, the event began with retrograde negative breakdown being initiated at the bifurcation point of two low-elevation sub-branches of channel E, and produced a strong positive burst at and beyond the far end of the left sub-branch (panel b of Figure 5.38). The burst is seen in the animation at 328.840 ms and appeared to occur a short time after the leader reached the main D channel. The sources are also seen in panel c) of Figure 5.38 as the high amplitude sources seen just beyond the region of leader inception. Preceding the leader by $\simeq$600 μs were two impulsive LMA events (shown in grey), whose locations coincided perfectly with the initiation point of the K-leader. Close to the same time, the interferometer located a cluster of low intensity sources slightly further down the E channel, at the location of the positive burst. The interferometer sources are obscured in the figure by the LMA symbols but can be seen in the animation. Panel d) of the figure shows the estimated 3D length and propagation velocity of the leader with time. The results illustrate what is also seen in the animation, namely that the leader propagated smoothly through the junction with D and along the full length of the flash to the far end of the upper-level A channel, at an average speed of about 1×10^7 m/s. As will be seen later, the speed decrease at the beginning the leader (from 2-3 $\times 10^7$ m/s down to $\simeq 1 \times 10^7$ m/s) is a statistically significant result when averaged over the different K-events of Table 5.2
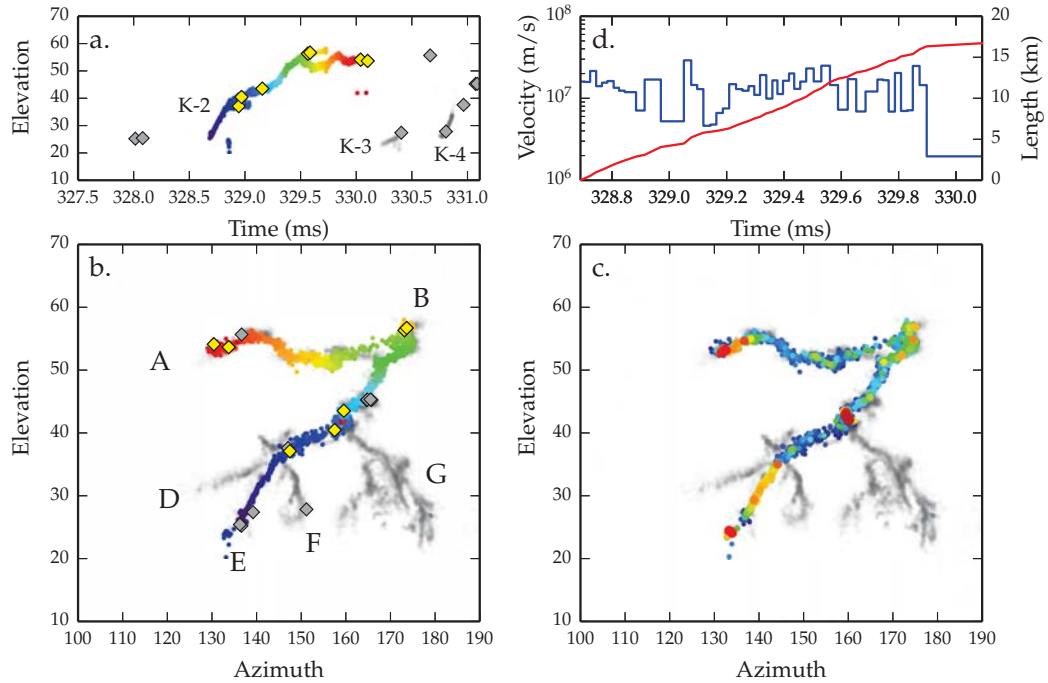
Figure 5.38: Extensive K event (K-2) at 328 ms in flash A. Figure shows the sources colored by time (a,b) and by radiation intensity (c). The intensity graph shows the occurrence of the strong positive burst beyond the starting point of the upward K-leader at the far end of channel E, and of two other strong bursts at the middle and far upper end of the negative leader. Seven LMA sources were located during the event (yellow diamonds) that are in excellent agreement with the interferometer observations, both temporally and spatially. Panel d) shows the estimated length and propagation velocity of the K-leader vs. time, obtained from the 3-dimensional reconstruction of the flash discussed in Sections 4.4 and shown in Figure 4.19. The gray LMA sources and interferometer channels show activity associated with events K-3 and K-4, and precursor activity prior to K-2 (see text).
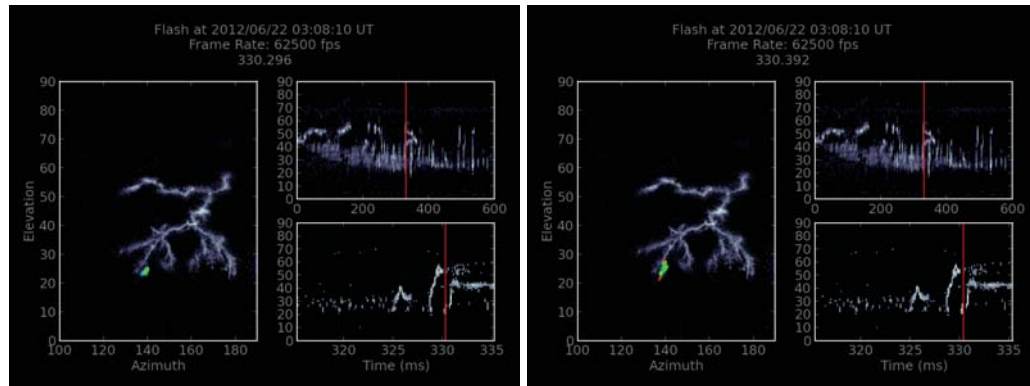
Figure 5.39: K-3 of flash A.

As mentioned previously, the above K-event was the second in a series (or 'swarm') of eight energetic K events between 325 and 350 ms and that originated in the lower left part of the storm. The K-events are identified as K-1 through K-8 in table 5.2. The first event, K-1, was confined to the lower-level channels and transferred negative charge from the left-most extremity of the D channel horizontally across to the G channels on the right side of the storm. This happened in the same manner as the horizontal charge transfer K-event at 266 ms discussed earlier – namely as retrograde negative breakdown up to the bifurcation point of channels D and G and then in a forward or prograde direction down the G channels. Having presumably neutralized a lateral charge imbalance between the two regions of lightning activity, the energetic K-2 event developed directly through the D-G bifurcaton point, ignoring channel G, along the upward connecting channel and into the upper positive charge region, where it traveled along the full extent of both the B and A channels.

Within 130 μs of K-2 dying out at the far end of channel A, new K breakdown (K-3) commenced at the opposite end of the flash, this time at the far tip of the righthand sub-branch of E, adjacent to the sub-branch involved at the beginning of K-2. K-3, seen starting at 330.216 ms in the animation and also as the minimally extensive interferometer sources in Figure 5.38a, propagated up to the bifurcation point of the two sub-branches, where its arrival was heralded by an impulsive LMA event. Shortly afterwards, at 330.376 ms, a strong positive burst occurred back at the inception point, presumably as a result of the K-leader having connected into the still conducting channel of the preceding strong K-event. This was followed in the next 16 μs frame by a strong VHF pulse at the bifurcation point, after which the VHF activity ceased. The entire event lasted 176 μs and is an excellent example of a K event whose VHF radiation was 'abbreviated', apparently by connecting into a conducting channel. A full understanding of such events requires fast electric field change observations and is the subject of continued study.
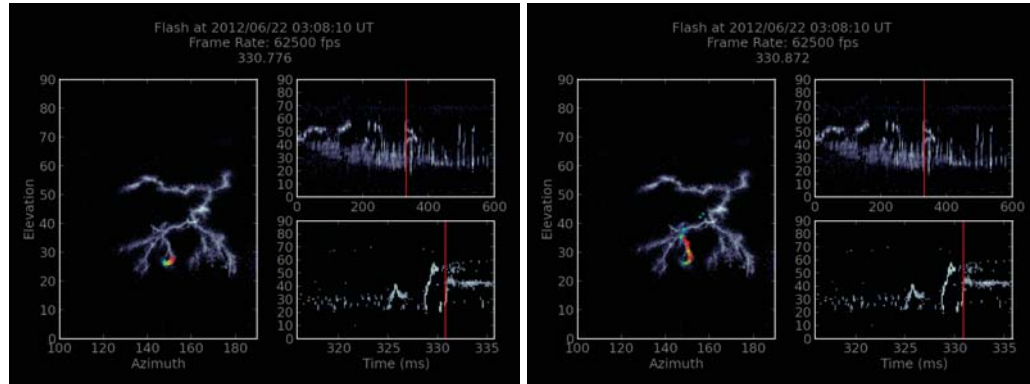
Figure 5.40: K-4 of flash A.

Immediately following K-3 (and possibly even as a result of it), the next major K event, K-4, began at 330.728 ms at the far end of channel F. In this case, and as seen in Figure 5.38a, an impulsive LMA source was detected at the very beginning of the K-leader, well co-located with the leader initiation point. As a result of occurring within 0.6 ms of K-2, and while the main channels were presumably at least partially conducting, VHF radiation from K-4 leader was sparsely detected along the main D, apparently indicating that D was at least still partially conducting. Sufficient radiation was produced to indicate that the leader traveled to the far upper extent of channel B, but apparently not into channel A. Rather, at the same time that activity ceased in channel B, at 331.288 ms, lateral breakdown activity began lower down along the mid-right side of the upward trunk, indicating the forging of new negative channels there. The lateral breakdown continued for about 1.1 ms until, at 332.408 ms, breakdown activity also started a bit further down the main trunk that formed the negative-polarity side channel C. Development of the C channel was relatively slow, requiring 10 ms to progress on the order of one kilometer distance, corresponding to a speed of $\simeq 10^5$ m/s – typical of negative breakdown into virgin air.

Formation of channel C ended at about 342.608 ms. 0.8 ms later, at 343.208 ms, weak breakdown began at the tip of the complex branch structure at the far end of the E channel that initiated brighter breakdown in a forward, positive-polarity direction into apparently virgin air, out to well beyond the tip. The positive breakdown occurred in parts of two frames, at 344.208 and 344.408 ms, before dying out. It effectively extended the detected F channel on the order of a couple hundred meters, finishing at about 344.408 ms. Subsequently, at 344.752 ms, a negative K-leader, K-5, initiated back at the starting point of the positive breakdown that propagated as a retrograde negative leader back up the E channel. The leader arrived at the junction with channel F at 345.168 ms, producing strong VHF radiation apparently just before arriving at the junction and continuing on through it. 32 μs after the strong radiation near the F junction, at 345.200 and
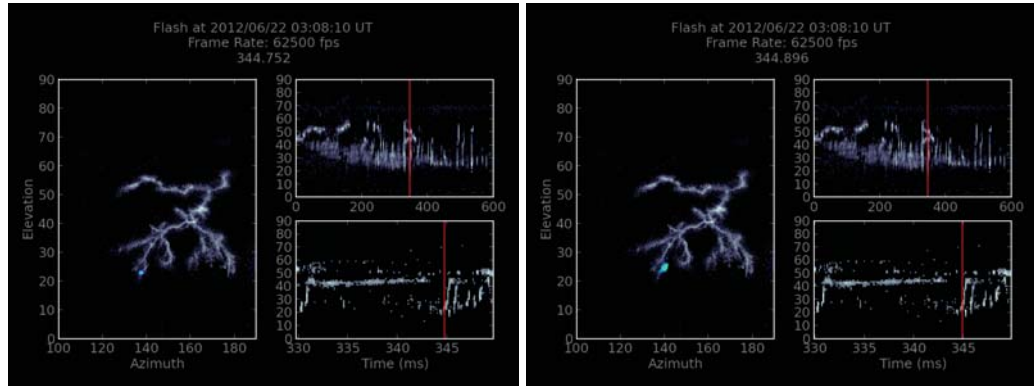
Figure 5.41: K-5 of flash A.

345.216 ms, a clear, strong positive burst and forward leader developed into virgin air in a slightly different divergent direction than the earlier positive leader at 344.2 ms. This is the second of three positive bursts discussed in the strong positive burst section. The path of this breakdown resembled that of electric field lines converging onto the tip of an elongated conductor. By the time of the second positive channel extension the K-leader was propagating in the main D channel, where it produced two weak, side extensions laterally away from D, seen at 345.200 and 355.216 ms in the animation. Upon arriving in the vicinity of channel C, instead of continuing on up the vertical connecting channel it turned into C and propagated laterally out along the C's full extent, ending at about 345.552 ms.

A strawman interpretation of the above activity, namely the formation of channel C and the diversion of K-5 into C, resulted from the upward channel above the flash initiation point becoming cut off by negative resistance effects and consequently 'filling up' with negative charge still trying to reach the positive charge region, thereby forcing K-4 to produce channel C and K-5 to be diverted
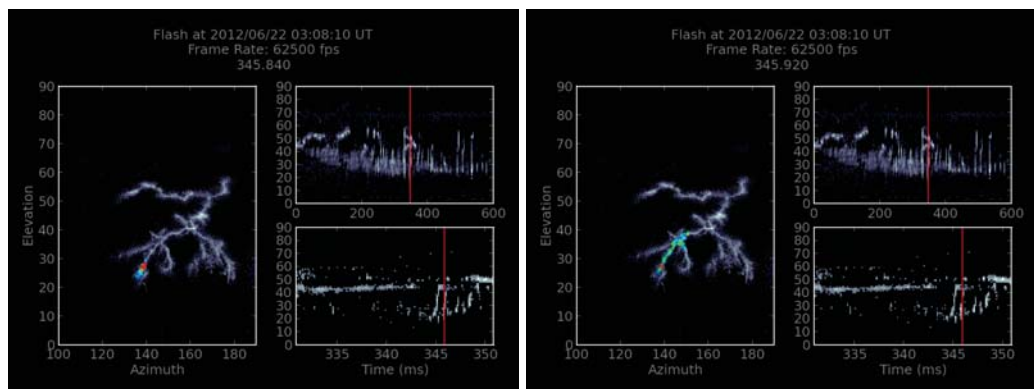
Figure 5.42: K-6 of flash A.
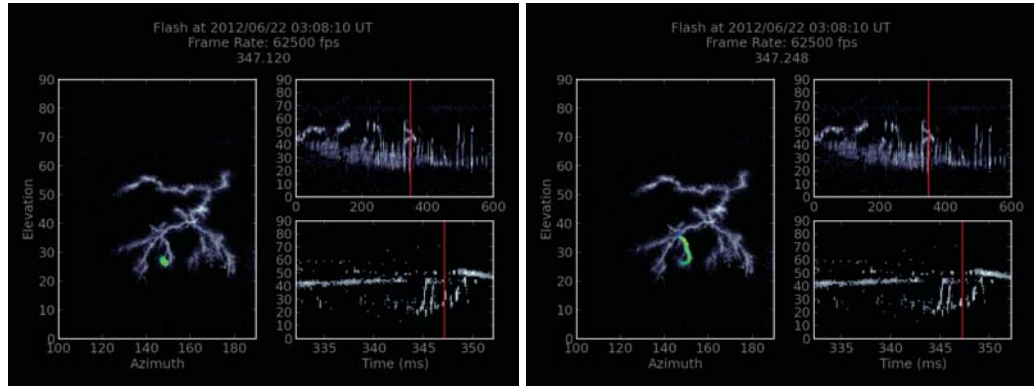
Figure 5.43: K-7 of flash A.

into C. This interpretation is probably questionable, as K-5 was immediately followed 1.0 ms later, at 345.776 ms, by K-6, that did not radiate along any of the upward channel or along the full length of A, but may have been the cause of a brief burst of VHF radiation 380 μs later, at 346.160 ms, beyond the far end of channel A. If the cause, the channels were likely fully conducting, in which case some other explanation is required for the channel C activity.

The above examples illustrate the kind of detailed information that is contained in the interferometer and LMA observations. Of particular note is the excellent agreement and complementary nature of the interferometer and LMA data.
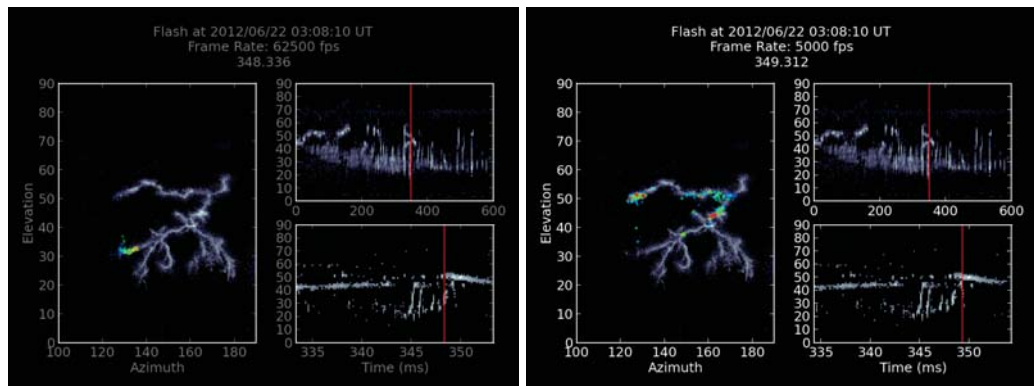
Figure 5.44: K-8 of flash A.

CHAPTER 6

SLOW PROCESSES

This chapter briefly covers the large topic of the behavior of normal leader propagation, that is the behavior of the stepped negative leader and the un-stepped positive leader. These leaders are slow processes in that (with few exceptions) they propagate at less than 10^6 m/s, whereas the processes discussed in Chapter 7 propagate much faster than this. In some cases, the leaders propagate in regions of extremely high electric fields, and in others the presence of the leader is enough to enhance the electric field ahead of it to allow continuing propagation outside of a storm. In addition, the negative leader propagates in fits and starts, while conversely the positive leader propagates relatively smoothly. As a result, the interferometer and electric field records for these slow processes are extremely varied.

The broadband interferometer has proven to be an ideal instrument for studying these leaders as they propagate through the cloud. The sensitivity of the instrument is sufficient to see faint negative streamer emission, as well as emission from the positive breakdown region. The accuracy of the images is also very good, such that the resulting maps appear analogous to the frames provided by high-speed video. However, optical and radio measurements are not the same; one of the chief differences is that radio observations of leader propagation are not obscured by the parent storm cloud, where as optical measurements are. The results presented in this chapter, while fascinating, are extremely preliminary.

6.0.1 Primary Novel Techniques/Findings

- Preliminary breakdown pulses appear to simply be negative leader steps.

- Direct measurements of negative leader behavior in the upper positive charge region.

- Characterization of negative leader behavior in the lower positive charge region.

- Positive leader tips produce VHF radiation.

6.1 The Negative Leader

The negative leader has turned out to be quite fascinating to study. Many of the published studies have used optical measurements to determine the properties of negative leader steps. This has provided quite a skewed view of negative leader activity in the community. As discussed in *Winn et al.* (2011) and *Edens* (2011), the negative leader at high altitude bears little resemblance to the negative leader seen below a cloud base. The leader steps high in the cloud are more spaced out in time, cover a larger distance, and are less branched than those seen at low altitudes.

The current description of negative leader activity while in the cloud leaves something to be desired. Because the cloud obscures the channel so that optical measurements cannot be made, the behavior of the negative leader in the cloud has been almost entirely gleaned through the examination of electric field records. In the last 15 years or so, VHF maps (such as those provided by the LMA) have added quite a lot to the story. Unfortunately, these systems are not quite capable of resolving individual leader steps. More recently, *Edens* (2011) photographed and recorded with high-speed video the negative leaders of bolt from the blue flashes as they left the cloud. This gave clear evidence of exceptionally long streamer zones and associated leader steps. However, it was unclear if the results for the negative leader of bolt from the blue flashes could be generalized to the leaders for normal intracloud discharges. The broadband interferometer is more than capable of resolving individual steps of negative leaders in the upper positive charge region, making it an ideal instrument to examine negative leader behavior in the cloud.

6.1.1 Initial Breakdown Pulses

Initial breakdown pulses (IBP) (also referred to as preliminary breakdown pulses, B pulses, and characteristic pulses) are trains of pulses seen near the beginning of a flash, typically within the first 5–20 ms of intracloud discharges. They have a characteristic shape: short duration (1–2 μs) sub-pulses superimposed on a longer duration (100–300 μs and longer) monotonic ramp of the same polarity (*Weidman and Krider*, 1979; *Marshall et al.*, 2013, 2014a,b). IBPs are associated with gamma ray bursts seen from space, and they occur during the vertical propagation of the negative leader (upward in the case of intracloud flashes, and downward in the case of cloud-to-ground flashes).

An example of IBPs from a selection of flashes is shown in Figure 6.1, adapted from *Marshall et al.* (2014a). In the particular study from which this figure was taken, Marshall was interested in the small field change seen at nearby
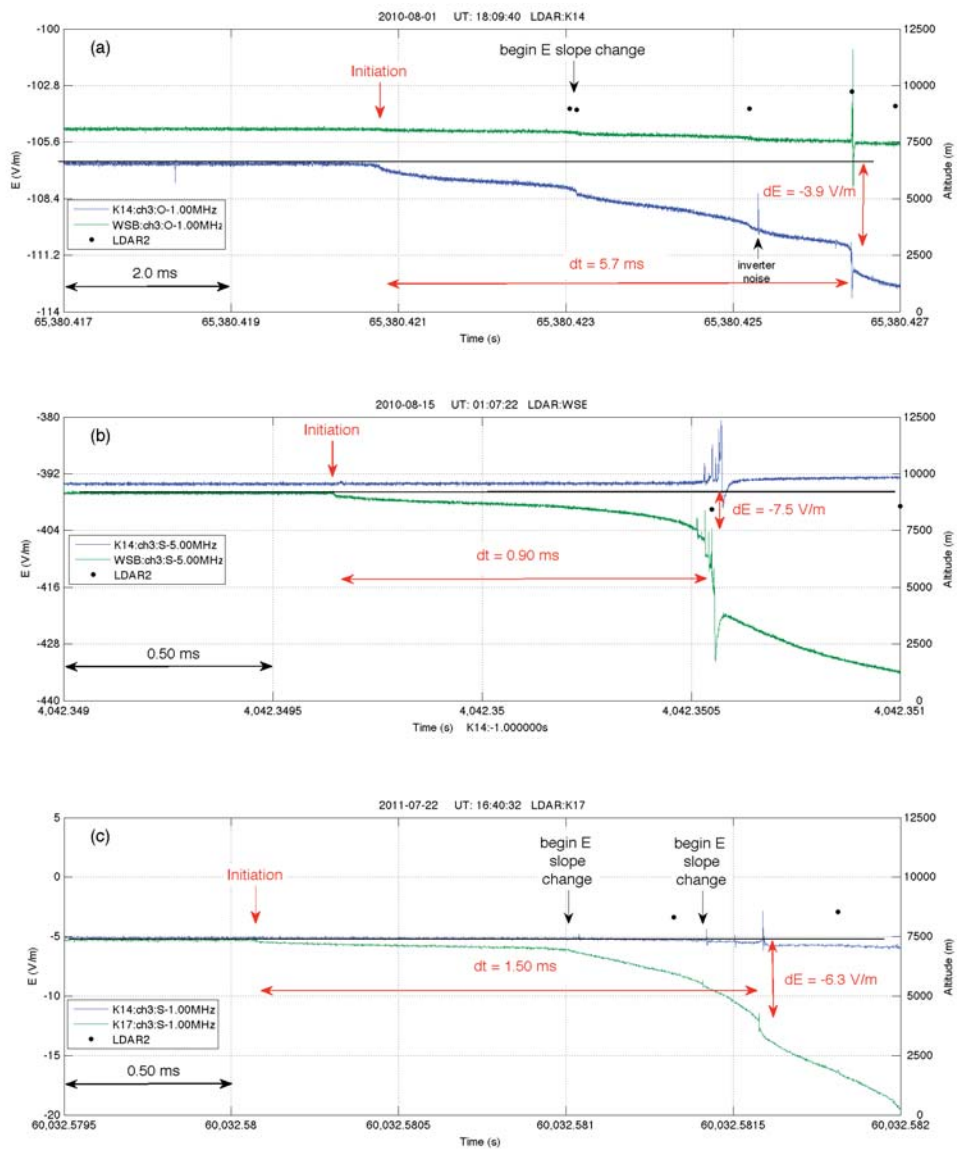
Figure 6.1: Initial Breakdown Pulses. Examples of the early electric field change record (decay time of 1 or 10 seconds) for 3 intracloud flashes. Each flash shows the field record at two different ranges from the flash (based on horizontal distance to LDAR2 source location). For 6.1a, 11.4 km (green) and 5.3 km (blue). For 6.1b, 4.3 km (green) and 11.7 km (blue). For 6.1c, 3.3 km (green) and 9.4 km (blue). Figure adapted from *Marshall et al.* (2014a).

stations, which will not be discussed here. The IBP of panel b is particularly easy to identify, occurring 900 μs after the first detectable field change.

Of the 3 flashes (D, E and F) of this study which have accompanying electric field records, 2 (D and E) show evidence of IBPs. This in itself is unusual, as *Marshall et al.* (2014b) found that only 2 out of 267 flashes recorded by sensors within 30 km of the flash lacked initial breakdown pulses[1]. Frequently the pulses can be small, such that they are below the noise level of flashes which occur a long distance away. However, flash F occurred a plan distance of only 1100 meters from the fast antenna; lack of sensitivity should not be a factor.

Figures 6.2 and 6.3 show the electric field record for flash E, which has very clear evidence of IBPs at 20:25:10.367 and 20:25:10.369 UT. In comparison to the records shown in Figure 6.1, the IBPs of flash E look quite different. The long duration field change and the short duration sub-pulses are of opposite polarity. This seeming contradiction is an effect of the range at which the measurements are taken; flash E initiated only 5.7 km northeast of the fast antenna site, while most published IBP waveforms were measured 10–30 km from the flash. As the sensor is moved away from the flash, the slow portions of the sferic (the electrostatic and induction components) will reverse in sign, while the fast portions of the sferic (the radiation component) will not (*Uman et al.*, 1975; *Uman*, 1987). Figure 6.1b shows a good example of the electric field inversion; the far field record (blue) has a positive slow deflection with positive sub-pulses, while the near field record (green) has a negative slow deflection with positive sub-pulses.

The other major difference between the observations of *Marshall et al.* (2014a) and those of this study concerns the time constants of the instruments. Marshall used an antenna with a time constant of 1 second or longer, whereas the time constant for the fast antenna of this study is 113 μs. A very short time constant was used so that a very sensitive antenna could be deployed which would not saturate on the bulk charge motions of a lightning flash. As a consequence, the waveforms in Figures 6.2 and 6.3 do not show the ramping field seen in Figure 6.1.

The exponential decay of the fast antenna can be removed from the data, a process called de-drooping. However, over long periods of time (several time constants), small errors in the de-drooped waveforms will add together, causing a large and incorrect DC offset. In the case of the fast antenna used in this study, de-dropping can not be reliably done for more than 1 ms of data. Figure 6.4 shows the results of de-drooping the waveform for the first initial breakdown pulse of Figure 6.3. As expected, the de-drooped electric field record now shows a strong ramp in the field strength, just as seen in the near field records of Figure 6.1.

---

[1] *Marshall et al.* (2014b) specifically studies cloud-to-ground flashes, however during personal communications with Tom Marshall, he has insisted that the fraction of all flashes (cloud-to-ground and intracloud) which have initial breakdown pulses is extremely close to 100%.
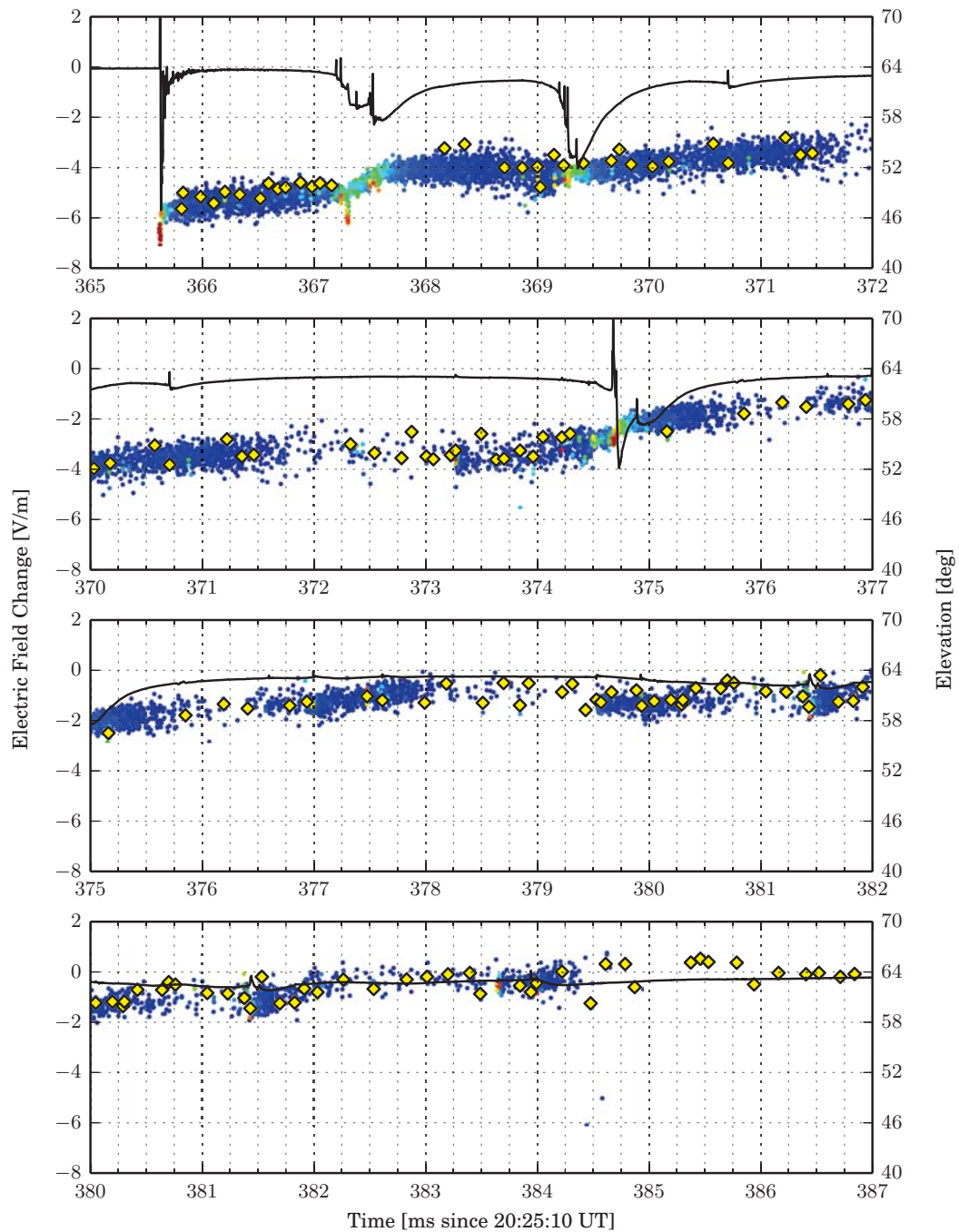
Figure 6.2: Electric field record for the initial 22 ms of flash E. Fast antenna record (left axis, black) overlaid on the elevation of interferometer sources colored by received power (right axis). Yellow diamonds show elevation and time of LMA sources.
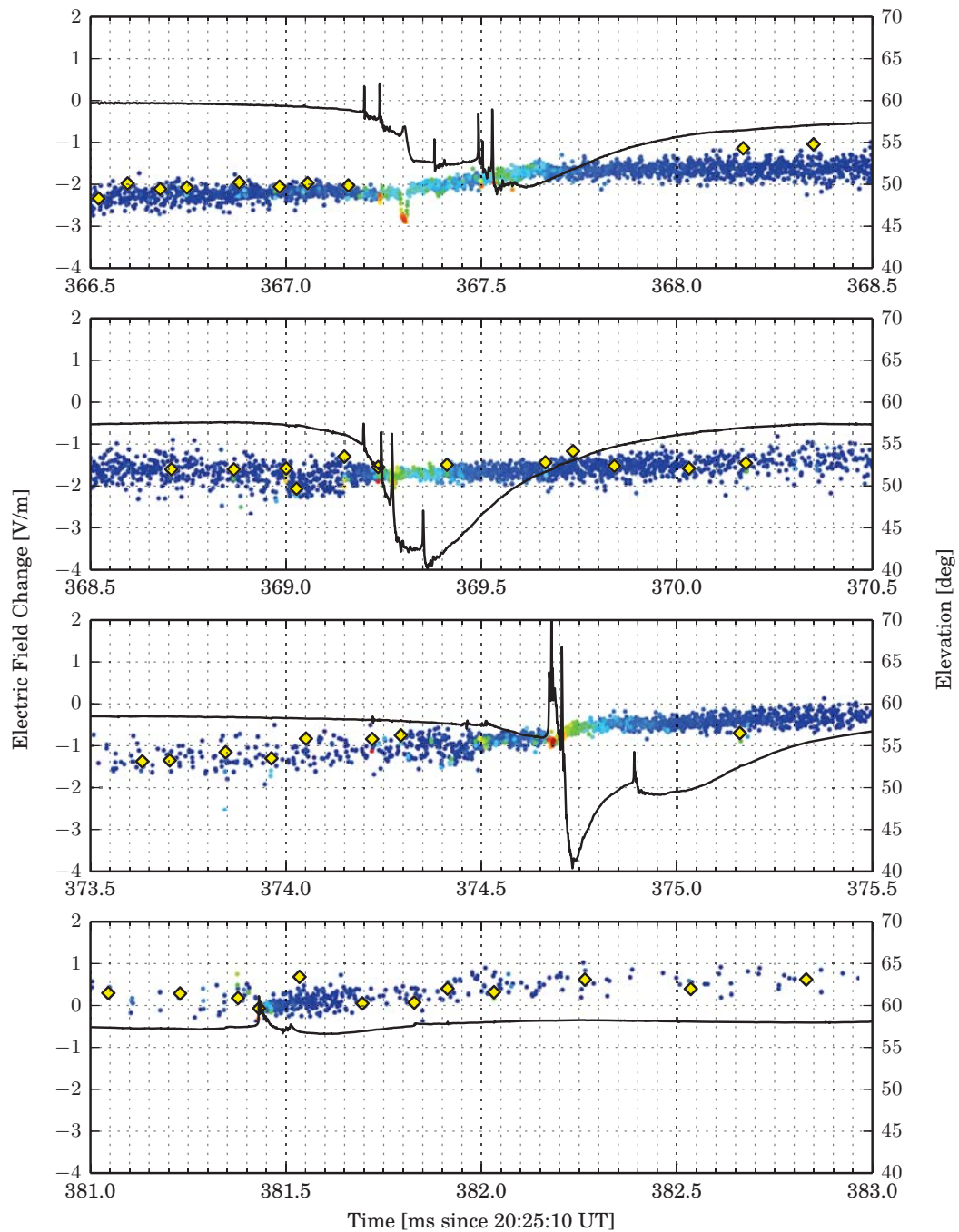
Figure 6.3: Electric field record of select initial breakdown pulses for flash E. Fast antenna record (left axis, black) overlaid on the elevation of interferometer sources colored by received power (right axis).
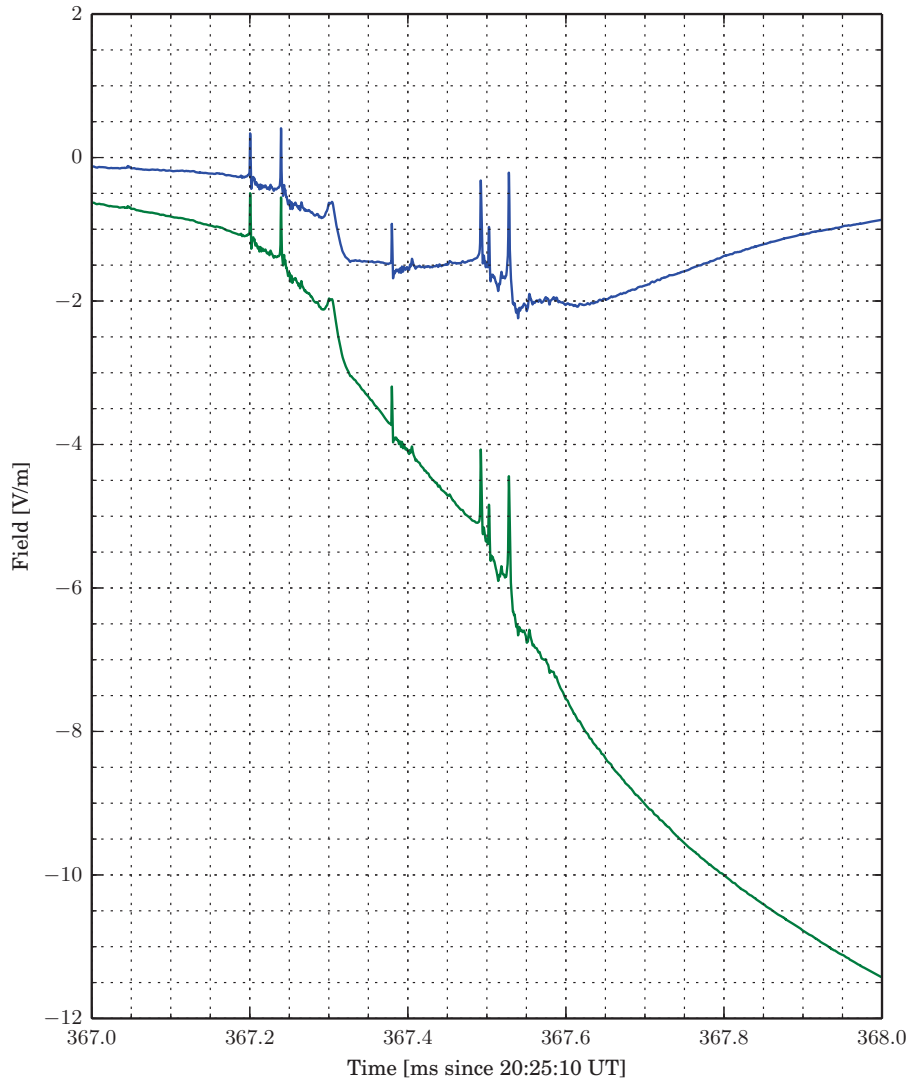
Figure 6.4: De-drooped electric field record for an initial breakdown pulse. (Blue) measured waveform (113 μs decay time constant), (green) de-drooped waveform.

Time [ms]	El [deg]	Az [deg]	R [m]	x [m]	y [m]	z [m]
367.197	49.8	38.9	8540	3770	4020	9640
367.624	52.4	36.8		3770	4260	10520
369.196	51.5	36.5	9330	3770	4280	10440
369.386	52.9	34.4		3840	4360	10670
374.669	55.2	25.7	9340	2940	4590	10650
374.914	57.2	20.9		2710	4410	10920
381.419	59.4	19.6	8860	1380	4120	11050
381.610	59.6	15.2		1660	3790	11000

Table 6.1: Summary of initial breakdown pulses shown for flash E.

In flash E, the initial breakdown sequence starts with a narrow bipolar event, the discussion of which is beyond the scope of this study. After the narrow bipolar event, the flash develops like a normal intracloud lightning discharge. The first IBP is seen 1.6 ms after the start of the flash, roughly in agreement with the time between the first electric field change and the first IBP seen by *Marshall et al.* (2014a). Overall, the first IBP (and all the IBPs in flash E) shows a negative deflection, indicating there is negative charge moving away from the fast antenna. Synchronous with the onset of the IBP, the VHF emission from the flash becomes brighter and begins traveling to higher elevation angles. Not shown in Figures 6.2 and 6.3, but summarized in Table 6.1, is that the azimuth also changes in the counterclockwise direction (lower azimuth angles). Overall, the first IBP propagated approximately 910 m in 430 μs (as determined by corresponding LMA source locations), giving a step velocity of 2.1×10^6 m/s. Immediately after the step, the negative leader mostly ceases propagation and, as a result, the average negative leader velocity is lower. Similar analysis can be applied to the other 3 IBPs shown in Figure 6.3, giving 250 meters in 190 μs (1.3×10^6 m/s), 400 meters in 250 μs (1.6×10^6 m/s), and 440 meters in 190 μs (2.3×10^6 m/s).

Some work has been done to attempt to model the field changes produced by IBPs in Florida by *Karunarathne et al.* (2014). They were able to get a good fit for the slow electric field change of several IBPs in cloud-to-ground flashes using a modified transmission line model with exponential attenuation of the pulse along the channel. The channel lengths which produced a good fit were 300-1200 meters, in good agreement with the results presented here, however, the velocity of propagation needed was 0.7–1.8×10^8 m/s, almost two orders of magnitude higher. A partial explanation for this is that the model was applied to cloud-to-ground flashes, which may have faster propagating steps, but it is unlikely that the pressure difference is enough to account for the entire discrepancy.

The monotonic ramp portion (the slow field change) of IBPs is certainly produced by negative charge being moved upward (in the case of intracloud flashes) during a step process. The interferometer measurements are quite clear that during the IBP, the emission quickly moves upward, and then pauses until the next pulse.

Interpreting the mechanism which produces the sub-pulses of an IBP is more difficult. An expanded view of the first IBP of flash E is shown in Figure 6.5. Each sub-pulse is accompanied by a small DC level shift of the electric field record, always in the same direction as the monotonic ramp. This seems to imply that the sub-pulses are produced by a very sudden charge movement. If the charge is moved quickly (at a velocity over 10^7 m/s), there will be a large radiation field component to the sferic. At the close distances at which the measurements above were made, the radiation component will be opposite in polarity from slower changing processes. This means that the sub-pulses could be produced by a positive charge moving downward or a negative charge moving upward.

The interferometer record shows a smooth increase in elevation angle over the entire duration of an IBP. At the time of a sub-pulse, the VHF emission brightens, but in general there is no motion (up or down) associated with the pulse. The obvious exception to this can be seen at 367.3 ms after 20:25:10 UT in Figure 6.5. In this case, a wider than normal sub-pulse is associated with very bright VHF sources located at lower elevation angles, and also offset in azimuth from the flash origin. The interferometer record also seems to show very fast movement at the beginning and trailing edges of the bright source, followed by a slower (but still fast) elevation decrease of the source. The very fast motion is likely an artifact of how the interferometer operates. The angular resolution of the interferometer is nominally 5°, so all the sources seen during the sub-pulse are not resolved. The image of the VHF radiation (Chapter 3) would not be able to differentiate between a single source and multiple sources. What is likely occurring during this sub-pulse is that a VHF source is turning on at a lower elevation angle, and then propagating downwards. As the low elevation source brightens, the interferometer source switches from one location to the other, causing the interferometer map to show a very rapid change in elevation angle. The bright source continues radiating for about 14 μs and then dims, causing the interferometer locations to return to their previous location. This interpretation is supported by the VHF waveform (Figure 6.6), which shows a smooth increase in VHF amplitude during the sub-pulse in question.

A close examination of the interferometer for the remaining record shows that other sub-pulses may also be associated with a slight elevation decrease, and are never associated with an elevation increase. This seems to imply that the sub-pulses are produced by a current suddenly traveling downward, instead

171
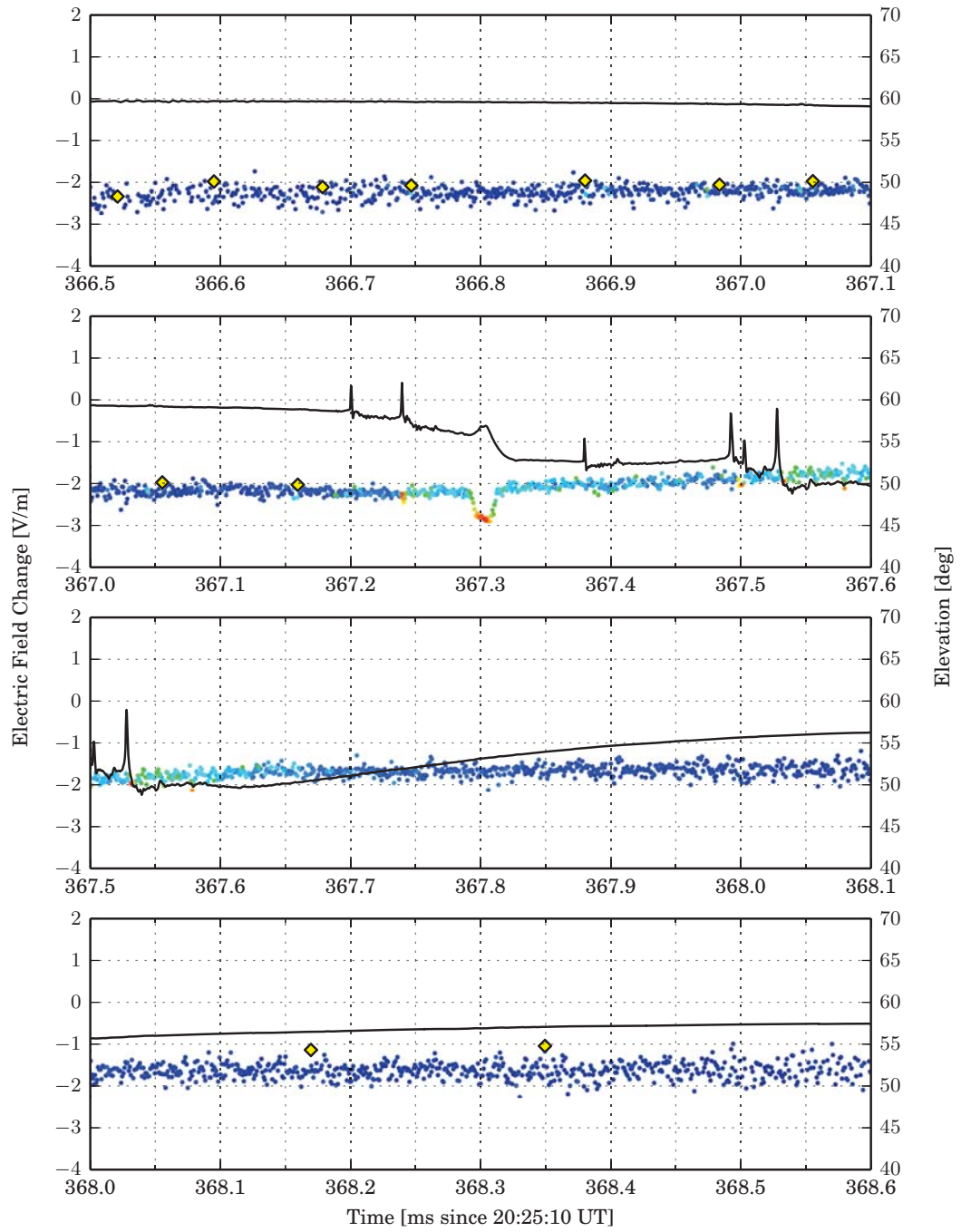
Figure 6.5: Expanded view of a single initial breakdown pulse.
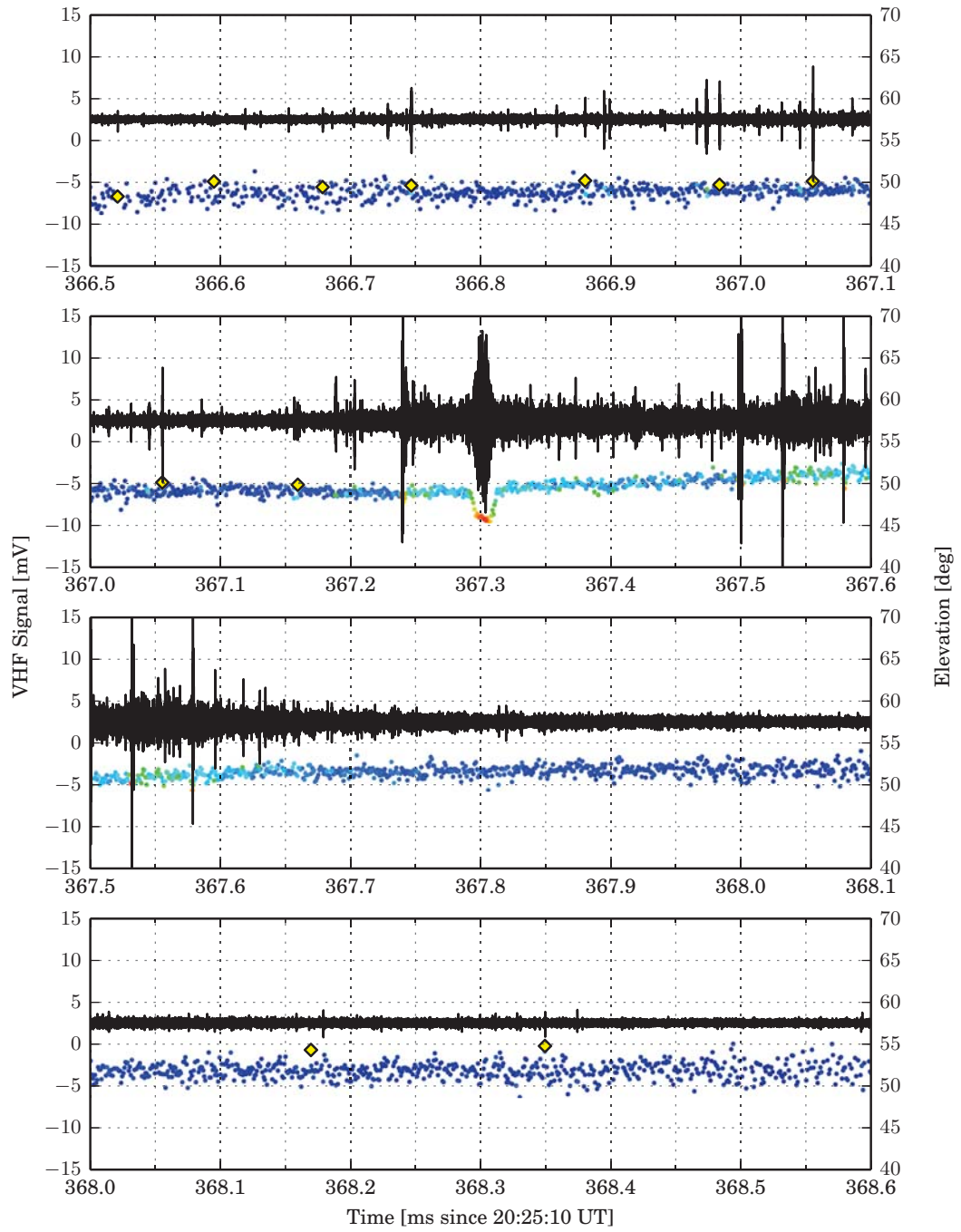
Figure 6.6: VHF record for a single initial breakdown pulse.

173

of negative charge suddenly moving upwards. There is some support of this interpretation in the literature; *Winn et al.* (2011) saw pulses traveling along a lightning channel which started at a negative leader step and propagated backwards towards the positive leader end. If an impulsive current is indeed traveling downwards, as soon as the current reaches a conducting channel, VHF radiation from the process should cease. Once the current pulse reaches the end of the positive leader, one expects there to be additional, but possibly faint, emission at the positive leader tip. It is unsurprising that such an emission at the positive tip is rarely (or never) seen, since at the same time the negative leader tip is brightly radiating in the VHF, masking any emission from the positive tip.

The analysis shown for flash E has not been applied to flashes D and F. Electric field records for the initial 20 ms of these flashes, as well as expanded views of selected segments, is shown later in this chapter (Figures 6.11–6.14). In addition, several other electric field records have been examined and found to be in rough agreement with the findings above.

6.1.2 Horizontal Negative Leader Steps

After the initial vertical extension of the negative leader, the propagation turns over and begins traveling horizontally into the upper positive charge region. When this happens, the behavior of the negative leader frequently changes. Among other things, as noted by *Behnke et al.* (2005), the propagation speed of the negative leader often slows. In addition to this, the time interval between negative leader steps becomes longer, making them easier to separate in the interferometer record, and the emission becomes less concentrated.

Figures 6.7–6.10 show interferometer and electric field data from the horizontal portion of negative leader extensions for two flashes (E and F). There are clearly bursts of VHF radiation, separated by substantial periods of quiescence in all of the records. In addition, the electric field changes for flash E have become less jagged and longer in duration.

Overlaid on top of the figure are $\times$ marks which show the time and location (in black) of LMA sources associated with each step. The LMA association is good but imperfect, causing some of the marks to not be quite aligned in time or location with the brightest VHF radiation located by the interferometer. However, LMA locations allow for the step lengths as well as step intervals to be examined, summarized in Table 6.2. The step start times were approximately determined by hand, and then a precise time was obtained from the time of the brightest VHF source located within 100 μs. The location of the step was found by averaging first two LMA source locations which occurred after the step.

	Flash E			Flash F	
Figure	Interval [ms]	Length [m]	Figure	Interval [ms]	Length [m]
6.7	5.177	432	6.9	3.115	477
	5.516	306		1.913	173
	4.484	257		5.064	534
	0.796	168		5.841	699
6.8	0.608	153	6.10	6.536	562
	2.539	394		0.347	210
	7.766	595		5.150	190
	2.656	391			
	4.279	394			

Table 6.2: Summary of step intervals and lengths.

There is some ambiguity in identifying steps. First there is frequently short duration emission that comes from the negative leader tip region which does not have a simultaneous electric field deflection. This is seen in all the figures, but especially in Figure 6.8. A lack of field deflection is taken as an indication that very little charge was moved during this period, and so the emission must not be from a step. Second, the VHF signature of a step is a group of sudden bright bursts, followed by a long duration, faint glowing emission. With many steps, the glow clearly ends before the next step begins, but this is not always the case. When the glow is continuous between steps, it can become unclear when one step ends, and the next begins. These ambiguities should be taken into account when interpreting the results of Table 6.2.

As has already been alluded to, the characteristic sub-pulses seen in the initial breakdown pulses are still present in these later, horizontally propagating steps, although smaller in amplitude. As before, each sub-pulse is associated with a brightening in the VHF emission, but there is no longer a discernible DC level shift. The lack of a DC level shift is expected for a leader which is moving largely tangentially to the fast antenna, and so not moving charge towards or away from the sensor. It is extremely likely that whatever physical process produced the characteristic sub-pulses early in the flash is still active later in the flash when the leader is propagating horizontally.

Figures 6.7 and 6.9 show 20 ms portions of the horizontal negative leader propagation immediately following the initial upward propagation. Both flashes E and F show approximately 5 leader steps in these 20 ms intervals. This is a large reduction to the approximately 8 (in flash E) and 10 (in flash F) seen in the first 20 ms of flash activity (Figures 6.2 and 6.11).

In flash E, the polarity of the field deflections is reversed in comparison to the records for the vertical propagating negative leader (Figures 6.2, 6.3, and 6.5).
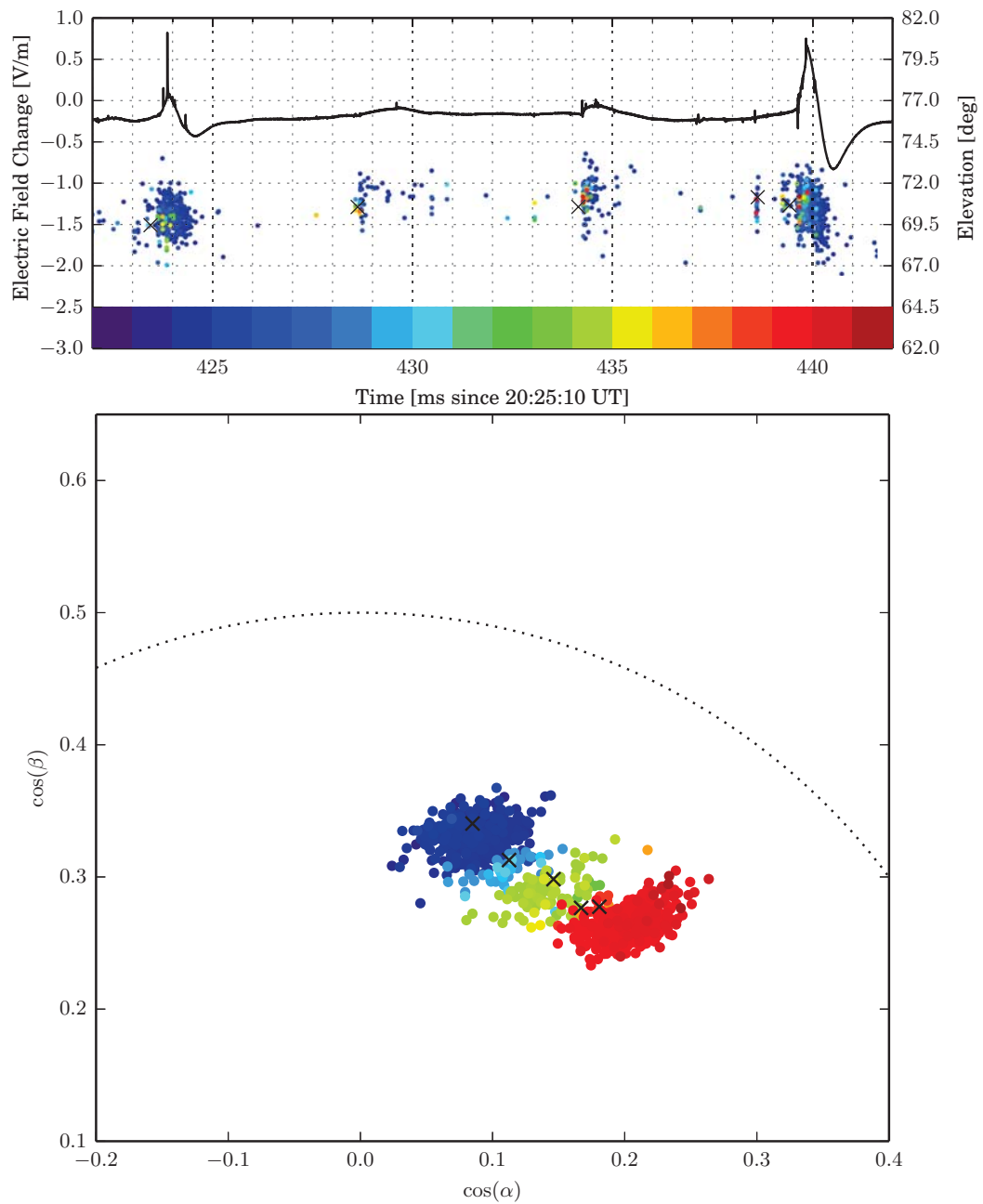
Figure 6.7: Early horizontal negative leader for flash E. Top – electric field record overlaid on elevation of interferometer located VHF sources. Bottom – cosine projection interferometer map colored by time (scale above). × marks show the time and location of LMA determined step locations.
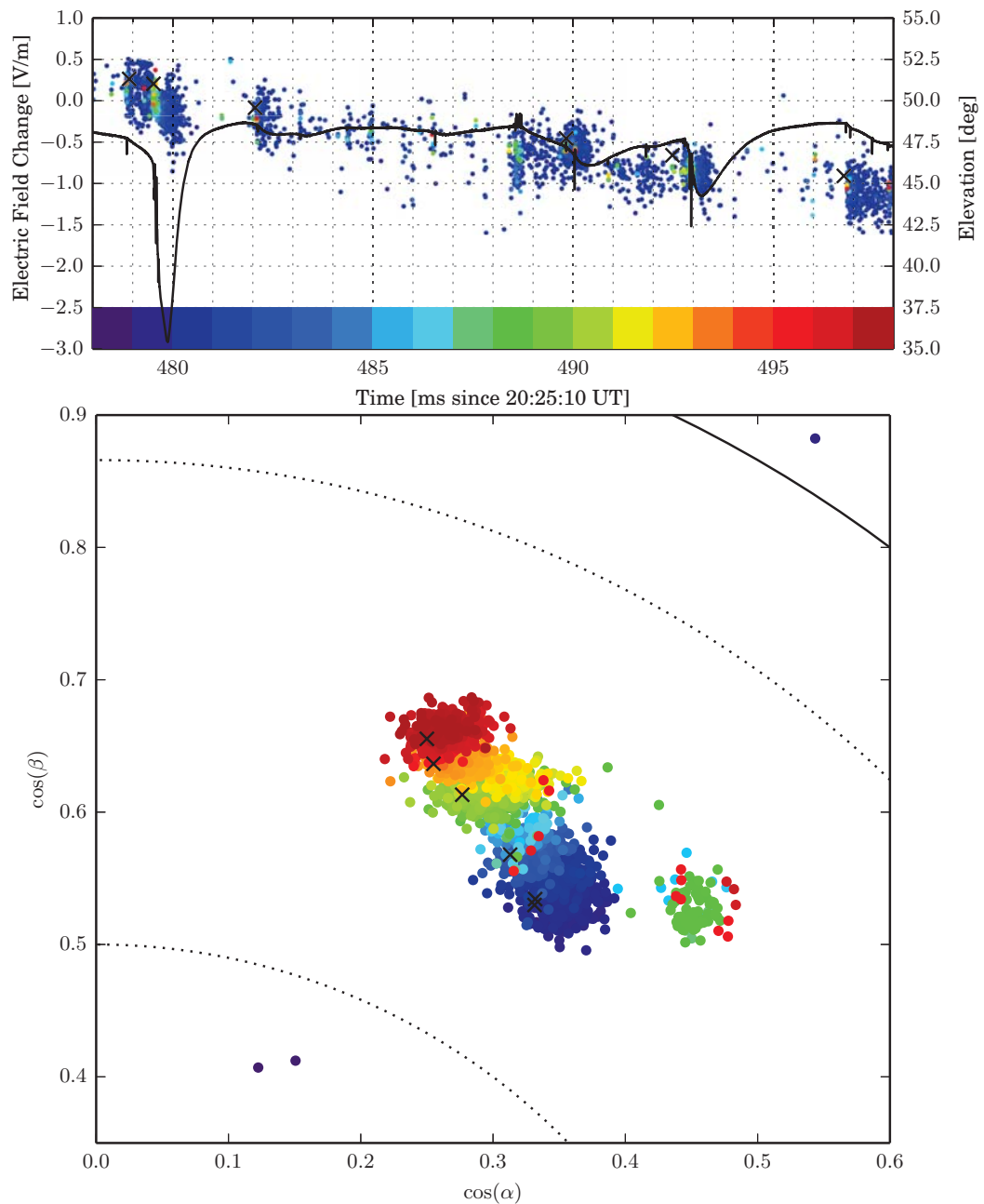
Figure 6.8: Late horizontal negative leader for flash E. Top – electric field record overlaid on elevation of interferometer located VHF sources. Bottom – cosine projection interferometer map colored by time (scale above). × marks show the time and location of LMA determined step locations.

The polarity reversal occurs because when the leader turns horizontal, it also turns towards the interferometer site. This can be seen in the cosine projection map, as the sources are moving towards higher elevation angles. The amplitude of the field deflection for each step has reduced in comparison to the vertical step, but this is likely due to the large tangential component to the propagation.

For flash F, by the time the negative leader turned horizontal, there was a large amount of activity in the positive breakdown region. The large negative deflection seen at 03:11:51.189 UT was produced not by activity of the negative leader, but by activity in the positive breakdown region (not shown in the interferometer map). The amplitude of the field deflections for the horizontal steps is approximately the same as that for the early vertical steps, since the negative leader propagation direction has a small tangential component relative to the interferometer site.

Figures 6.8 and 6.10 show negative leaders which occur later in flash E and F, respectively. Where the field records for early horizontal leaders of both flashes were fairly similar, this is not the case for these later leaders. In flash E, the negative leader is propagating into a distant stratiform region of the cloud. In flash F, the negative leader initiated late in the flash, near the flash origin, and is being fed by repeated K-changes from one positive leader channel.

The electric field record for the late horizontal leader of flash E (Figure 6.8) is again reversed in polarity, but otherwise very similar to the record of the early horizontal record. The polarity reversal is again an effect of propagation direction; the leader is now moving away to the north of the interferometer site. However, this 20 ms period shows approximately 6 leader steps with field deflections comparable to the earlier steps. The other big difference is that there is more inter-step activity; bursts of VHF radiation from the negative leader region which do not produce a significant electric field deflection. This inter-step activity is likely a result of increased activity in the positive breakdown region. Some of this positive breakdown activity can be seen in the positional map (bottom panel) in green to the right hand side of the negative leader.

The late horizontal leader in flash F (Figure 6.10) is very different. The excerpt shown is from the third negative leader seen in the flash. The third leader started near the origin, 649 ms after the beginning of the flash, immediately following a very extensive K-change from one of the active positive leaders. The very first, large amplitude field deflection shown in Figure 6.10 is produced by a K-change (seen in blue on the positional map) which traveled from the end of the positive leader to the tip of the negative leader. Immediately following the K-change is the first step; there is no gap in the faint VHF emission following the K-change and the brightening seen for the leader. This makes identifying the electric field record associated with the leader step very difficult. At the very end
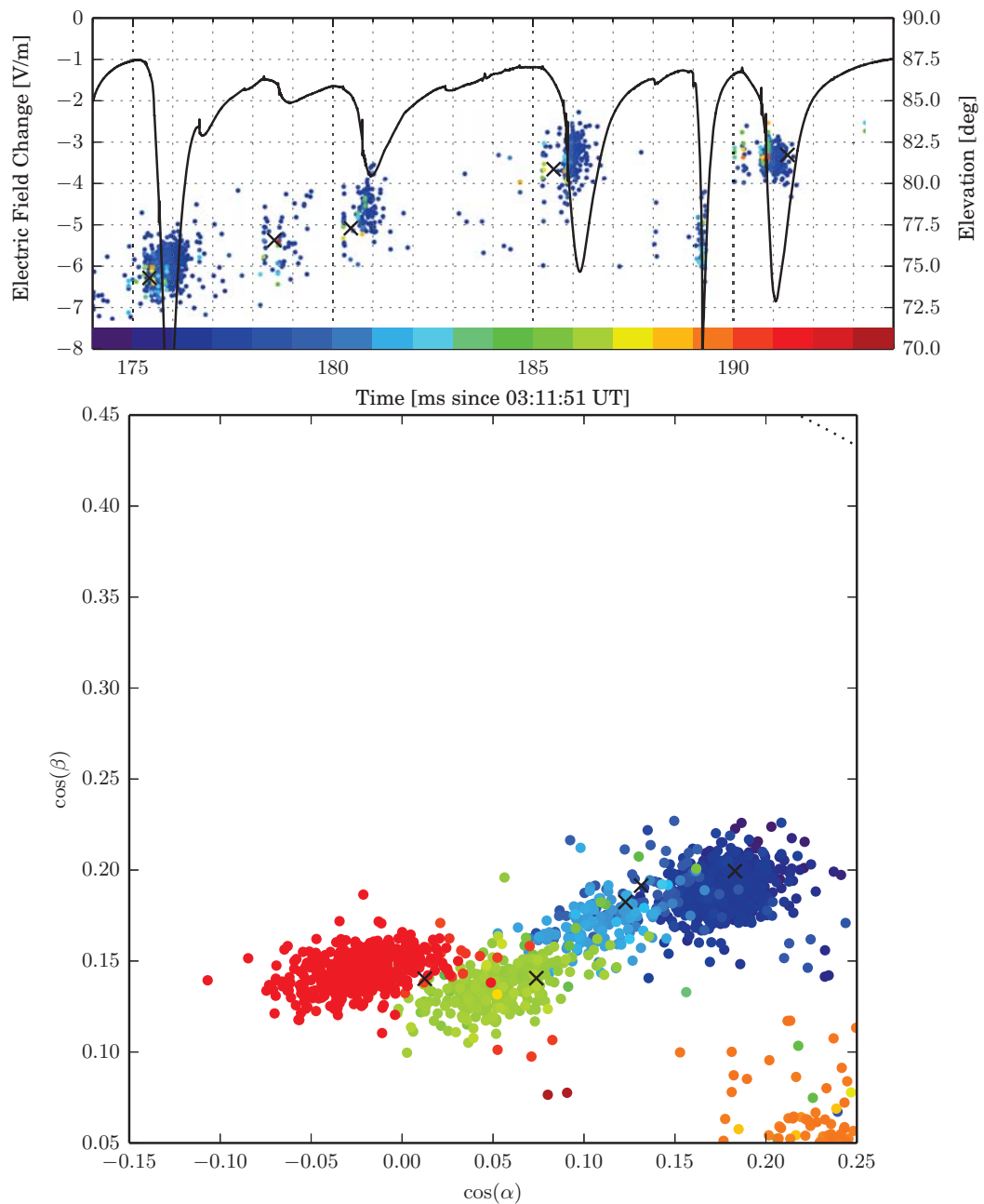
Figure 6.9: Early horizontal negative leader for flash F. Top – electric field record overlaid on elevation of interferometer located VHF sources. Bottom – cosine projection interferometer map colored by time (scale above). × marks show the time and location of LMA determined step locations.
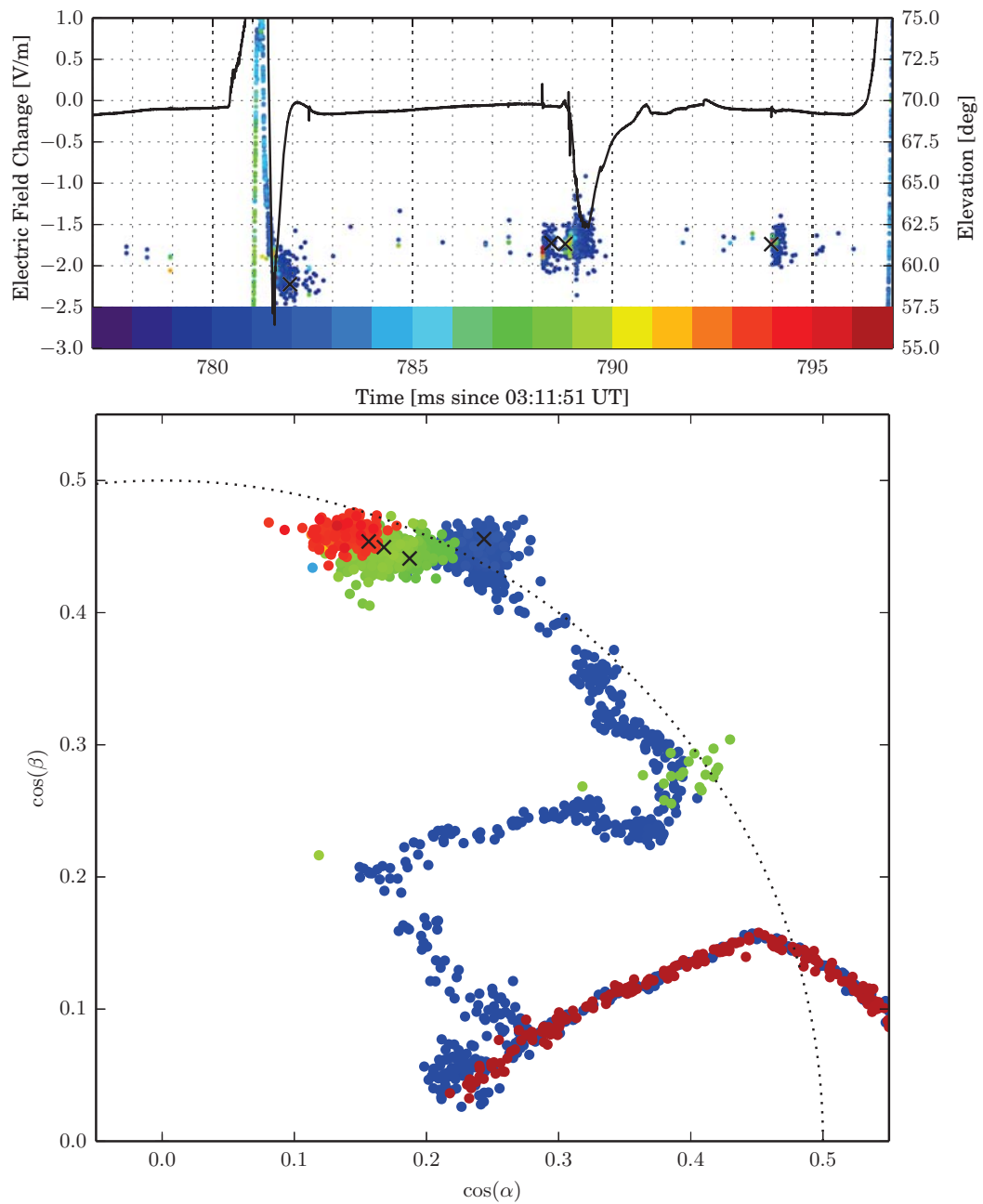
Figure 6.10: Late horizontal negative leader for flash F. Top – electric field record overlaid on elevation of interferometer located VHF sources. Bottom – cosine projection interferometer map colored by time (scale above). × marks show the time and location of LMA determined step locations.

of the 20 ms record is the beginning of the next K-change, which can be seen in the positional map in dark red. In between each K-change are 3 or 4 negative leader steps, and the inter-step period shows very little activity. In flash F, the negative leader tip is largely cut off from the rest of the flash (as indicated by the repeated K-changes). As a result, the electric field at the tip of the negative leader is likely just barely large enough to support leader propagation. Each K-change provides negative charge to the leader tip, and allows a few more leader steps.

6.1.3   Low versus High Altitude

A large majority of the observations of negative stepped leaders has taken place near the ground, and is still an active area of study. Recent high speed video observations of negative leaders reported step lengths of 13 to 273 meters and inter-step intervals between 3.2 and 55.6 μs near the ground (*Miki et al.*, 2014), which is in general agreement with other studies (*Schonland et al.*, 1935; *Schonland*, 1956; *Berger*, 1967; *Chen et al.*, 1999; *Hill et al.*, 2011). In comparison, the measurements in the cloud presented above give much longer step lengths (100–700 meters) and inter-step intervals (300–8000 μs).

However, the measurements shown here are in rough agreement with other measurement of step lengths at high altitude. *Winn et al.* (2011) observed current waves produced by negative leader stepping which had inter-step intervals of between 500 and 7000 μs, and then inferred step lengths using an average leader propagation speed of between 50 and 600 meters.

A likely cause for the difference between measurements near the ground and measurements in the cloud is the difference in pressure. At the tip of the negative leader is a large negative streamer zone, where electrons are accelerated into the surrounding medium (air). At low pressures, the mean free path of an electron is longer, and so the streamer zones are larger. The transition from high altitude to low altitude negative leader behavior can be seen in bolt from the blue cloud to ground flashes (flash C is an example). Here, the VHF emission gradually becomes less impulsive and more continuous as the leader travels from high altitude towards the ground (*Edens*, 2011).

The effects of pressure can also be seen in the difference in negative leader behavior in high and low altitude intracloud flashes. Figures 6.11–6.14 shows the electric field records and interferometer locations for an intracloud flash initiating between the main negative and upper positive charge layer (flash F), and an intracloud flash initiating between the main negative and lower positive charge layer (flash D).
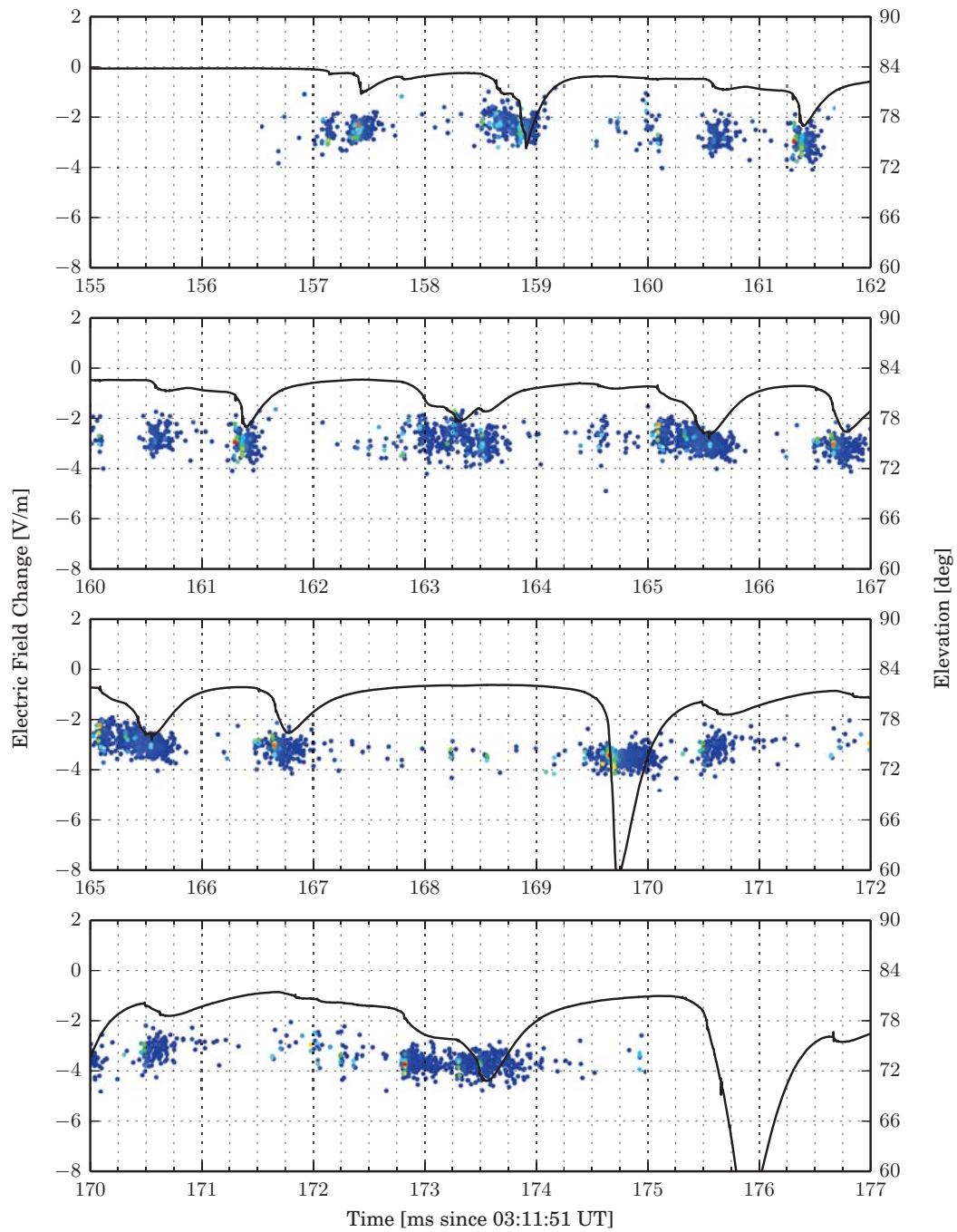
Figure 6.11: Electric field record for the initial 22 ms of flash F. Fast antenna record (left axis, black) overlaid on the elevation of interferometer sources colored by received power (right axis).

182
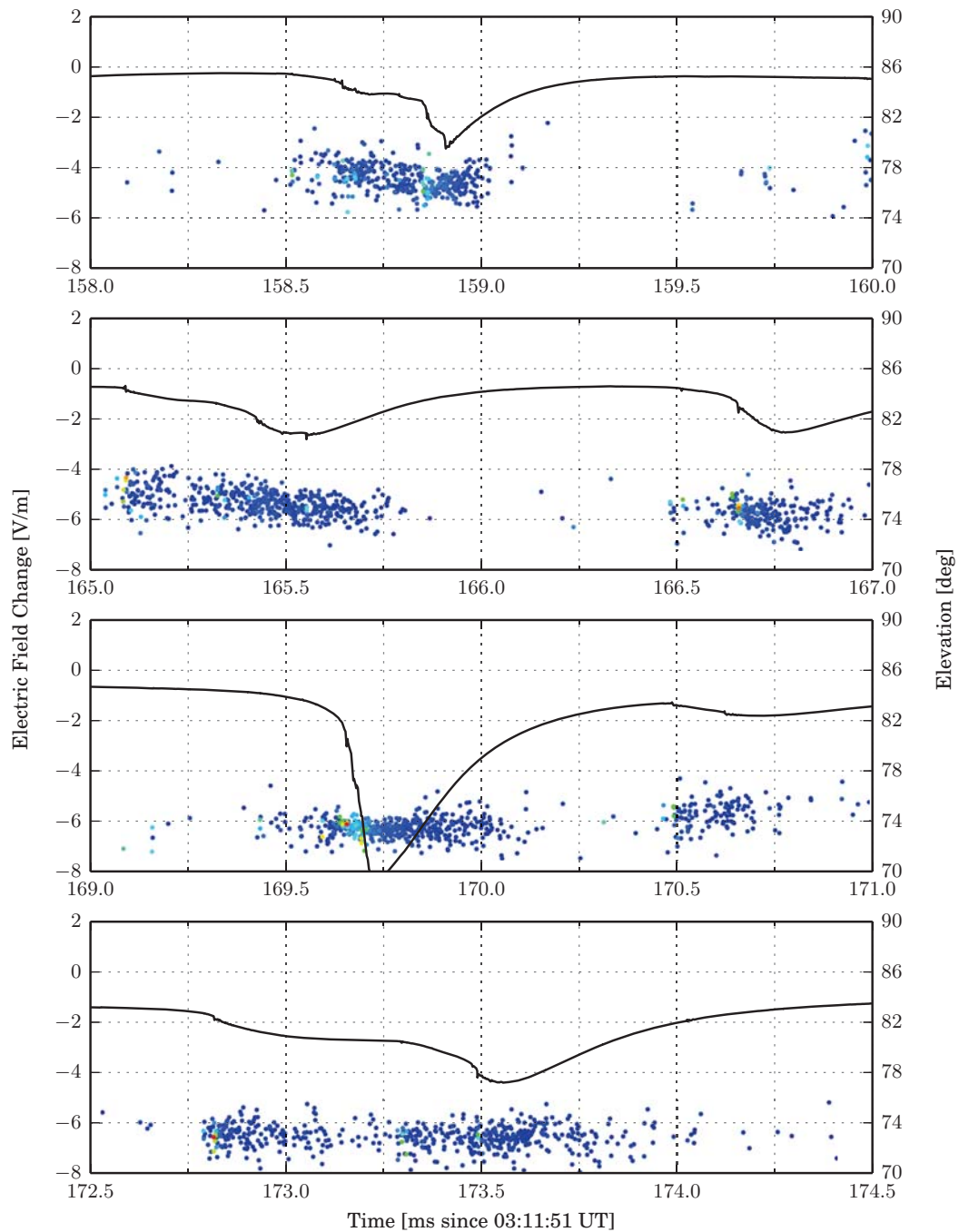
Figure 6.12: Electric field record of select initial steps for flash F. Fast antenna record (left axis, black) overlaid on the elevation of interferometer sources colored by received power (right axis).

Flash F (Figures 6.11 and 6.12) initiated at 8 km altitude, between the main negative and upper positive charge layers (as shown in Figure 5.19). The stepping behavior is in agreement with the numerical results presented above, that of discrete leader steps separated by long periods of VHF quiescence. The leader propagated approximately 3 km in the first 20 ms of activity, giving an average velocity of 1.5×10^5 m/s. The VHF record for each step shows a quick bright emission, followed by a longer (.5-1 ms) period of faint VHF radiation. The sources located by the interferometer are also not very compact, extending over 4-6° of the sky. Given the range from the interferometer to the initial portion of the flash (about 5100 meters), the observed extent in the sky corresponds to nominally a 350-530 meter diameter volume.

The picture is quite different in flash D, which initiated at 7.5 km altitude between the main negative and lower positive charge regions. For the first 9 ms of the flash, the steps are discrete, and separated by long periods of VHF quiescence. However, the inter-step period is shorter, between 100 and 1000 μs, causing the stepping rate to be higher. In addition, the located interferometer sources cover a smaller, 2-4° region of the sky. Flash D initiated 4700 meters from the interferometer site, so the sky extent corresponds to a 160-330 meter diameter volume. During the first 9 ms, the negative leader propagated downwards approximately 600 meters (6.6×10^4 m/s). At 21:33:47.775 UT, there is a dramatic change in the behavior of the negative leader. The stepping rate increases such that there is no longer a quiet period between steps, the VHF radiation brightens, and the leader also begins branching profusely. Over the next 11 ms, the negative leader propagates faster than it had in the initial 9 ms, traveling 1.8 km vertically (1.6×10^5 m/s), as well as a substantial horizontal distance which is not accounted for in the estimated velocity.

What physically changed at 6.9 km altitude to cause such a dramatic and sudden change is unclear. If pressure were the only factor affecting negative step behavior, the transition is expected to be more gradual. Another possibility is that as the leader propagated downwards, the leader entered a region of higher positive charge density. This view is supported by the fact that the flash initiated at the lower edge of the main negative charge region, and there was a gap between the negative and lower positive charge layers (Figure 5.5). Here, the top of the lower positive charge region is seen to be at between 6.5 and 7 km altitude, corresponding with the begining of heightened activity in the negative leader.

6.1.4 Discussion

The negative leader step processes seen in the upper positive charge layer are all more or less the same throughout the duration of a flash, with step lengths
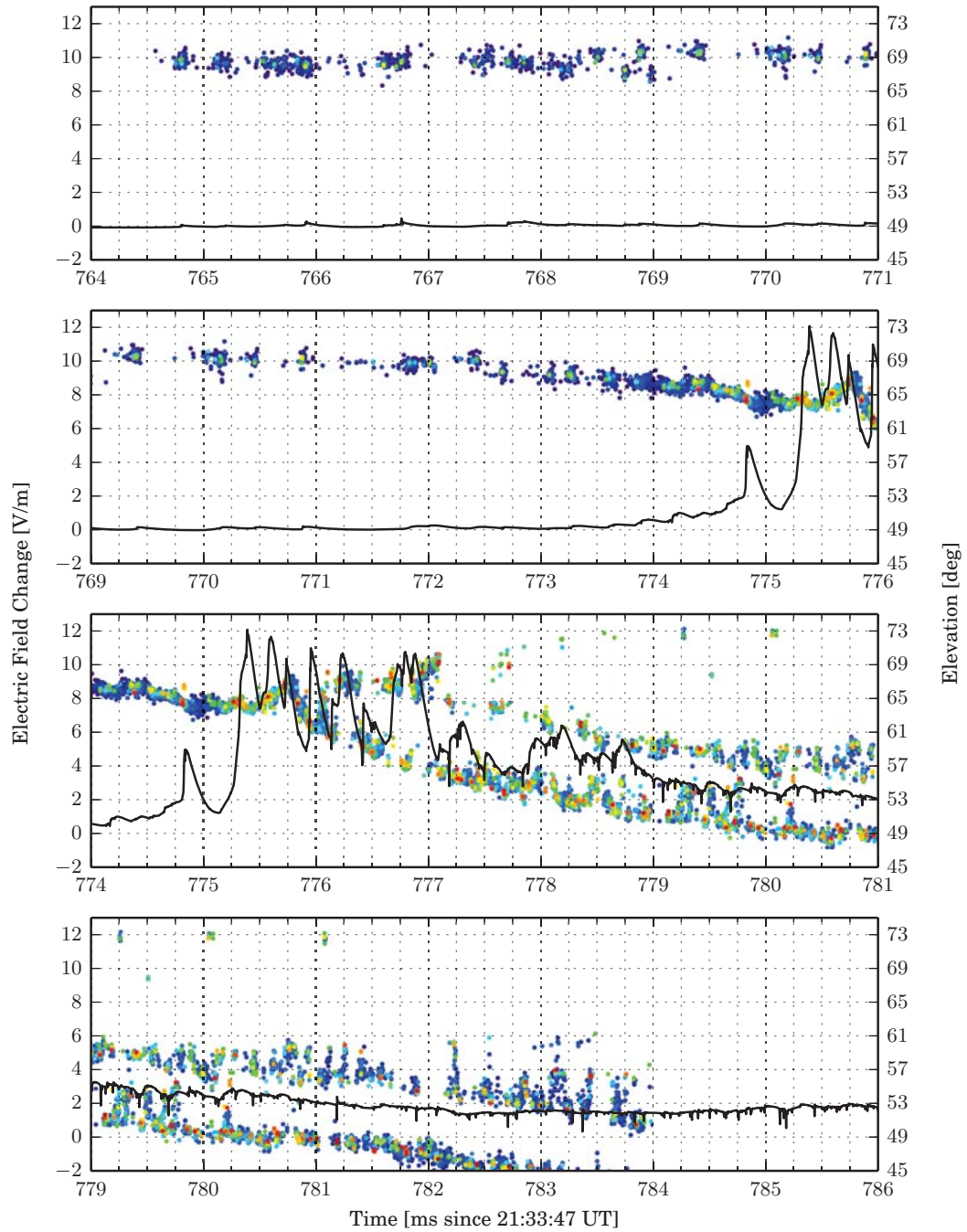
Figure 6.13: Electric field record for the initial 22 ms of flash D. Fast antenna record (left axis, black) overlaid on the elevation of interferometer sources colored by received power (right axis).
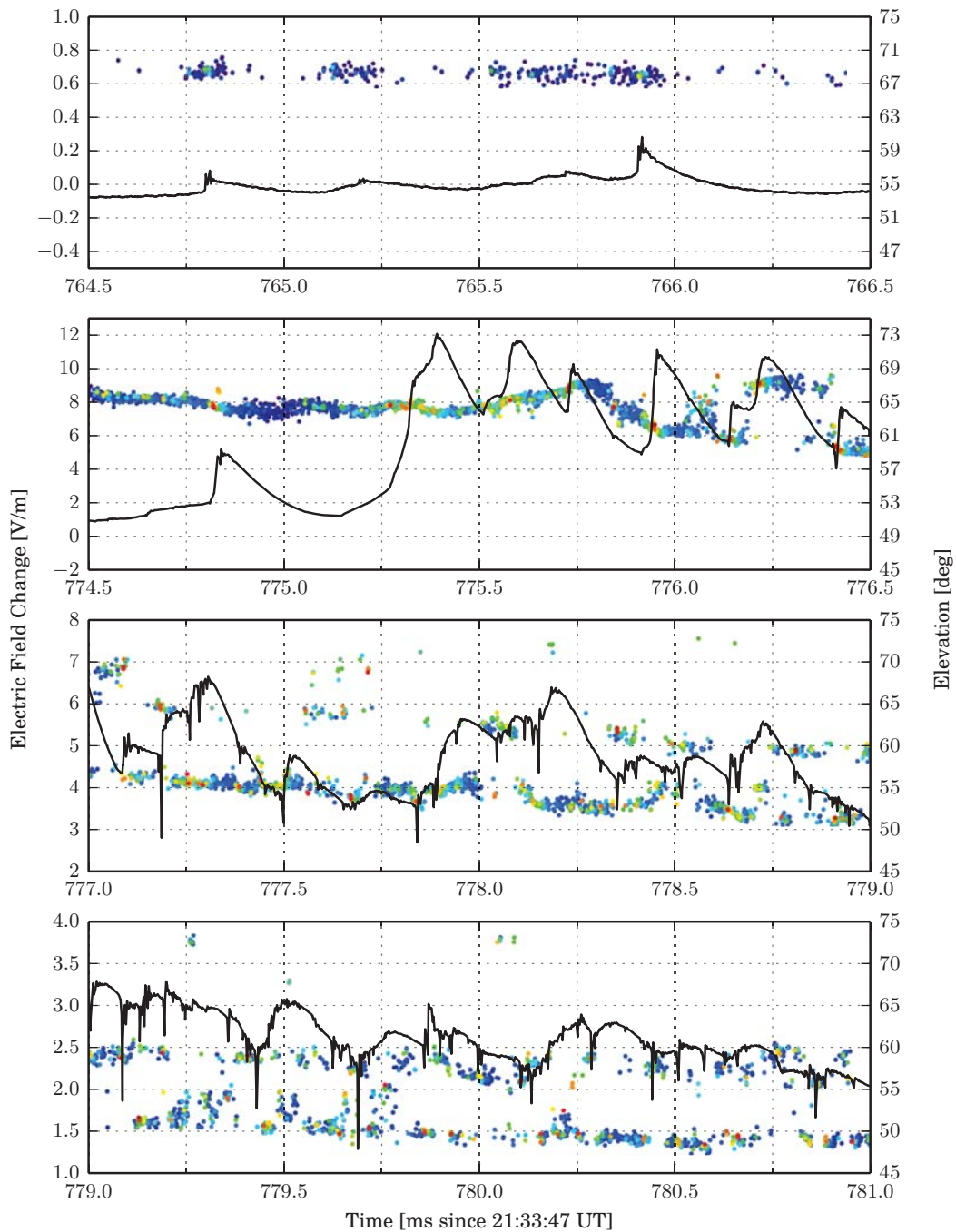
Figure 6.14: Electric field record of select initial steps for flash D. Fast antenna record (left axis, black) overlaid on the elevation of interferometer sources colored by received power (right axis). Note, left axis scale changes with each panel.

of a few hundred meters, and inter-step intervals of a few milliseconds. At the beginning of the flash, the stepping rate is frequently higher (the inter-step interval is lower), but the step lengths are unchanged. The higher stepping rate accounts for the higher average negative leader propagation velocity, and is likely a biproduct of higher ambient electric fields in the cloud. In comparison, the step lengths at lower altitudes are shorter in length, more frequent, and may propagate faster. It seems plausible that the difference between the step lengths of low and high altitude negative leaders is due to differences in pressure, and sometimes differences in the charge density of the cloud, but the results are inconclusive. By tabulating the step lengths of many more negative leaders, it should be possible to determine an empirical relation between pressure and step length, however, this would be a much more involved study.

The observations also indicate that initial breakdown pulses are simply normal negative leader steps. The VHF record for IBPs are very similar to the VHF records of later, horizontal negative leader steps to the point of being almost indistinguishable. In addition, the later horizontal steps also show sferics with features similar to the characteristic sub-pulses of the IBPs, although they are smaller in amplitude. The larger amplitude and number of the sub-pulses in IBPs is again likely a consequence of the higher ambient electric fields near the flash origin.

The physical mechanism producing the characteristic sub-pulses is still unclear. The sferic of each sub-pulse has a significant DC component, indicating that some charge was physically moved during the process. While the VHF record shows a brightening during each sub-pulse, usually no discernible motion can be seen. In the few cases where a direction of motion is indicated, the direction is towards the flash origin (down for normal intracloud flashes). This indicates that the characteristic sub-pulses are produced by a highly impulsive current carrying positive charge towards the origin of the flash.

Speculating further on the physical mechanism of initial breakdown pulses, it appears as though each negative leader step is made up of a number of miniature steps as the space leaders are connected to the main negative leader body. Each time a space leader is connected to the main channel body, a characteristic sub-pulses is produced, as as depicted in Figure 6.15. At the end of the negative leader tip, a number of space leaders (shown as polarized circles) forms in the streamer zone of the leader (shaded blue). At some critical point, positive breakdown joins the nearest space leader with the main negative leader body, producing a highly impulsive current carrying positive charge towards the flash origin. Once the first space leader is joined the rest follow in quick succession, like knocking over a row of dominoes. After all the space leaders are connected to the main leader channel, a new streamer zone with new space leaders must be formed before the process can repeat. In this way, steps a–e of Figure 6.15 occur over 100 μs or so, while step f–g can take several 1–8 ms to complete.
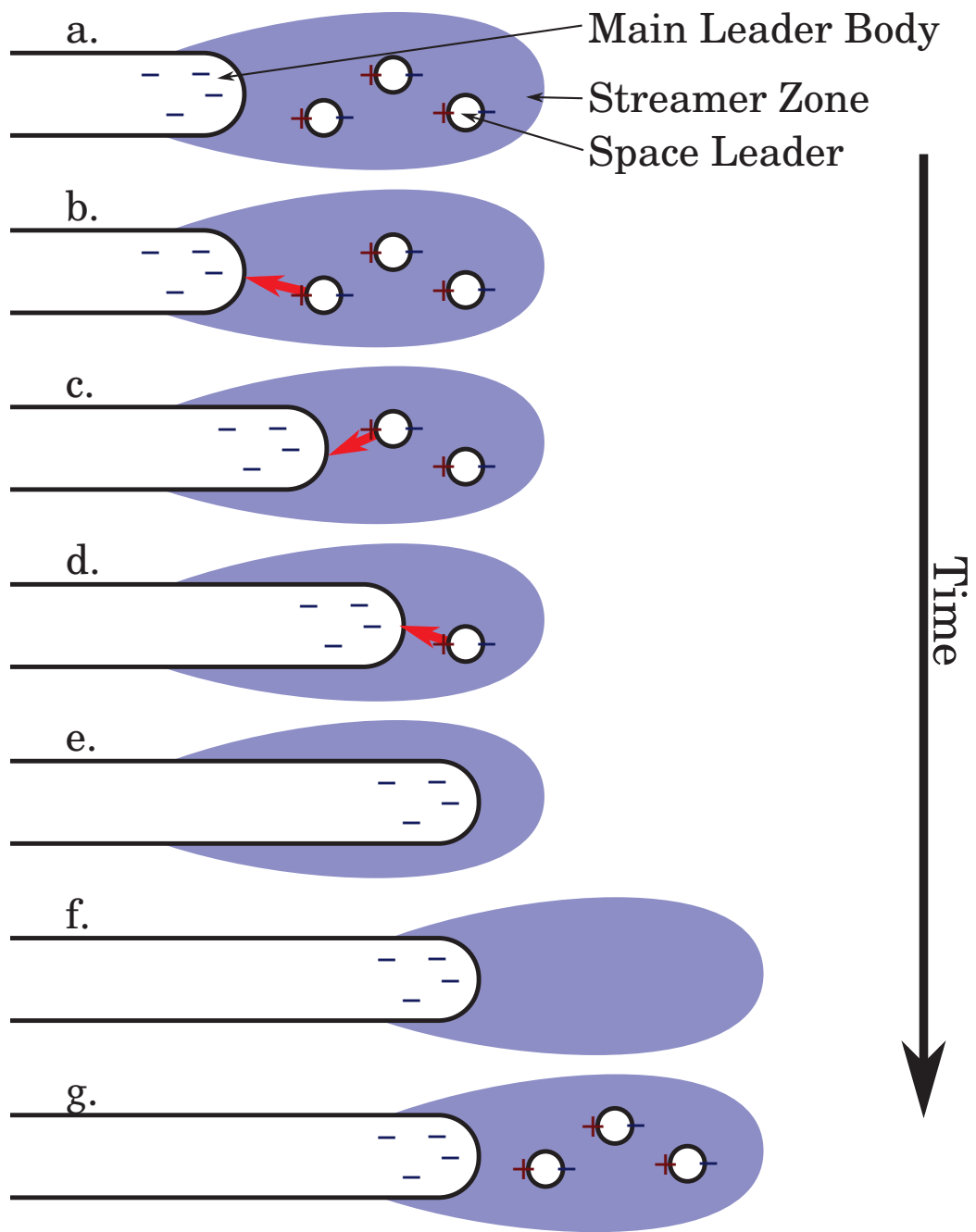
Figure 6.15: Mechanism which may produce initial breakdown pulses.

6.2 The Positive Leader

When the very first results from the continuous sampling interferometer were examined in 2012, one of the most striking features was the amount of emission located in the positive breakdown region. The overwhelming conclusion in the literature at the time was that the positive leader produced little or no VHF emission. The previous New Mexico Tech interferometer study of lightning mapped K-changes with great accuracy, and saw short bursts of positive breakdown during some K-changes, but saw little or no activity associated with the propagation of the tip of the positive leader itself in intracloud flashes (*Shao and Krehbiel*, 1996). Frequently, claims of no positive leader emission reference back to *Shao et al.* (1999), which showed that there was no detectable emission from several descending positive leaders of positive cloud-to-ground flashes measured in New Mexico. These measurements were made with essentially the same hardware used for the New Mexico Tech narrowband interferometer study, but without the location capability. The narrowband interferometer could not locate the VHF radiation produced by positive breakdown, likely due to the higher (274 MHz) operating frequency. It is therefor not surprising that no VHF radiation from positive breakdown was observed during the *Shao et al.* (1999) study. It would be instructive and interesting to compare observations of a positive cloud to ground strike with the measurements presented in *Shao et al.* (1999). Unfortunately, no nearby positive cloud-to-ground flashes have yet been observed with the broadband interferometer, so a direct comparison to these measurements cannot be made.

In addition to the above, VHF emission from the positive breakdown region is not seen immediately following the initiation of the flash when observed with any VHF location system (including the LMA). Instead, a negative leader is seen first, and a short time later faint sources are detected in the positive breakdown region (*Thomas et al.*, 2001). However, lab measurements have shown that positive leaders and streamers will propagate in lower background electric fields than negative leaders and streamers, indicating lightning flashes should initiate first with positive breakdown, and then negative should follow (the reverse of what is observed). If the positive leader produces VHF radiation, why is it not detected until the negative leader has propagated a significant distance?

There is no question that VHF radiation is produced in the positive breakdown region of the flash (the negative charge region of the storm), as such radiation has been observed by many instruments consistently over the last 20 or more years. What is in question is the production mechanism of this radiation. The traditional explanation for the observed VHF radiation originating in the positive breakdown region of a flash is that it is produced by retrograde negative breakdown (called K-events) which is retracing the ionized channel produced by

the positive leader. This provides a convenient explanation for the delayed onset of positive breakdown in a flash. No radiation will be seen in the positive breakdown region until the positive leaders are long enough to cut off and produce K-changes. However, the interferometer maps of lightning, and even recent maps of lightning made with the LMA (*Edens et al.*, 2012), see a qualitative difference between the radiation produced by K-changes, and the behavior of an increasing amount of the VHF radiation located in the positive breakdown region.

Figure 6.16 shows the interferometer map for flash F during a 20 ms period starting at 03:11:51.247 UT, early in the flash when the negative leader was not very active, but there was profuse emission being produced in the positive breakdown region. Flash F is shown as the initial example because it occurred directly over the interferometer, causing the measurement to be as sensitive as possible. The top panel shows a time series of the interferometer source (colored by received power) and the fast antenna record (black). The bottom panel shows the interferometer map in the cosine projection. The integrated VHF luminosity of all activity prior to the beginning of the time series shown above is displayed in grey-scale, and overlaid is the activity during the 20 ms time period colored by received power. The color scale used is arbitrary, but identical to that used in the interferometer maps of negative breakdown activity in the section above. The radiation seen in the positive breakdown region is mostly very faint, and so the sources are almost all colored in shades of blue.

The bright channel in the integrated luminosity map extending north is the vertical portion of the negative leader, and the channel extending west–southwest is the first horizontal negative leader, both of which are discussed in detail above. The positive breakdown is much less evident in the integrated luminosity map, with only the most active showing clearly. This is partially due to the activity of the negative leader just prior to the time period shown, which masked much of the faint radiation produced in the region.

The interferometer map of the time period appears scattered semi-randomly over all of the channels in the negative charge region (the positive leader channels), and extending up the vertical channel produced by the negative leader. A small part of the emission is produced by K-processes which are short in both time and spatial extent, and are identifiable in the time series of the figure as bright VHF sources, clustered tightly in time and with significant extent in elevation angle. The duration of these K-processes is quite variable, but is on the order of 50 μs. Because the K-processes move negative charge towards the flash origin, they also produce electric field deflections, although the deflection is not large due to the small size of the K-process. In addition to these K-processes, the interferometer observations show the occurrence of a steady but somewhat random sequence of what has been termed 'flickering' VHF activity. All of the radiation
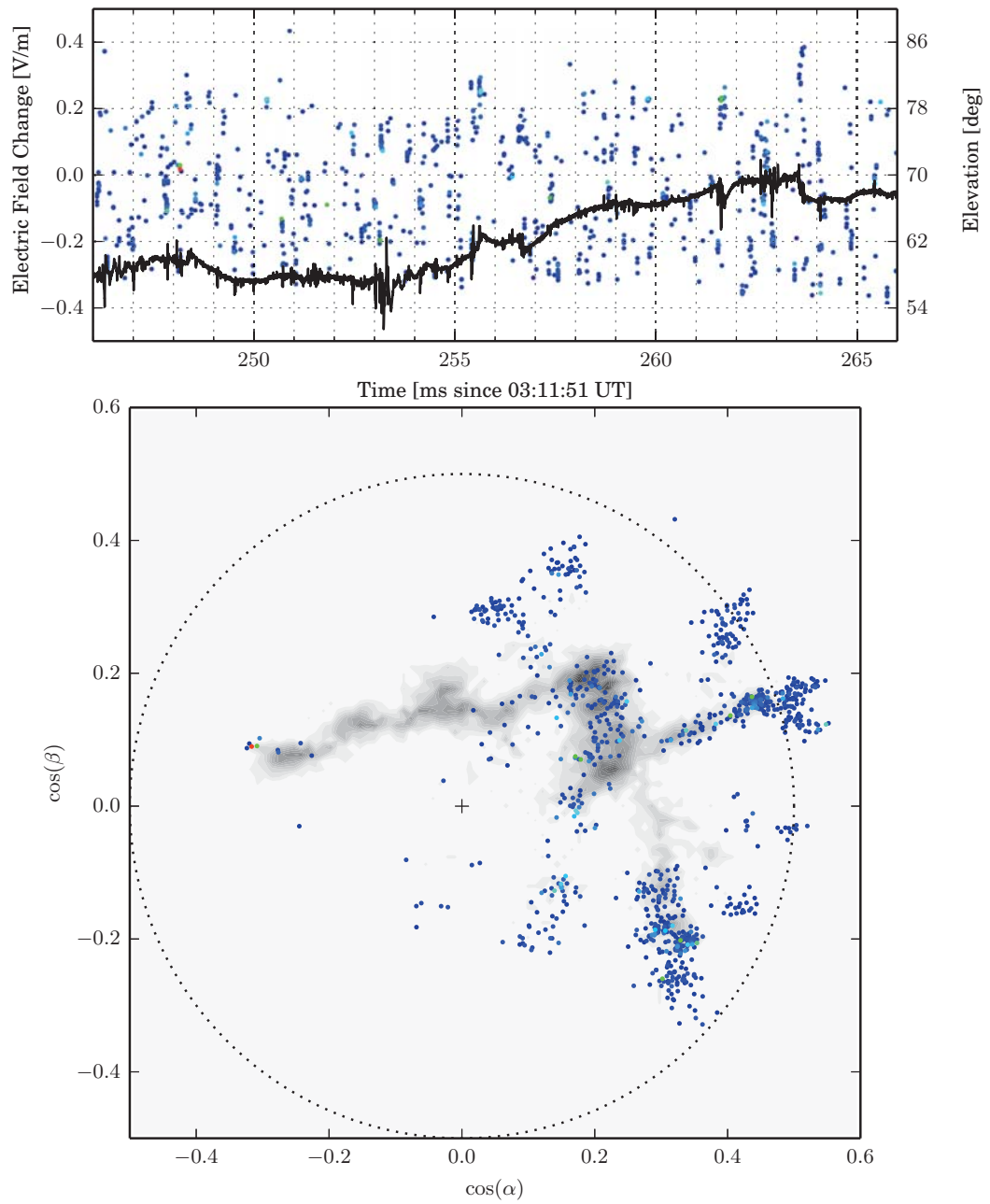
Figure 6.16: Positive breakdown in flash F.

located in the positive breakdown region (both the flickers and the K-processes) accumulate over time and space to reveal the developing positive channels.

Showing conclusively that the flickering emission is produced by a different physical mechanism than the small K-processes has proven extremely difficult. The flickering emission is faint, so the location uncertainty is relatively high. Added to this, the emission is extremely short lived and slow moving, such that a typical flicker moves a small distance. It is not surprising that attempts to measure the propagation direction have not met with success.

The best way to show that there is a qualitative difference between small K-processes and the faint flickering emission is by example. A clear, unambiguous example demonstrating a difference between K-emission and flickering emission has not yet been found, so several examples will be shown of different aspects of the radiation. First is a detailed look at a 10 ms portion of the interferometer and fast antenna record shown in Figure 6.16, starting at 03:11:51:252 UT. This has been done as a sequence of images, Figures 6.17–6.26, each showing 1 ms of data. As above, the sources are plotted on a time series with the fast antenna record, and overlaid in the cosine projection on the integrated VHF luminosity of all located sources before the beginning of the record. Each figure has two panels, covering the same time period: the left panel shows the sources located during the 1 ms period colored by source index, and the right panel colored by received power using the same scale as Figure 6.16. The panel colored by index is included so that clusters in time can be identified on the cosine projection map. During the period displayed, there is not negative stepped leader activity, so all interferometer activity with an associated electric field deflection is presumed to be a K-process, and identified in the figures with red circles.
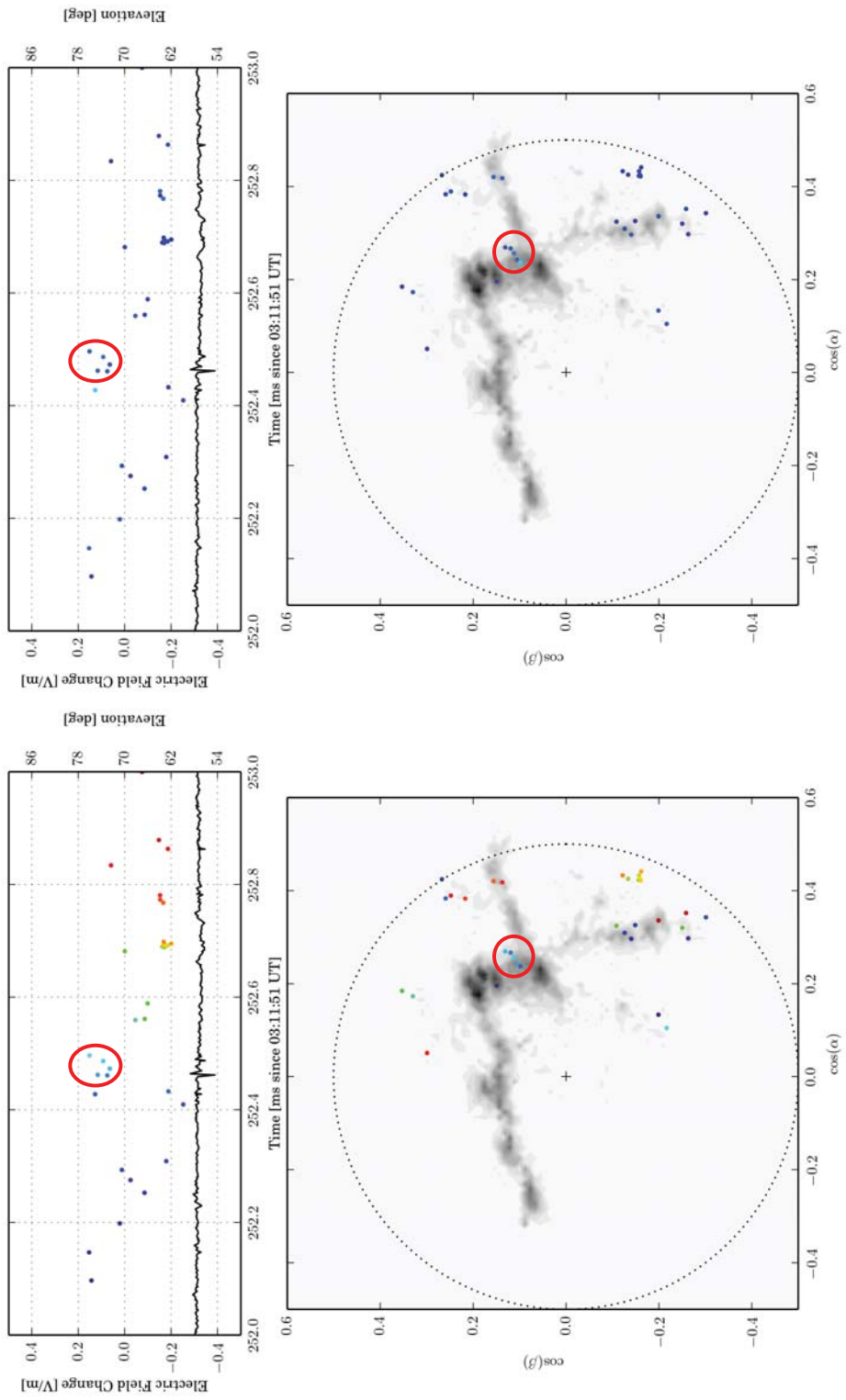
Figure 6.17: Flash F, positive breakdown 252–253 ms.

193
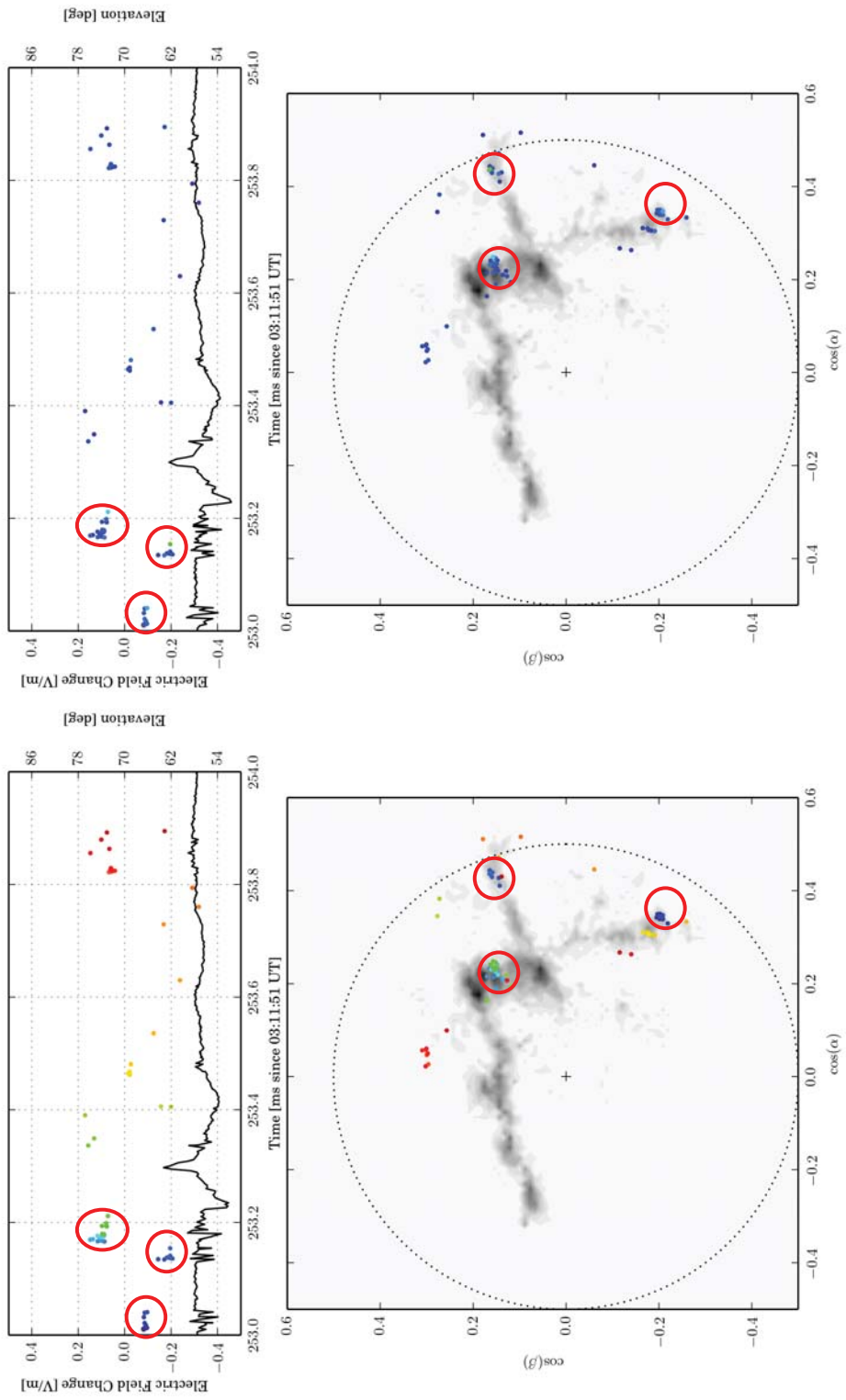
Figure 6.18: Flash F, positive breakdown 253–254 ms.

194
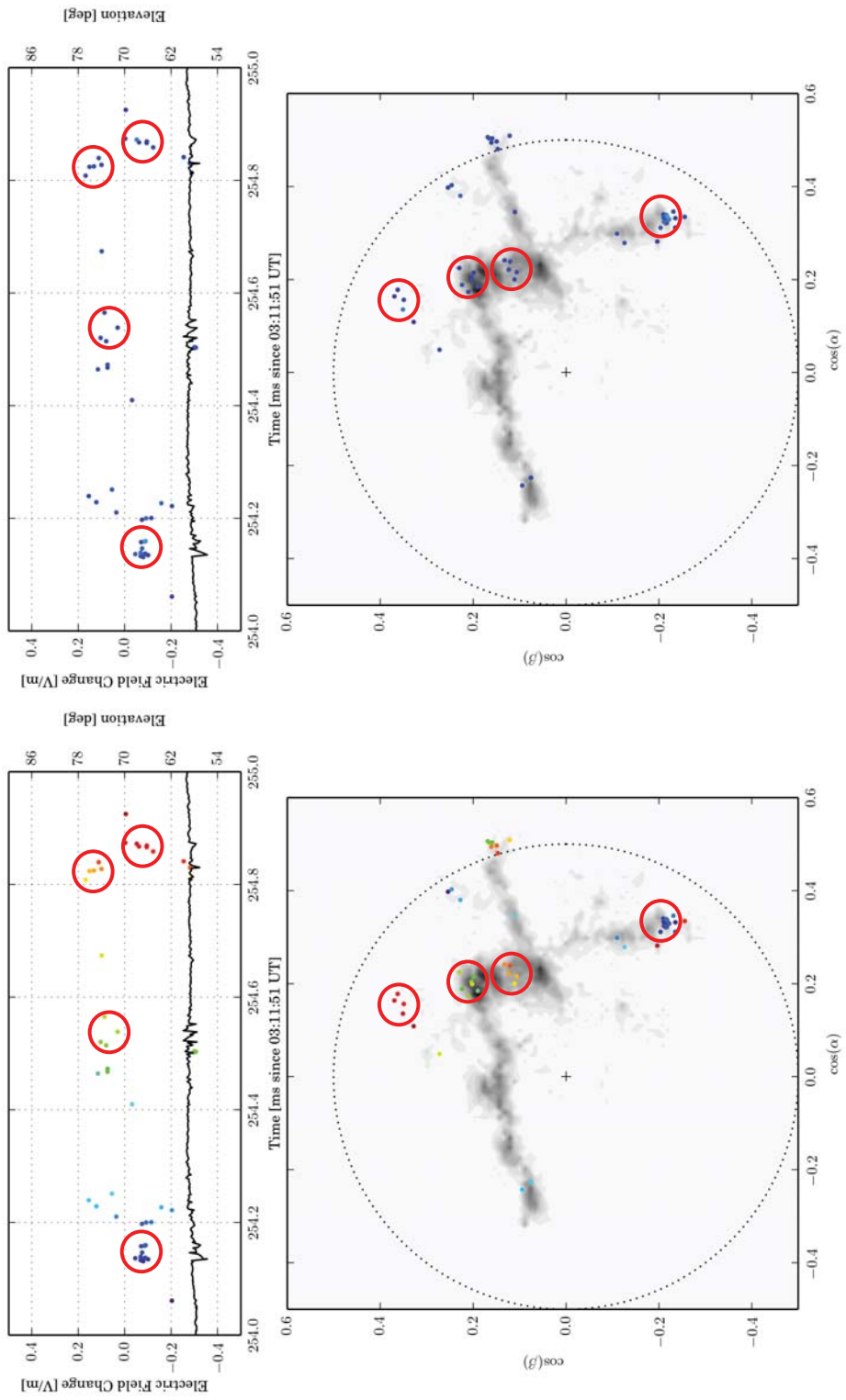
Figure 6.19: Flash F, positive breakdown 254–255 ms.

195
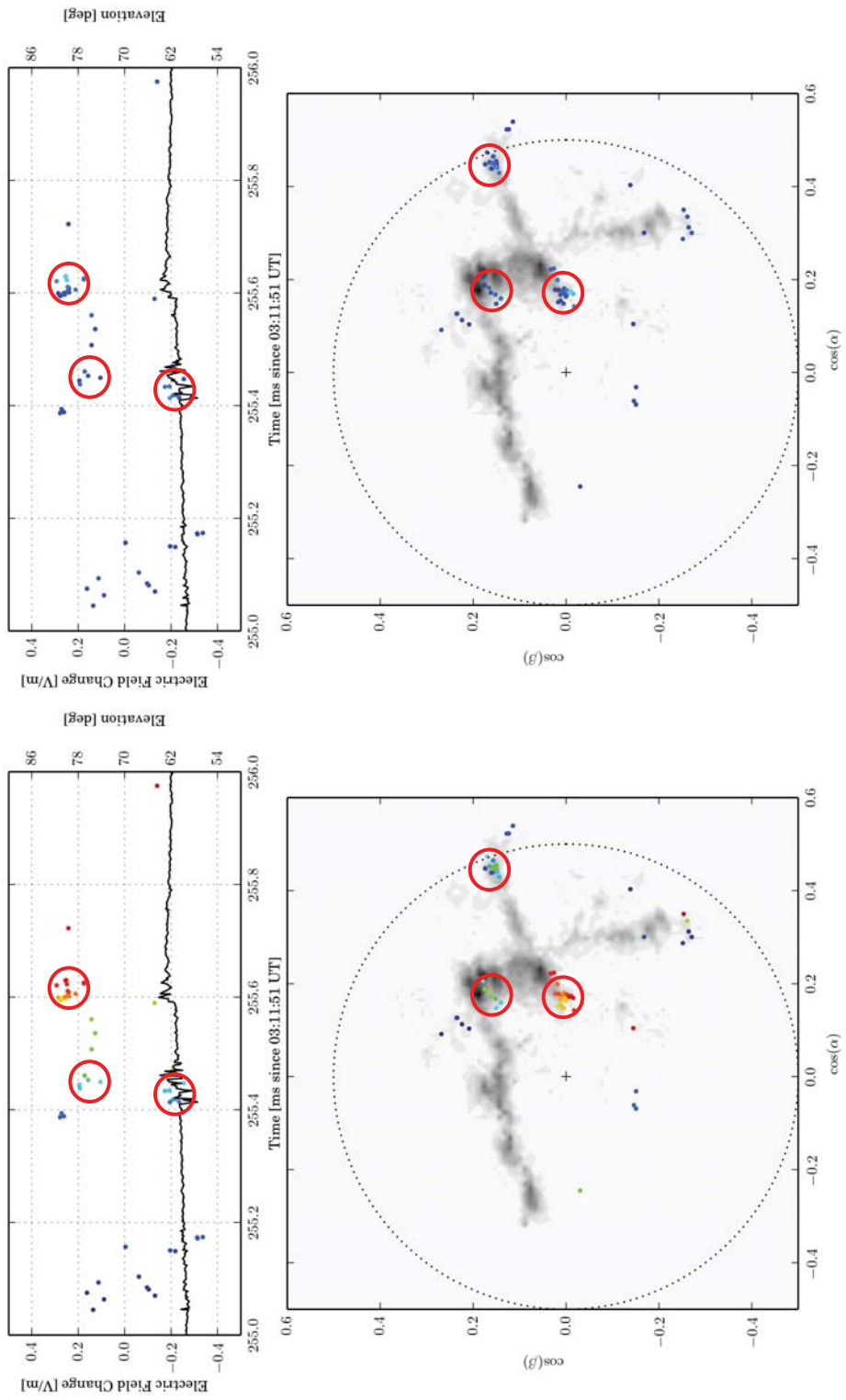
Figure 6.20: Flash F, positive breakdown 255–256 ms.

196
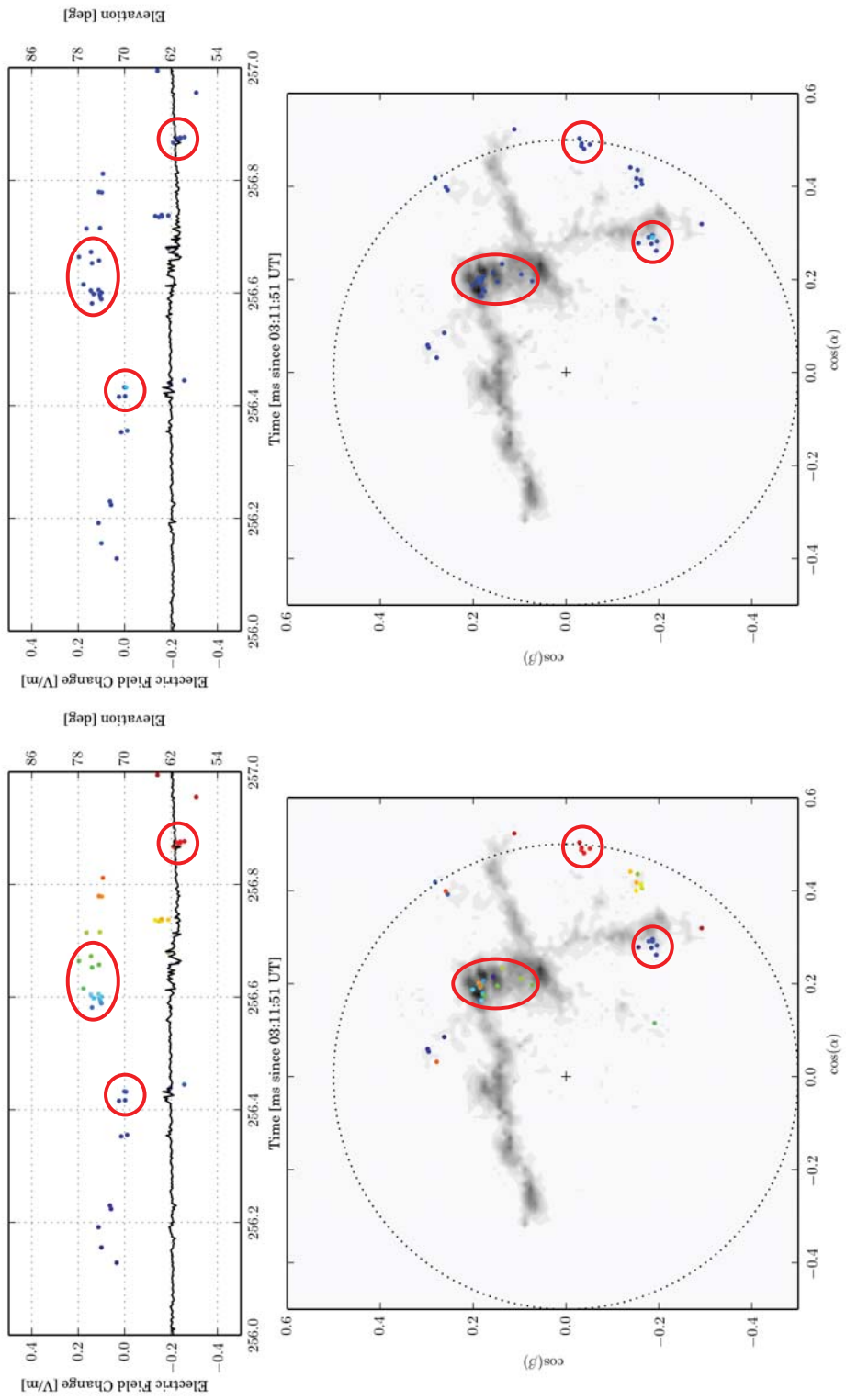
Figure 6.21: Flash F, positive breakdown 256–257 ms.
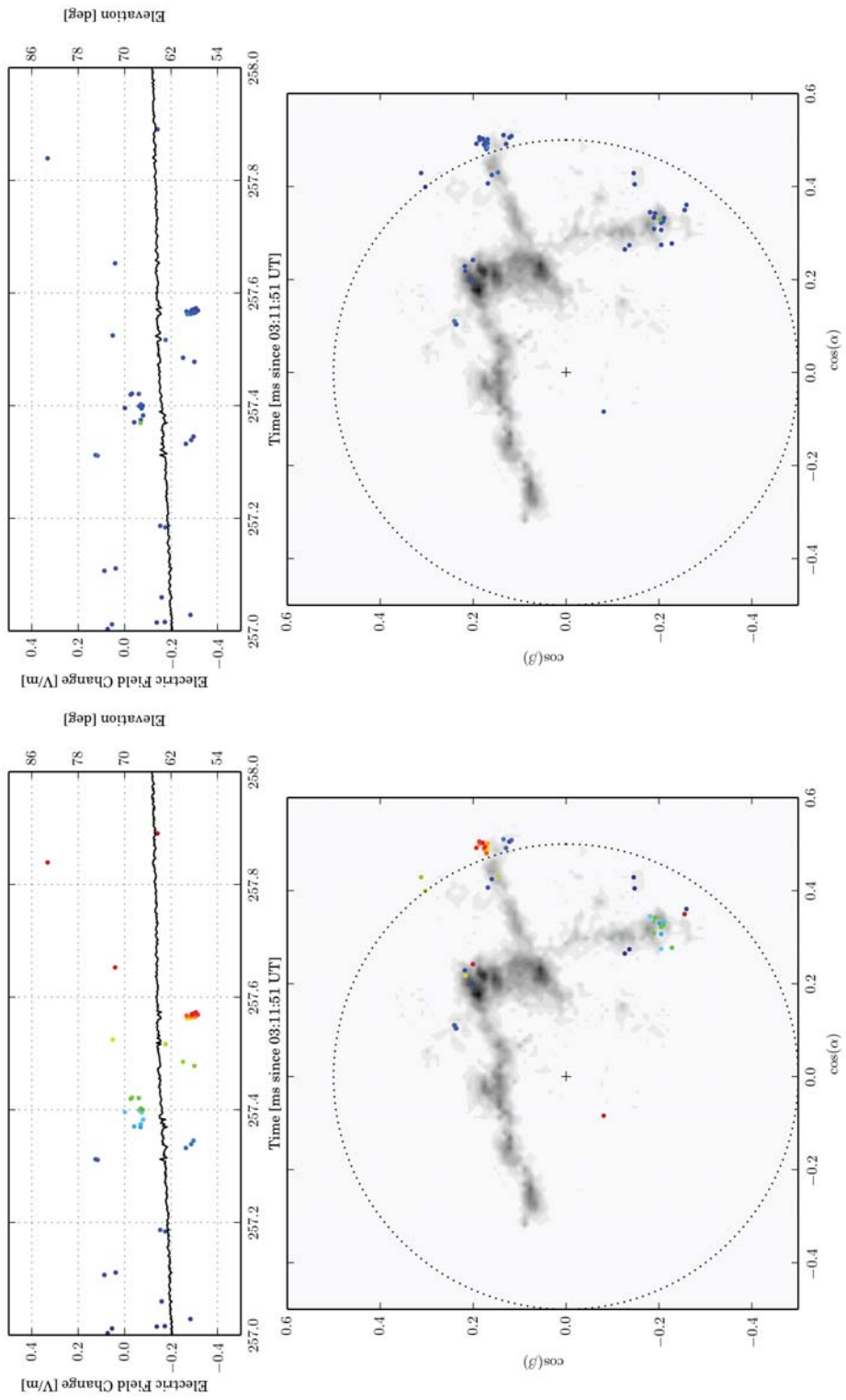
Figure 6.22: Flash F, positive breakdown 257–258 ms.

198
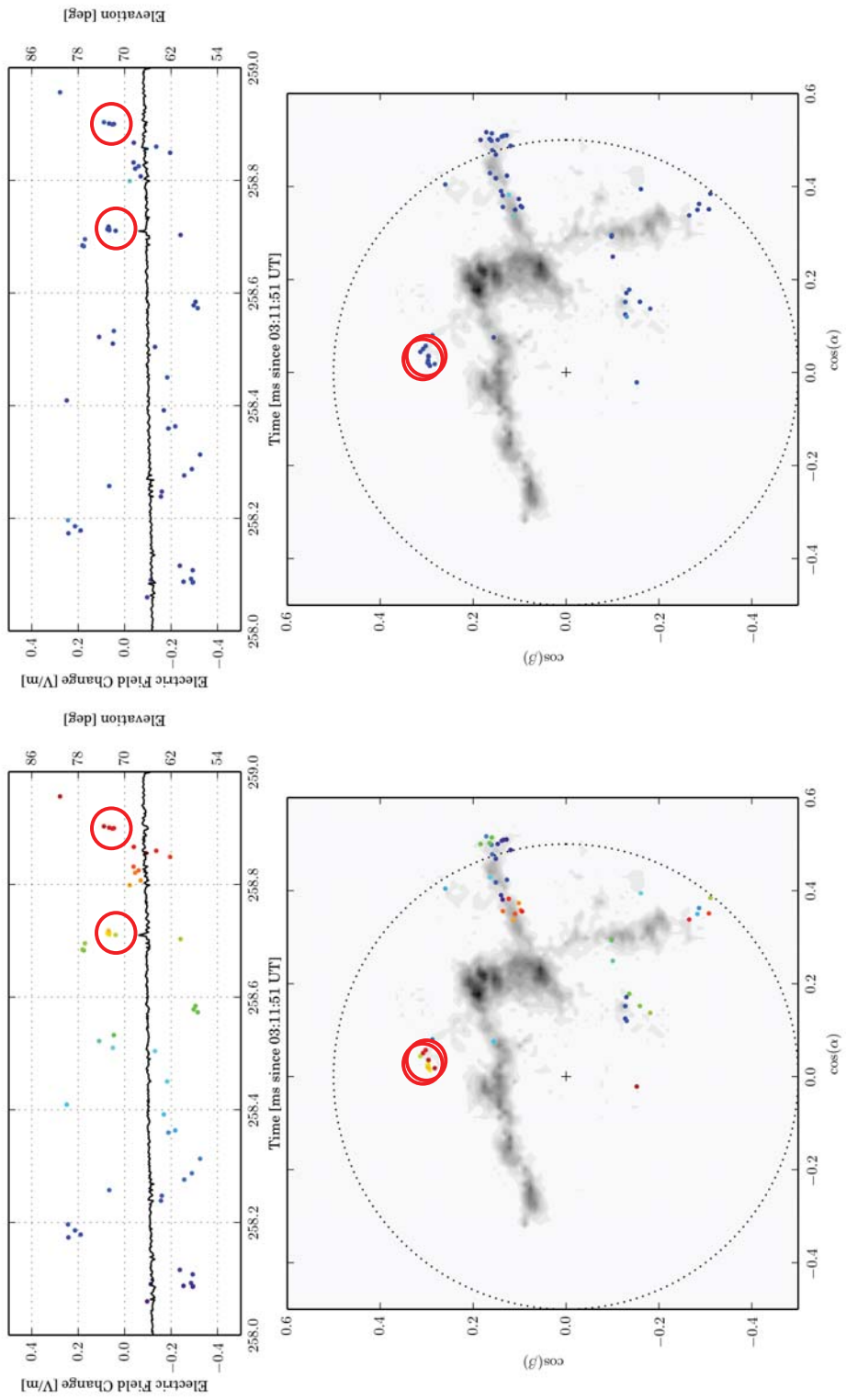
Figure 6.23: Flash F, positive breakdown 258–259 ms.

199
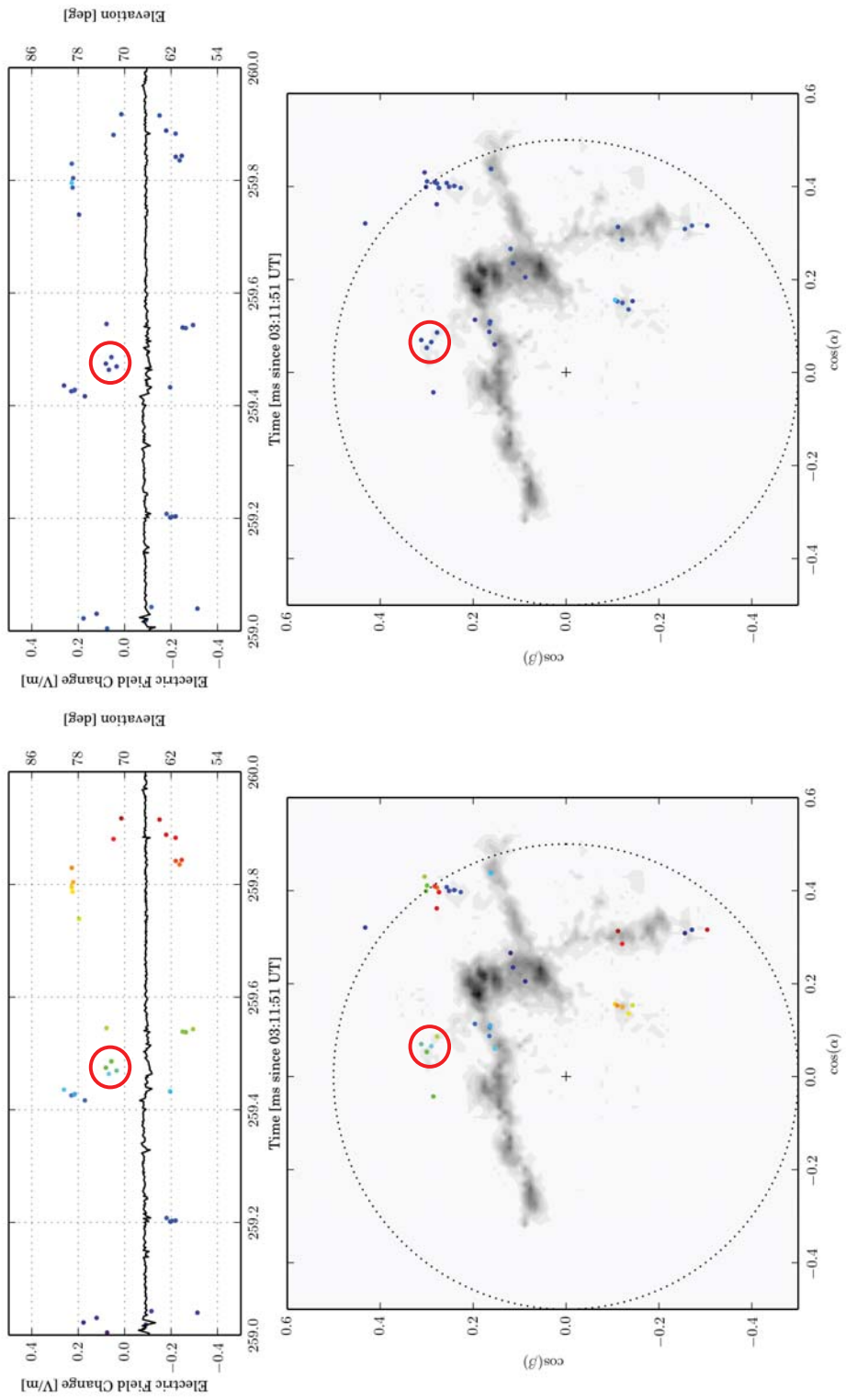
Figure 6.24: Flash F, positive breakdown 259–260 ms.
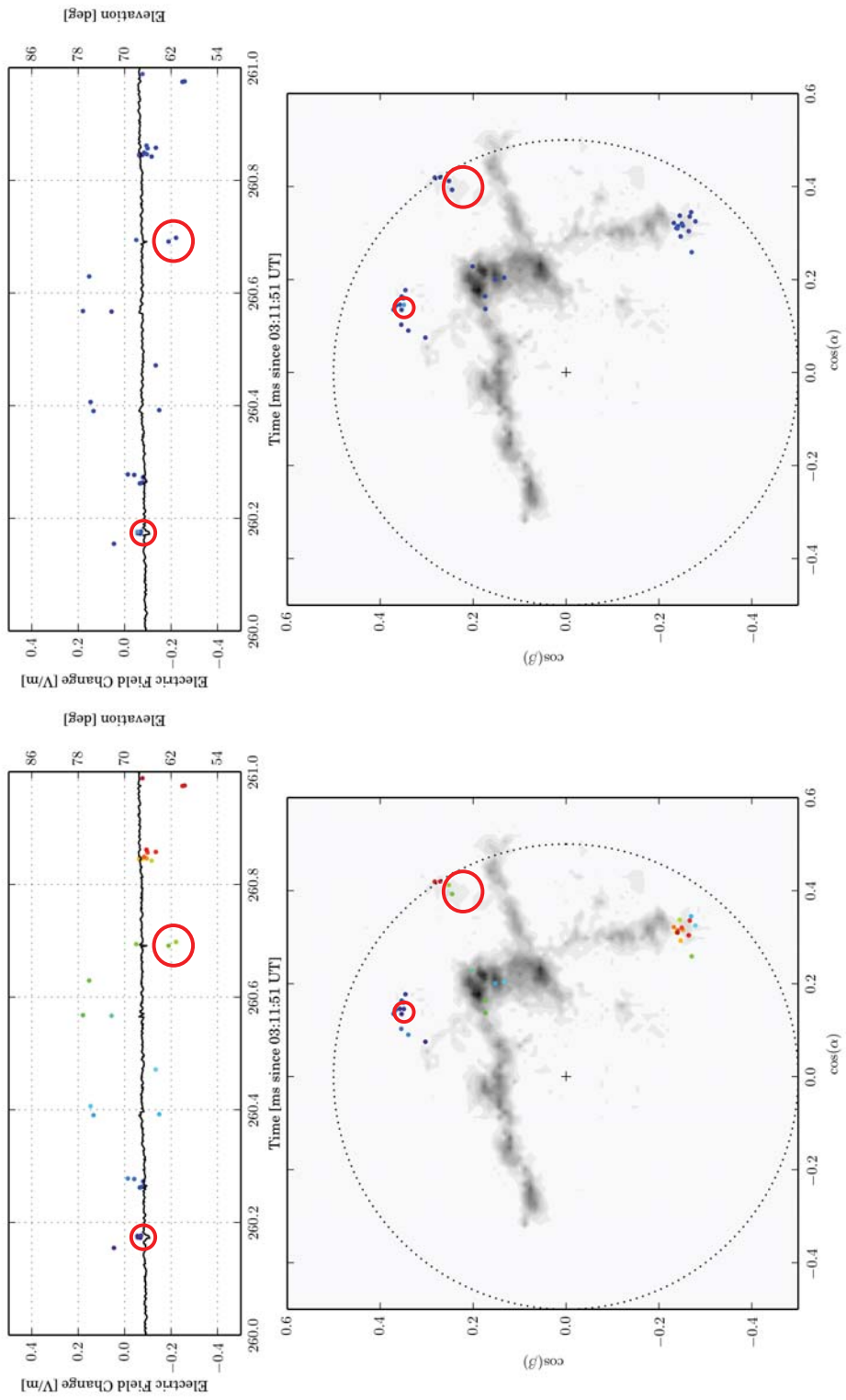
Figure 6.25: Flash F, positive breakdown 260–261 ms.
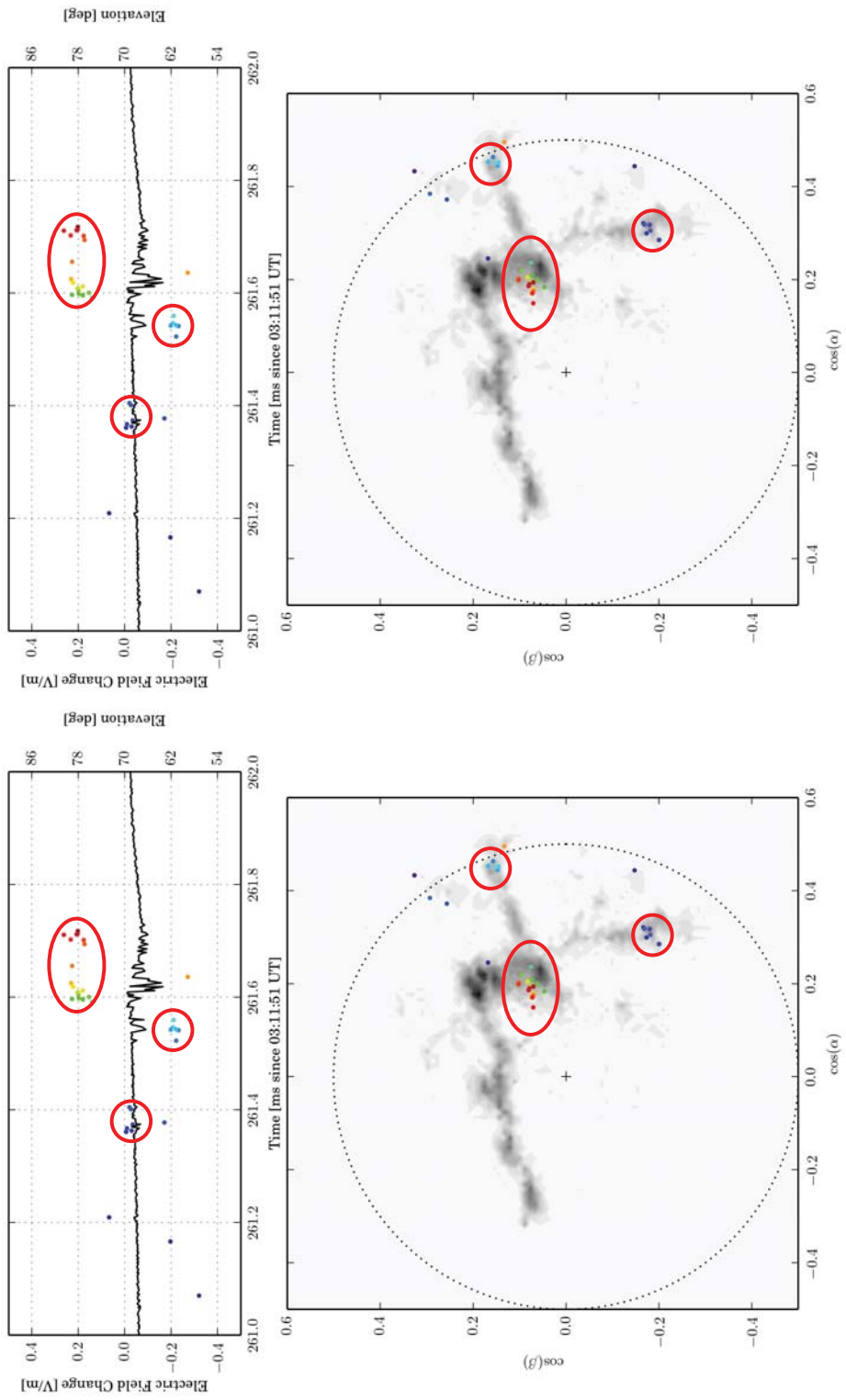
Figure 6.26: Flash F, positive breakdown 261–262 ms.

The clusters of sources not circled in red are produced by the flickering emission under investigation. The size of the flickers varies, from isolated single sources, to clusters of as many as 20 or 30 sources. Due to the manner in which the flickering emission was identified, none of the flickers have an associated electric field deflection. A deflection in the electric field is produced whenever charge is moved from one part of the lightning channel to another. Any process which does not produce an electric field deflection, but which does radiate in the VHF, much not produce a significant current or charge transfer. This does not preclude the flickers being produced by K-processes, and it is likely that the largest flickers are in fact produced by K-processes, but with currents small enough that a measurable electric field change is not produced.

The isolated sources have VHF radiation which is entirely contained in a single window in the interferometer record, 1.4 μs. Clusters of 2 or 3 sources are somewhat more common than the single isolated sources. Due to the overlap used in the interferometer processing technique, a cluster of 3 sources can be produced in as little as 2 μs. If these sources are being produced by K-processes, the K-process is extremely short lived in comparison to the 100–2000 μs duration of typical K-changes.

In the early part of the flash, the flickering emission is distributed all over the channels in and near the negative charge region, but even at this early time, the smallest clusters are predominently located near the furthest extent of the VHF radiation. In contrast, the identified K-processes and largest flickers are as likely to be located on the vertical trunk as near the positive leader tips. As the flash develops more, the flickering emission becomes even more concentrated near the tip of the propagating positive leader.

Figure 6.27 shows the flickering emission from a later portion of flash C, which has no electric field record. For this example, flash C was chosen because there is only a single active channel, resulting in a lower rate of K-changes than is seen in flash F. Similar but more complex behavior is seen in flash F. The time series of the emission looks very similar to those shown above for flash F: loose clusters of very faint sources with embedded K-processes. As before, the K-processes account for the brightest sources.

In the cosine projection, none of the radiation is located near the origin of the flash. What is more, almost all of the emission is tightly concentrated within a kilometer of the furthest extent of located VHF radiation. Also as before, the faintest clusters of sources are found preferentially closer to the apparent positive leader tip than the larger flickers and K-processes.

During this late period of the flash, the positive leader channel is being periodically reinvigorated by large scale K-changes which propagate a long distance from near the leader tip towards the flash origin. (The nature of K-changes
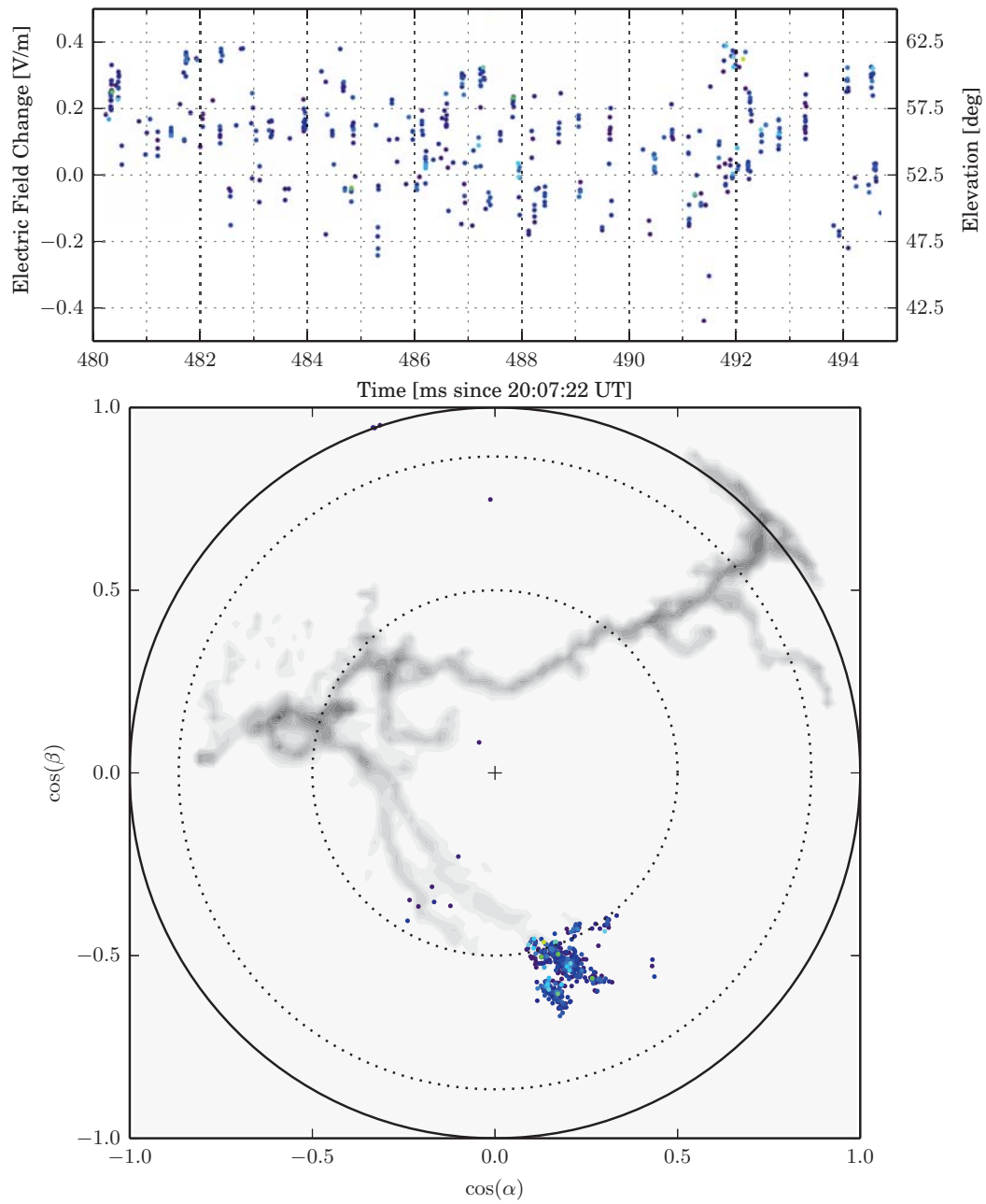
Figure 6.27: Positive breakdown in flash C.
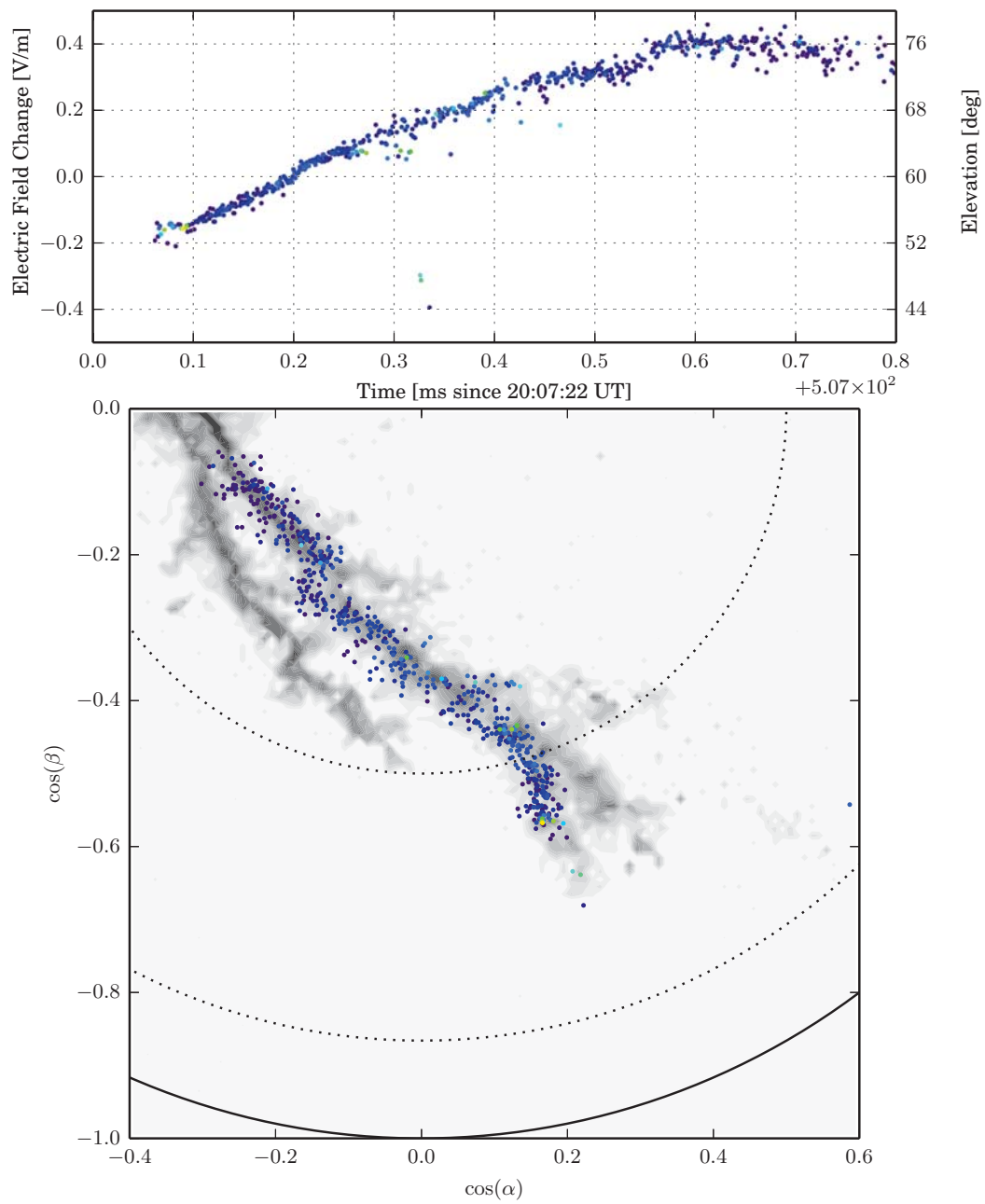
Figure 6.28: Origin of a K-change in flash C.

is discussed in more detail in Section 7.1.) Relevant to the discussion of positive breakdown is where the K-changes initiate, shown in Figure 6.28 for a K-change in flash C. The K-change initiated at 20:07:22.507 UT, and clearly starts propagating a significant distance behind the furthest extent of VHF radiation located before this time (shown in the background map in grey-scale). Approximately 300 μs after the K-change initiated, three sources (two bright, and one dim) were located a little beyond the origin of the K-change. These sources were produced by a small positive burst, which are discussed in more detail in Section 7.2, and can extend out beyond the positive leader tip. The presence of these sources slightly behind the furthest extent of previously located VHF radiation (the grey-scale background map) is further indication that the positive leader tips are producing VHF radiation and being located by the interferometer.

6.2.1 Discussion

The overall behavior of the faint flickering emission leads to the conclusion that it is in some way produced by the positive breakdown itself, as opposed to retrograde negative breakdown. However, at this stage the result is far from conclusive. Much of the data presented can be interpreted as being produced by retrograde negative breakdown, if it is present on the positive leader at all length and time scales. For example, the time series of Figure 6.27 for flash C shows the emission in the positive breakdown region to cluster in time, as would be expected for retrograde negative breakdown. The only way to conclusively determine if a VHF interferometer is capable of detecting and mapping radiation from positive leaders is to make coordinated high speed video and interferometer observations of positive leaders. The high speed video should be able to
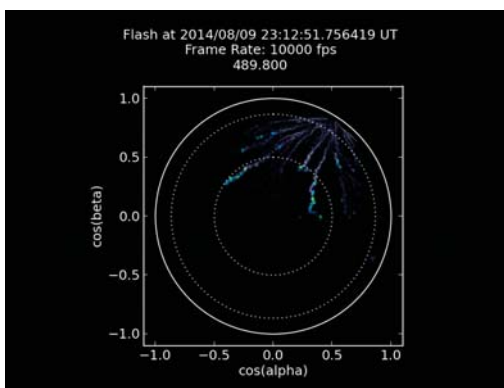
Figure 6.29: Interferometer map of triggered lightning.

unambiguously locate the tip of the positive leader, as well as determine time periods of even small K-processes. Then it is a simple matter of determining if the interferometer located emission from the negative leader tip. The good news is that, as of August 9, 2014, this measurement has now been made. In particular, a triggered lightning flash with upward propagating positive leaders was observed with both the broadband interferometer and high speed video. A still frame from a preliminary animation of the flash is shown in Figure 6.29. Due to the recent occurrence of this triggered flash, it is outside the scope of this dissertation, but does allude to exciting results soon to come.

CHAPTER 7

FAST PROCESSES

In addition to the slow moving leaders, there are many processes in a lightning flash that propagate at speeds in excess of 10^6 m/s. The two most commonly observed fast moving processes are return strokes and K-changes, but other more exotic processes exist as well. While the return strokes of cloud-to-ground flashes do not produce much VHF radiation, K-changes and other fast processes produce bright VHF radiation for their entire duration.

The Lightning Mapping Array (LMA) tends not to locate the VHF radiation from these fast moving processes. The LMA locates lightning by very accurately time tagging peaks seen in the VHF power. The technique works very well for locating impulsive bursts of VHF emission, which are produced in large quantities by, for example, a propagating negative leader. But fast processes radiate VHF noise that is slowly modulated over their duration (1-3000 μs), and so well defined peaks may not exist. Different LMA stations will time tag a different portion of the VHF emission, and the resulting location may not converge. Processing the LMA data with shorter time windows, 10 μs instead of 80 μs, helps but does not solve the problem.

In contrast, interferometers not only locate continuously radiating sources, but the location accuracy is better for this type of emission than it is for impulsive sources. This is because the interferometer integrates the phase difference of the radiation over a time window to compute a time delay between antennas. In the process, the phase difference of any noise present in the window will also be integrated, and contaminates the result. A continuously radiating source has the best possible signal to noise, and results in particularly accurate time differences. When interferometer maps of lightning are examined, the fast processes are often very tightly located, and the improved location accuracy is part of the reason why.

7.0.1 Primary Novel Techniques/Findings

- 3-dimensional measurements of time resolved K-change velocities.

- Characterization of fast positive breakdown.

7.1 Velocity of K-changes

K-changes are a consequence of a fundamental instability of the positive leader, and are seen in virtually all flashes which have positive leader channels over a certain length. The instability arises because the current produced by a traveling positive leader tip is not sufficient to maintain the temperature of the plasma it is made up of. Once the channel starts cooling, the resistivity of the channel increases and the current reduces even further, causing a cascading effect which ends with the channel cutting off. Interestingly, when the channel cuts off, the tip of the positive leader continues to propagate. Then a bright wave of negative breakdown is seen traveling from slightly behind the advancing positive leader tip backwards towards the origin.

The emission ceases when the negative breakdown wave: reaches a portion of the lightning channel structure which is still conducting (usually a branch point); deposits all the negative charge it is carrying along the previously formed channels; or reaches the end of the previously formed channels (the tip of the negative leader channel). Late in the flash, K-changes can be quite impressive, extending 10–20 km from one end of the lightning channel structure to the other. The K-processes very early in the flash (discussed but not explained in the previous chapter) occur in much the same way, but quickly reach a portion of the channel which is still conducting, along which they do not radiate significantly.

In this section, the 3-dimensional velocity of a large number of K-changes is measured, made possible by the quasi-3D conversion discussed in Section 4.4. The velocity is computed by fitting a piecewise linear function to the path traversed by the K-change in a least-squares manner. For each linear segment, a distance and velocity can be computed; in this way, not only is the velocity of each K-change measured, it is measured as a function of time. So that a large sample of such K-changes could be examined, the fitting is done semi-automatically, taking as an input only the time period of the K-change. A linear segment is fit to the sources within 2 km of the end of the last segment, including no more than 40 sources.

Two examples of the resulting fits are shown in Figure 7.1, one from each flash. On top is a map of the K-change in standard LMA format. Shown in black
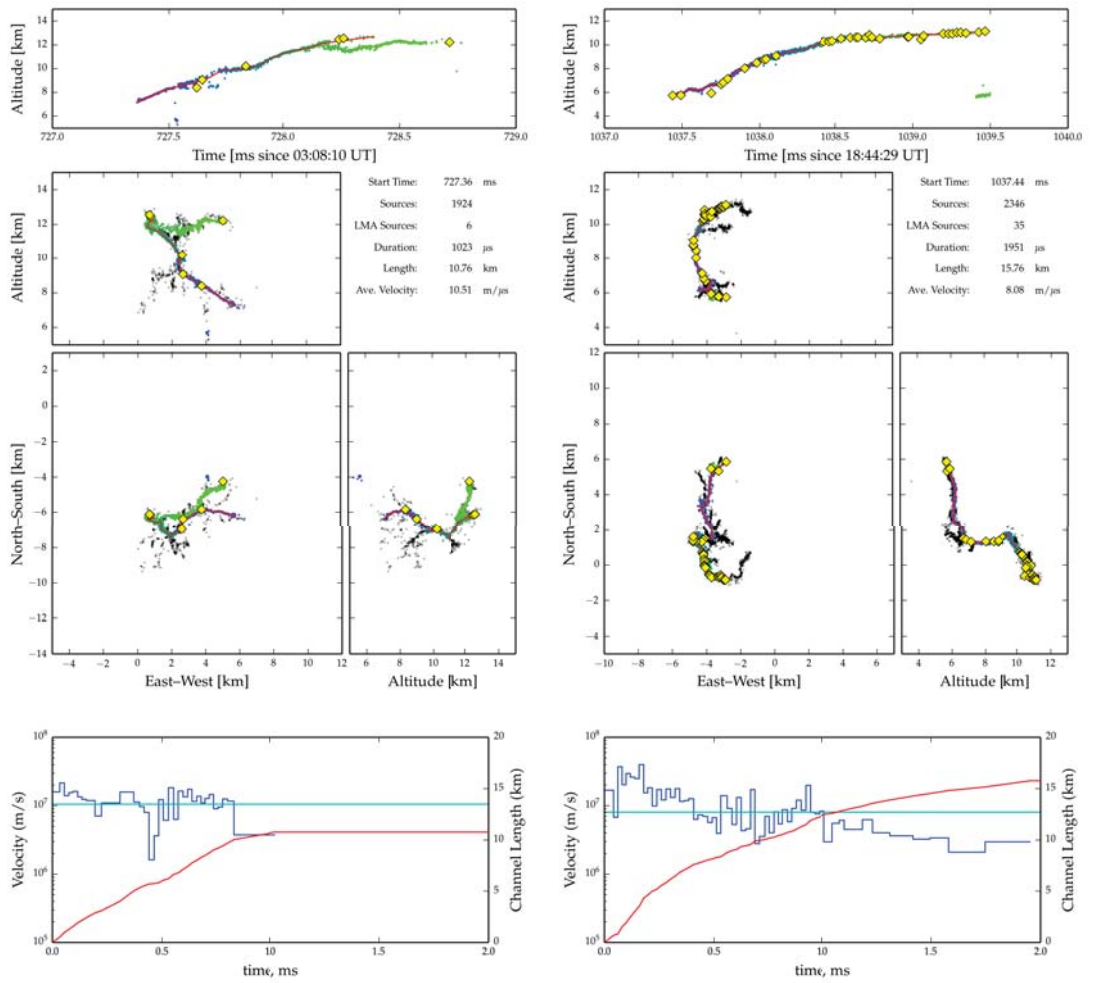
Figure 7.1: Example K-change piecewise linear fits.

are the LMA sources which occurred before the K-change, giving a reference of which channels had been formed at this point in the flash. Shown in blue-green are the quasi-3D interferometer sources, with color showing the progression of time. Overlaid in yellow diamonds are the LMA sources located during the K-change. Lastly the piecewise linear fit is shown in red. On bottom is a plot showing the velocity and length of the K-changes as a function of time. The velocity as a function of time appears stepped, this is an artifact of the piecewise linear fit. Each linear segment has a constant velocity.

In total, 47 K-changes from 2 flashes (A and B) have been fit in this manner, and a summary of their lengths and velocities is presented in Table 7.1. Only K-changes with durations longer than 200 μs were included in the set, as K-changes shorter than this are prone to inaccurate and ambiguous fitting. For each fit, a set of plots like those shown in Figure 7.1 was made to ensure that the piecewise linear path produced by the algorithm is correct.

The results show typical average K-change velocities of 1–10$\times10^6$ m/s. This is in line with measurements presented in previous studies, including 2-dimensional measurements by *Rhodes et al.* (1994), *Shao et al.* (1995), *Mazur et al.* (1995), *Shao and Krehbiel* (1996), and several others, and 3-dimensional measurements by *Bondiou et al.* (1990), *Akita et al.* (2010), and *Qiu et al.* (2012). In all the above measurements, only the average velocity of K-changes was reported, not as a function of time. Frequently the velocity drops at the end of longer events, such as the K-change for flash B shown in Figure 7.1. The change in velocity is accompanied by a change in VHF emission, where it transitions from nearly continuous to more impulsive. This is indicated by the large fraction of sources located by the LMA in the slower portion of this K-change.

The velocity produced by the piecewise linear fit for an individual K-change shows a lot of variation, making it difficult to identify trends in the behavior. However, because measurements have been made for such a large number of events, a better estimate of the velocity as a function of time since the beginning of the K-change can be made by averaging over all K-changes the velocity at each time period. This has been done in Figure 7.2 for flashes A and B for the first 1 ms of duration. The average velocity is shown in blue and is much less varied than the velocity of an individual K-change. A large fraction of the K-changes included in the measurement have a duration of less than 1 ms, so included in red is the number of K-changes that contributed to the average velocity measured at any time.

The trend seen for each flash is quite similar. For the first 200 μs, the velocity of the K-change increases. After the velocity peaks around 200 μs, the trend reverses and the velocity decreases. The largest K-changes, those that extend through the negative breakdown region, frequently have a duration longer than

	Flash A				Flash B		
Time (ms)	Duration (μs)	Length (km)	Velocity (m/μs)	Time (ms)	Duration (μs)	Length (km)	Velocity (m/μs)
637.7	920	6.50	7.06	887.1	1707	6.12	3.58
656.0	911	7.04	7.73	912.7	987	7.78	7.87
660.6	342	4.54	13.24	928.3	975	8.08	8.28
665.3	737	5.61	7.60	943.4	1115	5.83	5.23
666.8	346	2.06	5.96	958.2	2470	18.99	7.69
673.9	506	4.64	9.16	969.7	493	1.90	3.85
690.4	778	3.51	4.51	979.7	1113	7.63	6.86
692.1	478	4.05	8.46	984.2	1431	13.46	9.40
693.7	1295	11.24	8.68	1002.5	840	5.74	6.83
708.6	849	3.46	4.07	1011.4	360	3.73	10.34
724.0	1071	8.46	7.89	1025.8	911	7.46	8.18
727.2	1023	10.76	10.51	1037.4	1951	15.76	8.08
743.7	670	6.16	9.18	1068.0	822	11.45	13.92
744.5	265	4.76	17.89	1081.7	1667	16.46	9.87
745.7	206	3.67	17.76	1090.2	1228	11.86	9.66
746.9	335	3.82	11.41	1111.4	1489	13.14	8.82
770.3	670	5.81	8.66	1118.3	555	6.08	10.93
782.1	603	5.86	9.72	1140.2	944	6.87	7.28
799.5	688	6.05	8.78	1149.5	716	5.69	7.95
801.9	462	1.56	3.37	1150.8	1052	3.10	2.94
838.5	513	4.51	8.80	1174.8	1207	11.38	9.42
847.1	412	4.07	9.85				
853.5	418	2.85	6.80				
888.3	969	7.00	7.21				
891.0	897	11.97	13.33				
905.6	1550	12.01	7.75				
932.1	1252	11.94	9.53				

Table 7.1: Summary of length and velocity of K-leaders in flashes A and B.
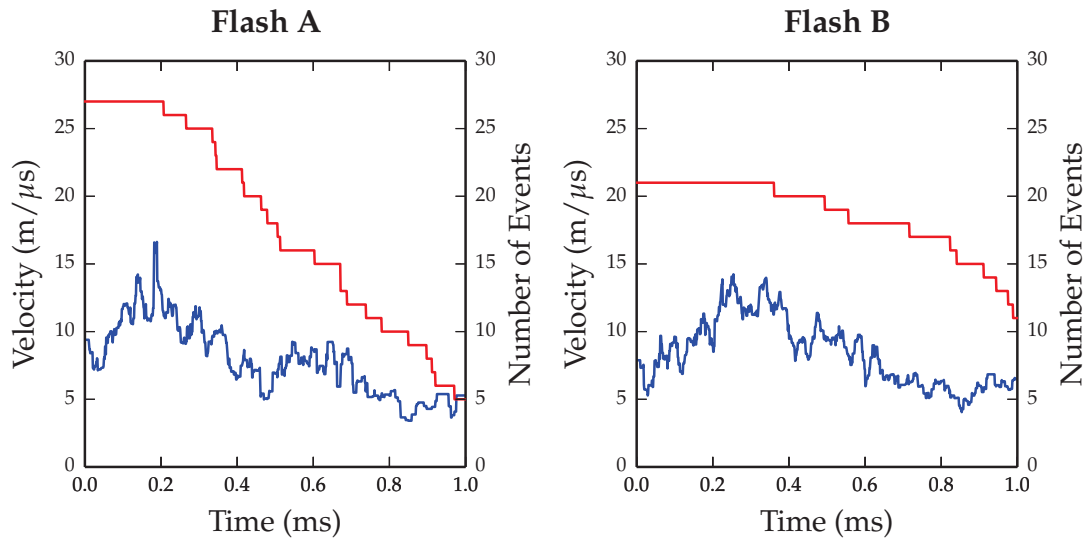
Figure 7.2: Average velocity versus time for K-changes in flashes A and B. (Blue) average velocity (left axis). (Red) Number of K-changes contributing to average.
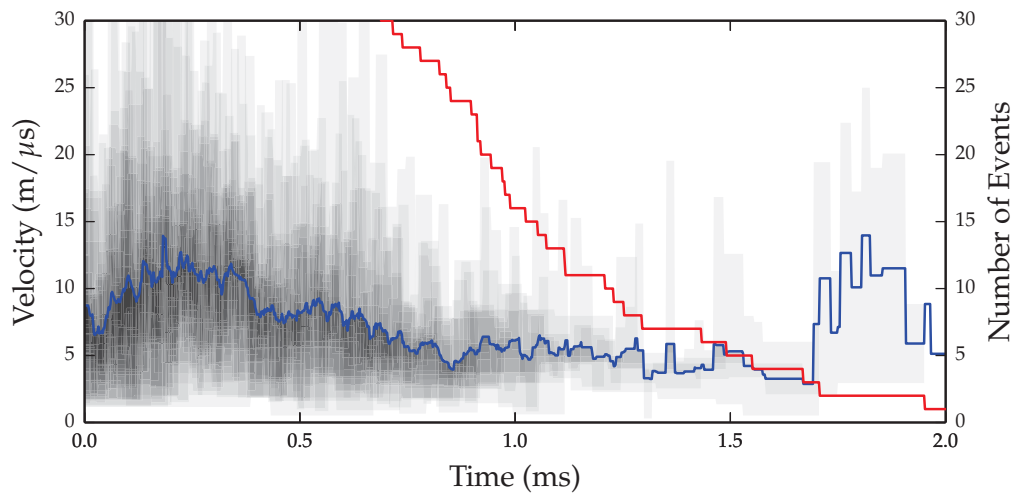
Figure 7.3: Average velocity versus time for K-changes in flashes A and B combined. (Blue) average velocity (left axis). (Red) Number of K-changes contributing to average. (Shaded) velocity of all K-changes contributing to the average, showing the spread of velocities.

1 ms. However, not enough large K-changes occur in a single flash for a reliable average velocity to be calculated. By combining the results from both flashes, the velocity trend can be extended, as shown in Figure 7.3

The decreasing velocity trend continues until for around 1.7 ms. There are very few K-changes with a duration longer than this, but these few K-changes show a sharp increase in velocity. The cause for the increase is not clear, and may not be significant.

7.2 Fast Positive Breakdown

In Section 7.1, fast propagating breakdown carrying negative charge (K-changes) was discussed is some detail. In addition to the common K-changes, there exists a fast propagating breakdown carrying positive charge. Much like K-changes, fast positive breakdown produces bright VHF radiation that is continuously emitted. The duration of positive breakdown events tends to be shorter, only 1–100 μs, but they also tend to be somewhat brighter than the K-changes. The radiation also has less modulation to it, such that time of arrival based lightning mapping system (like the LMA) are even less likely to locate fast positive breakdown than fast negative breakdown. As a result, studies of fast positive breakdown are relatively scarce.

The investigation into fast positive breakdown is very much a work in progress. This section will establish the existence of fast positive breakdown, and speculate on some of its properties, but offers very few specific measurements of the process.

Fast positive breakdown was observed in a cloud-to-ground flash by *Shao et al.* (1995). In this study, the return stroke of a flash produced a large potential difference between the tips of the positive leaders in the cloud, and the surrounding cloud. Then a burst of VHF radiation, approximately 100 μs long, was seen rapidly extending the positive leaders further into the cloud. Similar processes were seen on numerous occasions during the study, indicating it is a common event.

Unsurprisingly, fast positive breakdown immediately following return strokes has been seen in many of the negative cloud-to-ground lightning strikes recorded by the broadband interferometer as well. Figure 7.4 shows a burst of activity in flash C immediately following the only return stroke in the flash. Very little radiation is produced by the return stroke itself, but after 270 μs, the stroke reached the cloud channels and produced very bright VHF radiation. The channel to ground was approximately 12 km long in this flash, so the delay implies an average return stroke velocity of 4×10^7 m/s. This velocity is a little slow in comparison to other reported return stroke velocities, however, the channel of a bolt from the blue type flash is also exceptionally long.

The activity lasted for just over 1 ms, and formed several channels where no VHF activity had previously been observed. Only the tip of the newly formed channels produced VHF radiation, and the longer lived channels were initiated and then extinguished in approximately 150 μs. Even though the VHF radiation produced at this time was very bright, the LMA map for the flash located virtually none of the activity (as seen in Figure 5.6), and so the length of the newly

215
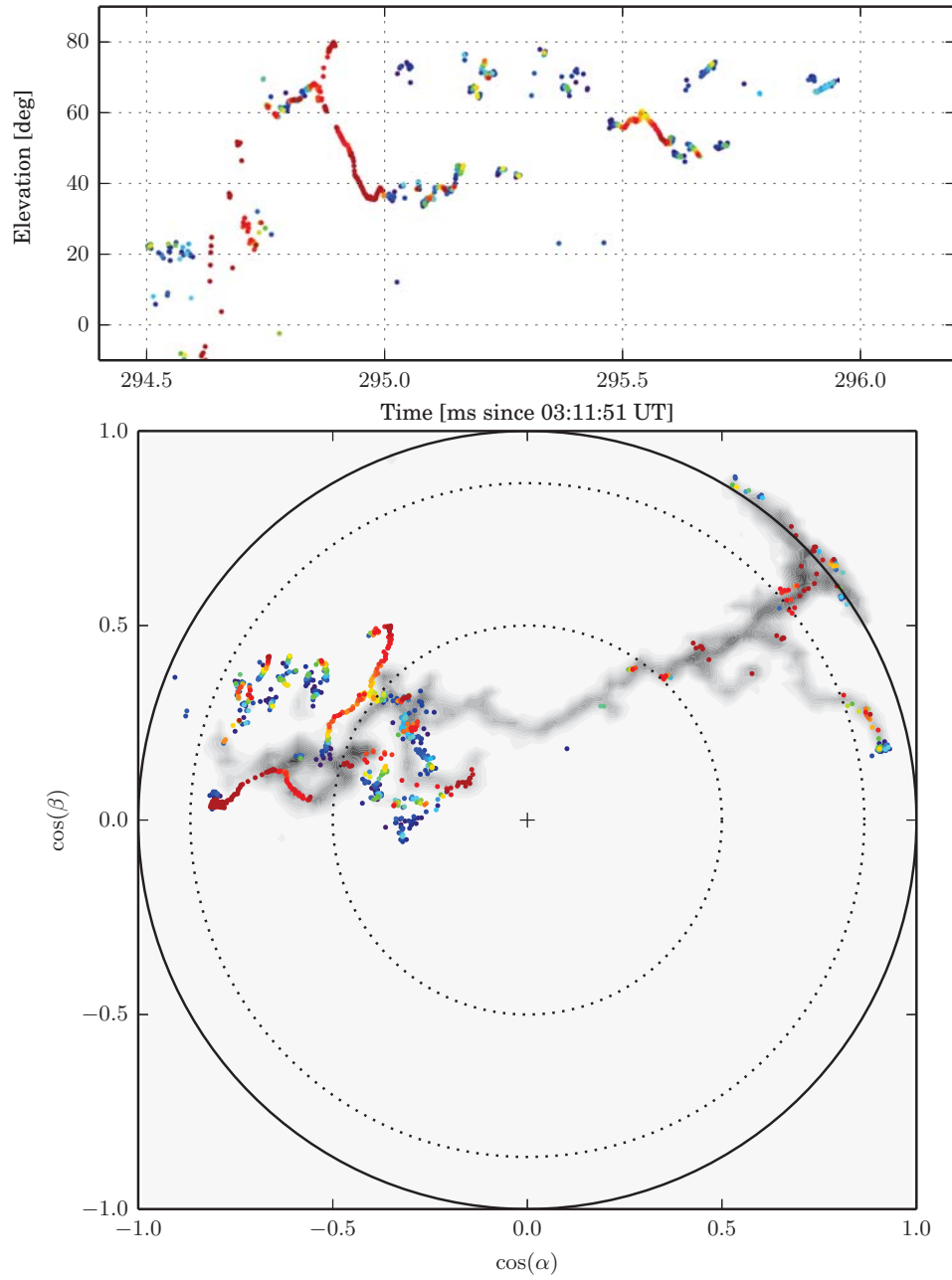
Figure 7.4: Positive breakdown after the return stroke in flash C.

formed channels is currently not known and difficult to estimate. However, the speed at which each channel was formed was as fast or faster than K-changes observed in the same region of the sky, implying an approximate velocity of 10^7 m/s.

There is no fast antenna record for flash C, so the sign of charge carried by the newly formed leaders cannot be ascertained by examining the direction of propagation and the polarity of the electric field deflection. However, flash C is a negative cloud-to-ground flash, and so the return stroke of the flash brings positive charge into the cloud (or removes negative charge from the cloud; the distinction here is not important). It follows then that the fast propagating activity must be carrying positive charge. After being formed, no further VHF radiation was seen from the channels for the remaining duration of the flash, indicating that the fast positive breakdown did not form a conducting channel.

Fast positive breakdown is also seen during K-changes, referred to as positive bursts (*Shao and Krehbiel*, 1996). In this case, once the channels of a lightning flash cut off, the body of the lightning channel structure and the still growing positive leader tip exist at different potentials. Therefore, when the negative breakdown front of a K-change joins with the main channel structure of the flash, the potentials are equalized and a potential wave travels from the junction to the positive leader tip. When the current reaches the positive leader tip, sometimes there is a burst of bright, continuous VHF radiation. While the LMA will frequently locate sources along the path followed by the negative breakdown front, it almost never locates positive bursts.

Several examples of positive bursts were pointed out in the detailed description of Section 5.6 for flash A. Positive bursts are common in lightning flashes, and have been observed in most intracloud flashes extensive enough to have well developed K-changes. Two examples are shown in Figures 7.5 and 7.6, which occurred in flashes C and F, respectively. Additionally, a small positive burst which occurred in flash C is shown, but not discussed, in Figure 6.28.

The positive burst seen in flash C is particularly spectacular, with several of the small branches at the end of the positive leader being excited. In the time series, the slope of the VHF sources associated with the positive burst are clearly moving towards lower elevation angles, which is the direction in which the positive leader is propagating. Unfortunately, the fast antenna was not operational during this flash, so the sign of the charge carried by the positive burst can only be inferred from the direction of motion: positive.

The positive burst for flash F happens very late in the flash, after the third and final negative leader has formed and ceased propagating. The first two bursts occur just after the K-change turns up the vertical channel, a distance of 8 km
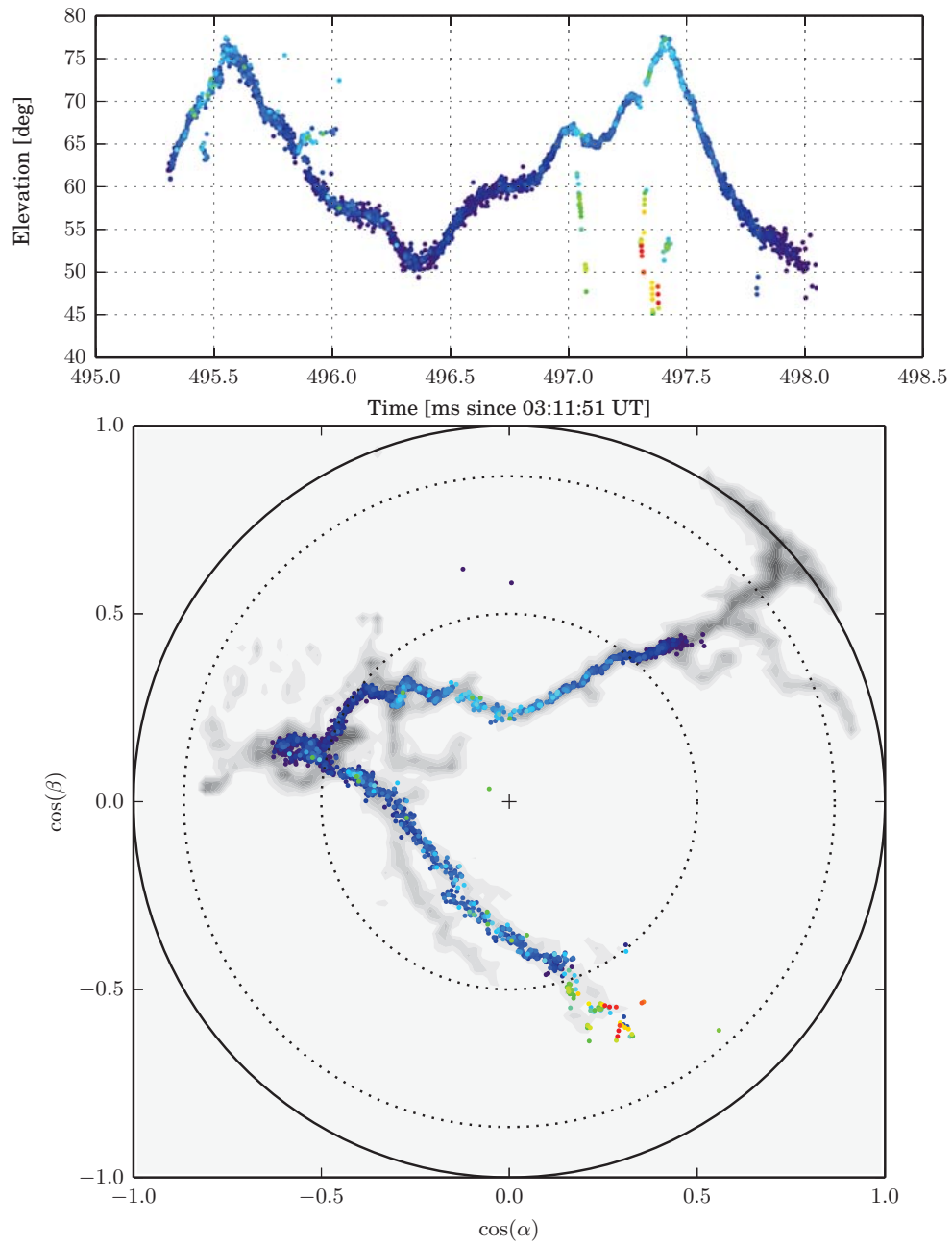
Figure 7.5: Positive burst in flash C.
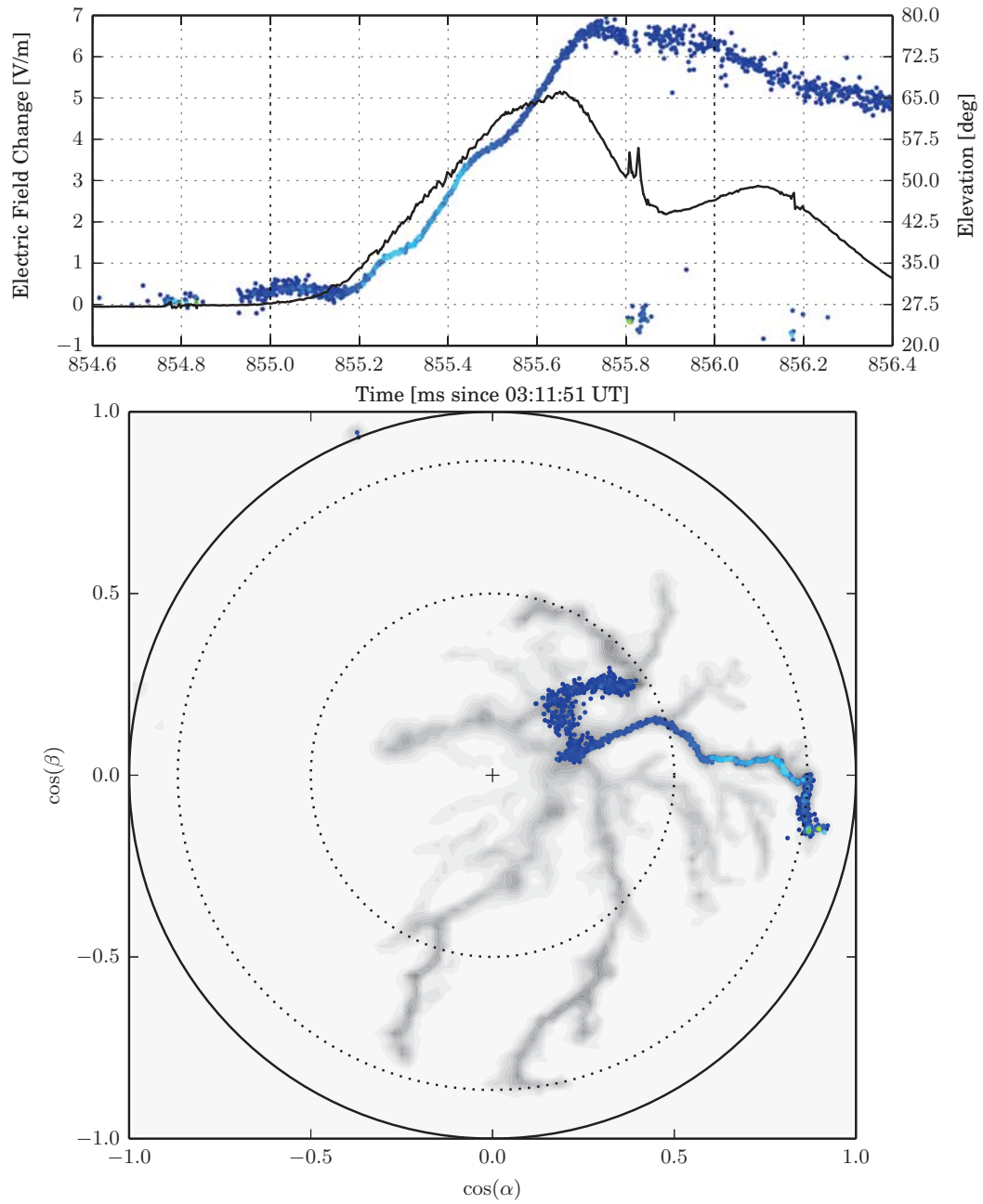
Figure 7.6: Positive burst in flash F.

from the positive leader tip at this time. If a current wave was produced when the K-change reached the vertical channel, then it reached the positive leader tip after a delay of 125 μs, implying a velocity of 6.4×10^7 m/s, which is close to the propagation speed of a return stroke. By this time in the lightning flash, the positive leader tip is far enough away from the interferometer site that the positive burst occurred at a fairly low elevation angle. As a result, it is impossible to reliably ascertain a direction of propagation of the VHF sources from the interferometer map. Assuming the direction of propagation of the burst is away from the positive leader tip (as was the case in flash C), then the sign of the field deflection is consistent with moving positive charge away from the fast antenna.

Whereas the fast positive breakdown seen following a return stroke produces long channels, the positive burst seen during K-changes usually produces fairly short channel extensions. After the positive burst, frequently the positive leader continues propagating in the vicinity of the burst. Because the positive burst channels are short, and because the VHF radiation produced by the propagating positive leader tip has a fairly high location uncertainty, it is not clear if the channel produced by the positive burst is incorporated into the positive leader channel.

Finally, a most unusual example of fast positive breakdown is seen in flash E. As discussed in Section 5.4, this is a normal intracloud flash with a particularly long lasting, extensive negative leader, and a significantly less developed positive leader. At 20:25:12.608 UT, there is a burst of activity where the positive and negative leaders are seen to cross in the interferometer perspective, which lasts for several milliseconds. Figure 7.7 shows an excerpt from this activity.

Based on the map shown in Figure 7.7 alone, it is not clear where the burst of activity originated. However, by examining Figure 5.15, the activity origin corresponds to the furthest extent of the VHF sources located by the LMA in the positive breakdown region. From this, it is clear that the burst of activity initiates near the end of the positive leader and extends outward. Unfortunately, but not unexpectedly, the LMA did not locate any sources along the newly form channels. As a result, an assumption must be made to determine the direction of propagation from the available VHF maps alone. In addition, the electric field records for the process is rather complex, having both sharp negative and positive deflections. Still, the VHF emission is clearly quite similar to the fast positive breakdown above, indicating that the burst of activity almost certainly carries positive charge.

The fast positive breakdown seen in flash E appears very similar to the activity following the return stroke of flash C, even though there is no return stroke in flash E to drive the process. The fast positive breakdown extends a relatively long distance into a region of the sky in which no VHF sources had been
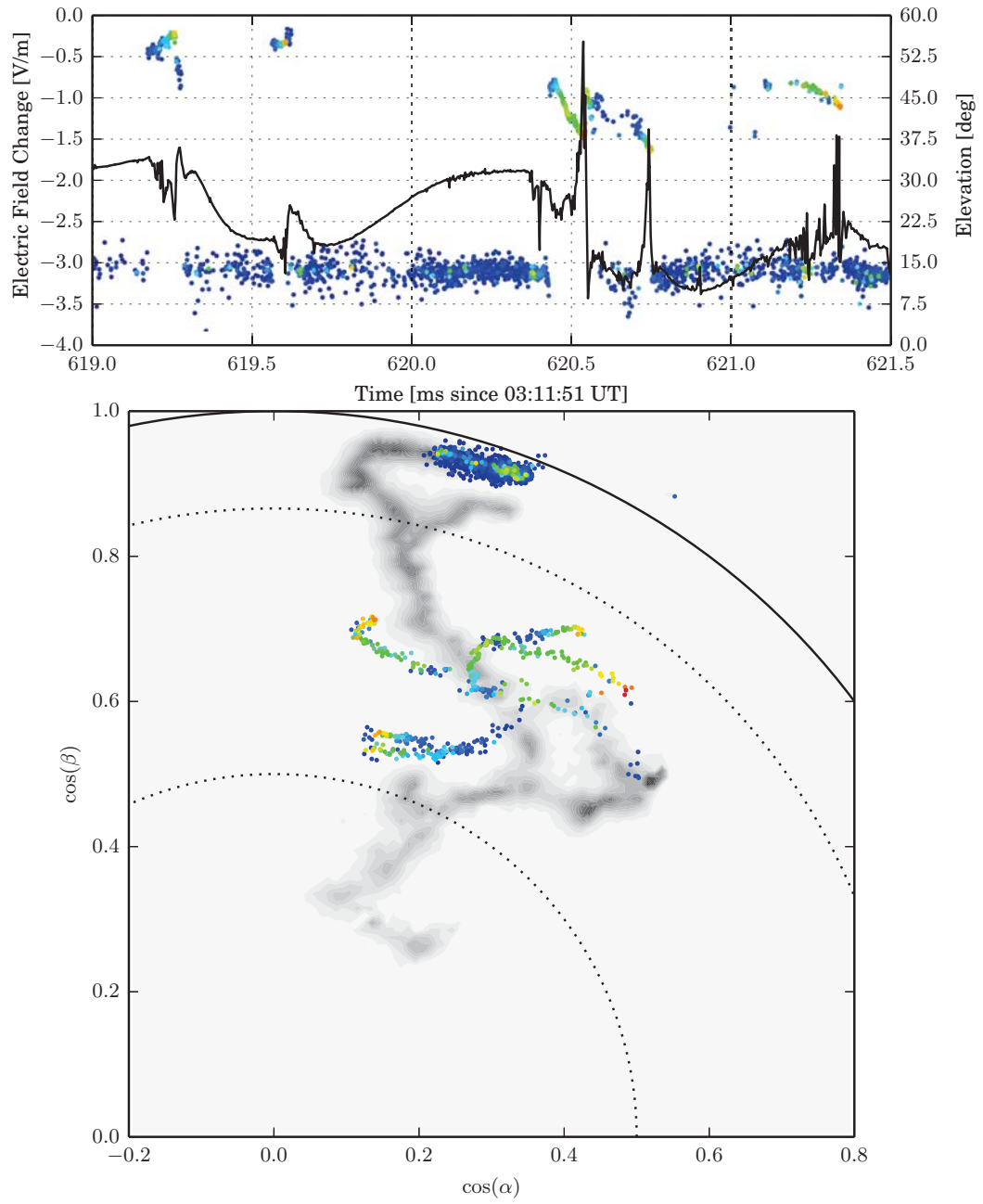
Figure 7.7: Fast positive breakdown in flash E.

previously located. The activity as a whole lasts for a few milliseconds, but each channel is formed and extinguished in approximately 150 μs. After the channels are formed, no further VHF sources are located along them for the remainder of the flash.

The length of the fast positive breakdown channels is puzzling given the lack of a return stroke or K-change to supply a current. There must be some process in the negative leader that is producing a large enough current to supply the fast positive breakdown. Nothing unusual is seen in the activity of the negative leader just prior to the onset of the fast positive breakdown and, after the activity ceases, there is also no change in the behavior of the negative leader. At this stage in the investigation, the cause for the fast positive breakdown in flash E remains a mystery.

7.2.1   Discussion

Investigation into the fast positive breakdown process is only just beginning, and at this stage there are more questions than answers. However, some conclusions into the nature of fast positive breakdown can still be drawn from the observations above. While on the surface, fast positive breakdown appears quite similar to the negative breakdown seen in K-changes, this is not the case. A K-change is a negative leader process which travels along a previously ionized channel, and re-heats the channel to a conducting temperature ($\sim 10,000K$). In contrast, fast positive breakdown extends into virgin air instead of following previously formed channels. Even so, the propagation speed of the process is very high, on the order of 10^7 m/s, which is substantially faster than the propagation speed of normal positive or negative leaders.

The fast positive breakdown process does not produce a conducting channel. If the channel were conducting, the electric field enhancement at the tip of the channel would very likely produce a propagating leader, or at least some additional VHF sources in the streamer zone, neither of which are observed. The implication is that fast positive breakdown is a streamer process, instead of a leader process. Fast positive breakdown does transport charge, as indicated by the substantial electric field deflections seen in flashes E and F. There is also the possibility that the non-conducting channel formed by fast positive breakdown may become conducting in the right conditions.

Even though there are relatively few published studies on the nature of fast positive breakdown, it appears to be a fairly common process in lightning flashes. In the selection of 6 flashes in this study, all but one (flash D) show signs

of fast positive breakdown in one form or another. Excluding the positive bursts seen during K-changes, 3 of the 6 flashes (A, C, and E) show signs of fast positive breakdown. While a rigorous survey of all the flashes seen during a season has not been attempted (some 100+ flashes), a cursory look indicates that these flashes are fairly representative of the entire data set.

CHAPTER 8

CONCLUSION

8.0.1 Processing

The broadband interferometer developed for this study presents a significant improvement over other lightning interferometers used in the past. By continuously sampling the VHF radiation arriving at the antennas, very faint radio point sources produced by lightning can be located. A processing algorithm has been developed which fully utilizes the additional data available by continuously sampling the lightning radiation. The algorithm will locate approximately 100,000 point radio sources in a typical flash, with location uncertainty that depends on received power, but is on the order of 0.1°.

The overall sensitivity of the current interferometer system is comparable to that of the Langmuir LMA, the most sensitive LMA currently deployed. Point sources radiating 20 mW (-20 dBW) in TV channel 3 (6 MHz bandwidth) are regularly located by the interferometer. In the ideal case of a perfect antenna, the minimum detectable signal would be limited by the galactic background noise in the 20-80 MHz range, which is bright compared to other astronomical sources. However, the sensitivity of the current design is limited by thermal noise at the first stage of amplification, indicating that the ultimate sensitivity of the interferometer has not yet been realized.

Algorithms to image the radiation arriving at the antennas have also been developed. Imaging allows for a natural way to increase the number of antennas used in the interferometer arrays, and improve the minimum detectable signal. Increasing the number of antennas also reduces the side lobes of the antenna pattern, making it less likely that a side lobe is mistakenly chosen as the location of a source. In principle, imaging will also allow multiple point sources to be located in a single integration period (currently 1.4 μs). During the exploratory study using 4 VHF antennas (instead of the normal 3), multiple sources could rarely be identified by hand in a single window. Experiments with synthetic data indicate that the dynamic range of a single 4 antenna image is on the order of 2:1. A second source in an integration window will not be apparent in a 4 antenna image

unless it is radiating at least half the power of the brightest source. Increasing the number of antennas in the array quickly improves the dynamic range of the image, but high power side lobes persist even in arrays with 8 antennas. The addition of deconvolution algorithms (such as CLEAN) should help in distinguishing secondary point sources from side lobes; such an algorithm is currently in development.

The lightning maps produced by the interferometer agree very well with maps produced by the LMA, however, the spatial agreement worsens at low elevation angles. It is suspected that the disagreement arises from two sources: spherical wave fronts, and dispersion. If a source is very close to the interferometer, the wave fronts which arrive at the interferometer are spherical instead of planer. In this case, the time delay between antennas is slightly increased, causing the cosine of the elevation angle to be increased at low elevation angles. The effect is especially apparent in cloud-to-ground flashes, as it will push the interferometer sources 'outside' the horizon by making the cosine of the elevation angle larger than 1. If a source is far away, it is also usually at low elevation angles with respect to the interferometer. In these cases, the radio emission propagates through a large amount of relatively high density air. The propagation velocity of the VHF radiation through air is slightly frequency dependent, causing an additional phase difference between the high and low frequencies. The added phase delay causes the time delay between antennas to appear larger, again causing the cosine of the elevation angle to increase. While a correction for spherical wave fronts is being developed, no work has been done to correct the effects of dispersion.

The maps produced by the current interferometer processing algorithm are of exceptional quality. With time, the limitations described above will also be corrected, producing even higher quality maps of lightning.

8.0.2 Observations

The broadband interferometer has proven to be an extremely powerful tool for observing lightning. VHF radiation is detected and located from many processes which occur during a lightning flash. A major exception is that no radiation is observed in conducting channels of the flash. Still, the picture of lightning presented by the broadband interferometer rivals those produced by high speed optical video without being obscured by clouds.

By itself, the broadband interferometer locates VHF lightning sources in two spatial dimensions, where as time of arrival lightning mapping systems (such

as the LMA) can locate sources in three spatial dimensions. The two data sets can be combined into a quasi-3D map, such that the LMA provides the three-dimensional structure of the lightning flash and the interferometer determines where a lightning source is on the channel structure as a function of time. In this way, the three-dimensional location of the LMA can be combined with the very high time resolution and improved continuously radiating source detection of the interferometer. In this study, quasi-3D maps have been used to investigate the velocity of propagation of K-changes.

Velocity measurements of K-changes have been made in the past, though the measurements were limited. Either only the component of the velocity tangential to the instrument was measured, or only the average propagation velocity of the K-change was measured, or both. Here, the high quality of the quasi-3D maps allowed the three-dimensional velocity of K-changes to be measured as a function of time. The results show that the average velocity of a K-change is around 1×10^7 m/s, and that the velocity increases quickly during the first 200 μs of the K-change, followed by a gradual deceleration for the remainder of the process.

In the case of negative leaders, the time and spatial resolution of the interferometer is more than good enough to resolve individual leader steps in the upper positive charge region. At these high altitudes, the leader steps are seen to be very long (100-500 meters), and separated by long periods of VHF quiescence (1-5 ms). The quiescent periods are not entirely devoid of VHF radiation, a glow persists which is thought to be produced by negative streamers. If the inter-step interval is short enough, the glow will completely fill the period between steps. A similar effect is expected if the sensitivity of the interferometer is increased, allowing fainter sources to be located.

The step lengths during the initial vertical and the subsequent horizontal development of the negative leader are roughly the same, but the inter-step interval is about a factor of 2 shorter near the beginning of the flash. Increased electric fields at the origin of the flash are expected to be the cause of the increased stepping rate near the beginning of the flash. The combination of increased step intervals and unchanged step lengths should produce a reduction in the average propagation speed of the negative leader as it propagates into the upper positive charge region. Average propagation velocities of the negative leaders were not measured in this study (but can be using the available LMA data), though a reduction of propagation speed has been observed in studies of negative leaders in the past (*Behnke et al.*, 2005).

Low altitude negative leaders behave quite differently from their high altitude counterparts. Both the step length and step intervals are reduced, as is

the volume of air filled with negative streamer emission. The change in behavior is partially due to the increased pressure at lower altitudes, where increased air density reduces the mean free path of electrons. Additionally, as the negative leader enters the lower positive charge region, the stepping rate rises dramatically. This is likely due to an increase in the electric field by the leader tip (carrying negative charge) and the surrounding cloud (carrying net positive charge in the lower positive charge layer). Interestingly, increased stepping and branching is not observed when the negative leader enters the upper positive charge layer in high altitude leaders.

These conclusions about negative leaders are based on a rather small sampling of leader steps; analysis of additional flashes is needed to make the result concrete. It would be informative to investigate the dependence of step length and interval on pressure. The step length appears to be dependent on the mean free path of electrons and so depends on pressure linearly, whereas the step interval is dependent on the volume of the streamer zone, which would depend on pressure to the third power. Conversely, the electric field at the tip of the leader apparently controls only the rate at which electrons are injected into the streamer zone and not the distance the electrons travel. This simple model predicts testable behavior of the negative leader, however many more steps from a much larger sample of flashes and pressures would have to be analyzed to attempt to validate it.

Copious amounts of faint VHF radiation is located in the positive breakdown region of a lightning flash. Instead of being concentrated at the tip of the propagating leader, as is the case in the negative breakdown region, the emission in the positive breakdown region flickers between widely separated portions of the channel structure. The flickering emission is qualitatively different from the radiation produced by K-changes, and some flickering emission remains, even after all identifiable portions of the interferometer map produced by retrograde negative breakdown are removed. As the flash develops, little or no radiation is seen from the established conducting channels, and the flickering emission loosely concentrates within a few kilometers of the tip of the propagating positive leader. During the later portion of a flash, when K-changes are seen, they are observed to initiate slightly behind the furthest extent of the flickering emission. These observations combine to strongly suggest that this flickering emission is produced by the positive leaders directly, as opposed to being produced by retrograde negative breakdown processes. However, it still remains possible that the flickers are produced by extremely small scale retrograde negative breakdown. For conclusive results, coordinated interferometer and high speed optical observations are needed. Such observations have just recently been obtained, and are the topic of continuing research.

The VHF radiation produced by positive breakdown is not limited to faint flickering. Fast positive breakdown produces very bright VHF radiation, and propagates as fast as a K-change. Unlike K-changes, however, fast positive breakdown begins propagating from the end of the positive breakdown region, and extends the channel. The process is surprisingly common in lightning flashes, and has been observed following return strokes of CG flashes, during K-changes in CG and IC flashes, and during extensive negative leader development in one IC flash.

In all cases, fast positive breakdown produces extremely bright, continuous VHF radiation. The larger events last on the order of 100 μs, and extend a few kilometers into virgin air. The events during K-changes are shorter in duration and extent, but otherwise appear similar. Even in the case of the larger events, the channel produced by the positive breakdown is rarely or never revisited later in the flash. The conclusion from this behavior is that fast positive breakdown does not in general produce a conducting channel, and must therefore be a positive stream process, instead of a leader process. However, it is suspected (but has not been observed) that in certain conditions the channel produced by fast positive breakdown may become conducting. If this is indeed the case, fast positive breakdown may have a role in the initiation of positive cloud to ground flashes.

Even though fast positive breakdown appears to be commonplace in lightning flashes, very few observations of the process have been published. Future studies of this interesting phenomena do face some challenges. Because the radiation produced by fast positive breakdown is continuous, the LMA rarely locates any sources produced by the process. As a result, future studies of fast positive breakdown must rely solely on interferometer measurements. In addition, the quasi-3D conversion used for the study of K-changes is not applicable to fast positive breakdown. However, this study promises to further understanding of lightning physics in general.

REFERENCES

Akita, M. (2011), Broadband interferometric observations of lightning processes in thunderstorms, Ph.D. thesis, Osaka University. 7, 9

Akita, M., Y. Nakamura, S. Yoshida, T. Morimoto, T. Ushio, Z. Kawasaki, and D. Wang (2010), What occurs in K process of cloud flashes?, *Journal of Geophysical Research*, *115*(D7), D07,106. 7, 8, 9, 211

Akita, M., M. Stock, Z. Kawasaki, P. Krehbiel, W. Rison, and M. Stanley (2013), Data processing procedure using distribution of slopes of phase differences for broadband VHF interferometer, *Journal of Geophysical Research*, *X*(X), X. 15, 100

Behnke, S. A., R. J. Thomas, P. R. Krehbiel, and W. Rison (2005), Initial leader velocities during intracloud lightning: Possible evidence for a runaway breakdown effect, *Journal of Geophysical Research: Atmospheres (1984–2012)*, *110*(D10). 145, 146, 174, 226

Berger, K. (1967), Novel observations on lightning discharges: Results of research on Mount San Salvatore, *Journal of the Franklin Institute*, *283*(6), 478–525. 181

Bondiou, A., I. Taudière, P. Richard, and F. Helloco (1990), Analyse spatio-temporelle du rayonnement VHF-UHF associé à l'éclair, *Revue de Physique Appliquée*, *25*(2), 147–157. 6, 211

Boucher, R., and J. Hassab (1981), Analysis of discrete implementation of generalized cross correlator, *Acoustics, Speech and Signal Processing, IEEE Transactions on*, *29*(3), 609–611. 31

Cao, D., X. Qie, S. Duan, J. Yang, and Y. Xuan (2010), Observations of VHF source radiated by lightning using short baseline technology, in *Electromagnetic Compatibility (APEMC), 2010 Asia-Pacific Symposium on*, pp. 1162–1165, IEEE. 1, 7, 26

Carter, G. (1987), Coherence and time delay estimation, *Proceedings of the IEEE*, *75*(2), 236–255. 66

Chen, M., N. Takagi, T. Watanabe, D. Wang, Z.-I. Kawasaki, and X. Liu (1999), Spatial and temporal properties of optical radiation produced by stepped leaders, *Journal of Geophysical Research: Atmospheres (1984–2012)*, *104*(D22), 27,573–27,584. 181

Cummins, K. L., M. J. Murphy, E. A. Bardo, W. L. Hiscox, R. B. Pyle, and A. E. Pifer (1998), A combined TOA/MDF technology upgrade of the US National Lightning Detection Network, *Journal of Geophysical Research: Atmospheres (1984–2012)*, *103*(D8), 9035–9044. 1

Defer, E., P. Blanchet, C. Théry, P. Laroche, J. E. Dye, M. Venticinque, and K. L. Cummins (2001), Lightning activity for the July 10, 1996, storm during the Stratosphere-Troposphere Experiment: Radiation, Aerosol, and Ozone-A (STERAO-A) experiment, *Journal of Geophysical Research: Atmospheres (1984–2012)*, *106*(D10), 10,151–10,172. 6

Dong, W., X. Liu, Y. Yu, and Y. Zhang (2001), Broadband interferometer observations of a triggered lightning, *Chinese Science Bulletin*, *46*(18), 1561–1565. 7, 26

Edens, H. (2011), Bolts from the blue, Ph.D. thesis, New Mexico Institute of Mining and Technology. 111, 164, 181

Edens, H., K. Eack, E. Eastvedt, J. Trueblood, W. Winn, P. Krehbiel, G. Aulich, S. Hunyady, W. Murray, W. Rison, et al. (2012), VHF lightning mapping observations of a triggered lightning flash, *Geophysical Research Letters*, *39*(19). 64, 104, 146, 150, 190

Gorham, P. W., P. Allison, B. M. Baughman, J. J. Beatty, K. Belov, D. Z. Besson, S. Bevan, W. R. Binns, C. Chen, P. Chen, J. M. Clem, A. Connolly, M. Detrixhe, D. De Marco, P. F. Dowkontt, M. DuVernois, E. W. Grashorn, B. Hill, S. Hoover, M. Huang, M. H. Israel, A. Javaid, K. M. Liewer, S. Matsuno, B. C. Mercurio, C. Miki, M. Mottram, J. Nam, R. J. Nichol, K. Palladino, A. Romero-Wolf, L. Ruckman, D. Saltzberg, D. Seckel, G. S. Varner, A. G. Vieregg, and Y. Wang (2010), Observational constraints on the ultra-high energy cosmic neutrino flux from the second flight of the ANITA experiment, *Phys. Rev. D*, *82*, 022,004, doi:10.1103/PhysRevD.82.022004. 41

Hartman, J. M., R. Sonnenfeld, and B. Rison (2012), High-time-resolution imaging of lightning with the Long Wavelength Array, *Bulletin of the American Physical Society*, *57*. 40

Hassab, J., and R. Boucher (1979), Optimum estimation of time delay by a generalized correlator, *Acoustics, Speech and Signal Processing, IEEE Transactions on*, *27*(4), 373–380. 30

Hayenga, C. (1984), Characteristics of lightning VHF radiation near the time of return strokes, *Journal of Geophysical Research*, *89*(D1), 1403–1410. 1, 64

Hayenga, C., and J. Warwick (1981), Two-dimensional interferometric positions of VHF lightning sources, *Journal of Geophysical Research*, *86*(C8), 7451–7462. 3, 4, 39

Hill, J., M. Uman, and D. Jordan (2011), High-speed video observations of a lightning stepped leader, *Journal of Geophysical Research: Atmospheres (1984–2012)*, *116*(D16). 181

Karunarathne, S., T. C. Marshall, M. Stolzenburg, and N. Karunarathna (2014), Modeling initial breakdown pulses of CG lightning flashes, *Journal of Geophysical Research: Atmospheres*. 170

Kawasaki, Z., R. Mardiana, and T. Ushio (2000), Broadband and narrowband RF interferometers for lightning observations, *Geophysical research letters*, *27*(19), 3189–3192. 1, 7, 9, 64

Kawasaki, Z., S. Yoshihashi, and L. J. Ho (2002), Verification of bidirectional leader concept by interferometer observations, *Journal of atmospheric electricity*, *22*(2), 55–79. 7

Kitagawa, N. (1957), On the mechanism of cloud flash and juction or final process in flash to ground, *Papers Meteorol. and Geophys.*, *7*. 21

Kitagawa, N., and M. Brook (1960), A comparison of intracloud and cloud-to-ground lightning discharges, *Journal of Geophysical Research*, *65*(4), 1189–1201. 21, 22

Krehbiel, P. (1981), An analysis of the electric field change produced by lightning, Ph.D. thesis, University of Manchester Institute of Science and Technology. 143, 155

Krehbiel, P. R., J. A. Riousset, V. P. Pasko, R. J. Thomas, W. Rison, M. A. Stanley, and H. E. Edens (2008), Upward electrical discharges from thunderstorms, *Nature Geoscience*, *1*(4), 233–237. 104

Lang, T. J., S. A. Rutledge, J. E. Dye, M. Venticinque, P. Laroche, and E. Defer (2000), Anomalously low negative cloud-to-ground lightning flash rates in intense convective storms observed during STERAO-A, *Monthly weather review*, *128*(1). 6

Laroche, P., A. Bondiou, P. Blanchet, and J. Pigere (1994), 3D VHF mapping of lightning discharge within a storm, paper presented at foudre et montage 94, *Chamonix, France*. 6, 7

Lennon, C. (1975), LDAR–A new lightning detection and ranging system, *Eos, Trans. Amer. Geophys. Union*, *56*, 991. 2

Liu, H., W. Dong, T. Wu, D. Zheng, and Y. Zhang (2012), Observation of compact intracloud discharges using VHF broadband interferometers, *Journal of Geophysical Research: Atmospheres (1984–2012)*, *117*(D1). 7

Maier, L., C. Lennon, T. Britt, and S. Schaefer (1995), LDAR system performance and analysis, in *Proceedings of the International Conference on Cloud Physics*. 1

Mansell, E. R., C. L. Ziegler, and E. C. Bruning (2010), Simulated electrification of a small thunderstorm with two-moment bulk microphysics, *Journal of the Atmospheric Sciences*, *67*(1), 171–194. 117

Marshall, T., M. Stolzenburg, C. Maggio, L. Coleman, P. Krehbiel, T. Hamlin, R. Thomas, and W. Rison (2005), Observed electric fields associated with lightning initiation, *Geophysical research letters*, *32*(3). 104

Marshall, T., M. Stolzenburg, S. Karunarathne, S. Cummer, G. Lu, H.-D. Betz, M. Briggs, V. Connaughton, and S. Xiong (2013), Initial breakdown pulses in intracloud lightning flashes and their relation to terrestrial gamma ray flashes, *Journal of Geophysical Research: Atmospheres*, *118*(19), 10–907. 164

Marshall, T., M. Stolzenburg, S. Karunarathne, and N. Karunaranthna (2014a), Electrical development in lightning before initial breakdown pulses, in *International Conference on Atmospheric Electricity, Norman, OK*. 164, 165, 166, 170

Marshall, T., W. Schulz, N. Karunarathna, S. Karunarathne, M. Stolzenburg, C. Vergeiner, and T. Warner (2014b), On the percentage of lightning flashes that begin with initial breakdown pulses, *Journal of Geophysical Research: Atmospheres*, *119*(2), 445–460. 164, 166

Mazur, V., P. R. Krehbiel, and X.-M. Shao (1995), Correlated high-speed video and radio interferometric observations of a cloud-to-ground lightning flash, *Journal of Geophysical Research: Atmospheres (1984–2012)*, *100*(D12), 25,731–25,753. 211

Miki, M., T. Miki, A. Asakawa, and T. Shindo (2014), Characteristics of negative upward stepped leaders in positive upward lightning, in *International Conference on Atmospheric Electricity, Normal OK*. 181

Moddemeijer, R. (1991), On the determination of the position of extrema of sampled correlators, *Signal Processing, IEEE Transactions on*, *39*(1), 216–219. 31

Morimoto, T., A. Hirata, Z. Kawasaki, T. Ushio, A. Matsumoto, and L. J. Ho (2004), An operational VHF broadband digital interferometer for lightning monitoring, *IEEE Transactions on Fundamentals and Materials*, *124*, 1232–1238. 7

Morimoto, T., Z. Kawasaki, and T. Ushio (2005), Lightning observations and consideration of positive charge distribution inside thunderclouds using VHF broadband digital interferometry, *Atmospheric research*, *76*(1), 445–454. 7

Ogawa, T., and M. Brook (1964), The mechanism of the intracloud lightning discharge, *Journal of Geophysical Research*, *69*(24), 5141–5150. 21

Orville, R. E. (1968), Spectrum of the lightning stepped leader, *Journal of Geophysical Research*, *73*(22), 6999–7008. 19

Proctor, D. (1981), VHF radio pictures of cloud flashes, *Journal of Geophysical Research*, *86*(C5), 4041–4071. 1, 2

Qie, X., T. Zhang, C. Chen, G. Zhang, T. Zhang, and W. Wei (2005), The lower positive charge center and its effect on lightning discharges on the Tibetan Plateau, *Geophysical research letters*, *32*(5), L05,814. 26

Qiu, S., B. Zhou, L. Shi, W. Dong, Y. Zhang, and T. Gao (2009), An improved method for broadband interferometric lightning location using wavelet transforms, *Journal of Geophysical Research*, *114*(D18), D18,211. 7, 26, 64

Qiu, S., B.-H. Zhou, and L.-H. Shi (2012), Synchronized observations of cloud-to-ground lightning using VHF broadband interferometer and acoustic arrays, *Journal of Geophysical Research: Atmospheres (1984–2012)*, *117*(D19). 26, 211

Rhodes, C. (1989), Interferometric observations of VHF radiation, Ph.D. thesis, New Mexico Institute of Mining and Technology. 4, 64

Rhodes, C., X. Shao, P. Krehbiel, R. Thomas, and C. Hayenga (1994), Observations of lightning phenomena using radio interferometry, *Journal of geophysical research*, *99*(D6), 13,059–13. 1, 28, 141, 211

Richard, P., A. Delannoy, G. Labaune, and P. Laroche (1986), Results of spatial and temporal characterization of the VHF-UHF radiation of lightning, *Journal of Geophysical Research*, *91*(D1), 1248–1260. 1

Rison, W., R. Thomas, P. Krehbiel, T. Hamlin, and J. Harlin (1999), A GPS-based three-dimensional lightning mapping system, *Geophysical research letters*, *26*(23), 3573–3576. 1, 6

Rust, W. D., D. R. MacGorman, E. C. Bruning, S. A. Weiss, P. R. Krehbiel, R. J. Thomas, W. Rison, T. Hamlin, and J. Harlin (2005), Inverted-polarity electrical structures in thunderstorms in the Severe Thunderstorm Electrification and Precipitation study (STEPS), *Atmospheric research*, *76*(1), 247–271. 104

Saba, M. M., K. L. Cummins, T. A. Warner, E. P. Krider, L. Z. Campos, M. G. Ballarotti, O. Pinto, and S. A. Fleenor (2008), Positive leader characteristics from high-speed video observations, *Geophysical Research Letters*, *35*(7). 150

Schonland, B., D. Malan, and H. Collens (1935), Progressive lightning II, *Proceedings of the Royal Society of London. Series A-Mathematical and Physical Sciences*, *152*(877), 595–625. 181

Schonland, B. F. J. (1956), The lightning discharge, *Handbuch der Physik*, *22*, 576–628. 181

Schultz, C. J., W. A. Petersen, and L. D. Carey (2011), Lightning and severe weather: A comparison between total and cloud-to-ground lightning trends, *Weather and forecasting*, *26*(5), 744–755. 1

Shao, X., and P. Krehbiel (1996), The spatial and temporal development of intracloud lightning, *Journal of geophysical research*, *101*(D21), 26,641–26. 5, 106, 143, 189, 211, 217

Shao, X., P. Krehbiel, R. Thomas, and W. Rison (1995), Radio interferometric observations of cloud-to-ground lightning phenomena in Florida, *Journal of geophysical research*, *100*(D2), 2749–2783. 5, 153, 211, 215

Shao, X., D. Holden, and C. Rhodes (1996), Broad band radio interferometry for lightning observations, *Geophysical research letters*, *23*(15), 1917–1920. 1, 6, 7

Shao, X., C. Rhodes, and D. Holden (1999), RF radiation observations of positive cloud-to-ground flashes, *Journal of Geophysical Research: Atmospheres (1984–2012)*, *104*(D8), 9601–9608. 189

Shao, X.-M. (1993), The development and structure of lightning discharges observed by VHF radio interferometer, Ph.D. thesis, New Mexico Institute of Mining and Technology. 143

Stock, M., M. Akita, P. Krehbiel, W. Rison, H. Edens, Z. Kawasaki, and M. Stanley (2014), Continuous broadband digital interferometry of lightning using a generalized cross-correlation algorithm, *Journal of Geophysical Research: Atmospheres*, *119*(6), 3134–3165. 15, 26, 39, 40, 64, 65, 103, 139

Sun, Z., X. Qie, M. Liu, D. Cao, and D. Wang (2012), Lightning VHF radiation location system based on short-baseline TDOA technique–validation in rocket-triggered lightning, *Atmospheric Research*. 7, 13, 26

Tantisattayakul, T., K. Masugata, I. Kitamura, and K. Kontani (2005), Broadband VHF sources locating system using arrival-time differences for mapping of lightning discharge process, *Journal of atmospheric and solar-terrestrial physics*, *67*(11), 1031–1039. 26, 64

Taylor, G. B., C. L. Carilli, and R. A. Perley (Eds.) (1999), *Synthesis imaging in radio astronomy II*, vol. 180, Astronomical Society of the Pacific. 43

Thomas, R., P. Krehbiel, W. Rison, T. Hamlin, J. Harlin, and D. Shown (2001), Observations of VHF source powers radiated by lightning, *Geophysical Research Letters*, *28*(1), 143–146. 74, 100, 143, 189

Thomas, R., P. Krehbiel, W. Rison, S. Hunyady, W. Winn, T. Hamlin, and J. Harlin (2004), Accuracy of the Lightning Mapping Array, *Journal of geophysical research*, *109*(D14), D14,207. 1, 6, 74

Trueblood, J. (2013), Triggered upward negative lightning leaders, Master's thesis, New Mexico Institute of Mining and Technology. 104

Uman, M. A. (1987), *The lightning discharge*, Courier Dover Publications. 166

Uman, M. A., D. K. McLain, and E. P. Krider (1975), The electromagnetic radiation from a finite antenna, *Am. J. Phys*, *43*(1), 33–38. 166

Ushio, T., Z. Kawasaki, Y. Ohta, and K. Matsuura (1997), Broad band interferometric measurement of rocket triggered lightning in japan, *Geophysical research letters*, *24*(22), 2769–2772. 1, 6, 7, 9

Warner, T. A. (2012), Observations of simultaneous upward lightning leaders from multiple tall structures, *Atmospheric Research*, *117*, 45–54. 150

Warner, T. A., M. Saba, R. Orville, K. Cummins, and L. WA (2013), Differences in positive and negative lightning leader appearance and behavior as observed by high-speed cameras, in *Presented at the Sixth Conference on the Meteorological Applications of Lightning Data, Austin, TX*. 145

Warwick, J. W., C. O. Hayenga, and J. W. Brosnahan (1979), Interferometric directions of lightning sources at 34 MHz, *Journal of Geophysical Research: Oceans (1978–2012)*, *84*(C5), 2457–2468. 1, 2, 3

Weidman, C. D., and E. P. Krider (1979), The radiation field wave forms produced by intracloud lightning discharge processes, *Journal of Geophysical Research: Oceans (1978–2012)*, *84*(C6), 3159–3164. 164

Willett, J., J. Bailey, and E. Krider (1989), A class of unusual lightning electric field waveforms with very strong high-frequency radiation, *Journal of Geophysical Research: Atmospheres (1984–2012)*, *94*(D13), 16,255–16,267. 124

Winn, W., G. Aulich, S. Hunyady, K. Eack, H. Edens, P. Krehbiel, W. Rison, and R. Sonnenfeld (2011), Lightning leader stepping, K changes, and other observations near an intracloud flash, *Journal of Geophysical Research: Atmospheres (1984–2012)*, *116*(D23). 164, 174, 181